# Fabrication, structure and thermoelectric properties of oriented and sequentially doped thin films of regioregular poly (3-hexylthiophene)

Viktoriia Untilova

# UNIVERSITÉ DE STRASBOURG

*ÉCOLE DOCTORALE de*
*Physique et Chimie-physique (ED-182)*

**INSTITUT CHARLES SADRON (UPR 22)**

# THÈSE

présentée par :

**Viktoriia UNTILOVA**

Soutenue le: **17 décembre 2020**

pour obtenir le grade de : **Docteur de l'Université de Strasbourg**
Discipline/ Spécialité : **Physique et Chimie-physique**

## *Fabrication, structure and thermoelectric properties of oriented and sequentially doped thin films of regioregular poly (3-hexylthiophene)*

**THÈSE dirigée par :**

**Dr. BRINKMANN Martin**
Directeur de Recherche CNRS, Institut Charles Sadron, Strasbourg, France

**RAPPORTEURS:**

**Dr. GRIGORIAN Souren** Dr. HDR., Head of SMPG, University of Siegen, Germany
**Dr. CARELLA Alexandre** Dr. HDR., Senior researcher at CEA, Grenoble, France

---

**AUTRES MEMBRES DU JURY :**

**Prof. LUDWIGS Sabine** Professor, University of Stuttgart, Germany
**Dr. LECLERC Nicolas** Dr. HDR, Chargé de recherché, ICPEES, Strasbourg, France
**Dr. BISKUP Till** Dr. HDR, Research fellow, University of Saarland, Germany

*To my dear father Stanislav*

*a man who followed his dream*

## Acknowledgements

*"As you start to walk on the way, the way appears."*

Rumi

Firstly, I would like to express my gratitude to Creator. I believe everything that is, is already perfect, all we need is to realize what we are truly grateful for.

I am happy for having gone through this extremely enriching experience at the ***Institute Charles Sadron*** in the surrounding of great people.

As my thesis director, **Dr. Martin Brinkmann** was an excellent mentor and beautiful teacher for me. Being always there to carefully guide me and help to clarify any scientific questions I had all along the way, Martin was a great supervisor I could possibly wish for. Martin, I am so grateful for your patience, openness and responsiveness. This means a lot to me! Thanks for sharing all your experience with us, thanks for the time and space you were constantly giving us to reflect on things. This amazing experience, you offered to us will serve as a cornerstone of future growth. I will simply say: Thank you, you are the best!

**Dr. Laure Biniek** were co-mentoring me during the first half of my thesis. Laure, I want to express my gratitude to you for being always of a great assistance to us, for your time you generously dedicated to us for discussions, experiments, helping with both scientific and personal cares. Thanks for being always kind, open and supportive! I wish you to have more productive students and collaborators all along your career path as a researcher.

I would like to thank to **Dr. Mark Schmutz** and **Dr. Christian Blanck** for teaching me to operate TEM CM12 and for maintaining TEM platform in excellent state. I feel proud for this experience passing hours in the room of TEM doing electron diffraction and high-resolution imaging! I am happy being taught by true passionate experts in TEM!

Many thanks to **Mr. Laurent Herrmann** for designing the rubbing machine which I used a lot in this scientific work. Thanks for being friendly and always there in case of any technical problem. Thanks for small talks we used to have in the couloirs of SYCOMMOR.

A special thanks to **Dr. Bernard Lotz**, I appreciate a lot having a chance to meet you! Thanks for giving a read to our papers. It was my honor.

I want to express my gratitude to all people that were collaborating with us all along the way: **prof. Dr. Christian Müller**, **Dr**. **Jonna Hynynen**, **Anna Hoffmann**, **prof. Dr. Sabine Ludwigs**, **Yannick Gross**, **Dr. Michael Sommer**, **Dr. Till Biskup**, **prof. Dr. Nicolas Leclerc**, **Pablo Durand**. Christian, many thanks for visiting our lab and giving a speech on IRTG Discussion meeting in Schluchsee. Thanks for a fruitful collaboration with you, Jonna and Anna! Many thanks, Till, for welcoming me in Freiburg in your lab and for performing EPR experiments with me. I enjoyed a lot our discussions during IRTG seminars and common diners within the scientific community, thanks for an exciting diner in Italian restaurant in Freiburg! I am grateful to Nicolas and Pablo for synthesising polymers and dopants for our group! Dear Jonna, Anna and Pablo, I wish all of you to have a successful future ahead!

I am very grateful for being a part of International Research Training Group (IRTG) led by **prof. Dr. Jörg Baschngel** and **Dr. Günter Reiter**. This experience allowed me to meet a lot of new interesting people, to participate and present my scientific results during several discussion meetings and workshops organised by IRTG and just to have a wonderful time traveling a lot in Germany! Personal thanks to Dr. Jörg Baschngel for helping to receive a financial support for current thesis. Also I had a great pleasure to follow your lectures during my Master-2 at IPCMS that I enjoyed a lot!

A special thanks to IRTG Coordinators: **Birgitta Zovko** and **Dr. Jana Husse**. You were incredible organizers, always being very kind and thoughtful to all students. Thanks for making my memories about the IRTG times simply unforgettable!

Many thanks and respect to Région GrandEst and French Government for giving a wonderful opportunity for growing as professionals for foreign citizens and for treating them like their own citizens! Many thanks for financial aid to ANR (Agence nationale de la recherche) and to IRTG Softmatter project.

Many thanks to **Mme Odile Lemblé** for helping with all administration processes. I would like to note a special thanks for helping to find an apartment!

Thanks to all jury members for agreeing to be in jury committee and granted me the title of Doctor of the University of Strasbourg:

- **Dr. Souren Grigorian**

Thanks for a great assessment you wrote for my thesis manuscript. Thanks for nice discussion during my thesis defense and for being amiable.

- **Dr. Carella Alexandre**

Thanks for fruitful discussion and we had during my thesis defense. Many thanks for a very positive assessment you wrote for my thesis manuscript.

- **Prof. Dr. Sabine Ludwigs**

Thanks for finding time to carefully go through my thesis manuscript and for a nice discussion during my defense. Also thanks for collaboration we had with you on n-type polymer materials.

- **Dr. Nicolas Leclerc**

I would like to thank you again for guiding the PhD defense as a president of a jury committee. I also grateful for co-working with you in the frame of ANR Anisotherm project which were a very pleasant experience.

- **Dr. Till Biskup**

I would like to thank you for a nice experience during the thesis defense. Thanks for a wonderful time I had with you while performing EPR measurements in Freiburg.

I want to thank to previous PhD students of our group: **Dr. Amer Hamidi-Sakr**, **Dr. Morgane Diebold** and **Dr. Vishnu Vijayakumar**. I was very happy to meet you as a Master/Doctoral student of SYCOMMOR. Thanks for being friendly, open and supportive! Thanks to Vishnu for you sense of humour and friendship all along two years you were present in the lab.

Thanks to my fellow PhD students **Marion Brosset**, **Huiyan Zeng**, **Duncan Schwaller, Ricardo Avila** and **Quentin Weinbach** for amazing time we had together! Thanks for extremely amazing PhD gifts! I wish you the best of luck for your future!

Thanks to other students of the institute: **Lisa, Fedir, Marina, George, Anastasiia, Yuhan, Eulalie, Felipe** for a friendly environment. And good luck for your future!

Thanks to my friends **Lyudmila** and **Anatolii** for your enormous support all along the way through my ups and downs. I appreciate you a lot! I have very nice memories from our trip to Croatia and small trips to Germany! Simply thanks for being my friends ☺

Thanks to my beloved – **Bogdan**. A magic of our encounter can't be described in words. I want to express my deep gratitude and appreciation for simply having you in my life. Despite a thousand miles between us I could feel your love and connection. Thank you for being a precious part of my life ♡

A special thanks to my guru **Dr. Viktor Kiryan**. Thanks for guiding me along the way which is the most essential although uneasy – *a path to yourself.* Thanks for helping me to find inner wisdom inside myself. You helped me a lot to overcome difficult feelings and to become more conscious. Without this my life experience would not be as wonderful as it is. No words can describe my deep gratitude to you, so I would like to simply say: Thank you!

Finally, endless appreciation and respect to my mom **Svitlana** and father **Stanislav** as well as to my brother **Vitalii**. Thanks for your patience, love and openness. Thanks to each one of you for being as you are, true and sincere.

## Table of contents

## List of abbreviations:

| | |
|---|---|
| $(SN)_x$ | polysulfur nitride |
| AcN | acetonitrile |
| AFM | Atomic Force Microscopy |
| BF TEM | Bright Field TEM mode |
| $Bi_2Te_3$ | bismuth telluride |
| $C_{12}$-pBTTT | Poly[2,5-bis(3-dodecylthiophen-2-yl)thieno[3,2-b]thiophene] |
| CB | chlorobenzene |
| CC | charge carriers |
| CP | conjugated polymers |
| $CHCl_3$ | Chloroform |
| CN6-CP | hexacyano-trimethylene-cyclopropane |
| $CS_2$ | Carbon disulfide |
| CSA | camphor sulphonic acid |
| CT | charge transport |
| CTC | charge transfer complex |
| DBSA | dodecyl benzene sulphonic acid |
| DD | direct doping |
| DFT | density functional theory |
| DPP | diketopyrrolopyrrole |
| DR | dichroic ratio |
| EA | Electron affinity |
| EBSA | ethyl-benzene sulphonic acid |
| ED | Electron diffraction |
| $E_g$ | band gap energy |
| $E_t$ | transport edge energy |
| $F_4$TCNQ | 2,3,5,6-Tetrafluoro-7,7,8,8-tetracyanoquinodimethane |
| $F_6$TCNNQ | 1,3,4,5,7,8-hexafluoro-tetracyanonaphthoquinodimethane |
| $F_8$BT | poly(9,9-di-n-octylfluorene-alt-benzothiadiazole) |

| | |
|---|---|
| $FeCl_3$ | Ferric Chloride |
| FET | Field Effect Transistor |
| FTS | Perflurooctyl-trichlorosilane |
| GIXD | Grazing X-ray diffraction measurement |
| HH | head-to-head coupling |
| HOMO | highest occupied molecular orbital |
| HR TEM | High-Resolution TEM mode |
| HT | head-to-tail coupling |
| $I_2$ | iodine |
| ICD | incremental concentration doping |
| ICT | integer charge transfer |
| IP | ionization potential |
| K−BrBz | potassium 4-bromobenzoate |
| kMC | kinetic Monte-Carlo method |
| LUMO | lowest unoccupied molecular orbital |
| Magic Blue | tris(4-bromophenyl)ammoniumyl hexachloroantimonate |
| $M_n$ | Number average molecular weight |
| $Mo(tfd\text{- }COCF_3)_3$ | Molybdenum tris(1-(trifluoroacetyl)-2-(trifluoromethyl)ethane-1,2-dithiolene) |
| $Mo(tfd)_3$ | Molybdenum tris(1,2-bis(trifluoromethyl)ethane-1,2-dithiolene) |
| MR | molar dopant fraction |
| $M_w$ | Molecular weight |
| NDI | naphthalene diimide |
| N-DMBI | 4-(2,3-Dihydro-1,3-dimethyl-1H-benzimidazol-2-yl)-N,N-dimethylbenzenamine |
| N-DPBI | 4-(1,3-Dimethyl-2,3-dihydro-1H-benzoimidazol-2-yl)-N,N-diphenylaniline |
| $NOPF_6$ | Nitrosonium hexafluorophosphate |
| oDCB | orthodichlorobenzene |
| OFET | Organic Field Effect Transistor |
| OLED | Organic Light Emitting Diodes |
| OP | order parameter |
| $OP_{P1}$ | order parameter of the polaron |
| P3AT | poly(3-alkylthiophenes) |

| | |
|---|---|
| P3DT | poly(dodecylthiophene) |
| P3HT | poly(3-hexylthiophene) |
| PA | polyacetylene |
| PBTTT | poly(2,5-bis(3-alkylthiophen-2-yl)thieno[3,2-b]thiophene) |
| PCBM | phenyl-C61-butyric acid methyl ester |
| PDI | polydispersity |
| PDMS | polydimethylsiloxane |
| PE | polyethylene |
| PEDOT | poly(3,4-ethylenedioxythiophene) |
| PET | polyethylene terephthalate |
| PF | power factor |
| PFB | poly(9,9-di-n-octylfluorene-alt-bis-N,N-(4-butylphenyl)-bis-N,N-phenyl-1,4-phenylenediamine) |
| PNDI2ODT2 | Poly{[N,N'-bis(2-octyldodecyl)naphthalene-1,4,5,8-bis(dicarboximide)-2,6-diyl]-alt-5,5'-(2,2'-bithiophene)} |
| poly[$K_x$(Ni-ett)] | poly[Kx(Ni-ethylenetetrathiolate)] |
| PPV | polyphenylene vinylene |
| PSS | polystyrene sulfonate |
| PT | polythiophene |
| PTFE | poly (tetrafluoroethylene) |
| PTV | poly(2,5-thienylene vinylene) |
| R | rubbing direction |
| RR | Regioregular |
| RRa | Regiorandom |
| SCP | Semiconducting polymer |
| SEM | Scanning Electron Microscopy |
| SqD | sequential doping |
| STM | scanning tunnelling microscopy |
| SWNT | single-wall carbon nanotube |
| $T_2$ | bithiophene |
| TCB | 1,3,5-trichlorobenzene |

| | |
|---|---|
| TCNQ | Tetracyanoquinodimethane |
| TE | thermoelectric(ity) |
| TEG | thermoelectric generator |
| TEM | transmission electron microscopy |
| TFB | poly(9,9-di-n-octylfluorene-alt-(1,4-phenylene-((4-sec-butylphenyl)imino)-1,4-phenylene) |
| Tos | Tosylate |
| tpp- | triphenylphosphine |
| $T_R$ | Rubbing temperature |
| TT | tail-to-tail coupling |
| UV–vis–NIR | Ultraviolet-Visible-near-Infrared |
| VRH | variable-range hopping |
| W | exciton bandwidth |
| WAXS | Wide angle X-ray scattering |
| zT | figure of merit |
| α-NPD | N,N’-di-[(1-naphthyl)-N,N’-diphenyl]-1,1’-biphenyl-4,4’-diamine |
| $\alpha$ | Seebeck coefficient |
| T | Temperature |
| $\sigma$ | electrical conductivity |
| $\kappa$ | thermal conductivity |
| $\mu$ | mobility |
| $(SN)_x$ | polysulfur nitride |

# Introduction

## Introduction

The net consumption of electricity worldwide has increased dramatically from 1980 to 2017, namely from 7.3 to 22.3 TWh, respectively.[1] Nearly 50% of that amount was generated from gas and coal. For example, in 2016 the total world energy came from oil 32%, gas 22%, coal 26%, biomass 10%, only 5% nuclear and 5% renewables.[2] Based on REN21's (Renewable Energy Policy Network for the 21st Century) 2017 report, renewables contributed 19.3% to humans' global energy consumption. Unfortunately, the consumption of the produced energy is accompanied by the release of the waste heat. Waste heat is heat that is produced by a machine, or other process that uses energy, as a byproduct of doing work.[3] Due to the limited efficiencies of power plants it is necessary to burn more fuels in order to achieve the desired energy output. This contributes to an increase of greenhouse gas emissions and global warming. For example, cars generate about two times more waste heat than actual useful work (with η≈25%).[4]

The waste heat conversion to electricity can be realized by means of thermoelectricity (TE). Over the last decades, the inorganic TE has progressed dramatically. Different technologies have been developed to build efficient TE generators (TEGs) such as silicon technologies both CMOS compatible (such as N- and P-type polycrystalline silicon, poly-SiGe and recently silicon nanowires (SiNW) and non-compatible materials like Bi–Sb–Te alloy.[5] The performance of TE material is usually characterized by the dimensionless figure of merit:

$$zT = \frac{\alpha^2 \sigma}{\kappa} T ,$$

where $\alpha$ - the Seebeck coefficient, $\sigma$ - the electrical conductivity, $\kappa$ - the thermal conductivity. A good TE material must have high $\sigma$ and $\alpha$, and low $\kappa$. The nominator of

$\alpha^2\sigma$ is also called power factor (PF) which represents the potential efficiency of the material. The material's TE efficiency can be compared through the PF value for materials having similar thermal conductivity.

Inorganic TE technologies have been well-developed over the last decades reaching high figure of merit zT > 1.[5] However, inorganic TE materials are expensive to micro-fabricate and contain highly toxic elements such as tellurium, antimony and lead.[6]

In 2000 Alan J. Heeger, Alan G. MacDiarmid and Hideki Shirakawa were awarded the Nobel Prize for the development of electrically conductive polymers. Since then, the development of organic thermoelectric materials has aroused real enthusiasm following a trend already observed in other fields such as photovoltaics, transistors, light emitting diodes, etc.[7] Conductive polymers were actively studied in the domains listed above, but the TE properties of the materials were uncovered only recently.[8]

Unlike inorganic TE materials, organic ones are easy to process. Simple modification of their molecular structure allows tuning the physico-chemical properties in fairly large range. Moreover, they are low-cost organic materials consisting of abundant elements such as carbon, nitrogen, sulphur and oxygen. Furthermore, polymers are characterized by a low thermal conductivity (ca. 0.2 W $m^{-1}$ $K^{-1}$) which makes them ideal for TE applications.

The true interest for organic TE has aroused after the seminal work of X. Crispin and O. Bubnova in 2011. They demonstrated that polymers such as poly(3,4-ethylenedioxythiophene) (PEDOT) doped with tosylate (Tos) can reach high zT values required for efficient TE devices e.g. zT = 0.25 ($\sigma$ ~ 300 S/cm) at room temperature.[9] The same polymer doped by polystyrene sulfonate (PSS) reaches zT = 0.42.[10] A general analysis on doped

polymers showed that $PF \sim \sigma^{1/2}$ , hence improving conductivity is a strategy to follow. Since then other polymer:dopant systems have been developed, e.g. P3HT (poly(3-hexylthiophene)), PBTTT (poly(2,5-bis(3-tetradecylthiophen-2yl)thieno(3,2-b)thiophene)), DPP (diketopyrrolopyrrole)-based copolymers etc. that can be doped by various oxidants such as $I_2$, $F_4$TCNQ (2,3,5,6-Tetrafluoro-7,7,8,8-tetracyanoquinodimethane), $F_6$TCNNQ (hexafluoro-tetracyanonaphtho-quinodimethane), FTS (ferric p-toluene sulfonate) and also metal-organic compounds such as Mo(tfd-$COCF_3$)$_3$ (Molybdenum tris(1-(trifluoroacetyl)-2 - (trifluoromethyl) ethane-1,2-dithiolene)) and $FeCl_3$ (iron(III) chloride). As all conjugated polymers are initially semiconducting, it is necessary to introduce the charge carriers in the system by means of doping.

Within the scope of this work only p-type systems are considered, meaning that the majority of the charge carriers are holes. PF can be significantly improved through better conductivity. Therefore, it plays a big role in the final device performance. According to X. Crispin et al, electrical conductivity of conjugated polymers depends a lot on: morphology, microstructure and number of counter ions that balance the positive doping charge carried by the conjugated polymer chain. [9]

Thin films of PBTTT-doped by fluoroalkylsilanes (FTS) allowed to reach the electrical conductivity of 1000 S/cm.[11] Semicrystalline P3HT films doped by $F_4$TCNQ reaches a conductivity of up to 12.7 S/cm.[12] Vapour-doped P3HT:$F_4$TCNQ films reaches higher PF value of 27 μW $m^{-1}$ $K^{-2}$, where conductivity was around 37 S/cm.[13]

Conductivity of doped polymers is determined by: i) the choice of dopant/polymer, ii) the doping method, iii) the morphology/structure of pristine and doped phase, iv) the orientation of the backbone.

i) The choice of dopant/polymer is first of all referred to the gap between dopant's LUMO and polymer's HOMO which allows an efficient charge transfer in case of p-type material.

ii) Different doping methods have been investigated in literature such as mixed solution/ sequential processing[14,15], vapour phase doping[12,13], and more recently incremental concentration doping (ICD).

Moulé et al. have demonstrated a drastic increase in conductivity for sequentially processed (SqP) films in compare to mixed-solution processed due to better structural order.[14] The difference between these two methods is the following: in SqP method films are deposited on a substrate with subsequent doping, whereas in mixed-solution method both polymer and dopant are co-dissolved and film is further prepared by drop-casting this mixture on a substrate. SqP allows to have a better solid-state order, the morphology can be semi-crystalline or liquid-crystalline as it is usually seen for conjugated polymer films.[12,14,15] Vapour-phase doping is another method that allows to intercalate dopant molecules progressively into the pristine polymer structure without the need for an organic solvent that can interact also with the polymer during doping. Chabinyc et al have reported a significant increase in conductivity of vapour doped P3HT:$F_4$TCNQ films up to 48 S/cm in compare to SqP.[13] These results underline the importance of the doping process on the resulting PF of doped polymers.

iii) The structure of pristine polymer films depends strongly on: chemical parameters of the polymer such as molecular weight, regioregularity, polydispersity, film preparation methods and crystallinity. Hynynen et al. demonstrated the correlation between the P3HT film's initial crystallinity and the final conductivity of $F_4$TCNQ doped films[12] whereas Scholes et al showed that a higher degrees of film crystallinity leads to higher mobility and greater

polaron delocalization in the doped state.[16] A similar result was also evidenced in oriented films of P3HT for which improved alignment and crystallinity result in improved TE properties in P3HT:$F_4$TCNQ system reaching $\sigma \sim 22$ S/cm.[16] Presence of the polymer backbone orientation within the film allows to further increase the device efficiency on a macroscale.

iv) The orientation of polymer backbones with respect to a substrate is a powerful tool to increase the TE performances. The unique alignment technique by high-T rubbing that was developed in the SYCOMMOR group allows to control orientation and crystallinity by adjusting the temperature of rubbing $T_R$.[17,18] This method was the main orientation technique used all along the current thesis.

The focus of this thesis is to explore the improvements in the performance of the p-type polymer/dopant system by enhancing the polymer orientation and degree of crystallinity. Several polymer/dopant systems are carefully studied and compared such as: P3HT/$F_4$TCNQ, P3HT/$F_6$TCNNQ, P3HT/$FeCl_3$ and P3HT/Mo(tfd-$COCF_3$)$_3$. Different techniques were used in order to obtain an insight into material's physical properties, such as: Polarized Optical Microscopy, Polarised UV-Vis Spectroscopy, Transmission Electron Microscopy, Electron Paramagnetic Resonance, 4-point probe conductivity measurements and Thermopower measurements.

The thesis is organised around four main chapters.

Chapter 1 describes the important concepts and the state-of-the-art of organic thermoelectricity necessary to understand the main results of the thesis. It consists of three parts. In the first part of this chapter, the general concepts on π-conjugated polymers, thermoelectricity as well as a small survey on practical applications are introduced. The

important literature relative to pristine P3HT especially structural aspects and the variety of alignment methods are introduced. The third part of this chapter deals with the doping process and existing doping methods for semiconducting polymers. Structural changes in polythiophenes upon doping are detailed. The chapter is concluded by a brief discussion on the correlation between conductivity and Seebeck coefficient in doped polymer semiconductors and the related theoretical background.

In the Chapter 2 we focus on the P3HT/$F_4$TCNQ system and more precisely how the variation of the rubbing temperature yields two possible P3HT structures: smectic-like and semi-crystalline and how this affects the system once in the doped state. We show that the semi-crystalline structure of aligned P3HT films shows superior thermoelectric properties as compared to the smectic-like phase because of both a higher in-plane orientation and a higher doping level. Conductivities up to 160 S/cm and power factors of 56 $\mu W\ m^{-1}\ K^{-2}$ along the rubbing direction are obtained versus a few $\mu W\ m^{-1}\ K^{-2}$ for non-oriented films. Different intercalation mechanisms of $F_4$TCNQ in the layers of alkyl side chains are evidenced by electron diffraction in doped oriented films of the smectic-like and the semi-crystalline phases. We provide compelling evidence that doping of the smectic-like phase promotes ordering of P3HT backbones along the chain direction within individual $\pi$-stacks whereas for the semi-crystalline phase, dopant intercalation reorganizes the arrangement of successive $\pi$ -stacks and perturbs the packing of alkyl side chains. Insight in the orientation of $F_4$TCNQ-anions in the layers of alkyl side chains of P3HT crystals was further retrieved from a detailed polarized UV-vis-NIR spectroscopic analysis. Our results demonstrate that both orientation of the polymer chains and crystallinity enhance the thermoelectric properties as well as the

doping level. We anticipate that detailed control of polymer morphology in films further improves the thermoelectric figure of merit of semiconducting polymers.

In Chapter 3, we compare two similar systems of semicrystalline P3HT doped by $F_4TCNQ$ and $F_6TCNNQ$. Peculiar attention is given to structural modifications taking place upon doping P3HT with $F_6TCNNQ$. In this contribution we investigate the effect of the dopant on optical, structural and thermoelectric properties in aligned P3HT films doped sequentially with $F_4TCNQ$ and $F_6TCNNQ$. We evaluate how the dopant size and electron affinity affect the final film structure as a function of dopant concentration. The main questions addressed in this study are the following: What are the differences between $F_4TCNQ$ and $F_6TCNNQ$ in terms of structure, optical and TE properties? How bulky dopant molecules such as $F_6TCNNQ$ will affect the resulting structure of doped film? What is the doping level in such a system? To answer these question, we used a combination of UV-Vis spectroscopy and low dose electron diffraction to provide an insight into how the doping by different molecules affects the final polymer structure and how the dopant molecules are distributed in the P3HT crystals. Measurements of DC conductivity and Seebeck coefficients in anisotropic films help to draw correlations between doped polymer structure and TE properties.

The TE performances between these two systems remain quite similar and the increase in conductivity is accompanied by a decrease of the Seebeck coefficient. Regarding the structural findings, both $F_4TCNQ$ and $F_6TCNNQ$ dope essentially the crystalline part of the film but the doping mechanisms are different. ED provides compelling evidence for the intercalation of $F_6TCNNQ$ dopants in the crystal lattice of P3HT. A tentative model for the structure of $F_6TCNNQ$-doped P3HT is obtained from ED analysis showing that the

stoichiometry of the doped phase is one dopant per four thiophene monomers i.e. a maximum doping concentration of approximately 25%.

Chapter 4 describes the doping of semicrystalline oriented P3HT films with the metal-organic compound - Mo(tfd-$COCF_3$)$_3$. We report a record thermoelectric power factor of up to 160 uW $m^{-1}$ $K^{-2}$ for the P3HT. This result is achieved through the combination of high-temperature rubbing of thin films together with the use of a large molybdenum dithiolene p-dopant with a high electron affinity. Comparison of the UV-vis spectra of the chemically doped samples to electrochemically oxidized material reveals an oxidation level of 10%, i.e. one polaron for every 10 thiophene units. The high power factor arises due to an increase in the charge-carrier mobility and hence electrical conductivity along the direction of rubbing. We conclude that P3HT, with its facile synthesis and outstanding processability, should not be ruled out as a potential thermoelectric material.

Finally, a general conclusion is given that draws the main conclusions of the thesis and proposes perspectives for the design of TE polymer films with enhanced TE properties.

**References:**

1. © Statista 2020.

2. 'Shell – World Energy Model – A View To 2100'. Shell International BV. 2017.

3. From Wikipedia, the free encyclopedia.

4. Yang, J. & Stabler, F. R. Automotive Applications of Thermoelectric Materials. *J. Electron. Mater.* **38**, 1245–1251 (2009).

5. Jaziri, N. *et al.* A comprehensive review of Thermoelectric Generators: Technologies and common applications. *Energy Rep.* (2019) doi:10.1016/j.egyr.2019.12.011.

6. Kroon, R. *et al.* Thermoelectric plastics: from design to synthesis, processing and structure–property relationships. *Chem. Soc. Rev.* **45**, 6147–6164 (2016).

7. Materiaux thermoelectrique polymers, Technique de l'Ingenieur library, 2011 by Jennifer PERON.

8. Patel, S. N. & Chabinyc, M. L. Anisotropies and the Thermoelectric Properties of Semiconducting Polymers. *J Appl Polym Sci* **134**, 44403 (2017).

9. Bubnova, O. *et al.* Optimization of the thermoelectric figure of merit in the conducting polymer poly(3,4-ethylenedioxythiophene). *Nat. Mater.* **10**, 429–433 (2011).

10. Kim, G.-H., Shao, L., Zhang, K. & Pipe, K. P. Engineered doping of organic semiconductors for enhanced thermoelectric efficiency. *Nat. Mater.* **12**, 719–723 (2013).

11. Kao, C. Y. *et al.* Doping of Conjugated Polythiophenes with Alkyl Silanes. *Adv. Funct. Mater.* **19**, 1906–1911 (2009).

12. Hynynen, J. *et al.* Enhanced Electrical Conductivity of Molecularly p-Doped Poly(3-hexylthiophene) through Understanding the Correlation with Solid-State Order. *Macromolecules* **50**, 8140–8148 (2017).

13. Lim, E., Peterson, K. A., Su, G. M. & Chabinyc, M. L. Thermoelectric Properties of Poly(3-hexylthiophene) (P3HT) Doped with 2,3,5,6-Tetrafluoro-7,7,8,8-tetracyanoquinodimethane (F4TCNQ) by Vapor-Phase Infiltration. *Chem. Mater.* **30**, 998–1010 (2018).

14. Jacobs, I. E. *et al.* Comparison of solution-mixed and sequentially processed P3HT:F4TCNQ films: effect of doping-induced aggregation on film morphology. *J Mater Chem C* **4**, 3454–3466 (2016).

15. Scholes, D. T. *et al.* Overcoming Film Quality Issues for Conjugated Polymers Doped with F4TCNQ by Solution Sequential Processing: Hall Effect, Structural, and Optical Measurements. *J. Phys. Chem. Lett.* **6**, 4786–4793 (2015).

16. Scholes, D. T. *et al.* The Effects of Crystallinity on Charge Transport and the Structure of Sequentially Processed F4TCNQ-Doped Conjugated Polymer Films. *Adv. Funct. Mater.* **27**, 1702654.

17. Hamidi-Sakr, A., Biniek, L., Fall, S. & Brinkmann, M. Precise Control of Lamellar Thickness in Highly Oriented Regioregular Poly(3-Hexylthiophene) Thin Films Prepared by High-Temperature Rubbing: Correlations with Optical Properties and Charge Transport. *Adv. Funct. Mater.* **26**, 408–420 (2015).

18. Biniek, L., Leclerc, N., Heiser, T., Bechara, R. & Brinkmann, M. Large Scale Alignment and Charge Transport Anisotropy of pBTTT Films Oriented by High Temperature Rubbing. *Macromolecules* **46**, 4014–4023 (2013).

# Chapter 1. State of the art & Fundamentals on organic thermoelectricity

## I. General concepts

### I.1 π-Conjugated polymers

Conjugated polymers (CPs) represent great opportunities for the future in general and for organic electronics in particular. CPs are organic macromolecules that are characterized by a backbone made of alternating double- and single-bonds. Their overlapping π-orbitals create a system of delocalised π-electrons whose band structure may lead to interesting charge transport properties. Intrinsically, most classical CPs such as poly(thiophene)s have a null dark conductivity since no free charges are present in the system. To observe conductivity in CPs it is necessary to produce free charge carriers by excitation of electrons from the valence into the conduction band. Charge carriers can be generated in different ways. In the case of conducting polymers, chemical or electrochemical oxidation/reduction referred to as p- / n-doping, respectively, is necessary. [1]

The development of the field of conductive polymers has started around 1980. Two key discoveries played a crucial role in the active development of the area of conducting polymers: the discovery of polysulfur nitride in 1977 [2] and iodine-doped polyacetylene in 1977 [3]. The room-temperature conductivity of intrinsically conducting polymer $(SN)_x$ was of the order of $10^3$ $(\Omega\cdot cm)^{-1}$ whereas the conductivity of copper is $\sim 6\cdot 10^5$ $(\Omega\cdot cm)^{-1}$. The explosive nature of $(SN)_x$ prevented it from practical use. The second major breakthrough was realized by Heeger and coworkers in their studies on conducting polyacetylene. In the pristine state, polyacetylene (PA) is insulating with a conductivity below $10^{-5}$ $(\Omega\cdot cm)^{-1}$. Exposure of PA to oxidizing agents such as iodine results in a strong increase of conductivity up to $10^5$ $(\Omega\cdot cm)^{-}$

[1,3] This fundamental discovery and development of conductive polymers justified the award of the Nobel Prize in Chemistry to Alan J. Heeger, Alan G. MacDiarmid and Hideki Shirakawa in 2000. [4]

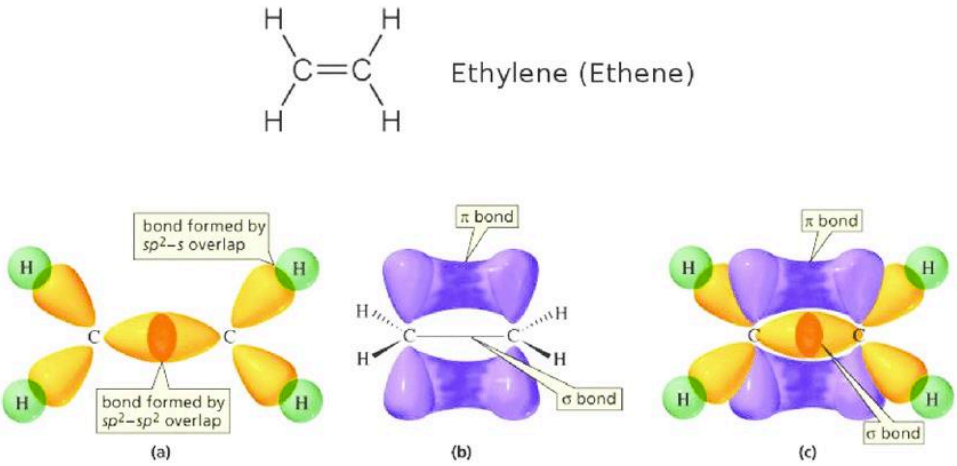


***Figure I.1*** *(a) Sigma (Single bond) hybridization for ethylene, (b) pi (Single bond) hybridization for ethylene and (c) both sigma and pi bond hybridization which give de-localization of pi-electron. Reproduced from the ref* [5]

Let us consider conductive polymers from the chemical point of view. A good model system is the ethylene molecule (see Figure I.1). Carbon atoms in the ethylene molecule are $sp^2$ hybridized. The 2s orbital of a carbon atom is mixed with $2p_x$ and $2p_y$ orbitals forming three $sp^2$ hybridized orbitals. They form two σ-bonds with hydrogen atoms and one σ-bond with the neighbouring carbon atom. The third 2p orbital ($2p_z$) remains unhybridized which gives rise to the formation of the additional π-bond due to side-on overlapping 2p orbitals (see Figure I.1). This in turn restricts rotation along the polymer axis which planarizes and stiffens the polymer backbone. π-electrons of each 2p orbital create delocalized collective orbitals.

Ideally, such delocalization should be spread over the whole length of the backbone, but it is never the case due to defects, twisting and chain folding that interrupt conjugation. π-bonding and π*-antibonding orbitals are formed due to the nature of the electron wave-function that can interfere either destructively or constructively. π-bonding and π*-antibonding can be referred as the highest occupied molecular orbital (HOMO) and the lowest unoccupied molecular orbital (LUMO) (see Figure I.2). This representation bears some analogy with the band diagram of classical inorganic semiconductors with the valence and conduction bands. The larger the conjugation length, the smaller the HOMO-LUMO gap.

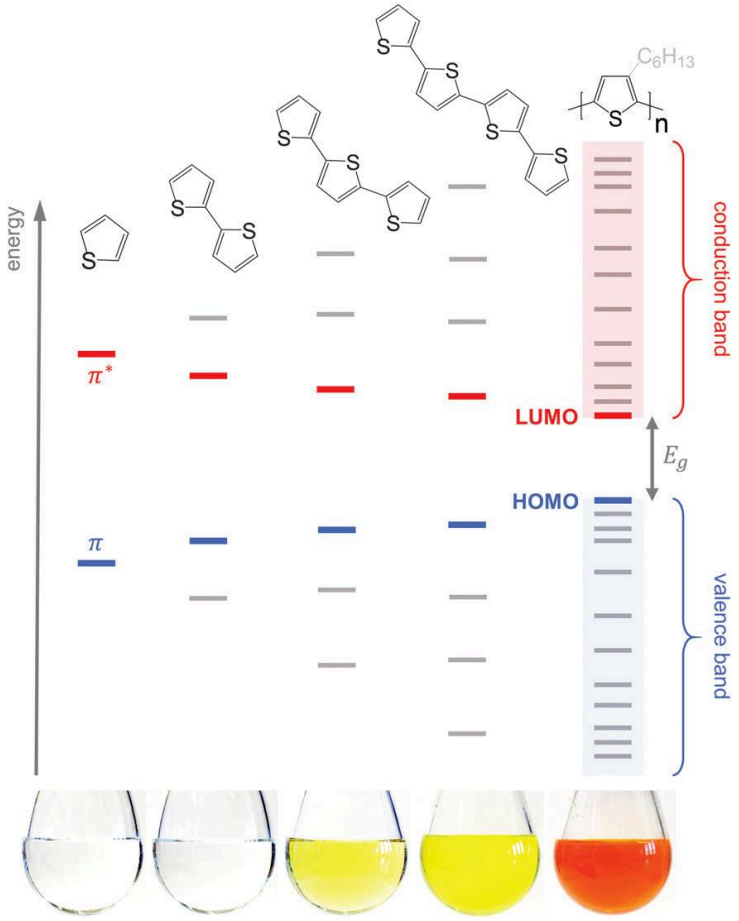


***Figure I.2*** *Evolution of the HOMO and LUMO levels as well as bandgap Eg with increasing number of thiophene repeat units, resulting in valence and conduction bands for polythiophene; the images of 5 g/l solutions in chloroform illustrate the narrowing of Eg,*

*which leads to a red-shift in absorption (the polymer is P3HT). Note that crystallisation will lead to a further decrease in Eg due to electron delocalisation across adjacent chain segments. Reproduced from the ref* [6]

## I.2 Conjugated polymers in organic electronics

The development of conducting polymers has opened the wide field of organic electronics with numerous potential applications, e.g. OFETs, photovoltaics, various sensors, displays, thermoelectrics, etc. Figure I.3 shows a set or representative conjugated polymers that have been widely studied in the literature. Interestingly, although polyacetylene has been one of the original most studied model systems for conducting polymers, it failed to become a major polymer in plastic electronics mainly because of its lack of processability.

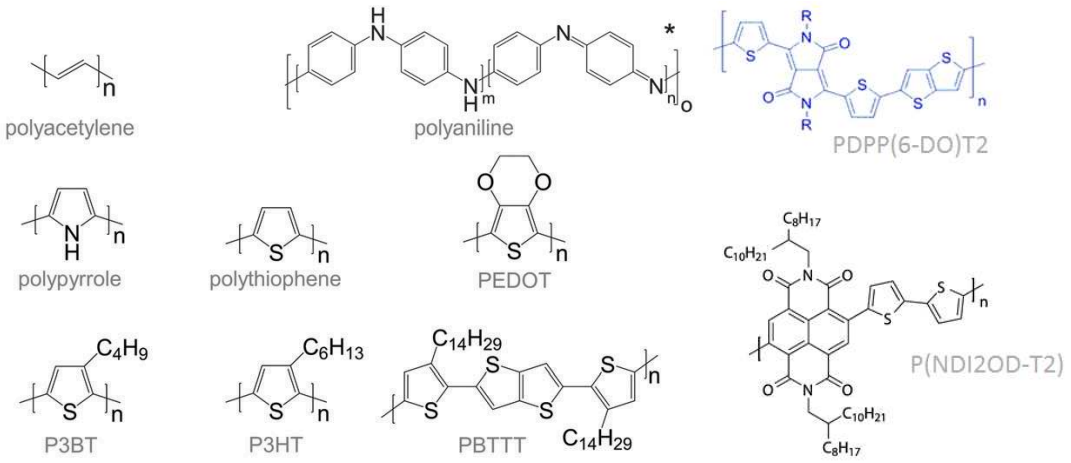


***Figure I.3*** *(a) Chemical structures of some common conjugated polymers. Reproduced from ref* [6]

Wearable electronics is currently becoming increasingly prevalent in many aspects of life, including sports, communications, health and wellness, expenditure tracking and wireless payment, wireless keys, socialization, and so forth.[7] In particular organic field effect transistors are widely used as constituents of various devices e.g. phototransistors[8], chemical sensors[9], pressure sensors[10], temperature sensors[11]. As an example for its potential applicability in plastic electronics, flexible OFETs are of particular interest as sensors for detecting gaseous pollutants[12], humidity level[13], pH[14] and even drug-abuse[15]. Numerous thiophene-, naphathalene diimide-, DPP-based copolymers are used for these purposes (see Figure I.3). [7] In photovoltaics, P3HT, polyphenylene vinylene (PPV) in combination with phenyl-$C_{61}$-butyric acid methyl ester (PCBM) or carbon nanotubes have been widely investigated to study the fundamental electronic processes at play in organic solar cells.[16,17] Electroluminescent properties of conjugated polymers have also been exploited in the design of Organic Light Emitting Diodes (OLED) that use conjugated polymers as semiconducting materials to produce flexible displays, indoor lighting, etc.[18]

## I.3 Chemical engineering of conjugated polymer units

Chemical engineering of CP units allows obtain specially tailored electronic, optical and structural properties of a resulting material. CPs made of an alternation of electron-rich and electron-poor units lead to so-called low-band gap polymers with a band gap energy ($E_g$) usually below 2eV. The band gap determines both optical properties (range of light absorption for photovoltaic applications) and charge transport. In particular, the energy levels of the HOMO/LUMO can be adjusted and determine the polymer ability to become a conducting polymer through oxidation/reduction of the backbone upon doping. [1] Theoretical calculations

can serve as guidelines for designing CP with particular electronic properties, such as e.g. band gap ($E_g$), electron affinity ($E_A$), ionization potential (IP). In particular, $E_g$ is strongly affected by the following parameters: the bond length alternation, the inter-ring torsion angle, inter-chain effects, the resonance energy and substituent effects. [19] Several strategies have been applied to reduce the band gap $E_g$ : fusion/substitution[20], ladder polymerization[21], copolymerization[22] and donor-acceptor polymerization[23].

The backbone planarity and rigidity of CP, which allows for charge delocalisation that is crucial for carrier transport, makes them difficult to process since these polymers are usually insoluble in organic solvents and show very high melting temperatures. This is why alkyl side chains have been introduced in CPs. Side chain tailoring allows to improve solubility in organic solvents, reduce the melting temperature and enhance the self-assembling of the polymers. [24–26] Poly(3-alkylthiophene)s (P3ATs) is a popular family of conjugated polymers that has been widely studied in the community of plastic electronics since they are easy to process from solution, thermally stable up to very high temperature and show versatile electronic properties that can be precisely tuned. [27]

## I.4 Organic thermoelectricity: basic concepts

Thermoelectric polymers combine the ability to directly convert heat to electricity, and *vice versa*.[6] The physical mechanism behind TE is the so-called Seebeck effect, that was discovered by Thomas Johann Seebeck in the early 1800s. It rests on a simple principle: when two dissimilar conductors are connected electrically in sequence and thermally in parallel, an electromotive force ΔV appears in a closed circuit. [28] The Seebeck coefficient is an intrinsic property of a given material. It is defined as:

$$\alpha = -\frac{\triangle V}{\triangle T}, \quad (1)$$

where $\triangle V$ - is the voltage gradient, $\triangle T$ - is the temperature difference between hot and cold ends.

Depending on the charge carriers in the material, $\alpha$ can be positive (holes) or negative (electrons). By convention the $\alpha$ sign is given by the potential of the cold side with respect to the hot one, thus indicating the majority charge carriers. [6] The Seebeck coefficient is usually very small for metals (several μV/K) and large for insulators (up to several mV/K).

The physical effect opposite to the Seebeck one is called the Peltier effect. In that case, if the current is passed through the same closed circuit (Figure I.4), a difference in the temperature appears on both p- and n-type junction with a metal. The thermoelectric cooling due to the Peltier effect is widely used in refrigerators for instance.

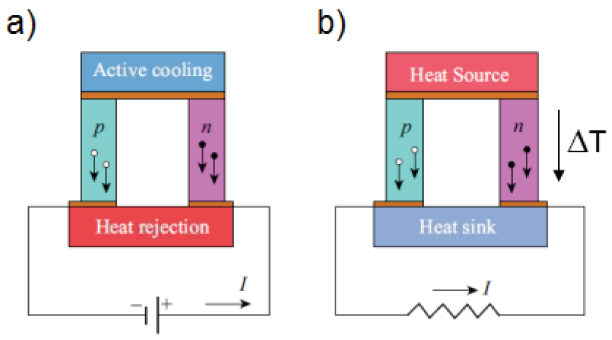


***Figure I.4*** *Cooling and power generation modes of a thermoelectric device: a) Peltier effect, b) Seebeck effect. Reproduced from ref* [29]

In 1959 Ioffe et al. have introduced a dimensionless figure of merit zT to quantify the thermoelectric efficiency of a material[30] :

$$zT = \frac{\sigma \cdot \alpha^2}{\kappa} T \,, \tag{2}$$

where $\sigma$ - electrical conductivity, $\alpha$ – Seebeck coefficient, $\kappa$ - thermal conductivity, and T – absolute temperature.

The thermal conductivity $\kappa$ has two contributions: the electronic contribution due to charge carriers $\kappa_e$ and the lattice contribution associated with the phonons in the material $\kappa_L$, i.e. $\kappa = \kappa_e + \kappa_L$.

The nominator in (2) is called the power factor PF, which is the potential efficiency of the device.

$$PF = \sigma \cdot \alpha^2 \,, \tag{3}$$

It is used quite often to compare TE performances of materials with similar thermal conductivities due to difficulties in measuring the last one.

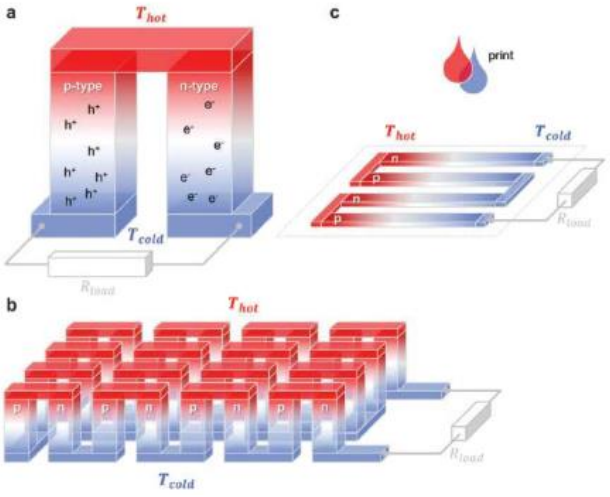


***Figure I.5*** *Schematics of (a) a thermoelectric element, (b) – TEG – an array of p- and n-type TE legs, (c) printable TEG. Reproduced from ref.*[6]

Figure I.4 represents the simplest model of a TE device, whereas more complex large-scale thermoelectric generators (TEGs) consisting of arrays of p- and n-type elements can be built (see Figure I.5). A TEG is usually made of a series of junctions whose ΔV add in order to generate a high thermovoltage.

**a) Inorganic TE**

The most common material of interest for inorganic TE is bismuth telluride ($Bi_2Te_3$). $Bi_2Te_3$ – based TE devices are characterized by zT ~ 1 at room temperature.[31] Inorganic TE materials are working quite effectively mainly at high temperatures (>400 K) and can reach zT as high as 2 at such temperatures. [32] The other materials of interest are lead telluride, silicon-germanium, Heusler alloys, tin selenide etc. They contain heavy-metals that may have high toxicity and low abundancy in nature. Despite the high TE efficiency and wide usage of inorganic TE, they have some disadvantages: expensive raw material, high processing cost, heavy metal pollution and difficulties to fabricate TEGs over large scale. The most common applications are medical and wearable devices, wireless sensor networks, industrial electronic devices, automobile engines, aerospace. [33]

***Table 1.*** *TE performance for different T ranges and materials. Reproduced from ref.*[33]

| Group | Material | Best temperature range (K) | Peak ZT |
|---|---|---|---|
| High Temperature (HT) (700–1000 K) | $CoSb_3$ (n-type) | 650–1100 | 0.9 |
| | PbTe (n-type) | 600–850 | 0.8 |
| | SiGe (n-type) | >1000 | 0.9 |
| | $Zn_4Sb_3$ (p-type) | >600 | 1.4 |
| | $CeFe_4Sb_{12}$ (p-type) | >850 | 1.5 |
| | SiGe (p-type) | 900–1300 | 0.5 |
| | TAGS (p-type) | 650–800 | 1.3 |
| | $CeFe_3RuSb_{12}$ | – | – |
| | $Mg_2Si$ (n-type) | 645 | 1.1 |
| Medium Temperature (MT) (400–700 K) | $Tl_9BiTe_6$ (p-type) | >400 | 1.3 |
| Low Temperature (LT) (300–400 K) | $Bi_2Te_3$ (n-type) | <350 | 0.7 |
| | $Bi_2Te_3$ (p-type) | <450 | 1.1 |
| | $(Bi,Sb)_2Te_3$ (p-type) | 375 | 1 |

**b) Organic TE**

Organic TE has gained enormous attention after the seminal work of Crispin et al.[34] The later authors have demonstrated that the accurate control of the oxidation level in poly(3,4-ethylenedioxythiophene):tosylate (PEDOT:Tos) can result in TE polymers with zT~0.25 (PF 324 $\mu W \cdot m^{-1} \cdot K^{-2}$) at room temperature that approaches the values required for efficient devices. [34] A similar order of magnitude efficiency was reported by Yu et al. in PEDOT:PSS carbon nanotube blends with PF = 160 $\mu W \cdot m^{-1} \cdot K^{-2}$.

Organic polymer-based materials are promising as a new generation of thermoelectric materials, owing to some unique characteristics such as: low cost, low thermal conductivity (under 0.5 $W \cdot m^{-1} \cdot K^{-1}$), easy synthesis, easy to process in different forms and on large scales. [35]

A general scheme illustrating the diversity of design methods for thermoelectric plastics materials of interest has been proposed by Kroon et al. and is depicted in Figure I.6. The thermoelectric tetrahedron represents four main building blocks of TE plastics: (1) organic semiconductors and in particular $\pi$-conjugated polymers, (2) dopants and counterions, (3) insulating polymers, and (4) conductive fillers such as carbon nanotubes, graphene and inorganic semiconductor nanowires. Both the organic semiconductor and filler can be used as the primary charge conducting components although they may be only poorly conducting in their intrinsic form. Dopant/counterion permit the modulation of the charge carrier concentration. Insulating polymer together with conductive filler can be used as extrinsically conducting TE materials. The current thesis is focused only on TE material systems of the type conjugated polymer:dopant.

Organic TE is a rapidly evolving field. New polymer backbone variations, dopant, and processing methods continuously emerge and boost the development of more effective materials for organic TE generators.

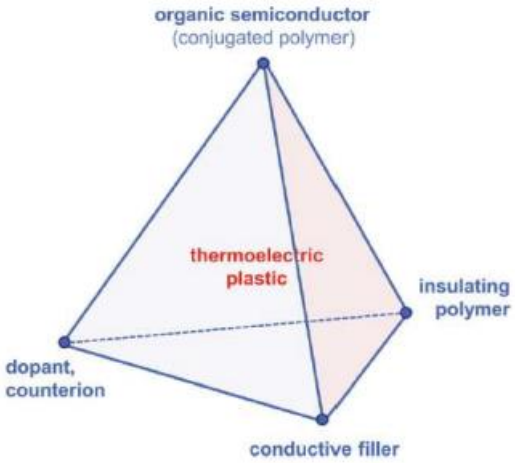


***Figure I.6*** *Thermoelectric tetrahedron representing four main building blocks of TE plastics.*

The most common p-type polymers used in organic TE are:

- poly(3-hexylthiophene) (**P3HT**)[36–40],
- poly(3,4-ethylenedioxythiophene) (**PEDOT**)[34,41–43],
- poly(2,5-bis(3-alkylthiophen-2-yl)thieno[3,2-b]thiophene) (**PBTTT**)[44,45],
- diketopyrrolopyrrole (**DPP**) copolymers[46,47]. [48,49]

All of them show a semi-crystalline structure which helps charge carrier transport. In this thesis we are focused on the model polymer system – P3HT.

## I.5 Importance of poly(thiophene)s in thermoelectricity

A large number of studies have been dedicated to the model system – poly(3-hexylthiophene) (P3HT) doped with 2,3,5,6-Tetrafluoro-7,7,8,8-tetracyanoquinodimethane ($F_4TCNQ$). P3HT is the working horse among CPs. It has been implemented in various organic electronic devices such as solar cells, field-effect transistors, light-emitting diodes and thermoelectric devices. P3HT is the model polymer for various fundamental studies on charge transport properties and film morphology due to its ease of synthesis and good opto-electronic properties.

Let us briefly demonstrate a few important findings on P3HT, relevant to its application for thermoelectric properties. Regarding the structure of P3HT, several important findings were made. In 2010 Kayunkid et al. have determined a structural model of P3HT using electron diffraction on highly oriented P3HT films grown by epitaxial crystallization method. The determined structural model underlines the importance of the hexyl side chains in the crystallization of P3HT as well as the existence of short π-stacking distances (0.34 nm) between successive polythiophene backbones. [50] Hamidi-Sakr et al. showed that high-T rubbing is an effective method to prepare highly oriented P3HT films with a lamellar morphology whose periodicity is precisely controlled by the rubbing temperature. A clear correlation is observed between the exciton bandwidth W and the average crystal size $l_c$ that limit the conjugation length in the films (extent of planarized chain segments).[51]

The high structural control for P3HT was an incentive to use this polymer in its doped form to investigate charge transport in $F_4TCNQ$-doped films. Pingel and Neher as well as Salleo et al. [49,50] studied solution-processed $F_4TCNQ$-doped conducting P3HT films. They found that the HOMO-derived density-of states distribution of P3HT is broadened upon doping with

$F_4TCNQ$ and that this broadening serves to explain the complex relationship between conductivity and molar doping ratios varied in this study. They demonstrated that there is an integer charge transfer between P3HT and $F_4TCNQ$.[52]

Regarding the doping methodology, Scholes et al. have introduced the sequential processing method to improve the doped thin film quality by overcoming structural issues related to the mixed solution processing. [53] This was an important step in improving the material's charge transport properties taking profit of the well-established structural control in pristine P3HT films.

The importance of solid state order in $F_4TCNQ$-doped P3HT was also investigated by Hynynen et al. Playing on the crystallinity level of pristine P3HT by adequate choice of solvent, they demonstrated that the degree of solid-state order of P3HT, quantified by the excitonic bandwidth W, strongly influences the electrical conductivity of vapor-doped films, leading to an electrical conductivity of up to 12.7 $S \cdot cm^{-1}$. Analysis of UV–vis–NIR spectra revealed an invariant $F_4TCNQ$ anion concentration for the majority of investigated samples. It was therefore concluded that the observed increase in electrical conductivity with the degree of solid-state order arises due to an increase in charge-carrier mobility.[40]

The importance of crystalline order was also demonstrated by Lim et al. They have made a study on $F_4TCNQ$-doped P3HT films made of blends of regiorandom (RRa) and regioregular (RR) P3HT. Surprisingly, they observed enhanced chain ordering in RR-P3HT upon doping with $F_4TCNQ$. Moreover, the crystalline regions show a higher doping efficiency than the amorphous regions due to energetic driving force for charge transfer. Electrical conductivity was strongly dependent on crystallinity in contrast to the Seebeck coefficient. [54]

Along the same line, Scholes et al. modified the crystallinity of P3HT films prior to doping and followed its impact on charge transport properties after molecular doping with $F_4TCNQ$. Increased polaron delocalization is a consequence of increased P3HT crystallinity. It leads to improved in-plane conductivity, reaching over 10 $S \cdot cm^{-1}$. AC field Hall effect measurements strongly suggest that the improved conductivity results directly from improved charge carrier mobility.[55]

In 2016 Ghosh et al. presented a theory describing the spatial coherence length of polarons in disordered conjugated polymer films. A simple relationship was revealed between the oscillator strength of the mid-IR absorption band and the coherence function of polarons. [56] It was found that the polymer molecular weight is a major factor in determining thin film morphology and thus the electronic properties of polarons. Ghosh et al. have investigated theoretically and experimentally the origin of the mid-infrared (IR) spectral features for hole absorption in doped poly(3-hexylthiophene) (P3HT) films. They have identified that in $F_4TCNQ$-doped films, polaron coherence lengths along the chain and stacking directions increase with molecular weight. The theory is robust, providing a quantitative description of the IR line shape for chemically induced ("bound") holes as well as photoinduced and electrically induced ("unbound") holes in P3HT. Spectral signatures are identified which can be used to extract the polaron coherence lengths along the chain and stacking directions.

The Coulombic interactions between the anion and the polaron were identified as a major factor influencing the charge transport properties in doped P3HT. [57]Screening of Coulombic forces is essential to have "unbound" polarons that lead to increased charge conductivity in P3HT. This screening can be obtained by using the appropriate dopants.

## I.6 Organic thermoelectric modules for practical application

The base unit of a TEG is a couple of two legs consisting of n-type and p-type materials connected through metallic electrodes.[58] TEG comprises hundreds of such connected couples in an array where couples are connected electrically in sequence and thermally in parallel.

Several studies report about TE performance of non-commercial TEG.[34,59–61]Bubnova et al. managed to fabricate a TE module based on PEDOT:tosylate. The fully organic TEG consisted of 54 legs with lengths of ~40 μm and with the following leg dimensions: 25mm x 25mm x 30 μm. The maximum power output provided 0.128 μW under a temperature gradient of 10K.[34]

Wei et al. reported the fabrication of TEG by screen-printing on paper using PEDOT:PSS and silver paste. The fabricated large-area devices provided sufficient power to illuminate light-emitting diodes.[62] (see Figure I.7a) This module was tested at 100 °C for over 100 h without any encapsulation. This devices gave a power output of over 50 μW at $\nabla T$ of about 100 K and a remarkable thermal stability in air. However, the performance of the module decreased with time due to the unstable interface between the silver paste and the polymer.

Liu and coworkers reported flexible polymer TEG based on poly[Kx(Ni-ethylenetetrathiolate)] (poly[Kx(Ni-ett)]).[59] (see Figure I.7c) The film was patterned via an electrochemical process on a pre-patterned PET substrate with a printed PDMS layer serving as a mask. The highest power density of a device containing 18 legs reached 577.8 μW·cm$^{-2}$ under $\nabla T = 12\,K$. An excellent stability was observed with a constant Seebeck coefficient over 28 hours.

Nonoguchi et al. developed a small fully-bendable TE module based on triphenylphosphine (tpp-), and TCNQ-doped single-wall carbon nanotube (SWNTs) as n-type

and p-type materials.[61] TCNQ-doped SWNTs film had a zT = 0.073. The module was laminated between fluorinated polymer films by hot-press under vacuum and generated roughly 6 mV of thermo-voltage and 110 nW of power output at $\nabla T = 20\,K$.

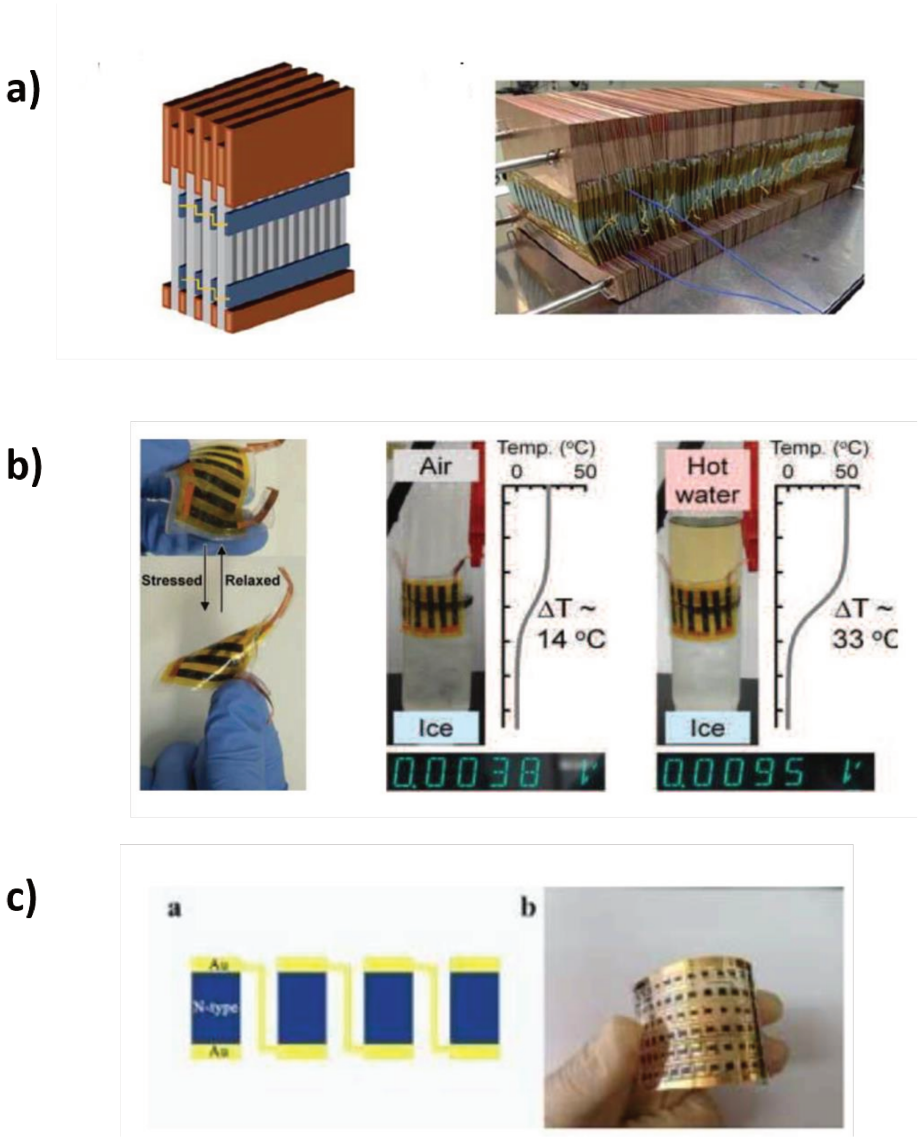


***Figure I.7*** *Examples of non-commercial TE modules: a) PEDOT:PSS modules printed on paper sandwiched between copper plates, b) a fully-bendable TEG made from three couples of tpp-, and TCNQ-doped SWNTs as a n-/p-type materials, respectively c) poly[Kx(Ni-ett)] TEG with 108 legs on a flexible PET substrate. Reproduced from refs*[59,61,62]*, respectively.*

Another interesting use of TE principles – is to fabricate a wearable electronics, such as TE fabrics. Fabric-based TE devices can serve for development of new power generating clothing. The PEDOT:PSS coated fabric with stable TE properties from 300 K to 390 K was presented by Du et al in 2015.[60] The measured values of Seebeck coefficient of a piece of such TE fabric was around 16 μV/K, with the PF of around 0.04 $\mu W \cdot m^{-1}K^{-2}$. Interestingly, such TE fabric could also be used in other areas, e.g. low-power sensors, equipment used by individual soldiers.[60]

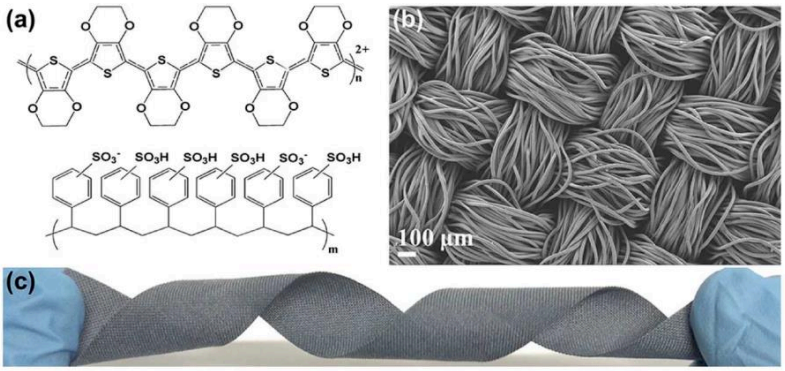


*Figure I.8 (a) Chemical structure of PEDOT:PSS, (b) SEM image and (c) digital photo of polyester fabric after coating treatment. Reproduced from ref*[60].

Another use of p-doped PEDOT:PSS for TE textile was reported by Lund et al in 2020.[63] They prepared an electrically conducting sewing thread, that was then embroidered into thick wool fabrics with out-of-plane conductivity. A TE textile device can generate a power as high as 1.2 μW at a $\nabla T$ of 65 K, and over 0.2 μW at a more modest $\nabla T$ of 30 K.

These few examples show that the field of application of polymeric thermoelectric devices happens to be quite vast with exciting new perspectives.

## II. P3HT: a working horse among semiconducting polymers

### II.1 P3HT as a good model system

Unsubstituted polythiophene were first synthesized in 1980 by Lin et al. which was quickly followed the discovery of its iodine-doped highly conductive form. [64,65] Later polythiophenes were substituted with alkyl side chains to overcome solubility and poor processing issues of the non-substituted poly(thiophene). In particular, the family of poly(3-alkylthiophenes) (P3AT) was developed, showing high solubility in organic solvents and easy processing in the form of thin films. Among all P3ATs, P3HT became one of the most popular polymer semiconductors due to its unique structural and electronic properties.

However, the addition of alkyl side chains creates an undesirable feature such as – variable regioregularity in P3ATs. Due to the fact that 3-alkylthiophene is an asymmetric monomer, there are three different regioisomers defined by the relative orientation of the two thiophene rings when coupled between the 2- and 5-position: 2-2’ or head-to-head coupling (HH), 2-5’ or head-to-tail coupling (HT), and 5-5’ or tail-to-tail coupling (TT).

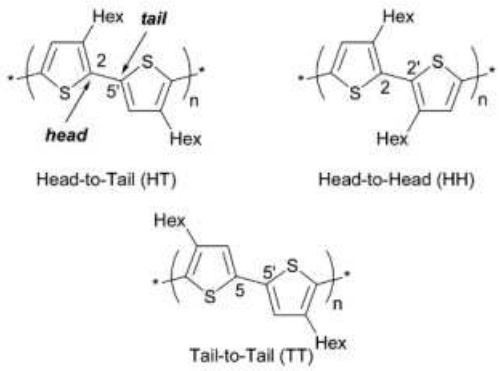


***Figure II.1*** *Coupling regiochemistry of P3HT isomers. Reproduced from ref*[66]

The mixture of coupling will produce RRa P3HT. The disordered positions of alkyl side chains induce twisting of thiophene units and as a result a strong reduction of the conjugation length. RRa P3HT cannot crystallize well and amorphous films are formed from solution with poor charge transport properties (<$10^{-5}$ $cm^2/V{\cdot}s$). The most favourable coupling in terms of structure and electronic performances is the HT one. RR polythiophenes, that contain exclusively HT coupling, can adopt a planar conformation of low energy with extended π-conjugation which is favourable for the semi-crystalline structure which in turn leads to good charge transport properties.[36]

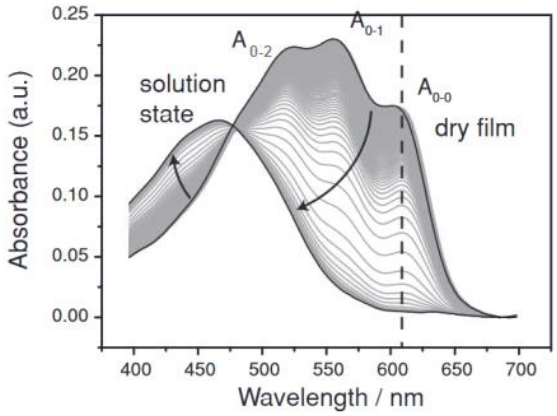


***Figure II.2*** *Controlled dissolution and recrystallization of P3HT thin films in $CS_2$ solvent vapour. Reproduced from ref*[67]

Efforts in the synthesis of RR P3HT made it possible to prepare almost 100% RR P3HT. [68] This is one of the reasons why this polymer focused a lot of attention from the scientific community.

Let us consider the correlation between optical properties and morphology in P3HT. Figure II.2 shows the evolution of the UV-Vis absorption spectra in thin films of P3HT subjected to a vapor of $CS_2$. Upon progressive reduction of the vapor pressure of $CS_2$, the film

transits from a solution-like swollen state to the solid state. It is a well-known that crystallisation of conjugated polymers results in a red-shift and appearance of a vibronic structure characteristic of the aggregated state. Spectra of the solution-like state has a maximum at 460 nm. Spectra in the aggregated state has three main peaks at 603 nm, 560 nm and 520 nm labelled as $A_{0\text{-}0}$, $A_{0\text{-}1}$ and $A_{0\text{-}2}$. $A_{0\text{-}0}$ dominates in J-aggregates whereas in H-aggregates $A_{0\text{-}1}$ is always more intense.

Clarke et al. and Spano et al. found that the redshift is closely related to the conjugation length of the planarized polymer backbone in the aggregates (crystals). The vibronic structure of the solid state crystalline P3HT is caused by different electronic transitions from the first vibrational state of the ground state to another vibrational state of the 1st excited state (0-0, 0-1, 0-2, …). This was deduced using Frank-Condon principle – the approximation that an electronic transition occurs without the change in position of the nuclei in the molecular entity. [69]

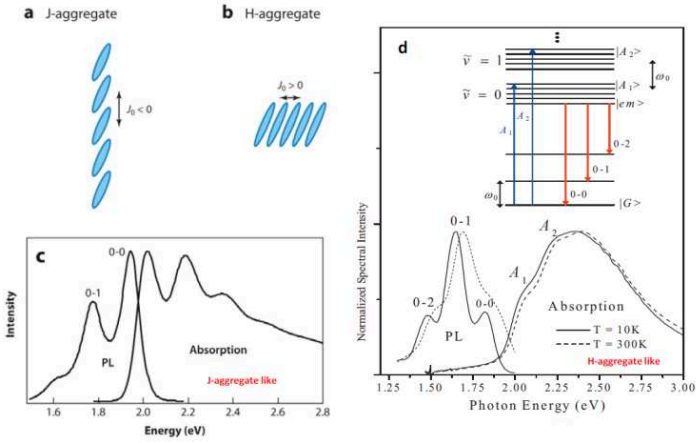


***Figure II.3*** *(a,b) Molecular orientations within conventional J- and H-aggregates, (c) Absorption and PL spectra of P3HT nanofibers grown in toluene, (d) Absorption and photoluminescence (PL) spectra of a P3HT film cast from a chloroform solution. Panels reprinted from refs* [70–72]

P3HT in solution forms aggregates whose structure depends on the nature of the solvent. Two possible aggregate types initially developed by Kasha et al. that can occur upon crystallization: H-aggregates and J-aggregate.[73] According to a definition given by Spano and Silva[72] : In **J-aggregates**, neighbouring chromophores are oriented in a head-to-tail fashion, resulting in a negative excitonic coupling. Conversely, in **H-aggregates**, nearest-neighbour chromophores are oriented in a more side-by-side manner, resulting in a positive excitonic coupling. This is directly related to the orientation of the transition dipole moments often called “side-by-side” transition dipoles with H-aggregates and “head-to-tail” transition dipoles with J-aggregates.

In this thesis we are interested in form I P3HT films i.e. H-aggregates where so-called “side-by-side” transition dipoles result in a strong delocalization of electron orbitals along the chain direction.

Form I P3HT shows a typical correlation between solid-state order and optical properties. Enhanced 0-0 transition is related to the level of crystallinity/conjugation length. The work by Spano et al. determined the following relation between the absorbances of the 0-0 and 0-1 transitions and the excitonic bandwidth W in a weakly interacting H-aggregate.[71]:

$$\frac{A_{0-0}}{A_{0-1}} \approx \left( \frac{1 - 0.24W / E_p}{1 + 0.073W / E_p} \right) \quad (4)$$

where Ep is the intramolecular vibration mode (0.18 eV) and the $A_{0-0}/A_{0-1}$ ratio is taken from the absorption spectra of the film.

## II.2 Structure of semi-crystalline P3HT

P3HT – by its nature is a semi-crystalline polymer. Most crystallizable polymers are never 100% crystalline material, they always contain a fraction of amorphous polymer. Semi-crystalline polymers consist of ordered crystalline domains with well packed polymer chains that alternate with amorphous parts containing chain ends, chain folds, chemical defects (e.g. break of conjugation). There are also so-called tie-chains connecting crystalline zones through amorphous interlamellar zones. This original semi-crystalline structure of polymers is a consequence of chain folding.

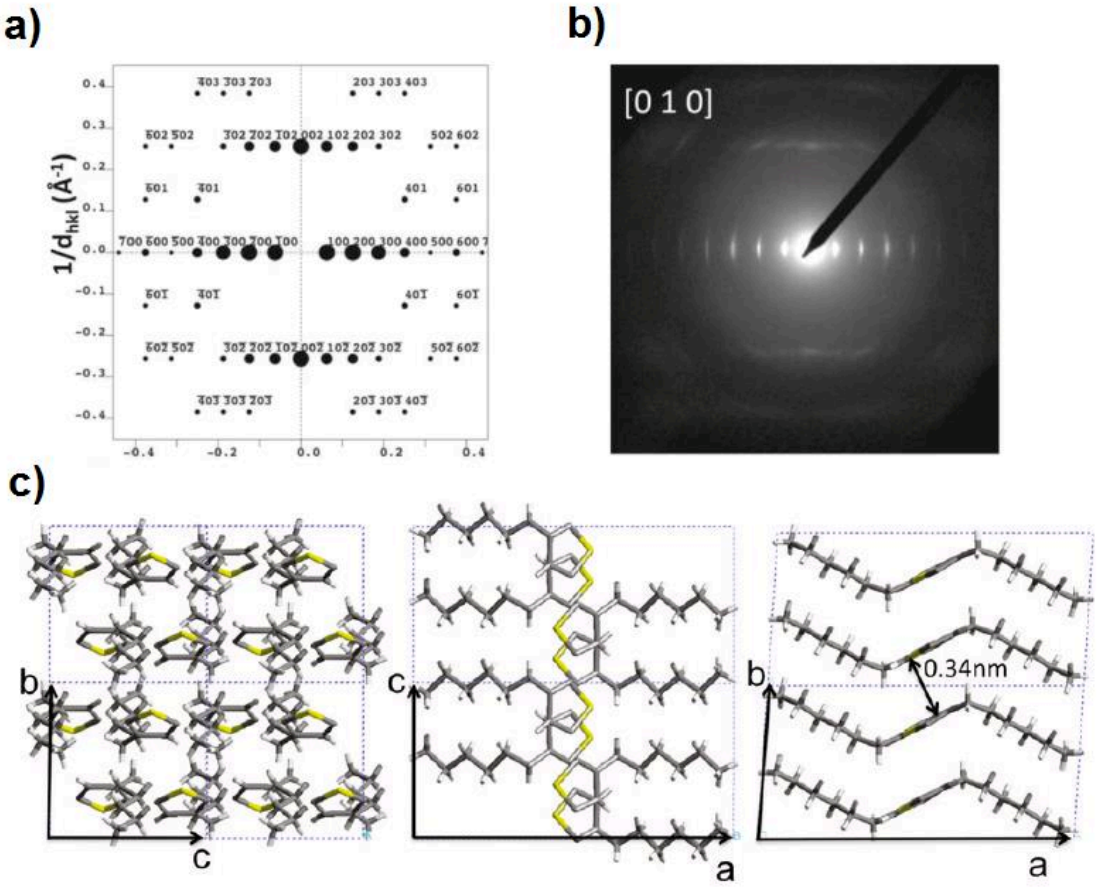


***Figure II.4*** *Calculated (a) and experimental (b) electron diffraction patterns corresponding to the determined crystal structure of P3HT, (c) - Projections of the P3HT crystal structure along the a, b, and c axes of the unit cell. Reproduced from ref* [50] **a**, **b** and **c** directions in the

unit cell of P3HT correspond to alkyl side chain direction, pi-stacking and monomer repeat directions, respectively.

Mena-Osteritz et al. studied chain folding in poly(alkylthiophene)s using scanning tunnelling microscopy (STM).[74] In their *in situ* measurements, they were able to achieve sub-molecular resolution and determine various molecular parameters of the conjugated polymers such as interchain distances, chain lengths.

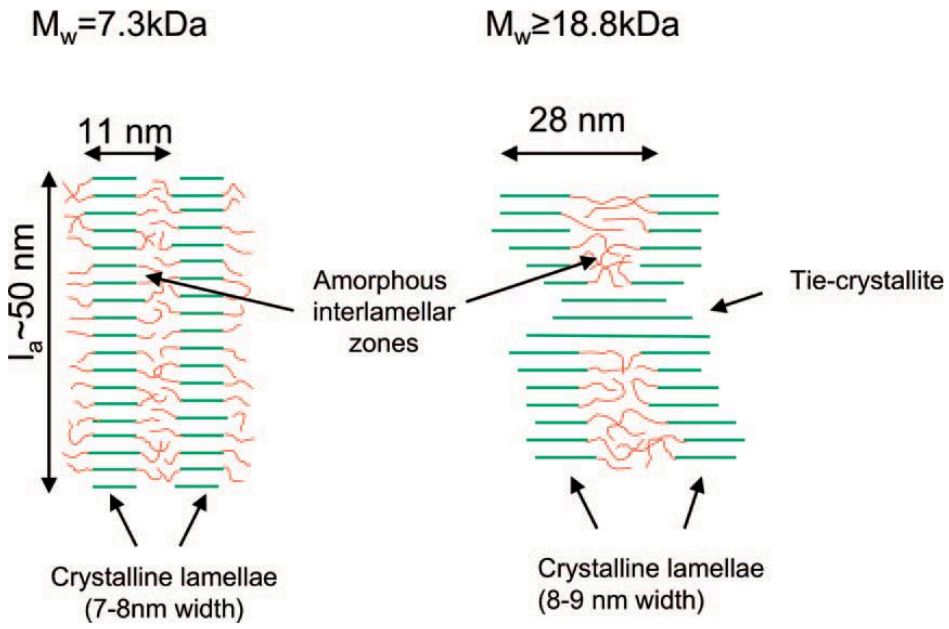


***Figure II.5*** *Schematic representation of the microstructure in semi-crystalline Rr-P3HT as a function of molecular weight. The crystalline domains are shown in projection along the π-stacking direction. The chains in the crystalline lamellae are drawn in green while their sections located in the amorphous interlamellar zones appear in red. Reproduced from ref* [75]

Beside linear chain segments, folding of the polymeric conjugated chains was observed and analysed. In 2006, Brinkmann and Wittmann studied the structure of thin P3HT films

prepared by epitaxy. They demonstrated the semi-crystalline structure of P3HT using transmission electron microscopy (TEM). A periodic alternation of crystalline lamellae separated by interlamellar amorphous zones with a total periodicity of approximately 28 nm was clearly observed in the bright field mode.[76] Later, Kayunkid et al. performed a more detailed structural analysis of thin P3HT films prepared by epitaxy by means of TEM. [50] Rotation-tilt experiments helped establish a structural model of form I of P3HT.

The unit cell was found to be monoclinic with a space group $P2_1/c$. The unit cell contains two chains with four monomers per unit cell (**a** = 1.60 nm, **b** = 0.78 nm, **c** = 0.78 nm and γ = 86.5°). (see Figure II.4) Brinkmann and Rannou have investigated the effect of molecular weight $M_w$ on chain packing and semi-crystalline structure of P3HT. They have observed semi-crystalline lamellar morphology in the bright field TEM mode.[75] (see Figure II.5). For low $M_w$, short polymer chains form crystalline lamellae with extended chains. Chain folding does not occur at $M_w$ < 7.3 kDa. The increase of the fluctuations of the lamellar thickness is observed whose average value does not scale with $M_w$. The increase of the total lamellar periodicity is mainly related to the increase of the width of the amorphous interlamellar zones. They have also found that the higher the $M_w$ of the polymer, the lower the average crystallinity.

In thin films, the crystalline domains consisting of array of π-stacked polymer backbones can have different orientations with respect to the substrate. Depending on the preparation conditions, P3HT domains can adopt either ***face-on*** or ***edge-on*** orientations relatively to the substrate. In case of the face-on orientation, thiophene rings are facing the substrate so that **a** and **c** axis are lying in the plane of the substrate. In case of the edge-on orientation, the π-stacking direction is in the plane so that **b** and **c** axes are lying in the substrate plane. Depending on the preparation method, both orientations can exist separately or together. Generally, the edge-on orientation is thermodynamically more favourable and therefore

easier to obtain by simple methods such as drop-casting and spin-coating from high boiling point solvents[77]. The face-on orientation of P3HT is often regarded as a kinetically trapped morphology [78]. It can be produced under shear forces, e.g. by the friction-transfer[79] method or by mechanical rubbing[51].

The crystallinity and the morphology of P3HT films can be affected by several parameters, such as:[80]

- the thin film preparation method (spin-coating, doctor-blading, drop-casting, etc.)
- the macromolecular parameters ($M_w$, RR, polydispersity (PDI))
- the nature of the substrate

In 2009 Clark et al. analysed the linear absorption spectrum of RR P3HT films spun from different solvents in order to probe directly the film microstructure and how it depends on processing conditions.[71] They demonstrated that the absorbance spectrum by itself can be used as a simple yet powerful probe of thin film excitonic coupling, intrachain order and fraction of crystalline regions within the film.[71]

Hynynen et al. have performed a systematic study on the effect of the solid-state order on conducting properties of $F_4$TCNQ doped P3HT films.[40] They used the excitonic bandwidth parameter W, extracted from the $A_{0\text{-}0}/A_{0\text{-}1}$ ratio as a marker of film crystallinity. The higher W, the lower is the crystallinity. Hynynen et al. prepared a series of P3HT spin-coated films from a large palette of organic solvents. Samples prepared from chloroform and cyclohexane showed the lowest degree of the solid-state order (W~130meV). In case of chlorobenzene (CB)/orthodichlorobenzene (oDCB) the excitonic bandwidth was 110-60 meV depending on a P3HT batch. A high degree of the solid state order was achieved in thin films prepared from solutions in p-xylene (W~50-30 meV).

### II.3 Lamellar structure of oriented P3HT

Brinkmann and Wittmann, in their original work on structure of thin P3HT films prepared by epitaxy, were able to uncover the semi-crystalline structure of P3HT using TEM. They demonstrated that P3HT is characterized by hierarchical order at three main length scales: i) the $\pi$-$\pi$ stacking distance of 0.38 nm between polythiophene backbones, ii) the interlayer distance of 1.6 nm between 2D sheets of conjugated polythiophene backbones separated by planes of alkyl side chains, and iii) a periodicity of 28 nm corresponding to the semi-crystalline lamellar organization.[76]

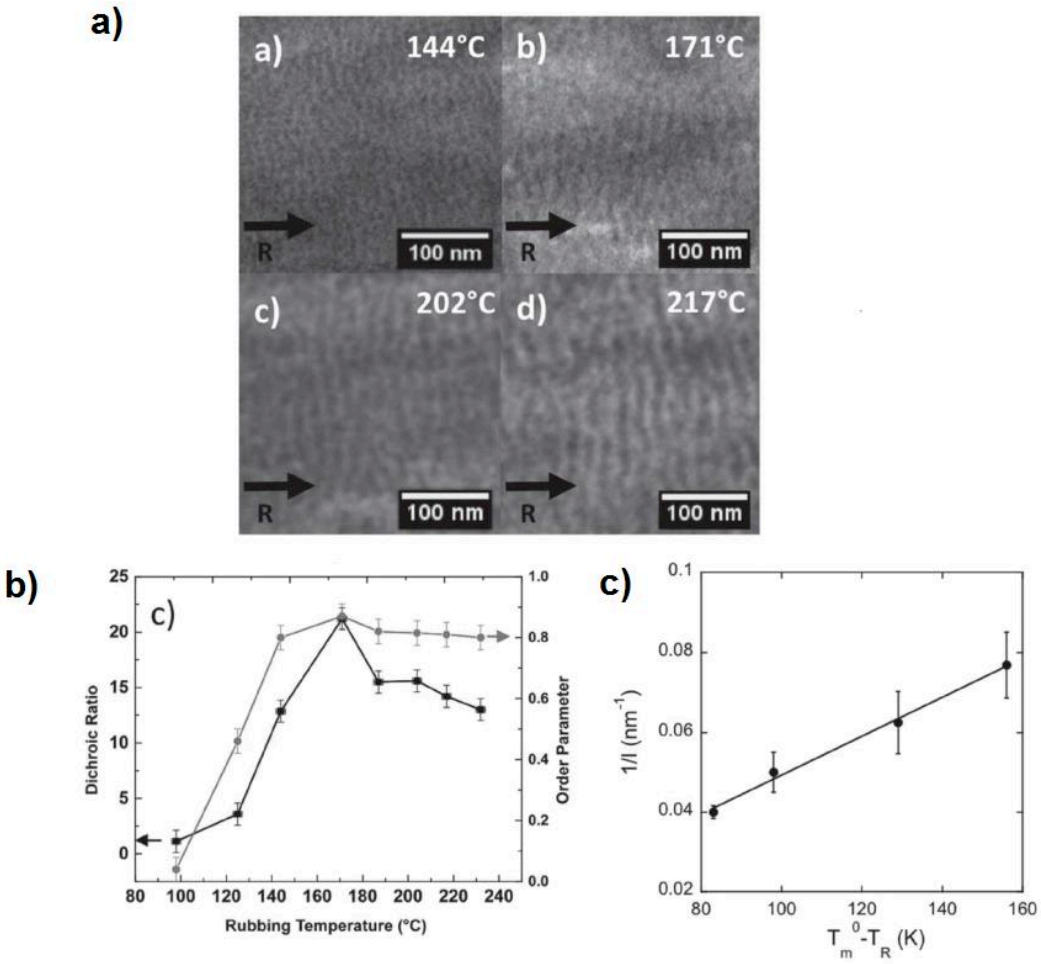


***Figure II.6*** *a) TEM BF images of the lamellar morphologies in oriented P3HT films prepared by rubbing at different temperatures $T_R$. b) Dependence of the dichroic ratio DR at 610 nm*

*(full squares) and of the 3D order parameter (full grey circles) defined as (DR − 1)/(DR + 2) as a function of $T_R$. c) Variation of the inverse of the lamellar period l extracted from the Power Spectrum of the TEM BF images as a function of the supercooling where $T_m^0$ is the melting temperature of an infinite-sized P3HT crystal. Reproduced from ref* [51]

Hamidi-Sakr investigated by TEM the effect of high-temperature rubbing at a temperature $T_R$ on the structure of P3HT films. [51] It was found that for $T_R$ < 100°C the dominant contact plane is mainly face-on with some non-oriented edge-on crystalline domains. For $T_R$ above 171°C, both oriented face-on and edge-on domains are present. The lamellar structure is clearly seen in the bright field TEM mode (see Figure II.6 (a)). The alternation of crystalline lamellae with amorphous regions is observed in the direction perpendicular to the rubbing direction **R**. Interestingly, the periodicity of the lamellae increases with the rubbing temperature. Hamidi-Sakr et al. were the first to observe the scaling of the lamellar periodicity of P3HT with the undercooling following the relation $l_c^{-1} \propto (T_m^0 - T_R)$ where $T_m^0$ is the equilibrium melting temperature of an infinite size crystal. Such an evolution of lamellar period with crystallization temperature is well known for classical polyolefins such as polyethylene. [81]

Figure II.7 schematically explains how the thin film morphology changes with $T_R$. Crystalline domains represented in red demonstrate stacks of planarized backbones both with face-on and edge-on orientation on the substrate. Disordered regions contain twisted backbones with disordered side chains and chemical defects, that interrupt the formation of the crystal.

Regarding the charge transport properties, the anisotropy of charge carrier mobility $\mu_{//}/\mu_{\perp}$ is shown to decrease with $T_R$. Interestingly, the mobility parallel to the chains, $\mu_{//}$, does

not substantially evolve with improved crystallinity. This is explained by the presence of amorphous interlamellar zones that hamper charge transport along the rubbing direction whatever the value of $T_R$ in the range 144 °C–217 °C. In strong contrast, the hole mobility perpendicular to **R**, $\mu_\perp$, that increases with $T_R$ is more clearly correlated to both the film crystallinity and the proportion of edge-on crystals in the films that also increase with $T_R$.

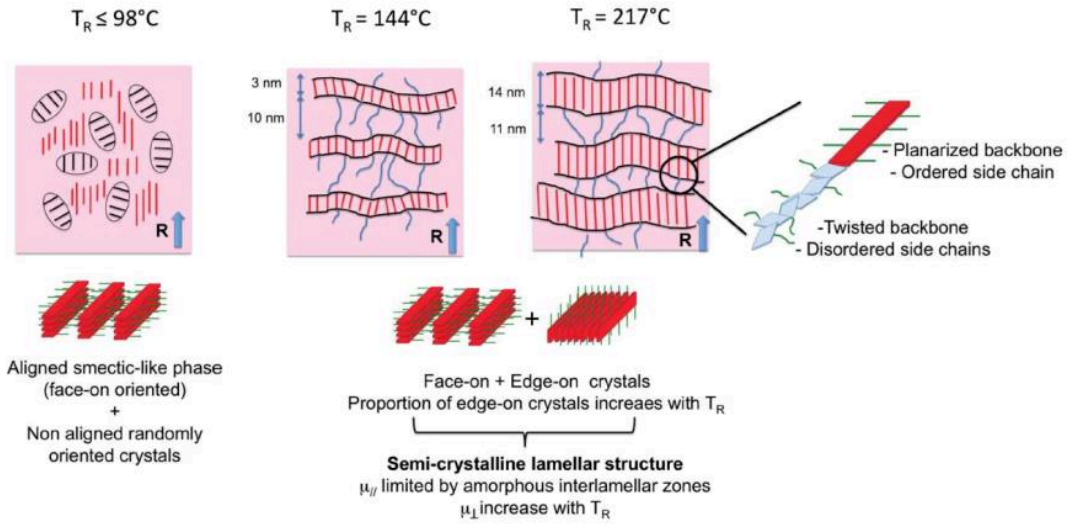


***Figure II.7*** *Schematic illustration of the structural evolution in rubbed P3HT films as a function of the rubbing temperature $T_R$ and impact on charge transport. For clarity, only the crystalline domains are represented, the amorphous areas are highlighted in light pink. A certain number of tie chains linking successive crystalline domains as well as chain ends are shown in blue within the amorphous zones. Reproduced from ref*[51]

## II.4 Structure of smectic-like P3HT

Hartmann et al. have studied the structure of P3HT thin films prepared by two different methods such as epitaxy and mechanical rubbing at room temperature. Both methods result in two different structural morphologies semi-crystalline and smectic-like, respectively. (see

Figure II.8) The so-called smectic-like P3HT structure bears characteristics of a liquid crystalline mesophase and differs from the classical semi-crystalline phase. In the case of the semi-crystalline phase, crystalline domains are composed of pi-stacks of P3HT backbones, for which one has a strict periodic order along the **c** direction within individual (b,c) planes. Every second backbone along the b axis has a **c**/2 shift with respect to the next one so that there is a regular translational order from one layer to another. (see Figure II.8)

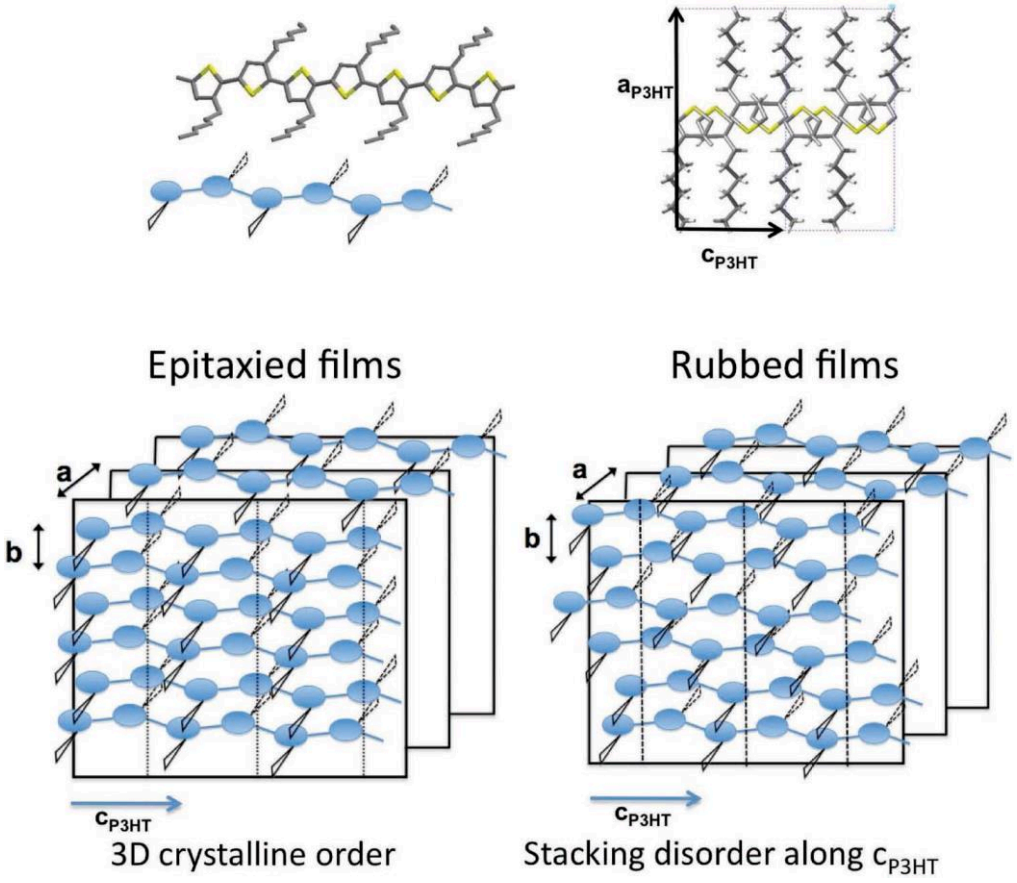


***Figure II.8*** *Schematic comparison of the P3HT film structure prepared by epitaxy and mechanical rubbing. In epitaxial layers, translational order is present along all three unit-cell directions. As seen in the upper right corner, the unit cell of P3HT contains two P3HT chains with a well-defined shift along the b axis. Epitaxial films grow in the semi-crystalline structure whereas films rubbed at ambient temperature show the smectic-like phase due to the stacking disorder along the c axis. Reproduced from ref*[82]

In the of case of the smectic-like phase, no such regular translational order is observed within the (b,c) planes. Stacking disorder is present along the direction of the polymer backbone as evidenced by the absence of the 0 0 2 reflexion on the diffraction pattern of the rubbed P3HT films (it corresponds to the periodicity between successive monomers along the backbone direction).[82] The level of order in the smectic-like films is much lower as compared to the semi-crystalline phase as evidenced from UV-Vis absorption spectra of both films and the difference in the $A_{0-0}$/ $A_{0-1}$ ratio. Overall, 3D translational order is present in epitaxied P3HT films. This is expected to favor electronic delocalization contrary to the RT-rubbed P3HT films that show a 2D smectic-like order.

**II.5 Variety of polymer alignment methods**

Polymer orientation methods are powerful tools to introduce the alignment of polymer backbones within the film and as a result improve the structural, optical and charge transport properties of the material. Aligned polymer films demonstrate improved crystallinity, polarized absorbance/luminescence and anisotropic charge transport (mobility).[38,44,76,83–85] Different orientation techniques can give different film morphologies, that will result in different optical and charge transport properties. Below, we describe the main polymer orientation techniques reported in the literature that can be classified in four groups:

- orientation by applying a shear force (friction transfer, mechanical rubbing)
- orientation using orienting substrates with matching unit cell parameters (epitaxy)
- orientation by stretching (strain alignment, tensile drawing)

- orientation by flow of a polymer solution (flow-coating)

The efficiency of the orientation depends on the orientation technique and polymer characteristics such as molecular weight, rigidity of the polymer backbone, nature and length of side chains, film thickness, etc.

**a) Friction transfer**

This method was pioneered by Smith and Wittmann to prepare oriented poly (tetrafluoroethylene) (PTFE) layers. [86] The method is based on friction-transfer of a thin polymer film using a solid polymer pellet. First, a polymer powder is compressed in the form of a pellet/cylinder, then by applying a high pressure on the pellet (a few bars) using a pneumatic piston, a thin film is deposited on a continuously moving hot substrate.

Nagamatsu et al. reported high dichroic ratio of 10-100 for P3HT and poly(dodecylthiophene) (P3DT) deposited by friction transfer. [79] The polarized UV–vis absorption spectra showed large dichroism along the direction of friction-transfer. The order parameter determining the level of orientation was found to be close to unity. GIXD measurements show that alkyl side chains lie in the film plane, and the polymer backbones are well-ordered along the direction of friction-transfer within ±10° for P3HT and ±13° for P3DT to the drawing direction.[79]

The hole mobility along the drawing direction was enhanced by a factor of 25 compared with that of spin-coated film. [87] This technique can be applied to insoluble polymers. [88] The main disadvantage of this method is that the film thickness is difficult to control and the

substrate has to be heated at a sufficiently high temperature for film deposition. Furthermore, production of pellets requires large amounts of material.

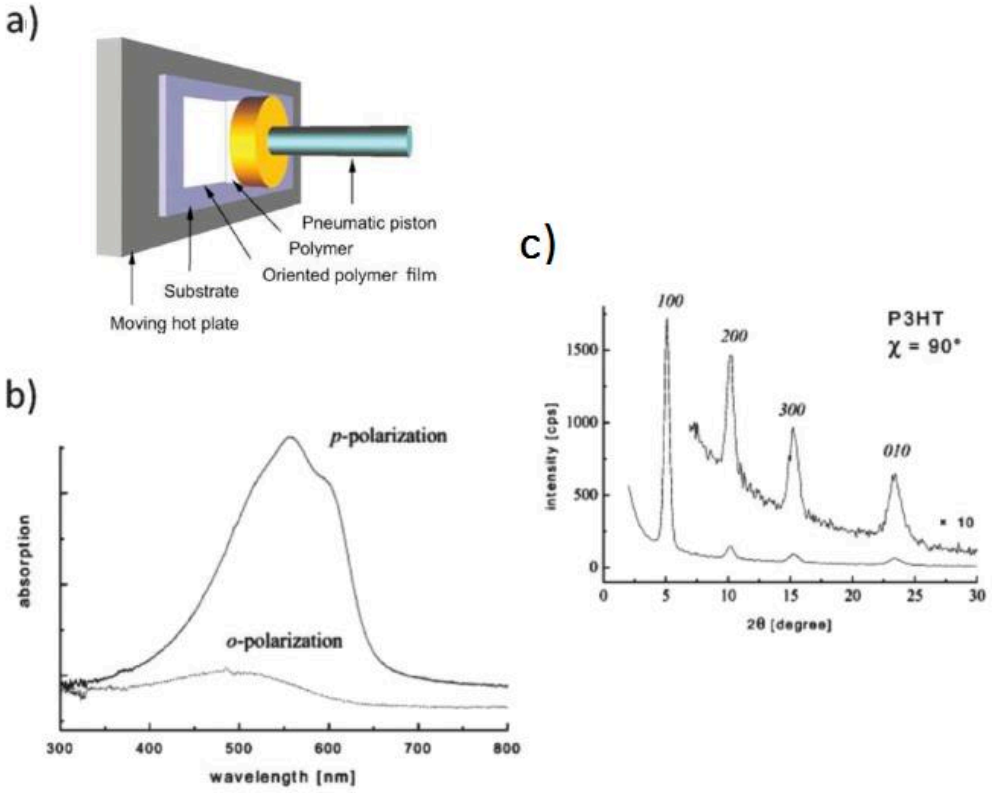


***Figure II.9*** *a) Friction transfer deposition of an oriented SCP film. A polymer pellet is applied with a given pressure against a moving hot substrate whereby a thin oriented polymer layer is deposited. b) Polarized UV–vis absorption spectrum of P3HT films oriented by friction transfer. c) GIXD line scans obtained for friction-transferred P3HT Reproduced from ref* [79,89]

**b) Flow-coating**

Orientation using doctor-blade is another technique for polymer alignment. A hot polymer solution is deposited between the blade and the substrate while the stage is subsequently moved at a speed of 2 mm/s so that the solution spread evenly underneath the blade. Delongchamp et al. have investigated this technique by producing thin oriented PBTTT

films.[38] This films were found to show a new and original morphology called " terraced ribbons" using Atomic Force Microscopy (AFM). The lateral widths of the domains is around 60 nm and their length exceeds 10 μm. Adjacent ribbons share a common orientation as indicated by AFM.[38] However as-coated films did not show very high orientation and further annealing was required to improve the orientation.

.

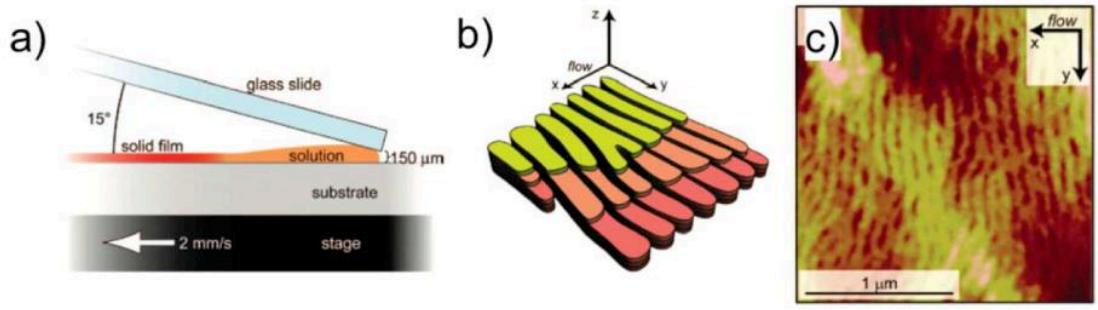


***Figure II.10*** *a) Orientation of a pBTTT film using the flow-coating method. b) Schematic illustration of the oriented ribbon phase of pBTTT. c) AFM image of a flow-coated pBTTT film after thermal annealing. Reproduced from ref*[38,89]

**c) Epitaxy**

Epitaxy can be defined as a directed growth of a material on the surface of a crystalline substrate along one or several preferential crystallographic directions.[89] Epitaxy is largely used in the semiconductor industry in silicon-based devices. Interestingly, this method can be effectively used for semi-crystalline polymers. A variety of substrates such as NaCl, KCl, aromatic crystals (e.g. 1,3,5-trichlorobenzene (TCB)) can be used fro this purpose. The substrate must be chosen using certain criteria for a given polymer. For epitaxy to be

effective, it is admitted that a mismatch less than 10-15% between the unit cell parameters of the substrate and the polymer must be observed.

In 1980s Wittmann and Lotz have extensively studied epitaxial growth polyethylene (PE), n-paraffins, aliphatic polyesters, and various polyamides using benzoic acid crystal substrates with specific crystal faces consisting of the periodic arrangement of aromatic units. [90] Using electron diffraction, they found that PE offers a wide range of interchain distances in its two phases: orthorhombic and monoclinic. [91]

Later in 2000s Brinkmann and Wittmann have studied directional epitaxial crystallization of P3HT on TCB substrate.[76] A P3HT solution was crystallized using TCB crystals that played the dual role of solvent and orienting substrate. TCB is a unique solvent that has a form of a powder at room temperature. Furthermore, along the direction of the fiber axis of P3HT, which is parallel to $\mathbf{c}_{TCB}$, a very close matching between the repeat distance of the thiophene units in P3HT ($|\mathbf{c}_{P3HT/2}|$ = 0.385 nm) and the repeat distance of TCB molecules (0.39 nm) along $\mathbf{c}_{TCB}$ is observed. This allows to mix directly P3HT and TCB between two glass slides and heat it at 63° to obtain a solution that can subsequently be crystallized unidirectionally in a temperature gradient to obtain an oriented semi-crystalline polymer. Once crystallized, the TCB crystals that served as an orienting substrate can be evaporated under vacuum. The typical fingerprint of the semi-crystalline structure of P3HT is the periodic alternation of crystalline lamellae separated by amorphous zones as observed by TEM and AFM. [76] Later, Brinkmann and Rannou studied the effect of molecular weight ($M_w$) of P3HT on the structure and morphology of the oriented thin films grown on TCB. It was found that the overall crystallinity as well as the orientation of the crystalline lamellae decrease significantly with increasing $M_w$.[92] In 2012, Brinkmann et al have studied the crystalline structure of the naphthalene diimide (NDI)-based alternated copolymer (PNDI2ODT2) films prepared by

epitaxy on TCB and friction-transferred PTFE. Oriented films of two polymorphs of PNDI2ODT2 (form I and form II) were prepared.

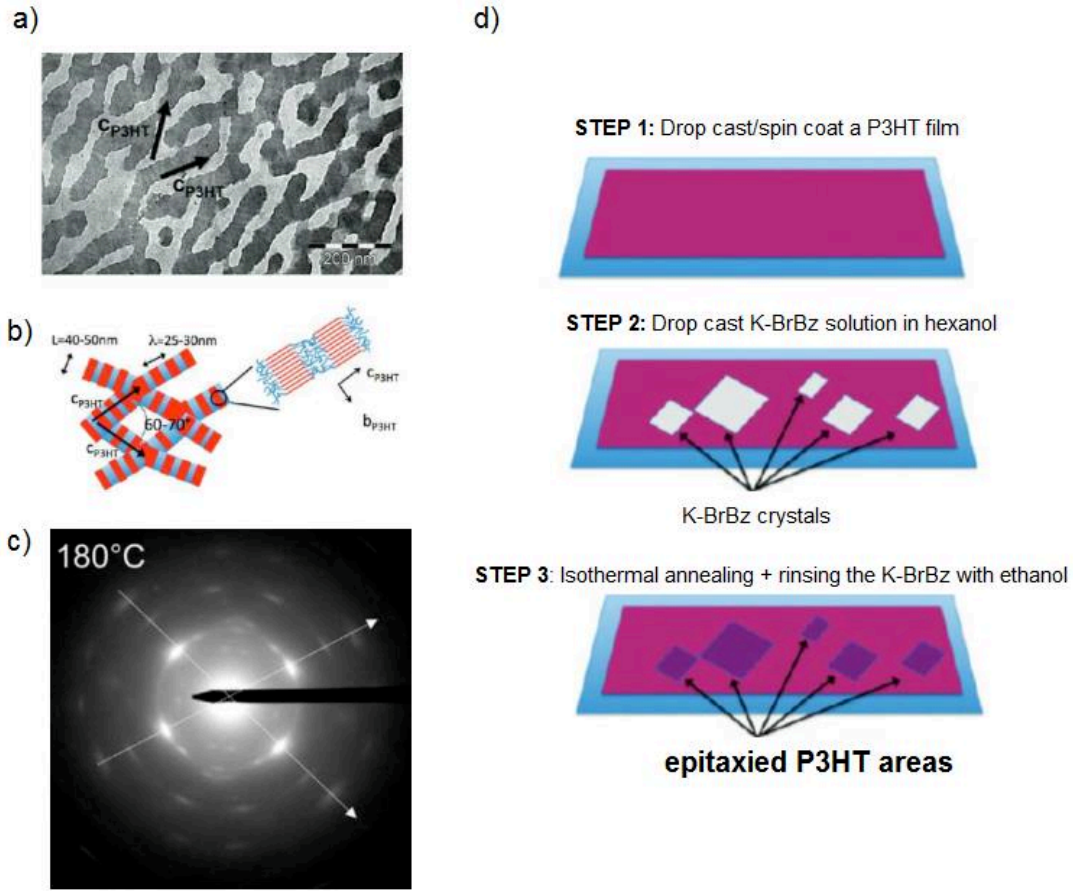


***Figure II.11*** *Bright field (a) TEM image and electron diffraction pattern (c) of an oriented P3HT film grown on the 100 crystal surface of K−BrBz at 180°C. Note the alternation of dark and brighter stripes in the oriented domains. The two preferential in-plane orientations of the P3HT chains ($c_{P3HT}$) are depicted by two arrows. (b) Scheme showing the organization of the nanostructured P3HT films grown on K-BrBz substrate. Crystalline zones are shown in red while amorphous interlamellar zones are colored in blue. (d) Scheme illustrating the three main steps of the epitaxial growth of oriented P3HT thin film prepared on K−BrBz. Reproduced from ref* [93]

Form I was obtained by epitaxy on TCB, where segregated stacks of bithiophene (T2) and naphthalene diimide occurs. Highly oriented films of form II with mixed stacks of two the NDI and T2 units were obtained by epitaxy on PTFE substrates after melting at T = 300 °C and cooling at 0.5 K/min.[94] In 2010, Brinkmann et al. studied the structure of epitaxially grown P3HT films on the surface of platelet-shaped crystals of (potassium 4-bromobenzoate) (K−BrBz). The preparation method of highly oriented and nanotextured P3HT films consist of three steps: 1) forming a drop-cast P3HT film on a glass substrate, 2) drop-casting a K-BrBz solution in hexanol atop the P3HT film to form large K-BrBz crystals, and 3) isothermal annealing of the P3HT film to induce orientation of the polymer on K-BrBz. Upon further rinsing with ethanol, the K-BrBz substrate is removed leaving large areas of highly oriented P3HT on the glass substrate. Transmission Electron Microscopy showed that the oriented P3HT films consist of a regular network of interconnected semi-crystalline domains oriented along two preferential in-plane directions of K-BrBz.[93] (see Figure II.11) Most importantly, the mechanism of orientation is not a true epitaxy based on surface-lattice matching but involves the step edges of the K-BrBz substrate.

**d) Mechanical rubbing**

The technique of mechanical rubbing was widely used for orienting polyimides for the alignment of liquid crystal molecules. [95] At first, a polymer film is deposited by spin-coating, drop-casting or doctor-blading on a substrate. Second, the film is rubbed by using a rotating cylinder covered with the microfiber cloth and a translating plate on which the polymer film is fixed. The mechanism of alignment is based on the shear forces at the interface between the polymer and the microfiber cloth on the rotating cylinder.

Controlled parameters during the rubbing process are:

- ✓ Number of rubbing cycles
- ✓ Rotational speed of the cylinder
- ✓ Speed of the translating stage
- ✓ Temperature of the stage ($T_R$)

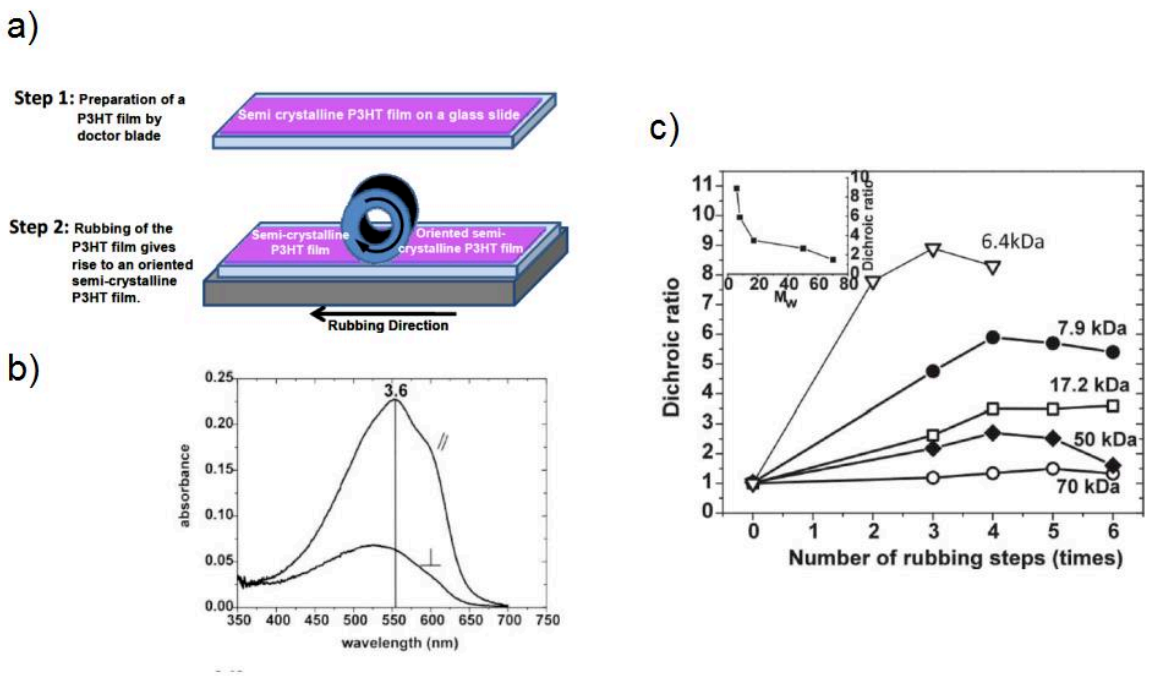


***Figure II.12*** *(a) Schematic representation of the rubbing method. In a first step a non-oriented film is deposited onto a solid substrate. In a second step, the film is rubbed using a rotating cylinder covered with the microfiber cloth. Reproduced from ref*[96]*, (b) - UV-vis absorbance spectra of P3HT thin films ($M_w$ = 17.2 kDa) oriented by rubbing at $T_R$, (c) Evolution of the dichroic ratio measured at 550 nm for rubbed P3HT films corresponding to different molecular weights in the range 6.4–70 kDa as a function of the number of rubbing cycles. Reproduced from ref*[82]

Kajiya et al. report 8-times improvement of out-of-plane mobility in thin P3HT film. [97] According to the results of grazing-incidence X-ray diffraction measurements, the increase of face-on component of P3HT by rubbing was observed and corresponds to the increase of π–π staking of thiophene rings along the out-of-plane direction.[97] Hartmann et al compared the structure of P3HT films prepared by epitaxy and mechanical rubbing at room temperature. The molecular weight was found to impact strongly the level of orientation: the lower the $M_w$, the higher the in-plane orientation induced by rubbing (see Figure II.12.c). Anisotropy of charge transport was studied in OFETs. It was observed that P3HT with low $M_w$ of 6.4 kDa demonstrates remarkable anisotropy of the hole mobility $\mu_{//}/\mu_{\perp} \approx 20$, whereas films with $M_w$ of 35 kDa rubbed at ambient show a limited value of $\mu_{//}/\mu_{\perp} \approx 2$.

Brinkmann and coworkers further developed the method of rubbing by changing the temperature of the film upon rubbing. Together with Tremel et al. they we able to test it on P(NDI2OD-T2) alternated copolymer and obtain FET mobility of 0.1 $cm^2 \cdot V^{-1} \cdot s^{-1}$ along the rubbing direction.[98] Biniek et al. applied the so-called high-temperature rubbing to $C_{12}$-pBTTT and p(NDI2ODT2), respectively.[99] The increased plasticity of the conjugated polymer films of PBTTT for 50°C ≤ $T_R$ ≤ 125°C gives high in-plane orientation by mechanical rubbing of the films. High resolution TEM shows the in-plane alignment of $C_{12}$-pBTTT chains and increase in size of the oriented domains with $T_R$.[99]

**e) Strain alignment**

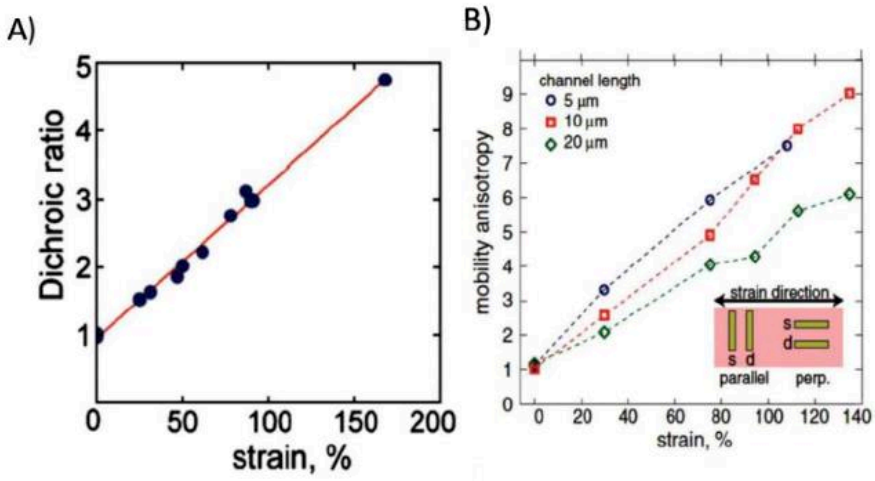


***Figure II.13.*** *a) Evolution of the dichroic ratio $A_{//} / A_{\perp}$ as a function of strain applied to the P3HT thin films. b) Anisotropy of mobility in strain aligned P3HT films in OFETs. The lower inset illustrates the orientation of the gold electrodes relative to the strain direction. Reproduced from ref*[100]

Strain alignment is a technique whereby a stretchable substrate such as polydimethyl-siloxane (PDMS) is used to communicate strain to the polymer semi-conductor layer. A polymer film is deposited on a PDMS substrate which is stretched afterwards and polymer crystals are subsequently aligned with their chain direction along the stretching direction. O'Connor and co-workers applied a method of strain-alignment to P3HT, showing several important features of charge transport. The in-plane mobility increases in the applied strain direction and decreases in the perpendicular direction. The obtained optical dichroic ratio is 4.8 and the charge-mobility anisotropy $\mu_{//}/\mu_{\perp}$ is close to 9 (see Figure II.13). This alignment method provided a simple and effective mean to investigate charge-transport correlations in polymer semiconductors albeit the obtained alignment is rather limited and much lower than

for high-T rubbing.[100] Xue et al. improved this method to orient PBTTT with large ordered domains by adjusting the temperature of the PBTTT films upon drawing. The temperature is kep above the crystal->LC transition so that side chains become liquid-like and thus the polymer can be readily aligned .[83]

**f) Tensile Drawing**

Tensile drawing differs from other technique by the fact that it concerns free standing films i.e. films several micrometers in thickness. The film is fixed on both sides and the force is applied on both ends in opposite directions at constant speed. (see Figure II.14a) Mechanical properties of different polymers were studied using this method. The drawing behaviour above the glass transition temperature has been studied for various viscosities of polyethylene terephthalate. [101] Mechanical and electrical properties of oriented poly(2,5-thienylene vinylene) (PTV) films have been investigated by Zhang and Smith. They have demonstrated that the drawing process is quite efficient for this polymer. PTV films were obtained with Young's moduli of ~7 GPa and with an electrical conductivity of $10^3$ S/cm, after doping with iodine.[102] Hynynen et al. have studied tensile-drawing on free standing P3HT films. Sequential doping of the oriented P3HT films with a molybdenum tris(dithiolene) complex lead to a 5-fold enhancement of the power factor up to 16 µW $m^{-1}$ $K^{-2}$ and a conductivity of about 13 S·$cm^{-1}$ along the drawing direction.[40] (see Figure II.14c) A disadvantage of this technique is related to the fact that it applies to bulk P3HT films i.e. requires a large amount of polymer.

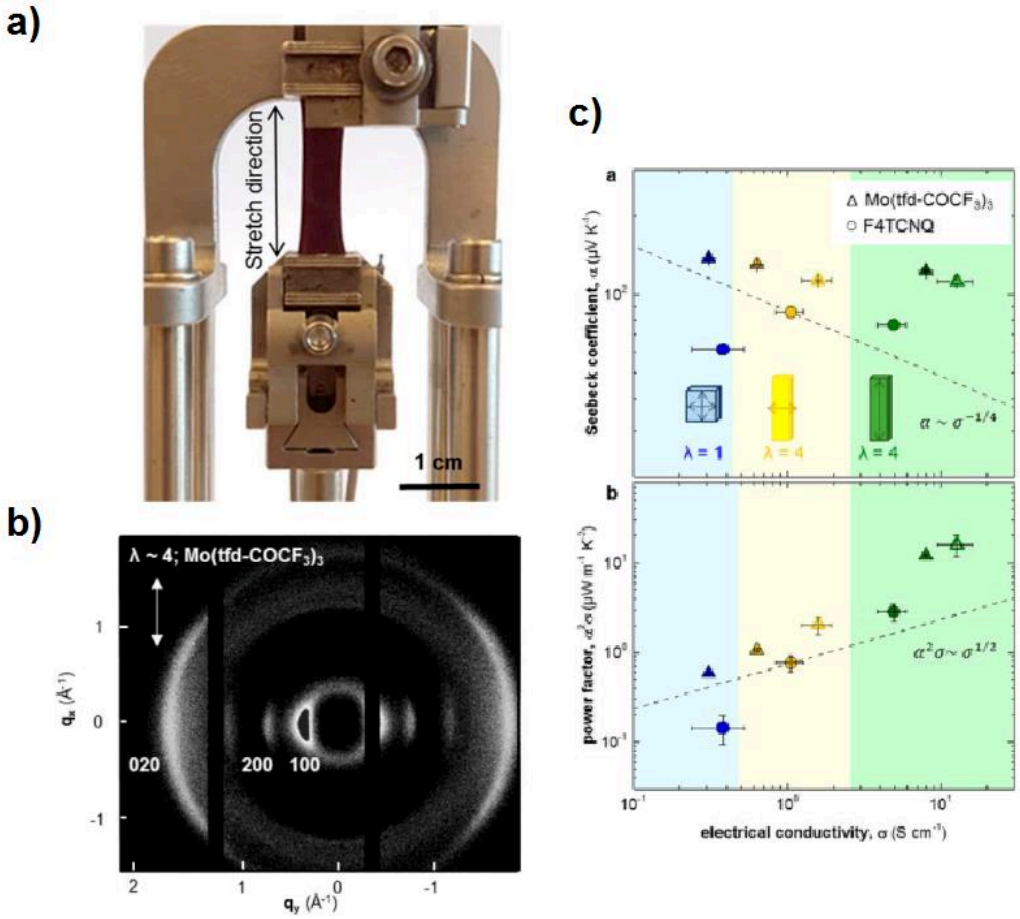


***Figure II.14*** *(a) Stretched film of P3HT, clamped in a DMA instrument, (b) - Wide angle X-ray scattering (WAXS) patterns of and tensile drawn P3HT (λ ~4; arrows indicate drawing direction) sequentially doped with Mo(tfd-COCF₃)₃, (c) - (a) Seebeck coefficient α and (b) power factor $\alpha^2\sigma$ as a function of electrical conductivity σ for P3HT doped with Mo(tfd-COCF₃)₃ (triangles) and F₄TCNQ (circles). Reproduced from ref*[103]

## II.6 Anisotropy of charge transport in polythiophenes

Anisotropy of charge transport (CT) in polythiophenes is an important feature due to the well-defined monoclinic unit cell. Monoclinicity implies that the three axes of the unit cell have unequal lengths and that one angle of the unit cell is different from 90°. This results in highly anisotropic CT, which is the most efficient along the backbone direction (**c**), less efficient along the pi-stacking direction (**b**) and quite poor along the side chain direction (**a**). CT along the **c**-direction is also called – intrachain, whereas the other ones are referred as interchain CT.

Lan et al. applied quantum mechanical calculations and molecular dynamic methods to examine CT in P3HT in both ordered and disordered states. [104] Typical values of the intrachain hole mobility is about 1 $cm^2\ V^{-1}\ s^{-1}$, which is larger by several orders of magnitude than that along the interchain direction ($\sim 10^{-2}\ cm^2\ V^{-1}\ s^{-1}$). This clearly illustrates that the main dominating CT route within the P3HT ordered domains is along the intrachain direction instead of the interchain direction. Lan et al. used the P3HT single fibril as the transport medium. Calculated mobility values of $10^{-2}\ cm^2\ V^{-1}\ s^{-1}$ are close to the experimental values in the literature. They also reported that in the disordered domains, the CT can occur via the interchain route through so-called crossing points formed by close contacts between chain ends/loops or the intrachain route along the bridging chains.[104]

Following the directional epitaxied crystallization method proposed by Brinkmann et al.[76], Jimison and coworkers have studied CT anisotropy due to grain boundaries in such films.[105] They showed that grain boundaries anisotropy leads to substantial charge-transport anisotropy at least one order of magnitude higher along the chain than in the

perpendicular direction. O'Connor et al. were able to achieve anisotropy of mobility up to $\mu_{//}/\mu_{\perp} \approx 9$ in the strain-aligned P3HT films.[100] Hamidi-Sakr et al. achieved FET anisotropy of mobility ≈ 15 for thin P3HT films oriented by high-temperature rubbing. [51] Hartmann et al. have compared CT and structural properties of P3HT films prepared by directional epitaxial crystallization and high-temperature rubbing for P3HT of different $M_W$. For low-$M_W$ batches, the anisotropy reaches the value of $\mu_{//}/\mu_{\perp} \approx 22$.

CT anisotropy in oriented PBTTT was investigated by Biniek et. al.[99] The hole transport anisotropy was measured in OFETs for highly in-plane oriented face-on as well as edge-on oriented films. Different annealing conditions were applied for oriented films to further improve the in-plane alignment. The anisotropy of hole mobility varied in the range 7−70 with the highest mobility value around $4 \cdot 10^{-3}$ $cm^2$ $V^{-1}$ $s^{-1}$ along the rubbing direction and the highest anisotropies for the films showing oriented face-on crystals.

In the current thesis we applied the high-T rubbing method in order to improve the in-plane alignment of the P3HT films oriented at different $T_R$. Orientation at high temperature allows to improve both alignment and crystallinity of polymer layers prior introducing the charge carriers in the structure. Introduction of the charge carriers in the polymer film by doping is a necessary step to make the polymer films highly conductive. In the next subsection we will consider in details the doping process of conjugated polymers as well as different doping methods and doping mechanisms.

## III. Doping as a doorway to highly conductive TE material

Doping is a way to introduce charge carriers into a pure semiconductor in order to improve its electrical performance. Brédas and Street stated that the doping of conjugated polymers is best viewed as a redox reaction: [106] "*The insulating neutral polymer is converted into an ionic complex consisting of a polymeric cation (or anion) and a counterion which is the reduced form of the oxidizing agent (or the oxidized form of the reducing agent).*" Therefore, the important criterion in the choice of the polymer:dopant system is the ease of oxidation/reduction. π-conjugated polymers are suitable for this kind of reaction due to presence of delocalized π-electrons.

### III.1 Charge carriers in conducting polymers

Introduction of the charge carriers (CC) in the polymer system can be done by several ways: chemically, electrochemically or using so-called acid-base doping. Chemical doping is performed by means of redox reaction between polymer and dopant. Whereas electrochemical doping is performed in the electrochemical cell when the polymer is placed on one of the electrodes in the electrolyte solution and doping occurs when the potential is applied between electrodes. [107,108] In the current thesis, we are only interested in chemical doping.

When charge carriers are introduced in the polymer, new energetic levels appear in the polymer bandgap ($E_g$). Doping of CPs always includes the following processes:

- the positive/negative charge introduced in the π-electron system of the polymer gets neutralized by reduced/oxidized dopant;

- this leads to a local lattice distortion that possess a spin 1/2 due to the presence of the charge on the polymer backbone. Such an electron/hole moving through a periodic potential of the crystal lattice is called a polaron.

Polarons are the main charge carriers in polymer SCs. The polaron is a radical ion (with a spin 1/2) associated with a lattice distortion and the presence of localized electronic states in the gap referred to as polaron states.[106] (see Figure III.1)

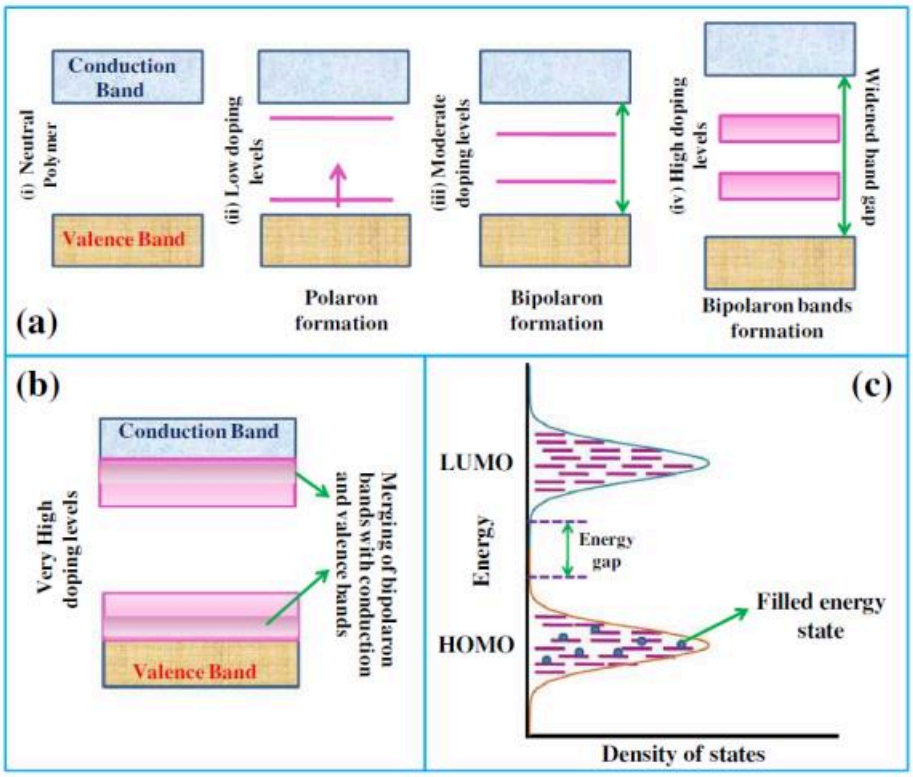


***Figure III.1*** *Schematic illustration showing (a) Formation of polaron, bipolaron and bipolaron bands as a function of doping of CPs; (b) Merging of bipolaron bands with conduction and valence bands at very high doping levels; (c) Gaussian distribution of localized states in the HOMO and LUMO orbitals of CPs. Reproduced from ref* [109]

Further removal/addition of an electron from the polaron can further, give rise to new spinless specie known as bipolaron which is a radical ion pair linked with polaronic distortion. This is possible only at very high doping levels when the CC concentration reaches a certain level.[109]

In the case of p-type doping, an electron form the CP is removed from the highest occupied molecular orbital (HOMO) and transferred to the lowest unoccupied molecular orbital (LUMO) of the dopant molecule, thus turning a dopant molecule into its anionic form while leaving a hole on the polymer backbone. The hole is delocalized over several monomers turning the semiconducting polymer into a conducting one.

The charge carrier transport mechanism in semiconducting (SC) polymers is affected by both energetic and spatial disorder. Due to the electrostatic interactions between the polaron and the dopant, the chagre carrier can be trapped on the polymer chain. Trapping of the polaron due to the presence of the anion is very important for lightly doped organic materials due to the low dielectric constant ($\varepsilon \sim 3$) of the medium. Such traps reduce significantly the CC mobility. The force of the electrostatic interaction is defined as the well-known Coulomb force: $|\vec{F}| = \frac{q_1 q_2}{4\pi\varepsilon\varepsilon_0 r^2}$. As seen from the formula, besides the charges of two species $q_1$, $q_2$, two important parameters affecting the interaction between the polaron and the anion are the dielectric constant $\varepsilon$ and the distance $r$ between them. A low dielectric constant results in a large size of the trap, thus interrupting the efficient charge transport (CT). However, at higher anion concentration, the influence of these traps tend to be reduced due to the overlap between the Coulombic fields of successive traps: the charge carriers experience an average electric field.[109] The increase of $\varepsilon$ is a crucial point for any conducting organic material. For instance, in a solar cell, a low dielelectric constant leads to a higher charge recombination

rate which directly affects the solar cell efficiency. [110] In the case of thermoelectric organic materials, ε can be increased by choosing for instance metal-organic dopants that significantly improve the polaron delocalization, hence the charge conductivity or by tuning the polymer side chains. [111,112] Qi et al. report a strong enhancement of hole injection in N,N'-di-[(1-naphthyl)-N,N'-diphenyl]-1,1'-biphenyl-4,4'-diamine (α-NPD) – standart hole transporting material via formation of a narrow depletion region upon doping with molybdenum dithiolene complex.[113]

Hynynen et al have studied P3HT films oriented by tensile drawing and doped by $F_4TCNQ$ and $Mo(tfd\text{-}COCF_3)_3$. They evidenced a 4-fold increase in conductivity for Mo-based dopant as compared to $F_4TCNQ$.[103] It has been previously reported that Molybdenum trisdithiolene complex is a stronger oxidant than $F_4TCNQ$, with a LUMO around -5.6eV *versus* -5.2eV for $F_4TCNQ$. [114] Liang et al. studied a series of dopants (including Mo-based dopants and $FeCl_3$) with varying sizes and electron affinities with polymers of differing ionization energies.[115] They demonstrated that large molybdenum complexes led to more delocalized polarons in comparison to $FeCl_3$ and therefore reduced to Coulombic interaction between the polaron and dopant anion leading to a better electrical conductivity.

### III.2 Doping mechanisms and the most common types of dopants

Two doping mechanism are possible through chemical doping of organic semiconductors: i) acid-base doping and ii) redox doping.

Basically, in case of the acid-base doping the transfer of either a cation (proton, $H^+$) or an anion (hydride, $H^-$) to the semiconductor occurs upon doping (see Figure III.2b). When a hydride is transferred to the polymer backbone, one talks about n-type doping (base-doping),

whereas in case of a proton - p-type doping is involved (acid-doping). [6] Polythiophenes such as P3HT and PBTTT can be acid-doped as well as polyaniline. Patel et al. report high electronic conductivity and, in turn, a large power factor of 100 $\mu W \cdot m^{-1} \cdot K^{-2}$ in thin films of PBTTT vapour-doped by FTS (see Figure III.2 below). [116] Numerous studies report successful doping of polyaniline with camphor sulphonic acid (CSA), dodecyl benzene sulphonic acid (DBSA) and other protic acids. [117,118] Kroon et al. reported thermally activated doping of P3HT free-standing films using ethyl-benzene sulphonic acid (EBSA) yielding a maximum conductivity of $4 \cdot 10^{-2}$ S·cm$^{-1}$.

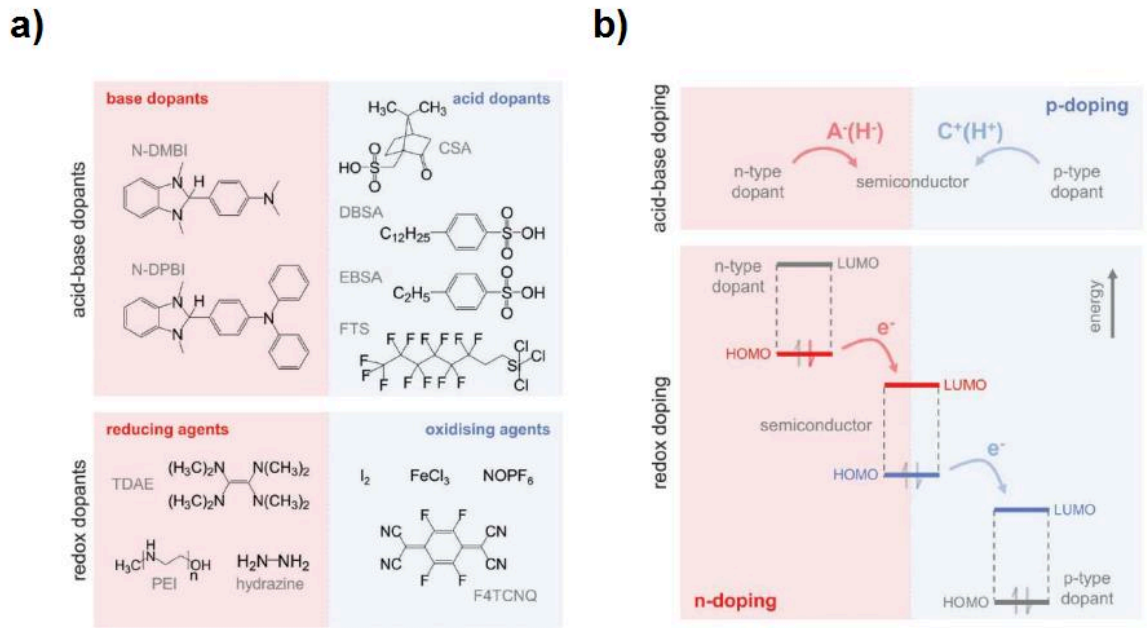


***Figure III.2*** *a) Variety of dopants: acid–base (top) and redox dopants (bottom), b) Energetic diagrams illustrating the principles of acid-base (top) and redox doping (bottom). Reproduced from ref*[6]

Base-doping were actively used in order to dope alternated block copolymers such as P(NDI2OD-T2) and other naphthalene diimide-based low-bandgap alternated copolymers with either 4-(2,3-Dihydro-1,3-dimethyl-1H-benzimidazol-2-yl)-N,N-dimethylbenzenamine

(N-DMBI) or with a similar compound - 4-(1,3-Dimethyl-2,3-dihydro-1H-benzoimidazol-2-yl)-N,N-diphenylaniline (N-DPBI). [108,119–121]

Redox doping occurs through the electron transfer from donor to acceptor. Transfer of an electron from the HOMO of the conjugated polymer to the LUMO of the acceptor dopant molecule gives rise to **p-doping**, whereas transfer from the HOMO of a donor dopant molecule to the LUMO of the polymer leads to **n-doping**. (see Figure III.2b) Therefore a match between HOMO/LUMO levels of a polymer and dopant as well as a sufficient offset between the two levels involved in the charge transfer are crucial parameters for successful doping.

One of the first reported redox doping experiments on a conjugated polymer concerns polyacetylene doped with iodine (($I_2$) as an oxidizing agent). [122,123] Diatomic halogens such as $I_2$, $Br_2$ are attractive dopants because of their volatility i.e. they can be used in the form of a gas that can easily diffuse in the organic semiconductor and form anions causing the reversible doping of the polymer.[124] However, these dopants are highly unstable in ambient which limits their application. Other very common redox dopant molecules used to dope polythiophenes can be classified by their structure (see Figure III.2):

1. Planar molecules: $F_n$TCNQ (n = 0, 2, 4), 2,3,5,6-Tetrafluoro-7,7,8,8- tetracyano-quino-dimethane ($F_6$TCNNQ), hexacyano-trimethylene-cyclopropane (CN6-CP), Nitrosonium hexafluorophosphate ($NOPF_6$)
2. 3D molecules: $FeCl_3$, $Mo(tfd\text{-}COCF_3)_3$, $Mo(tfd)_3$, and others.

Among them, $F_4$TCNQ is the most studied one and used as a strong doping agent since a decade.[45,125] It has a LUMO level of -5.24eV which is suitable for doping of polythiophenes. $F_2$TCNQ and $F_6$TCNNQ are two other derivatives with a TCNQ (tetracyanoquinodimethane) core. The latter two dopants possess a LUMO of -4.59eV and -5.37eV, respectively. As a

general trend, addition of fluorine atoms tends to lower the LUMO level. $F_6$TCNNQ was first applied for the doping of vacuum-processed hole-conductive materials in OLEDs[126] and subsequently used by Karpov et al. to dope DPP-based copolymers.[47]

The strongest p-type dopant yet reported in the literature is CN6-CP having an electron affinity $E_A$ of −5.87 eV. This dopant is capable of doping efficiently DPP-based copolymers.[127]

$FeCl_3$ molecule is a strong Lewis acid possessing a small $E_A$ of ~4.65 eV.[115] It is capable of accepting an electron pair from a Lewis base and besides form an acid-base complex. Sakai et al. have studied $FeCl_3$-doped polyacetylene thin films using Mössbauer spectroscopy and revealed two iron species: $FeCl_2$ and $FeCl_4^-$.[128] Based on their experimental observations, they proposed a mechanism of electron transfer between $FeCl_3$ and polyacetylene, where one $FeCl_3$ molecule over two acts as an electron acceptor from polyacetylene and the other stabilizes the Cl- ion that is produced as a result of the reduction of $FeCl_3$.

Finally, a bulky Mo(tfd-$COCF_3$)$_3$ molecule is an organometallic dopant with three side rings. It demonstrates a high $E_A$ of −5.6 eV and good stability under ambient condition. It is perfectly suitable for doping of hole transporting materials.[111,113,114]

In the framework of my thesis, I will be focused on the TE properties resulting from the doping of P3HT with both planar ($F_4$TCNQ, $F_6$TCNNQ) and bulky ($FeCl_3$, Mo(tfd-$COCF_3$)$_3$) dopants. The effect of doping on structural, thermoelectric and optical properties in thin oriented P3HT films will be highlighted in the scope of this work.

### III.3. Doping methods:

Several doping methods exist and have been widely used for doping of polythiophenes, such as: i) Mixed solution processing, ii) Sequential Doping, iii) Vapour phase doping, and iv) Incremental concentration doping. We will describe in the following these methods in detail.

#### a) Mixed solution processing

This method implies the mixing of the polymer and the dopant solutions together in a common solvent and deposit a thin film by drop-casting or spin-coating from the Polymer/dopant solution. (see Figure III.3) In 2008, Yim et al. studied controlled p-doping of poly(3-hexylthiophene) (P3HT), poly(9,9-di-n-octylfluorene-alt-bis-N,N-(4-butylphenyl)-bis-N,N-phenyl-1,4-phenylenediamine) (PFB), poly(9,9-di-n-octylfluorene-alt-(1,4-phenylene-((4-sec-butylphenyl)imino)-1,4-phenylene) (TFB) and poly(9,9-di-n-octylfluorenealt-benzothiadiazole) (F8BT) conjugated polymers by co-blending with $F_4TCNQ$ with different wt% concentration of dopant. At a doping ratio of 10% w/w, the conductivity of P3HT films increases by almost four orders of magnitude to ~$10^{-1}$ S·cm$^{-1}$ when compared with pristine films.[129]

Aziz et al. have studied the charge transfer interaction between P3HT and $F_4TCNQ$ in their original work.[130] They claimed that the interaction between the polymer and the dopant involves a charge transfer complex (CTC) state. They reported a conductivity of ~ 1 S·cm$^{-1}$ for solution processed P3HT:F4TCNQ films. Their CTC model was later disproved by Pingel and Neher who showed that integer charge transfer (ICT) between P3HT and $F_4TCNQ$ is observed. [52] Duong et al. have analysed the effect of the dopant concentration on the in-plane conductivity in P3HT:$F_4TCNQ$. [131] Films were spin-cast from solutions at 80 °C with different

mass ratios of $F_4TCNQ$ to P3HT from CB. The concentration of all solutions was 2 mg solute per 1 mL of solvent, thus a 50:50 F4TCNQ:P3HT solution (dopant molar fraction (MR) of 0.376) contained 1 mg of $F_4TCNQ$ and 1 mg of P3HT per 1 mL of CB.

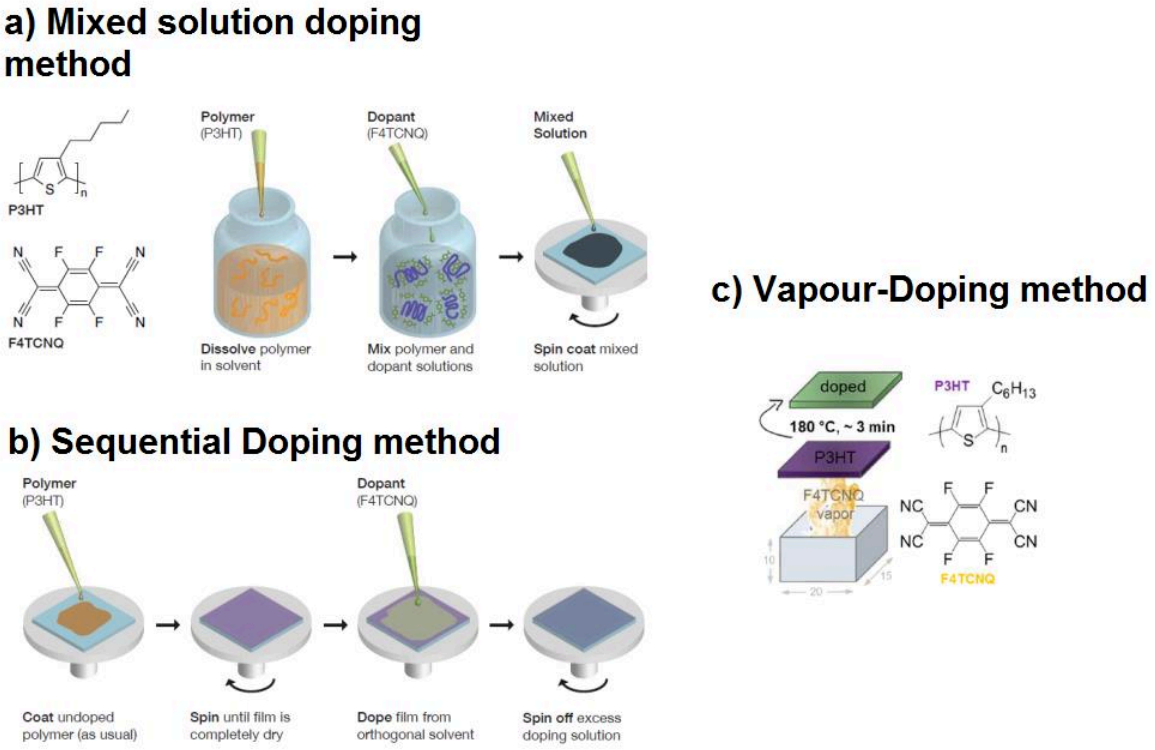


***Figure III.3*** *Schematic of the doping methods: mixed solution doping (a), sequential doping method (SqD) (b), vapour-phase doping (c). Reproduced from refs*[40,132]

They showed that addition of $F_4TCNQ$ increases the in-plane conductivity of P3HT thin films by about four orders of magnitude up to a concentration of 17 dopant molecules per 83 monomer units (molar fraction or concentration of 0.17). The in-plane conductivity was peaking at 1.82 ± 0.22 $S \cdot cm^{-1}$ and was decreasing upon further addition of dopant. They distinguished two different doping regimes.

In the ‘‘weak doping regime’’ (molar dopant fraction (MR) ≤ 0.012), dopant molecules reside in amorphous polymer regions in thin films and the conductivity is minimally improved as compared to pristine films. In the ‘‘strong doping regime’’ ( 0.17 > MR ≥ 0.03), charged complexes are formed in solution. This leads to the nucleation of doped crystalline polymer domains in thin film and the conductivity increases by up to four orders of magnitude. [131] Successful doping of the PBTTT-$C_{14}$ by $F_4$TCNQ was reported by Glaudell et al.[133] Electrical conductivity was found to range from $4 \times 10^{-5}$ S/cm for the neat polymer to 2 S/cm for the blend with MR of 0.25.

Jacobs et al. reported that in this preparation method, the resulting film which is drop-cast from aggregated solution is composed of highly conductive doped crystalline domains. However, these regions are not well connected by tie chains. As a result, conductivity is limited by the high electrical resistance between the conductive crystallites.[132] Such spatial disorder negatively affects charge transport properties of the material.

In conclusion, mixed solution processing method has a minor influence on the structural properties due to a spontaneous charge transfer between polymer and dopant and as a result form aggregates in solution. This leads to a poorly controlled formation of crystalline domains in the drop-cast film.

**b) Sequential Doping (SqD)**

While mixed solution doping was the classical method to prepare doped conducting polymers, a better doping strategy was developed that is based on sequential processing. In this method, first the polymer film is deposited onto the substrates by means of common deposition methods (drop-casting/spin-coating/doctor-blading). Then, the polymer film is exposed to the dopant solution in an orthogonal solvent (a solvent that does not dissolve the

pre-cast polymer film). (see Figure 3b) This method allows for a better morphology control as the pristine polymer structure can be precisely tuned prior to doping. In 2015, Scholes and coworkers introduced the SqD method on P3HT:$F_4$TCNQ and compared the values with mixed-solution processing developed in the work of Duong et al.[53,131] Profilometry measurements showed that the SqD method produces doped films with the same surface roughness as pristine films. 2-D grazing-incidence wide-angle X-ray scattering (GIWAXS) confirmed that SqD preserves both the size and orientation of the pristine polymer's crystallites. Scholes et al. were able to obtain reproducible conductivities reaching high values of 5.5 S/cm even when measured over macroscopic distances (>1 cm).[53]

Jacobs et al. compared mixed-solution processing and sequential doping methods on P3HT:$F_4$TCNQ. Using AFM, they showed that doping does not significantly change the pristine film morphology, allowing for higher conductivity at a given doping level. They reported that the morphology/structure was set by the initial polymer film deposition method, thus creating a morphology with many tie chains between crystalline domains. [132] Jacobs et al. report that the charge conductivity is higher for SqD by a factor in the range 5 - 15 as compared to a mixed-solution processing.

SqD proved to be an efficient solution to dope oriented P3HT films as demonstrated by Hamidi-Sakr et al.[37] They studied F4TCNQ-doped oriented P3HT films. After film deposition by doctor-blading, films were oriented by mechanical rubbing at high temperature and doped from $F_4$TCNQ:acetonitrile solution. They clearly demonstrated that high orientation results in anisotropic charge conductivity (σ) and Seebeck coefficient ($\alpha$) that are both enhanced in the direction of the polymer chains ($\sigma = 22 \pm 5$ S·cm$^{-1}$ and $\alpha = 60 \pm 2$ μV·K$^{-1}$). The structure of doped P3HT films was studied by TEM. Upon doping with $F_4$TCNQ, an expansion along the side chain direction and a contraction along the π-stacking direction was confirmed by

electron diffraction analysis. The increase of the alkyl sidechain periodicity $d_{100}$ with doping concentration was observed, which was directly influenced by the amount of incorporated $F_4TCNQ$ in the layers of side chains.[37]

**c) Vapour phase doping**

Vapor phase doping reminds SqD because it involves also a two-step process where the pristine polymer is firstly deposited onto a substrate and is subsequently doped. In this method, the pristine polymer film is exposed to the vapours of the dopant. This can be realized in a "home-made" small chamber in which the dopant powder is placed at the bottom of the chamber at a controlled temperature to promote its evaporation whereas the film is fixed on top of the chamber in direct contact with vapours. As reported by several studies, this method turned to be an efficient doping technique that allows to preserve remarkably the pristine film morphology/structure and as a result to reach high charge conductivities once in the doped state. [39,134,135]

Patel and co-workers studied the influence of different doping methods (solution vs vapour) on the thermoelectric power factor of PBTTT p-doped with $F_nTCNQ$ (n = 2 or 4).[135] The vapour-doped films have more than two orders of magnitude higher charge conductivity as-compared to SqD films. The most performing samples were those with the largest orientation correlation length (length scale of aligned backbones) upon doping. Vapour-doped PBTTT:$F_4TCNQ$ thin film, reaches the conductivity as high as 670 S/cm and a power factor of 120 $\mu W \cdot m^{-1} K^{-2}$.[135] Hynynen et al. have studied the thermoelectric performance of vapour-phase doped P3HT films spin-coated from different solvents. They found that the thermoelectric power factor increases with the degree of crystalline order from 0.2 to 2.7 $\mu W \cdot m^{-1} \cdot K^{-2}$ due to the enhanced electrical conductivity whereas the Seebeck coefficient

remained almost unimpacted. [134] Another study of Lim et al. confirmed the local ordering of P3HT, the texture and form factor of crystallites, and the long-range connectivity of crystalline domains have a strong impact on the electrical conductivity in thin films.[39] They found that the thermopower of P3HT films doped with $F_4TCNQ$ from the vapour phase did not evolve relatively to films doped from solution. On the other hand, they found that the electrical conductivity is significantly higher, yielding enhanced thermoelectric power factors.[39]

**d) Incremental concentration doping (ICD)**

Incremental concentration doping is a new recently reported way of preparing highly conductive polymer layers. This doping method is based on SqD method. In ICD, the polymer film is first deposited onto a substrate and subsequently doped in a dopant solutions in an orthogonal solvent whose concentration is progressively increased. The polymer film is doped by dipping in solutions starting with the lowest concentration and ending with the highest one. This allows a gradual doping of the polymer film.

Vijayakumar and co-workers used this way of doping in their comparative study on oriented PBTTT/P3HT doped with ferric chloride ($FeCl_3$).[136] A remarkable electrical conductivity along the chain axis was reported for PBTTT:$FeCl_3$ of the order of the conductivity of copper ~$2 \times 10^5$ $S \cdot cm^{-1}$ after using ICD in $FeCl_3$:nitromethane (0.1 to 5 mM concentration). Films of PBTTT directly doped at higher concentration of 5 mM $FeCl_3$ show conductivity that is one order of magnitude below that observed for films doped by ICD.

A similar strategy was used earlier, e.g. by Jacobs et al. however in a slightly different way. To reach higher doping levels, P3HT films were first doped with $F_4TCNQ$ using a 0.1 mg/ml acetonitrile solution. This would render the film insoluble. After, the film was further doped from a more concentrated dopant solution in chlorobenzene. [132]

### III.4 Survey on TE performance of doped P3HT

Table III.1 represents a non-exhaustive set of important results regarding TE performance of P3HT doped by various dopants.

| Doping agent | Doping method | $\sigma$, $S/cm$ | $\alpha$, $\mu V/K$ | $\sigma \cdot \alpha^2$, $\mu W \cdot m^{-1} \cdot K^{-2}$ | Reference |
|---|---|---|---|---|---|
| **$PF_6^-$** | *SqD* | 1 | 25 | 0.14 | Xuan et al.[137] (2010) |
| **FTS** | *vapour* | 28 | 60 | 10 | Glaudell et al.[133] (2014) |
| **$F_4TCNQ$** | *mixed solution* | 1.8 | - | - | Duong et al.[131] (2013) |
| | *mixed solution* | 0.1 | - | - | Yim et al.[129] (2008) |
| | *mixed solution* | 0.1 | - | - | Kiefer et al.[138] (2017) |
| | *mixed solution* | 1 | - | - | Aziz et al.[130] (2007) |
| | *vapour* | 12.7 | 43 | 2.3 | Hynynen et al.[134] |
| | *SqD* | 5.5 | - | - | Scholes et al.[53] (2015) |
| | *SqD* | 3 | - | - | Jacobs et al.[132] (2016) |
| | *mixed solution* | 8 | - | - | Jacobs et al.[132] (2016) |
| | *SqD on oriented films* | 22 | 60 | 8.5 | Hamidi-Sakr et al.[37] (2017) |
| | *SqD* | 2 | 76 | 1.2 | Lim et al[39] (2018) |
| | *vapour* | 37 | 85 | 27 | Lim et al[39] (2018) |

| | | | | | |
|---|---|---|---|---|---|
| | *vapour on 100% RR P3HT* | 13.4 | 77 | 8 | Lim et al. [54] (2019) |
| | *vapour on 5% RR P3HT* | 0.37 | 110 | 0.45 | Lim et al. [54] (2019) |
| | *SqD of RRa P3HT* | 0.02 | - | - | Yee et al.[139] (2019) |
| | ***SqD of oriented P3HT*** | 160 | 59 | 56 | ***This work*** |
| **$F_6TCNNQ$** | *mixed solution* | 7 | - | - | Karpov et al. [47] (2017) |
| | ***ICD on oriented P3HT*** | 276 | 48 | 63 | ***This work*** |
| **$FeCl_3$** | *vapour* | 63 | - | - | Yamamoto et al. [140] (2015) |
| | *SqD of RRa P3HT* | 0.01 | - | - | Yee et al.[139] (2019) |
| | *SqD of P3HT-coated PET fibers* | 350 | - | - | Fanous et al.[141] (2012) |
| | *SqD* | 42 | 105 | 46 | Jung et al.[142] (2017) |
| | ***ICD on oriented P3HT*** | 570 | 5.4 | 21 | ***This work*** |
| **$Mo(tfdCOCF_3)_3$** | *SqD of tensile-drawn P3HT* | 13 | 110 | 16 | Hynynen et al. [111] (2019) |
| | ***SqD of oriented P3HT*** | 509 | 56 | 160 | ***This work*** |

*For oriented samples highest reported values measured along the direction of alignment are given.

### III.5 Structural changes induced by doping of polythiophenes

One of the first doping experiments on P3HT revealing structural changes upon doping was done by Tashiro in early 1990s with iodine as a doping agent. [143] P3HT was cast from chloroform solution under ambient and stretched on a hot stage to about 4 times of their original length. The analysis of the iodine-doped structure was performed using a combination of X-Ray diffraction and structural modelling and calculation of electron diffraction patterns. Tashiro et al. proposed that the crystal structure of the pristine polymer is composed of stacked polythiophene (PT) layers constructed by a side-by-side arrangement of alkyl chains. They found that iodine doped P3HT possess a tunnel structure due to incorporation of polyiodide ions such as $I_3^-$ and $I_5^-$ into the layers of the alkyl side chains (see Figure III.4e). They managed to simulate the structural changes by constructing four possible models with energetically minimized structure. They were able to obtain X-Ray fiber diagrams that were more or less close to the experimental one. In the models 3 and 4 (see Figure III.4) a shift of PT chains along the c-axis generates tunnels along the b-axis wherein dopant anions can be hosted.

Lim et al. studied the effect of ordering on TE properties of blends of RR and RRa P3HT that were subsequently doped with $F_4$TCNQ from the vapour phase.[54] Grazing incidence wide angle X-ray scattering (GIWAXS) was used to reveal the crystalline structure of (un)doped blended films. Pristine films of RRa:RR P3HT blends show a lamellar morphology with preferential edge-on orientation of crystals. Lim et al. demonstrated that neat RRa P3HT films have no scattering features other than a broad amorphous background and cannot form a true crystal. Surprisingly, dopant molecules act as additives that induce ordering in the RRa P3HT films which leads to the appearance of out-of-plane h 0 0 peaks on 2D GIWAXS images upon doping.[54]

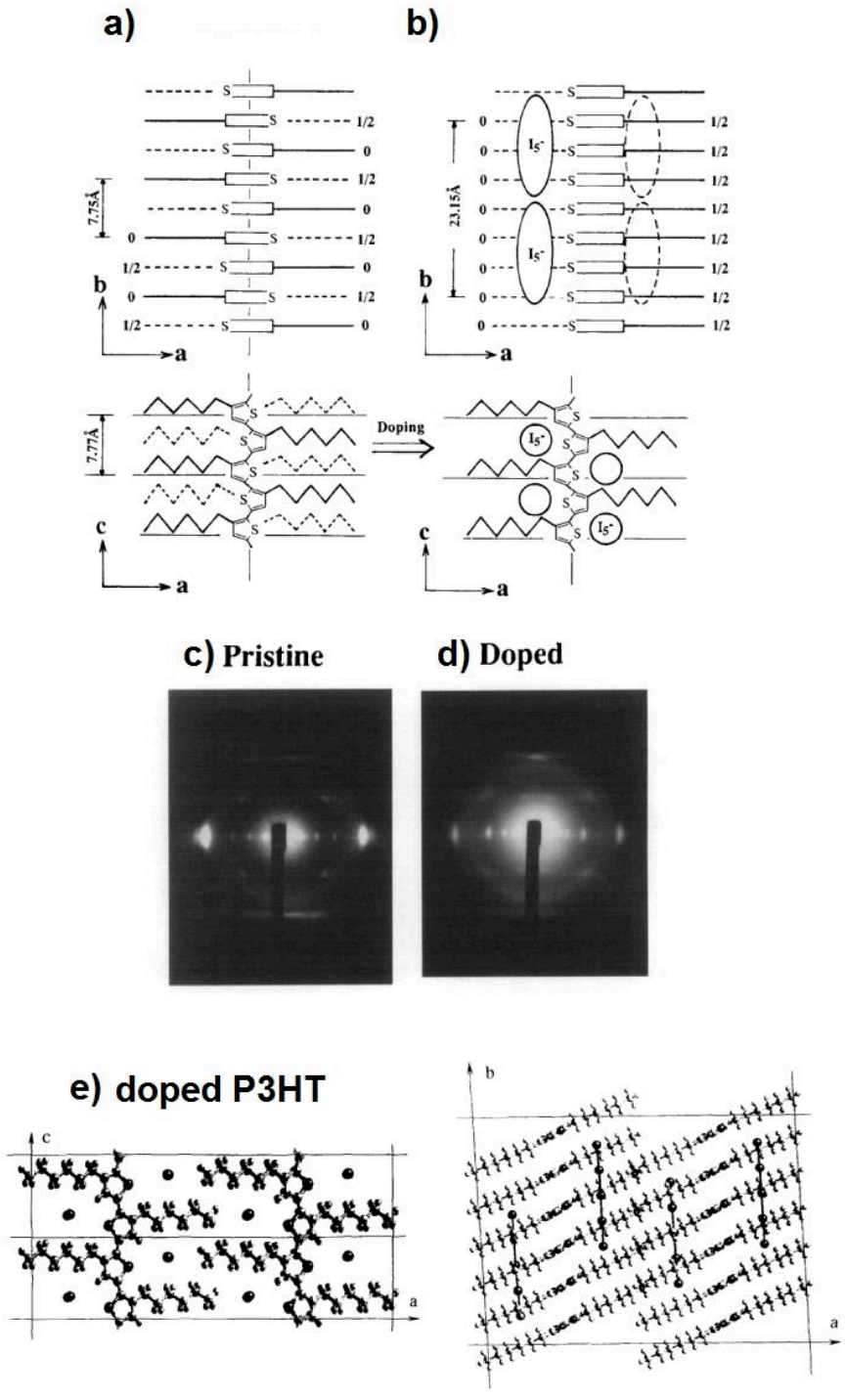


***Figure III.4*** *(a) and (b) Schematic illustration of the structural change in P3HT induced by iodine doping; electron diffraction patterns of pristine (c) and iodine-doped (d) P3HT oriented films, (e) - Energetically minimized crystal structures of doped P3HT. Reproduced from ref*[143]

Hamidi-Sakr et al. revealed the structure of oriented $F_4TCNQ$-doped P3HT films using TEM.[37] POM images demonstrate that the doped films remain birefringent: the pristine orientation of the rubbed layers is not altered upon doping (a full light extinction is observed under crossed polarizer and analyzer). Pristine polymer films rubbed at $T_R$~200 °C demonstrate lamellar film morphology seen in Bright Field (BF) TEM mode that is not altered upon doping. Crystalline orientation is found to be face-on as seen from images done in High-Resolution (HR) TEM mode.[37]

Electron diffraction (ED) was used to probe the crystal structure of P3HT prior/upon doping. Both pristine and doped films exhibited a well-defined ED pattern. One of the major structural changes due to doping is the increase of the periodicity along the side-chain direction from ~16.6 Å to ~17.5 Å (confirmed in HR-TEM). On the contrary, the π-stacking distance shows an opposite trend decreasing from 3.75 Å to 3.55 Å. UV-Vis-NIR spectroscopy helped to determine the relative orientation of $F_4TCNQ^-$ anions with respect to PT backbones. Parallel to the rubbing direction **R,** polaronic features P1 and P2 are observed, whereas for light polarization perpendicular to **R**, the pure anionic signal is observed. The transition dipole for the $F_4TCNQ$ anion is along the dopant's long axis, hence, polarized UV-vis-NIR confirms the fact that $F_4TCNQ$ dopant molecules intercalate in the layers of side-chains with their long axis perpendicular to the polymer backbone. (see Figure III.5d) The effect of doping concentration was also studied. The $d_{100}$ periodicity tends to increase, whereas the π-stacking distance $d_{020}$ decreases with the increase of doping concentration.[37] (see Figure III.5c)

Worthy to mention some information about structural changes in PEDOT which is also a substituted polythiophene (see Figure I.3). Kim and Brédas in 2008 studied the correlation between electronic and structural properties in pristine and tosylate-doped

PEDOT using a combination of density functional theory (DFT) and refined structural models built upon crystallographic data of PEDOT and other substituted polythiophenes.[42]

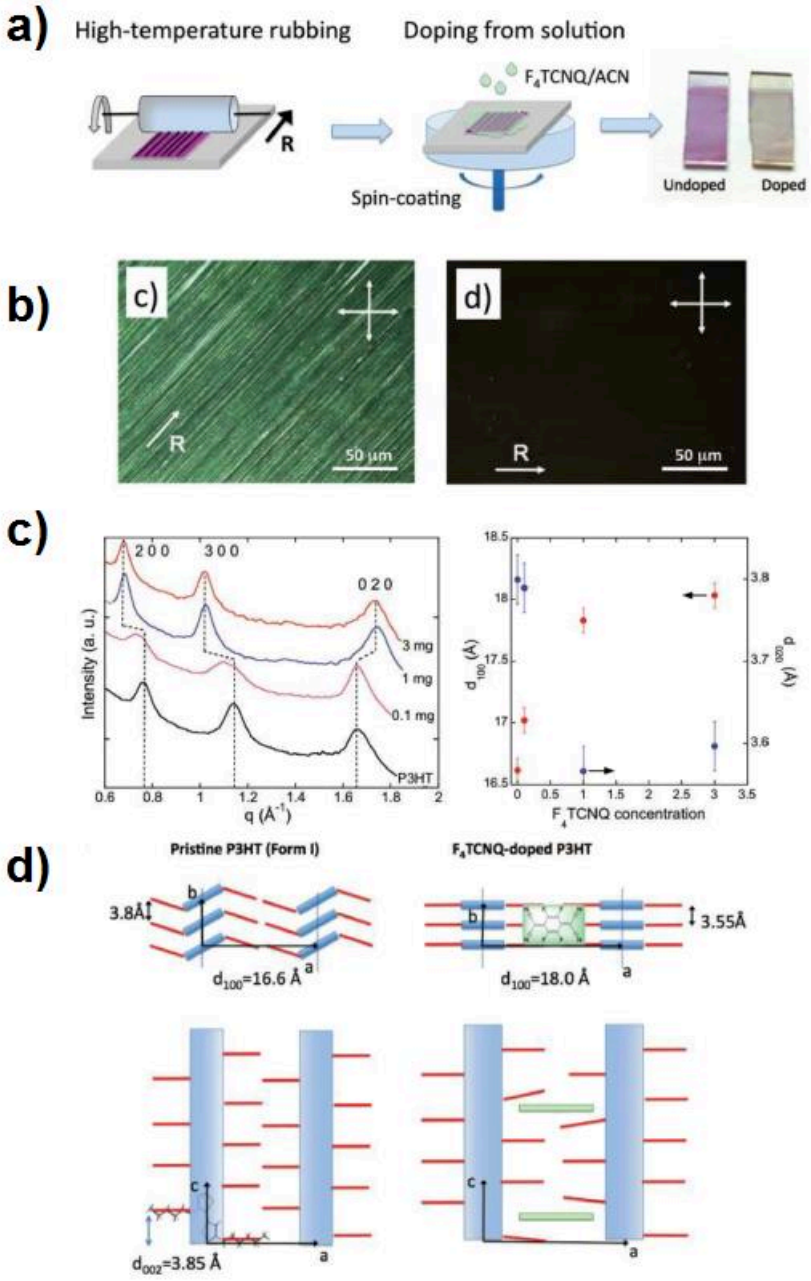


***Figure III.5*** *a) Schematic representation of preparation of highly oriented and doped P3HT films, b) Polarized optical microscopy images under crossed polarizers of the doped P3HT, c) Intensity profile along the equator of the ED pattern for films doped at different concentrations of $F_4TCNQ$ and evolution of the layer spacing $d_{100}$ and the π-stacking period*

*$d_{020}$ as a function of the doping level. d) Schematic illustration of the structural change in the packing of P3HT chains induced by doping with $F_4$TCNQ. Reproduced from ref*[37]

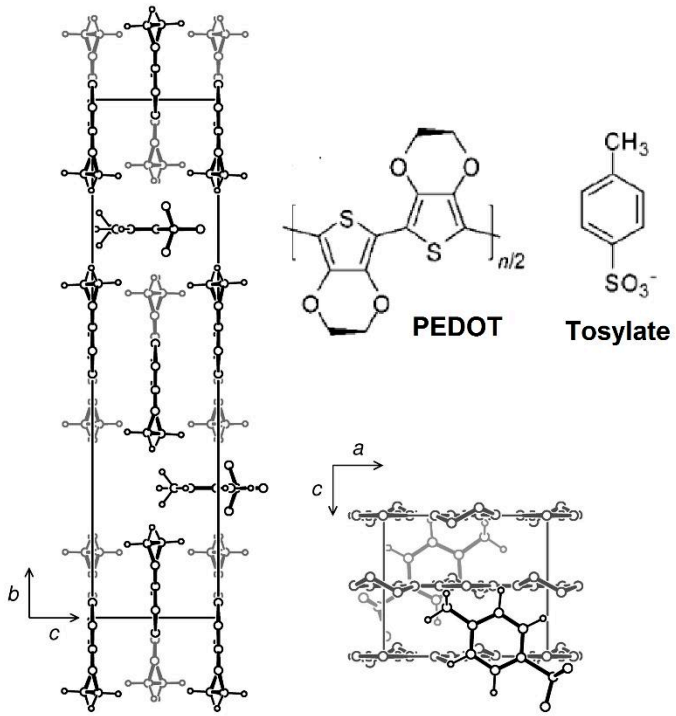


***Figure III.6*** *Calculated structure of PEDOT:Tosylate. Reproduced from ref*[42].

Ethylenedioxy-substitution planarizes the polymer backbones. It was found that the calculated crystal of pristine PEDOT adopts a monoclinic lamellar structure (with the space group - *P2/c*). Within the π-stacks, polymer backbones are slightly rotated around the chain axis by ~9° in the pristine PEDOT crystal contrary to the doped one. The crystal of the tosylate-doped form is found to have twice the unit cell size than the experimentally proposed structure. The unit cell proposed in their work has $Pmn2_1$ symmetry. (see Figure III.6) It has a mirror plane between adjacent PEDOT stacks. Tosylate molecules are

sandwiched in a monolayer between PEDOT stacks and are locked 33° off the chain axis, which causes the individual stacks to zigzag.[42]

### III.6 Correlations between conductivity and Seebeck coefficient in doped semiconductors

The description of the transport in organic semiconductors is relatively complex due to the existence of spatial and energetic disorders in materials that are intrinsically semi-crystalline and composed of highly ordered and disordered domains.

In general, the electrical conductivity $\sigma$ is directly related to the charge carrier concentration $n$ and to the charge mobility $\mu$.[133] In the free-electron approximation for the band structure, the conductivity $\sigma$ is a function of the free charge carrier concentration $n$ and the charge mobility $\mu$ (electron elementary charge $e$) :

$$\sigma = |e| \cdot \mu \cdot n \qquad [4]$$

An empirical correlation for doped organic semiconductors was experimentally observed first by Kaiser et al.[144] and subsequently by Glaudell et al.[133] for doped PBTTT. Glaudell et al. have performed a fruitful study on three polymers, namely P3HT, PBTTT-$C_{14}$ and poly(2,5-bis(thiphen-2-yl)-(3,7-diheptadecantyltetrathienoacene)) (P2TDC$_{17}$ -FT4) doped by two different doping methods: using SqD by $F_4$TCNQ and vapour phase doping with fluoroalkyl trichlorosilanes (FTS).[133] Surprisingly, for two different doping methods and different dopants a clear correlation between thermopower and electrical conductivity was observed following the scaling law $S \sim \sigma^{-1/4}$. This was a clear evidence of the fact that the thermoelectric properties are dominated primarily by the polymer and

not by the specific doping mechanism or dopant chemical nature.[133] Similarly, Patel et al. observed the same correlation in $F_n$TCNQ-doped (n=2, 4) PBTTT.[135]Accordingly, a power law is found to reproduce quite well the correlation between electrical conductivity and Seebeck coefficient:

$$\alpha \sim \sigma^{-1/s} \quad [5]$$

Where $s$ in the scaling exponent. Across a wide range of materials thermopower scales with conductivity with the exponent of -1/4, however some studies report an exponent of −1/3 depending on the range of experimental data set chosen for the fit.[145]

The power factor consequently then has a square root dependence on conductivity:

$$PF \sim \sigma^{1/2} \quad [6]$$

The theoretical description of the charge transport in doped polymers and the resulting correlation between charge conductivity and thermopower was performed recently by Kang and Snyder. They have built a generalized charge-transport model.[145] In their model the electrical conductivity $\sigma$ can be characterized using the transport function $\sigma_E$ :

$$\sigma = \int \sigma_E \left(\frac{\partial f}{\partial E}\right) dE$$
$$\sigma_E(E,T) = \sigma_{E_0}(T) \cdot \left(\frac{E - E_t}{k_B T}\right)^s, E > E_t \quad [7]$$

Most importantly in this model, the conductivity has two essential features that help to identify the transport mechanism: a transport edge $E_t$ and a transport parameter s.

They also relate the Seebeck coefficient to the the transport function versus charge carrier energy following the relation:

$$\alpha \sim \frac{1}{\sigma}\int\left(\frac{E-E_F}{k_BT}\right)\cdot\sigma_E\cdot\left(-\frac{\partial f}{\partial E}\right)dE \qquad [8]$$

After extensive analysis of doped polymer systems such as P3HT, PBTTT, PEDOT, the electrical conductivity and Seebeck coefficient was analysed. It was found that most polymers (except PEDOT:tosylate) show $s=3$ and possess thermally activated conductivity. In strong contrast, $s=1$ typical for "itinerant" conductivity is found in crystalline semiconductors and metals.[145] It is worth to stress that s=3 should imply a s=1/3 exponent, which is not observed experimentally.

Lim et al. has found that P3HT films vapour doped by $F_4TCNQ$ follow the trend $\alpha \sim \sigma^{-1/4}$.[39] Tanaka et al. in their study on PBTTT doped by electrolyte gating were able to analyse the $\alpha vs \sigma$ correlation over a large range of conductivities (about six orders of magnitudes). They have found two distinct regimes: non-metallic and metallic. The $S vs \sigma$ relation observed followed the empirical trend of $\alpha \sim \sigma^{-1/4}$ in the low-conductivity region ($\sigma$ < 100 S/cm), whereas it deviates from this relation as $\sigma$ increases, approaching the scaling law $\alpha \sim \sigma^{-1}$.[146]

Lepinoy et al. have shown that the TE properties of one of the most promising conducting polymer PEDOT:Tosylate follows actually a generic behaviour as $\alpha \sim \sigma^{-1/4}$. They managed to develop a theory that explains such a behaviour for PEDOT. They claim that Dirac fermions scattered by unscreened ionized impurities can account for this scaling behaviour. [147]

Vijayakumar et al. have studied the charge transport properties in oriented $FeCl_3$-doped $C_{12}$-PBTTT and P3HT thin films. [136] Both polymers exhibit a common trend in the direction parallel to the chain direction $\alpha_{\parallel} \sim \sigma_{\parallel}^{-1/4}$. Whereas in the direction normal to the chain axis the trend differs much. It followed the trend reported earlier by Mateeva et al. in stretch-aligned polyacetylene, polypyrrole, and polyaniline[148]:

$$\alpha_{\perp} = -\frac{1}{\beta}\left(\frac{k_B}{e}\right)\ln\left(\frac{\sigma_{\perp}}{\sigma_{\perp}^{\max}}\right) \quad [9]$$

In the direction perpendicular to the chain axis for both polymers $\alpha_{\perp} \sim -\ln(\sigma_{\perp})$ trend is observed supporting a different charge transport mechanism.[136]

**References:**


1. Bakhshi, A. K., Kaur, A. & Arora, V. Molecular engineering of novel low band gap conducting polymers. *INDIAN JOURNAL OF CHEMISTRY SECTION A-INORGANIC BIO-INORGANIC PHYSICAL THEORETICAL & ANALYTICAL CHEMISTRY* vol. 51 57–68 (2012).
2. Walatka, V. V., Labes, M. M. & Perlstein, J. H. Polysulfur Nitride---a One-Dimensional Chain with a Metallic Ground State. *Phys. Rev. Lett.* **31**, 1139–1142 (1973).
3. Chiang, C. K. *et al.* Electrical Conductivity in Doped Polyacetylene. *Phys. Rev. Lett.* **39**, 1098–1101 (1977).
4. Press release. NobelPrize.org. Nobel Media AB 2020. Tue. 25 Aug 2020. <https://www.nobelprize.org/prizes/chemistry/2000/press-release/>.
5. Moiz, S. A., Khan, I., Younis, W. & Karimov, K. Space Charge–Limited Current Model for Polymers Provisional chapter Space Charge–Limited Current Model for Polymers. in 91–117 (2016). doi:10.5772/63527.
6. Kroon, R. *et al.* Thermoelectric plastics: from design to synthesis, processing and structure–property relationships. *Chem. Soc. Rev.* **45**, 6147–6164 (2016).
7. Yuvaraja, S. *et al.* Organic field-effect transistor-based flexible sensors. *Chem. Soc. Rev.* **49**, 3423–3460 (2020).
8. Baeg, K.-J., Binda, M., Natali, D., Caironi, M. & Noh, Y.-Y. Organic Light Detectors: Photodiodes and Phototransistors. *Adv. Mater.* **25**, 4267–4295 (2013).
9. Torsi, L., Magliulo, M., Manoli, K. & Palazzo, G. Organic field-effect transistor sensors: a tutorial review. *Chem. Soc. Rev.* **42**, 8612–8628 (2013).
10. Darlinski, G. *et al.* Mechanical force sensors using organic thin-film transistors. *J. Appl. Phys.* **97**, 093708 (2005).

11. Khan, M. A., Allemand, C. & Eagar, T. W. Noncontact temperature measurement. I. Interpolation based techniques. *Rev. Sci. Instrum.* **62**, 392–402 (1991).
12. Zhang, F. *et al.* Ultrathin Film Organic Transistors: Precise Control of Semiconductor Thickness via Spin-Coating. *Adv. Mater.* **25**, 1401–1407 (2013).
13. Park, Y. D. *et al.* Polyelectrolyte Interlayer for Ultra-Sensitive Organic Transistor Humidity Sensors. *ACS Appl. Mater. Interfaces* **5**, 8591–8596 (2013).
14. A. Caboni, E. Orgiu, M. Barbaro & A. Bonfiglio. Flexible Organic Thin-Film Transistors for pH Monitoring. *IEEE Sens. J.* **9**, 1963–1970 (2009).
15. Jang, Y. *et al.* Point-of-Use Detection of Amphetamine-Type Stimulants with Host-Molecule-Functionalized Organic Transistors. *Chem* **3**, 641–651 (2017).
16. Get, R., Islam, S. M., Singh, S. & Mahala, P. Organic polymer bilayer structures for applications in flexible solar cell devices. *MICROELECTRONIC ENGINEERING* vol. 222 (2020).
17. Siva, U. *et al.* Single walled carbon nanotube incorporated Titanium dioxide and Poly (3-hexylthiophene) as electron and hole transport materials for solar cells. *MATERIALS LETTERS* vol. 276 (2020).
18. Park, M.-J., Lee, J.-H. & Hwang, D.-H. Synthesis and light-emitting properties of new polyfluorene copolymers containing a triphenylamine based hydrazone comonomer. *15th Mol. Electron. Devices Symp.* **6**, 752–755 (2006).
19. Roncali, J. Synthetic Principles for Bandgap Control in Linear π-Conjugated Systems. *Chem. Rev.* **97**, 173–206 (1997).
20. Perepichka, I. F., Levillain, E. & Roncali, J. Effect of substitution of 3,4-ethylenedioxythiophene (EDOT) on the electronic properties of the derived

electrogenerated low band gap conjugated polymers. *J Mater Chem* **14**, 1679–1681 (2004).

21. Yang, S. & Kertesz, M. Theoretical Design of Low Band Gap Conjugated Polymers through Ladders with Acetylenic Crosspieces. *Macromolecules* **40**, 6740–6747 (2007).
22. Hou, J. *et al.* Synthesis of a Low Band Gap Polymer and Its Application in Highly Efficient Polymer Solar Cells. *J. Am. Chem. Soc.* **131**, 15586–15587 (2009).
23. Li, X. *et al.* Low Bandgap Donor-Acceptor π-Conjugated Polymers From Diarylcyclopentadienone-Fused Naphthalimides. *Front. Chem.* **7**, 362 (2019).
24. Heckler, I. M. *et al.* The Influence of Conjugated Polymer Side Chain Manipulation on the Efficiency and Stability of Polymer Solar Cells. *Mater. Basel Switz.* **9**, 181 (2016).
25. Chen, C.-A., Yang, P.-C., Wang, S.-C., Tung, S.-H. & Su, W.-F. Side Chain Effects on the Optoelectronic Properties and Self-Assembly Behaviors of Terthiophene–Thieno[3,4-c]pyrrole-4,6-dione Based Conjugated Polymers. *Macromolecules* (2018) doi:10.1021/acs.macromol.8b01073.
26. Guo, Z. *et al.* Tuning the thermal conductivity of solar cell polymers through side chain engineering. *PHYSICAL CHEMISTRY CHEMICAL PHYSICS* vol. 16 7764–7771 (2014).
27. McCullough, R. D. The Chemistry of Conducting Polythiophenes. *Adv. Mater.* **10**, 93–116 (1998).
28. Seebeck, T. J. *Der, Abhandlungen der Deut Schen Akad. Berlin, Wissenshafften zu 1823, 265, 1822.*
29. Eslamian, M. Inorganic and Organic Solution-Processed Thin Film Devices. *NANO-MICRO LETTERS* vol. 9 (2017).
30. *A. F. Ioffe, L. S. Stil'bans, E. K. Iordanishvili, T. S. Stavitskaya, A. Gelbtuch, G. Vineyard, Phys. Today 1959, 12, 42.*

31. Yoon, S. M. *et al.* Fabrication of large-scale p-type 75%Sb2Te3-25%Bi2Te3 thermoelectric materials by gas atomization and hot isostatic pressing. *Mater. Res. Bull.* **130**, 110924 (2020).

32. Venkatasubramanian, R., Siivola, E., Colpitts, T. & O'Quinn, B. Thin-film thermoelectric devices with high room-temperature figures of merit. *Nature* **413**, 597–602 (2001).

33. Jaziri, N. *et al.* A comprehensive review of Thermoelectric Generators: Technologies and common applications. *Energy Rep.* (2019) doi:10.1016/j.egyr.2019.12.011.

34. Bubnova, O. *et al.* Optimization of the thermoelectric figure of merit in the conducting polymer poly(3,4-ethylenedioxythiophene). *Nat. Mater.* **10**, 429–433 (2011).

35. Zhang, Y., Heo, Y.-J. & Park, S.-J. Advances in Organic Thermoelectric Materials: Principle Mechanisms and Emerging Carbon-Based Green Energy Materials. *Polymers* **11**, 167 (2019).

36. Ludwigs, S. *P3HT Revisited - From Molecular Scale to Solar Cell Devices*. (Springer Berlin Heidelberg, Berlin, Heidelberg, 2014).

37. Hamidi-Sakr, A. *et al.* A Versatile Method to Fabricate Highly In-Plane Aligned Conducting Polymer Films with Anisotropic Charge Transport and Thermoelectric Properties: The Key Role of Alkyl Side Chain Layers on the Doping Mechanism. *Adv. Funct. Mater.* **27**, 1700173 (2017).

38. DeLongchamp, D. M. *et al.* Controlling the Orientation of Terraced Nanoscale "Ribbons" of a Poly(thiophene) Semiconductor. *ACS Nano* **3**, 780–787 (2009).

39. Lim, E., Peterson, K. A., Su, G. M. & Chabinyc, M. L. Thermoelectric Properties of Poly(3-hexylthiophene) (P3HT) Doped with 2,3,5,6-Tetrafluoro-7,7,8,8-tetracyanoquinodimethane (F4TCNQ) by Vapor-Phase Infiltration. *Chem. Mater.* **30**, 998–1010 (2018).

40. Hynynen, J. *et al.* Enhanced Electrical Conductivity of Molecularly p-Doped Poly(3-hexylthiophene) through Understanding the Correlation with Solid-State Order. *Macromolecules* **50**, 8140–8148 (2017).

41. Fan, Z., Li, P., Du, D. & Ouyang, J. Significantly Enhanced Thermoelectric Properties of PEDOT:PSS Films through Sequential Post-Treatments with Common Acids and Bases. *Adv Energy Mater* **7**, 1602116 (2017).

42. Kim, E.-G. & Brédas, J.-L. Electronic Evolution of Poly(3,4-ethylenedioxythiophene) (PEDOT): From the Isolated Chain to the Pristine and Heavily Doped Crystals. *J. Am. Chem. Soc.* **130**, 16880–16889 (2008).

43. Panigrahy, S. & Kandasubramanian, B. Polymeric thermoelectric PEDOT: PSS & composites: Synthesis, progress, and applications. *Eur. Polym. J.* **132**, 109726 (2020).

44. Biniek, L., Leclerc, N., Heiser, T., Bechara, R. & Brinkmann, M. Large Scale Alignment and Charge Transport Anisotropy of pBTTT Films Oriented by High Temperature Rubbing. *Macromolecules* **46**, 4014–4023 (2013).

45. Vijayakumar, V. *et al.* Effect of alkyl side chain length on doping kinetics, thermopower and charge transport properties in highly oriented F4TCNQ doped PBTTT films. *ACS Appl Mater Interfaces* **11**, 4942 (2019).

46. Genevaz, N. *et al.* Tuning crystallochromism in diketopyrrolopyrrole-co-thieno[3,2-b]thiophene derivatives by the architecture of their alkyl side chains. *J. Mater. Chem. C* **6**, 9140–9151 (2018).

47. Karpov, Y. *et al.* Molecular Doping of a High Mobility Diketopyrrolopyrrole–Dithienylthieno[3,2-b]thiophene Donor–Acceptor Copolymer with F6TCNNQ. *Macromolecules* **50**, 914–926 (2017).

48. Chew, A. R. & Salleo, A. Spectroscopic studies of dopant-induced conformational changes in poly (3-hexylthiophene) thin films. *MRS Commun* **7**, 728 (2017).

49. Chew, A. R., Ghosh, R., Shang, Z., Spano, F. C. & Salleo, A. Sequential Doping Reveals the Importance of Amorphous Chain Rigidity in Charge Transport of Semi-Crystalline Polymers. *J. Phys. Chem. Lett.* **8**, 4974–4980 (2017).

50. Kayunkid, N., Uttiya, S. & Brinkmann, M. Structural Model of Regioregular Poly(3-hexylthiophene) Obtained by Electron Diffraction Analysis. *Macromolecules* **43**, 4961–4967 (2010).

51. Hamidi-Sakr, A., Biniek, L., Fall, S. & Brinkmann, M. Precise Control of Lamellar Thickness in Highly Oriented Regioregular Poly(3-Hexylthiophene) Thin Films Prepared by High-Temperature Rubbing: Correlations with Optical Properties and Charge Transport. *Adv. Funct. Mater.* **26**, 408–420 (2015).

52. Pingel, P. & Neher, D. Comprehensive picture of $p$-type doping of P3HT with the molecular acceptor F${}_{4}$TCNQ. *Phys. Rev. B* **87**, 115209 (2013).

53. Scholes, D. T. *et al.* Overcoming Film Quality Issues for Conjugated Polymers Doped with F4TCNQ by Solution Sequential Processing: Hall Effect, Structural, and Optical Measurements. *J. Phys. Chem. Lett.* **6**, 4786–4793 (2015).

54. Lim, E., Glaudell, A. M., Miller, R. & Chabinyc, M. L. The role of Ordering on the Thermoelectric Properties of Blends of Regioregular and Regiorandom Poly(3-hexylthiophene). *Adv Elect Mater.* **5**, 1800915 (2019).

55. Scholes, D. T. *et al.* The Effects of Crystallinity on Charge Transport and the Structure of Sequentially Processed F4TCNQ-Doped Conjugated Polymer Films. *Adv Funct Mater* **27**, 1702654 (2017).

56. Ghosh, R., Pochas, C. M. & Spano, F. C. Polaron Delocalization in Conjugated Polymer Films. *J Phys Chem C* **120**, 11394 (2016).

57. Aubry, T. J. *et al.* Tunable Dopants with Intrinsic Counterion Separation Reveal the Effects of Electron Affinity on Dopant Intercalation and Free Carrier Production in Sequentially Doped Conjugated Polymer Films. *Adv. Funct. Mater.* **30**, 2001800 (2020).

58. McGrail, B. T., Sehirlioglu, A. & Pentzer, E. Polymer Composites for Thermoelectric Applications. *Angew. Chem. Int. Ed.* **54**, 1710–1723 (2015).

59. Liu, J. *et al.* Thermal Conductivity and Elastic Constants of PEDOT:PSS with High Electrical Conductivity. *Macromolecules* **48**, 585 (2015).

60. Du, Y. *et al.* Thermoelectric Fabrics: Toward Power Generating Clothing. *Sci. Rep.* **5**, 6411 (2015).

61. Nonoguchi, Y. *et al.* Systematic Conversion of Single Walled Carbon Nanotubes into n-type Thermoelectric Materials by Molecular Dopants. *Sci. Rep.* **3**, 3344 (2013).

62. Wei, Q., Mukaida, M., Kirihara, K., Naitoh, Y. & Ishida, T. Polymer thermoelectric modules screen-printed on paper. *RSC Adv.* **4**, 28802–28806 (2014).

63. Lund, A., Tian, Y., Darabi, S. & Müller, C. A polymer-based textile thermoelectric generator for wearable energy harvesting. *J. Power Sources* **480**, 228836 (2020).

64. Lin, J. W.-P. & Dudek, L. P. Synthesis and properties of poly(2,5-thienylene). *J. Polym. Sci. Polym. Chem. Ed.* **18**, 2869–2873 (1980).

65. Yamamoto, T., Sanechika, K. & Yamamoto, A. Preparation of thermostable and electric-conducting poly(2,5-thienylene). *J. Polym. Sci. Polym. Lett. Ed.* **18**, 9–12 (1980).

66. Marrocchi, A., Lanari, D., Facchetti, A. & Vaccaro, L. Poly(3-hexylthiophene): synthetic methodologies and properties in bulk heterojunction solar cells. *Energy Env. Sci* **5**, 8457–8474 (2012).

67. Crossland, E. J. W., Rahimi, K., Reiter, G., Steiner, U. & Ludwigs, S. Systematic Control of Nucleation Density in Poly(3-Hexylthiophene) Thin Films. *Adv. Funct. Mater.* **21**, 518–524 (2011).

68. Bronstein, H. A. & Luscombe, C. K. Externally Initiated Regioregular P3HT with Controlled Molecular Weight and Narrow Polydispersity. *J. Am. Chem. Soc.* **131**, 12894–12895 (2009).

69. Condon, E. *Phys. Rev.* 1182–1201 (1926).

70. Niles, E. T. *et al.* J-Aggregate Behavior in Poly-3-hexylthiophene Nanofibers. *J. Phys. Chem. Lett.* **3**, 259–263 (2012).

71. Clark, J., Chang, J.-F., Spano, F. C., Friend, R. H. & Silva, C. Determining exciton bandwidth and film microstructure in polythiophene films using linear absorption spectroscopy. *Appl Phys Lett* **94**, 163306 (2009).

72. Spano, F. C. & Silva, C. H- and J-Aggregate Behavior in Polymeric Semiconductors. *Annu. Rev. Phys. Chem.* **65**, 477–500 (2014).

73. Hochstrasser, R. M. & Kasha, M. *Photochem. Photobiol.* **3(4)**, 317–331 (1964).

74. Mena-Osteritz, E. *et al.* Two-Dimensional Crystals of Poly(3-Alkyl- thiophene)s: Direct Visualization of Polymer Folds in Submolecular Resolution. *Angew. Chem. Int. Ed.* **39**, 2679–2684 (2000).

75. Brinkmann, M. & Rannou, P. Molecular Weight Dependence of Chain Packing and Semicrystalline Structure in Oriented Films of Regioregular Poly(3-hexylthiophene) Revealed by High-Resolution Transmission Electron Microscopy. *Macromolecules* **42**, 1125–1130 (2009).

76. Brinkmann, M. & Wittmann, J.-C. Orientation of Regioregular Poly(3-hexylthiophene) by Directional Solidification: A Simple Method to Reveal the Semicrystalline Structure of a Conjugated Polymer. *Adv. Mater.* **18**, 860–863 (2006).

77. Na, J. Y., Kang, B., Sin, D. H., Cho, K. & Park, Y. D. Understanding Solidification of Polythiophene Thin Films during Spin-Coating: Effects of Spin-Coating Time and Processing Additives. *Sci. Rep.* **5**, 13288 (2015).

78. DeLongchamp, D. M. *et al.* Variations in Semiconducting Polymer Microstructure and Hole Mobility with Spin-Coating Speed. *Chem. Mater.* **17**, 5610–5612 (2005).

79. Nagamatsu, S. *et al.* Backbone Arrangement in "Friction-Transferred" Regioregular Poly(3-alkylthiophene)s. *Macromolecules* **36**, 5252–5257 (2003).

80. Brinkmann, M. Structure and morphology control in thin films of regioregular poly(3-hexylthiophene). *J. Polym. Sci. Part B Polym. Phys.* **49**, 1218–1233 (2011).

81. Lotz, B. & Wittmann, J.-C. Structure of Polymer Single Crystals. in *Materials Science and Technology* (American Cancer Society, 2006). doi:10.1002/9783527603978.mst0134.

82. Hartmann, L. *et al.* 2D Versus 3D Crystalline Order in Thin Films of Regioregular Poly(3-hexylthiophene) Oriented by Mechanical Rubbing and Epitaxy. *Adv. Funct. Mater.* **21**, 4047–4057 (2011).

83. Xue, X. *et al.* Oriented Liquid Crystalline Polymer Semiconductor Films with Large Ordered Domains. *ACS Appl. Mater. Interfaces* **7**, 26726–26734 (2015).

84. Pandey, M., Kumari, N., Nagamatsu, S. & Pandey, S. S. Recent advances in the orientation of conjugated polymers for organic field-effect transistors. *J Mater Chem C* **7**, 13323–13351 (2019).

85. Yasuda, T. Anisotropic carrier transport properties of stretch-oriented π- conjugated polymers in organic field-effect transistors. *Phys Status Solidi C 8* **8**, 604 (2011).

86. Wittmann, J. C. & Smith, P. Highly oriented thin films of poly(tetrafluoroethylene) as a substrate for oriented growth of materials. *Nature* **352**, 414–417 (1991).

87. Nagamatsu, S. *et al. Appl. Phys. Lett.* **84**, 4608 (2004).

88. Hosokawa, Y. *et al. Appl. Phys. Lett.* **100**, 203305 (2012).

89. Brinkmann, M., Hartmann, L., Biniek, L., Tremel, K. & Kayunkid, N. Orienting Semi-Conducting π-Conjugated Polymers. *Macromol. Rapid Commun.* **35**, 9–26 (2014).

90. Wittmann, J. C., Hodge, A. M. & Lotz, B. Epitaxial crystallization of polymers onto benzoic acid: Polyethylene and paraffins, aliphatic polyesters, and polyamides. *J. Polym. Sci. Polym. Phys. Ed.* **21**, 2495–2509 (1983).

91. Wittmann, J. C. & Lotz, B. Epitaxial crystallization of monoclinic and orthorhombic polyethylene phases. *Polymer* **30**, 27–34 (1989).

92. Brinkmann, M. & Rannou, P. Effect of Molecular Weight on the Structure and Morphology of Oriented Thin Films of Regioregular Poly(3-hexylthiophene) Grown by Directional Epitaxial Solidification. *Adv. Funct. Mater.* **17**, 101–108 (2007).

93. Brinkmann, M., Contal, C., Kayunkid, N., Djuric, T. & Resel, R. Highly Oriented and Nanotextured Films of Regioregular Poly(3-hexylthiophene) Grown by Epitaxy on the Nanostructured Surface of an Aromatic Substrate. *Macromolecules* **43**, 7604–7610 (2010).

94. Brinkmann, M. *et al.* Segregated versus Mixed Interchain Stacking in Highly Oriented Films of Naphthalene Diimide Bithiophene Copolymers. *ACS Nano* **6**, 10319–10326 (2012).

95. Aerle, N. A. J. M. V., Barmentlo, M. & Hollering, R. Effect of rubbing on the molecular orientation within polyimide orienting layers of liqui_crystal displays. in (1993).

96. Hartmann, L. Elaboration and characterization of oriented and nanostructured hybrid materials of interest for organic electronics.

97. Kajiya, D., Ozawa, S., Koganezawa, T. & Saitow, K. Enhancement of Out-of-plane Mobility in P3HT Film by Rubbing: Aggregation and Planarity Enhanced with Low Regioregularity. *J. Phys. Chem. C* **119**, 7987–7995 (2015).

98. Tremel, K. *et al.* Charge Transport Anisotropy in Highly Oriented Thin Films of the Acceptor Polymer P(NDI2OD-T2). *Adv. Energy Mater.* **4**, 1301659.

99. Biniek, L., Leclerc, N., Heiser, T., Bechara, R. & Brinkmann, M. Large scale alignment and charge transport anisotropy of pBTTT films oriented by high temperature rubbing. *Macromolecules* **46**, 4014 (2013).

100. O'Connor, B. *et al.* Anisotropic Structure and Charge Transport in Highly Strain-Aligned Regioregular Poly(3-hexylthiophene). *Adv. Funct. Mater.* **21**, 3697–3705 (2011).

101. Engelaere, J. C., Cavrot, J. P. & Rietsch, F. Tensile drawing behaviour of polyethylene terephthalate: Influence of molecular weight and pre-orientation. *Polymer* **23**, 766–770 (1982).

102. Zhang, C. & Smith, P. Tensile drawing of fully conjugated poly(2,5-thienylene vinylene). *Synth. Met.* **46**, 235–242 (1992).

103. Hynynen, J. *et al.* Enhanced Thermoelectric Power Factor of Tensile Drawn Poly(3-hexylthiophene). *ACS Macro Lett.* **8**, 70–76 (2019).

104. Lan, Y.-K. & Huang, C.-I. Charge Mobility and Transport Behavior in the Ordered and Disordered States of the Regioregular Poly(3-hexylthiophene). *J. Phys. Chem. B* **113**, 14555–14564 (2009).

105. Jimison, L. H., Toney, M. F., McCulloch, I., Heeney, M. & Salleo, A. Charge-Transport Anisotropy Due to Grain Boundaries in Directionally Crystallized Thin Films of Regioregular Poly(3-hexylthiophene). *Adv. Mater.* **21**, 1568–1572 (2009).

106. Bredas, J. L. & Street, G. B. Polarons, bipolarons, and solitons in conducting polymers. *Acc. Chem. Res.* **18**, 309–315 (1985).

107. Trefz, D. *et al.* Electrochemical Investigations of the N-Type Semiconducting Polymer P(NDI2OD-T2) and Its Monomer: New Insights in the Reduction Behavior. *J. Phys. Chem. C* **119**, 22760–22771 (2015).

108. Gross, Y. M. *et al.* From Isotropic to Anisotropic Conductivities in P(NDI2OD-T2) by (Electro-)Chemical Doping Strategies. *Chem. Mater.* **31**, 3542–3555 (2019).

109. Bharti, M., Singh, A., Samanta, S. & Aswal, D. K. Conductive polymers for thermoelectric power generation. *Prog. Mater. Sci.* **93**, 270–310 (2018).

110. Crovetto, A., Huss-Hansen, M. K. & Hansen, O. How the relative permittivity of solar cell materials influences solar cell performance. *Sol. Energy* **149**, 145–150 (2017).

111. Hynynen, J. *et al.* Enhanced Thermoelectric Power Factor of Tensile Drawn Poly(3-hexylthiophene). *ACS Macro Lett.* **8**, 70–76 (2019).

112. Wang, C. *et al.* High Dielectric Constant Semiconducting Poly(3-alkylthiophene)s from Side Chain Modification with Polar Sulfinyl and Sulfonyl Groups. *Macromolecules* **51**, 9368–9381 (2018).

113. Qi, Y. *et al.* A Molybdenum Dithiolene Complex as p-Dopant for Hole-Transport Materials: A Multitechnique Experimental and Theoretical Investigation. *Chem. Mater.* **22**, 524–531 (2010).

114. Qi, Y. *et al.* Use of a High Electron-Affinity Molybdenum Dithiolene Complex to p-Dope Hole-Transport Layers. *J. Am. Chem. Soc.* **131**, 12530–12531 (2009).

115. Liang, Z. *et al.* Influence of dopant size and electron affinity on the electrical conductivity and thermoelectric properties of a series of conjugated polymers. *J Mater Chem A* **6**, 16495–16505 (2018).

116. Patel, S. N., Glaudell, A. M., Kiefer, D. & Chabinyc, M. L. Increasing the Thermoelectric Power Factor of a Semiconducting Polymer by Doping from the Vapor Phase. *ACS Macro Lett.* **5**, 268–272 (2016).

117. Hatchett, D. W., Josowicz, M. & Janata, J. Acid Doping of Polyaniline: Spectroscopic and Electrochemical Studies. *J. Phys. Chem. B* **103**, 10992–10998 (1999).

118. Geethalakshmi, D., Muthukumarasamy, N. & Balasundaraprabhu, R. CSA-doped PANI semiconductor nanofilms: synthesis and characterization. *J. Mater. Sci. Mater. Electron.* **26**, 7797–7803 (2015).

119. Nava, D. *et al.* Drastic Improvement of Air Stability in an n-Type Doped Naphthalene-Diimide Polymer by Thionation. *ACS Appl. Energy Mater.* **1**, 4626–4634 (2018).

120. Shin, Y. *et al.* Improving Miscibility of a Naphthalene Diimide-Bithiophene Copolymer with n-Type Dopants through the Incorporation of “Kinked” Monomers. *Adv. Electron. Mater.* **4**, 1700581 (2018).

121. Kiefer, D. *et al.* Enhanced n-Doping Efficiency of a Naphthalenediimide-Based Copolymer through Polar Side Chains for Organic Thermoelectrics. *ACS Energy Lett.* **3**, 278–285 (2018).

122. Nogami, Y. *et al.* On the metallic states in highly conducting iodine-doped polyacetylene. *Solid State Commun.* **76**, 583–586 (1990).

123. Pukacki, W., Płocharski, J. & Roth, S. Anisotropy of thermoelectric power of stretch-oriented new polyacetylene. *Synth. Met.* **62**, 253–256 (1994).

124. Jacobs, I. E. & Moulé, A. J. Controlling Molecular Doping in Organic Semiconductors. *Adv. Mater.* **29**, 1703063 (2017).

125. Pingel, P. & Neher, D. Comprehensive Picture of p-Type Doping of P3HT with the Molecular Acceptor F4TCNQ. *Phys Rev B Condens Matter Mater Phys* **87**, 115209 (2013).

126. Tietze, M., Burtone, L., Riede, M., Lüssem, B. & Leo, K. Fermi Level Shift and Doping Efficiency in p-Doped Small Molecule Organic Semiconductors: A Photoelectron Spectroscopy and Theoretical Study. *Phys. Rev. B* **86**, 035320 (2012).

127. Karpov, Y. *et al.* High Conductivity in Molecularly p-Doped Diketopyrrolopyrrole-Based Polymer: The Impact of a High Dopant Strength and Good Structural Order. *Adv. Mater.* **28**, 6003–6010 (2016).

128. Sakai, H. [Kyoto Univ., Osaka, Japan], Maeda, Y., Kobayashi, T. & Shirakawa, H. Mossbauer spectroscopic study of FeCl/sub 3/-doped polyacetylene. *Bull Chem Soc Jpn Jpn.* (1983) doi:10.1246/bcsj.56.1616.

129. Yim, K.-H. *et al.* Controlling Electrical Properties of Conjugated Polymers via a Solution-Based p-Type Doping. *Adv. Mater.* **20**, 3319–3324 (2008).

130. Aziz, E. F. *et al.* Localized Charge Transfer in a Molecularly Doped Conducting Polymer. *Adv. Mater.* **19**, 3257–3260 (2007).

131. Duong, D. T., Wang, C., Antono, E., Toney, M. F. & Salleo, A. The chemical and structural origin of efficient p-type doping in P3HT. *Org. Electron.* **14**, 1330–1336 (2013).

132. Jacobs, I. E. *et al.* Comparison of solution-mixed and sequentially processed P3HT:F4TCNQ films: effect of doping-induced aggregation on film morphology. *J Mater Chem C* **4**, 3454–3466 (2016).

133. Glaudell, A. M., Cochran, J. E., Patel, S. N. & Chabinyc, M. L. Impact of the Doping Method on Conductivity and Thermopower in Semiconducting Polythiophenes. *Adv Energy Mater* **5**, 1401072 (2015).

134. Hynynen, J., Kiefer, D. & Müller, C. Influence of crystallinity on the thermoelectric power factor of P3HT vapour-doped with F4TCNQ. *RSC Adv* **8**, 1593–1599 (2018).

135. Patel, S. N. *et al.* Morphology Controls the Thermoelectric Power Factor of a Doped Semiconducting Polymer. *Sci. Adv.* **3**, e1700434 (2017).

136. Vijayakumar, V. *et al.* Bringing Conducting Polymers to High Order: Toward Conductivities beyond 105 S cm−1 and Thermoelectric Power Factors of 2 mW m−1 K−2. *Adv. Energy Mater.* **0**, 1900266.

137. Xuan, Y. *et al.* Thermoelectric properties of conducting polymers: The case of poly(3-hexylthiophene). *PHYSICAL REVIEW B* vol. 82 (2010).

138. Kiefer, D. *et al.* A Solution-Doped Polymer Semiconductor:Insulator Blend for Thermoelectrics. *Adv. Sci.* **4**, 1600203 (2017).

139. Yee, P. Y., Scholes, D. T., Schwartz, B. J. & Tolbert, S. H. Dopant-Induced Ordering of Amorphous Regions in Regiorandom P3HT. *J. Phys. Chem. Lett.* **10**, 4929–4934 (2019).

140. Yamamoto, J. & Furukawa, Y. Electronic and Vibrational Spectra of Positive Polarons and Bipolarons in Regioregular Poly(3-hexylthiophene) Doped with Ferric Chloride. *J. Phys. Chem. B* **119**, 4788–4794 (2015).

141. Fanous, J., Schweizer, M., Schawaller, D. & Buchmeiser, M. R. Crystalline and Conductive Poly(3-hexylthiophene) Fibers. *Macromol. Mater. Eng.* **297**, 123–127 (2012).

142. Jung, I. H. *et al.* High Thermoelectric Power Factor of a Diketopyrrolopyrrole-Based Low Bandgap Polymer via Finely Tuned Doping Engineering. *Sci. Rep.* **7**, 44704 (2017).

143. Tashiro, K., Kobayashi, M., Kawai, T. & Yoshino, K. Crystal structural change in poly(3-alkyl thiophene)s induced by iodine doping as studied by an organized combination of X-ray diffraction, infrared/Raman spectroscopy and computer simulation techniques. *Polymer* **38**, 2867–2879 (1997).

144. Kaiser, A. B. Systematic Conductivity Behavior in Conducting Polymers: Effects of Heterogeneous Disorder. *Adv. Mater.* **13**, 927–941 (2001).

145. Kang, S. D. & Snyder, G. J. Charge-transport model for conducting polymers. *Nat. Mater.* **16**, 252 (2016).

146. Tanaka, H. *et al.* Thermoelectric properties of a semicrystalline polymer doped beyond the insulator-to-metal transition by electrolyte gating. *Sci. Adv.* **6**, (2020).

147. Lepinoy, M., Limelette, P., Schmaltz, B. & Van, F. T. Thermopower scaling in conducting polymers. *Sci. Rep.* **10**, 8086 (2020).

148. Mateeva, N., Niculescu, H., Schlenoff, J. & Testardi, L. Correlation of Seebeck coefficient and electric conductivity in polyaniline and polypyrrole. *JOURNAL OF APPLIED PHYSICS* vol. 83 3111–3117 (1998).

# Chapter 2. Control of chain alignment and crystallization helps enhance charge conductivities and thermoelectric power factors in sequentially doped P3HT:$F_4$TCNQ films

## I. Introduction

The scientific community of plastic electronics witnesses in the last decade a renaissance of interest for conducting polymers and doped polymer semi-conductors used as thermoelectric materials.[1,2] Besides classical conducting polymers such as PEDOT:PSS, doped polymer semi-conductors appear as interesting alternative candidates for TE applications since the processing and crystallization of the polymer semi-conductor can be decoupled from doping to ensure optimal control over both crystallinity and doping levels. It is of particular importance to master the doping process in order to tune the charge carrier densities since it determines the type of targeted application. Improved On/Off ratio and charge mobilities are obtained in Organic Field Effect Transistors (OFET)[3,4] for low dopant concentrations in blends with semi-conducting and insulating polymers. Interesting thermoelectric properties of conducting polymers such as poly(3,4-ethylenedioxythiophene): poly(styrenesulfonate) (PEDOT:PSS) can be achieved by fine tuning the doping level in the thin films through sequential post-treatments with common acids and bases.[5] Among other polymers, regioregular poly(3-hexylthiophene) (P3HT) doped with 2,3,5,6-tetrafluoro-7,7,8,8-tetracyanoquinodimethane ($F_4$TCNQ) is a model system to better understand the correlation between structure, charge transport and thermoelectric properties.[6-19] The electronic process

of doping in P3HT/$F_4$TCNQ implies an integer charge transfer from the HOMO of the P3HT (approx. -4.9 eV) to the LUMO of the dopant (approx. -5.2 eV) (see Figure 1).[20]

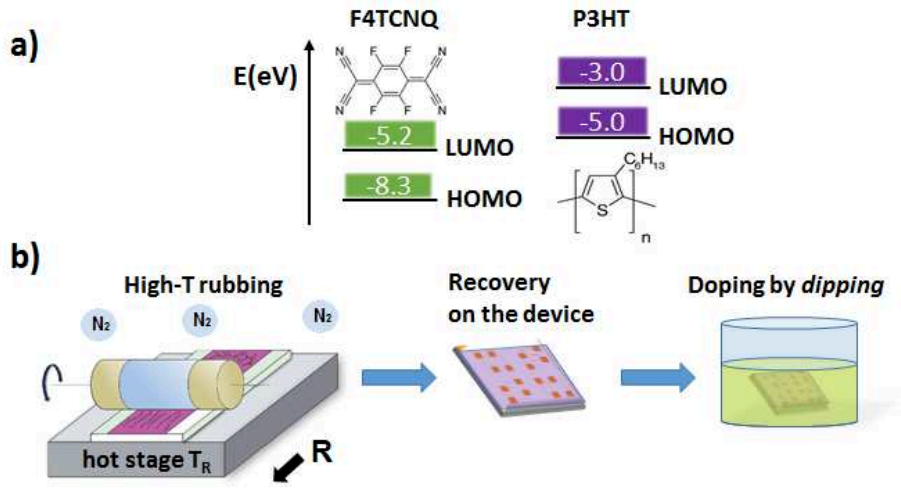


***Figure 1:*** *a) Chemical structures and schematic energy diagram of $F_4$TCNQ and P3HT. b) Preparation method of in-plane oriented and conducting polymer films. First of all, chain alignment and crystallization of the P3HT films are generated by high-temperature rubbing (R is the rubbing direction). Thin oriented films are floated on distilled water and recovered on glass substrates with gold electrodes and doped by dipping into the solution of $F_4$TCNQ in acetonitrile (AcN).*

But this redox reaction depends strongly on the proximity of dopant molecules and polymer backbone,[10] hence, on the diffusion of dopant molecules and on their location in the polymer matrix. Transmission Electron Microscopy and polarized UV-Vis-NIR spectroscopy analysis of highly oriented thin films of $F_4$TCNQ-doped P3HT demonstrated that the $F_4TCNQ^-$ anions are located in the layers of alkyl side chains within crystalline P3HT domains with the molecular long axis of $F_4TCNQ^-$ oriented perpendicular to the polymer backbone.[21] Recent

studies on a family of poly(2,5-bis(3-alkyl-2-yl)thieno[3,2-*b*]thiophene) (PBTTT) with varying alkyl side chains showed that the ultimate doping level is determined by both the side chains length and packing.[22] The structure of side chains (branched versus linear) is equally important in determining the ultimate doping level in thin films.[17]

Numerous studies on P3HT/$F_4$TCNQ have demonstrated that the method of doping impacts the final doping level and corresponding charge conductivity. Blending P3HT with $F_4$TCNQ in solution[6,7] results in poor charge conductivities whereas sequential doping of P3HT films by spin-coating or by dipping into a solution of $F_4$TCNQ[8,9] leads to enhanced conductivities of up to 10 S cm$^{-1}$. Even higher conductivities are obtained upon vapor phase doping.[14,15] Hence a large spread of conductivities in $F_4$TCNQ-doped P3HT is reported in the literature depending on the doping method. Crystallinity of pristine P3HT films is also an essential factor controlling the conductivity in $F_4$TCNQ-doped films.[10,11,13] For instance, Hynynen *et al.* have evidenced a clear correlation between the crystallinity of P3HT measured via the free exciton bandwidth, and the charge conductivity.[11] This correlation relates to the higher charge carrier mobility as the degree of solid state order increases.

Although many studies have focused on non-oriented thin films, it can be highly advantageous to study doped oriented thin films.[21-24] We have previously demonstrated that a two-step process can afford highly in-plane oriented conducting polymer layers of interest for thermoelectric applications.[21] Soft doping of P3HT films rubbed at 220°C with a solution of $F_4$TCNQ in acetonitrile (1 mg/ml) in ambient leads to charge conductivities up to 22 S cm$^{-1}$ and power factor of 8.5 µW m$^{-1}$K$^{-2}$. Most importantly, alignment of P3HT enhances both charge conductivity $\sigma$ and thermopower $\alpha$ along the polymer chain direction resulting in improved TE power factors PF= $\sigma \cdot \alpha^2$.[21] The anisotropy of the thermopower is explained in

terms of a heterogeneous material model that takes into account the semi-crystalline nature of the films.[23] Interestingly, adjusting the temperature applied during the rubbing process ($T_R$) provides a handle to tune in-plane orientation, structure and crystallinity of the films. Regarding alignment, increase of $T_R$ from room temperature to 220°C results in a remarkable increase of the order parameter up to 0.84.[25] The 3-D order parameter is defined as following (with the dichroic ratio at 610 nm):

$$OP = \frac{DR - 1}{DR + 2} \quad (1)$$

$$DR = \frac{Abs_{//}}{Abs_{\perp}} \quad (2)$$

Concerning the structure, for 50 °C < $T_R$ < 150 °C; the films consist of a small fraction of non-oriented crystalline phase and an oriented "smectic-like" phase with face-on oriented domains. In the smectic-like structure, P3HT chains show translational order along the π-stacking direction ($b_{P3HT}$ axis) but no translational order along the chain direction within stacks of backbones (the 002 reflection is absent in the diffraction pattern). In addition, the layers of alkyl side chains are highly disordered.[25] When a film of P3HT is rubbed above 150°C, oriented crystallization parallel to the rubbing direction **R** sets in and leads to a well-defined semi-crystalline lamellar morphology. In the semi-crystalline phase, the packing of P3HT backbones displays well-defined translational order along both the chain and the π-stacking directions, and relatively well packed alkyl side chains.[26,27] Finally, increasing $T_R$ from 140°C to 220°C results in an increase of both crystallinity (from 25% to 60-62%) and lamellar periodicity (that scales inversely to the undercooling).

# Chapter 2. Control of chain alignment and crystallization helps enhance charge conductivities and thermoelectric power factors in sequentially doped P3HT:$F_4$TCNQ films

In this chapter, we use the structural variety achieved by controlling the rubbing temperature to investigate the doping mechanism in aligned P3HT films and how it impacts the resulting charge conductivity and TE properties. The fundamental questions we address are the following: How does the original structure of the P3HT films (smectic *versus* semi-crystalline) affect the final doping level? How are the dopant molecules distributed in the structure of P3HT and to what extent are the TE properties affected? To answer these questions, we use a combination of UV-Vis-NIR absorption and electron paramagnetic resonance (EPR) spectroscopies, Transmission Electron Microscopy and Electron Diffraction, conductivity and Seebeck coefficient measurements. We uncover correlations between film structure and crystallinity and corresponding charge conductivity and TE properties. As a main result, the semi-crystalline structure of aligned P3HT films shows superior conductivity and TE efficiencies (power factor) as compared to the smectic-like phase. Polarized UV-vis-NIR absorption spectroscopy shows that the distinct phase behavior relates to different in-plane orientations and doping levels. A combination of electron diffraction and polarized absorption spectroscopy gives a detailed insight into the mechanism of dopant intercalation in the P3HT structure both in terms of structural modification and orientation distribution of dopant molecules in the layers of alkyl side chains. Correlations between the order parameter and the anisotropy in charge transport are analyzed. High conductivities up to 160 S/cm and power factors of 56 $\mu W\ m^{-1}\ K^{-2}$ are reached.

## II. Results and Discussion

### II.1. Fabrication of highly in-plane oriented conducting polymer films

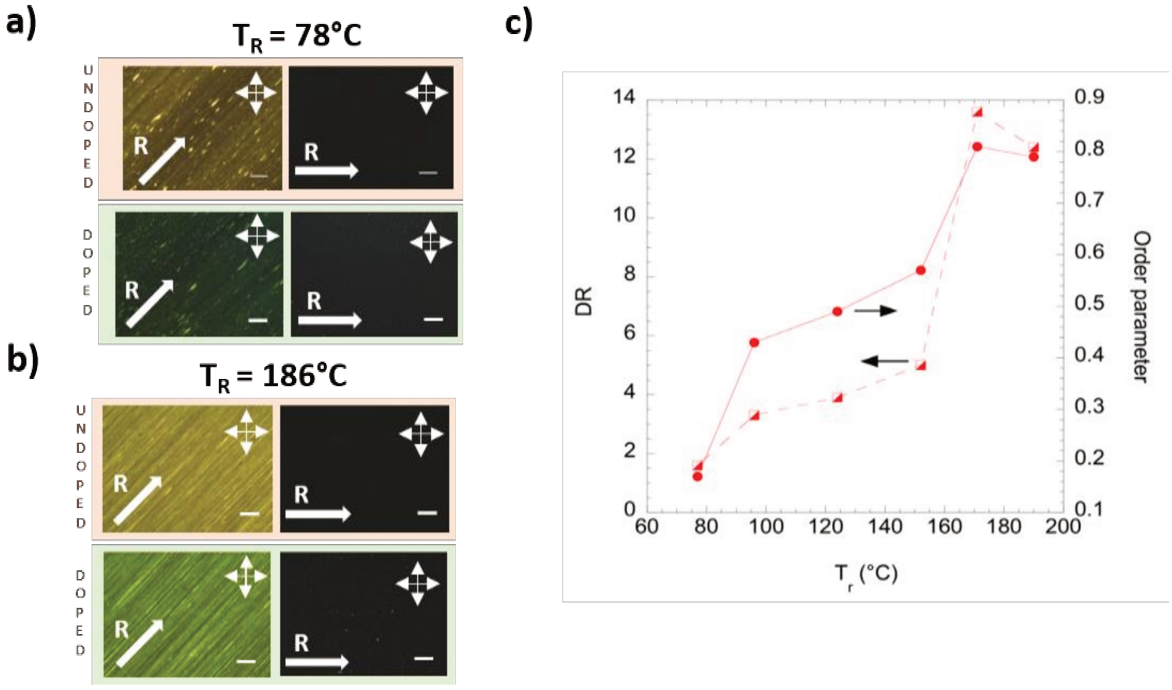


***Figure 2:*** *Polarized optical microscopy images under crossed polarizers of the P3HT films aligned at $T_R$ = 78 °C (a) or 186°C (b) before and after doping ($C_{F4TCNQ}$ = 1 mg $mL^{-1}$). The white bar in the bottom right corner of each image scales with 50 µm. Cross polarized Images indicate the strong birefringence at 45°, while full extinction is observed at 0° when the rubbing direction R is set parallel to the polarization of the incident light; c) Evolution of the dichroic ratio at 610nm and the 3D order parameter of oriented P3HT films as a function of rubbing temperature $T_R$.*

In-plane oriented P3HT thin films were prepared by mechanical rubbing at different temperatures $T_R$ (78 °C to 186 °C). The oriented P3HT films were then subjected to a soft doping by dipping the films for 10 s into a solution of $F_4$TCNQ in acetonitrile (AcN) (1 mg $mL^{-1}$) (see Figure 1) . A particular attention has been paid to prepare the samples and perform the charge conductivity and Seebeck coefficient measurements under inert atmosphere (in our previous work, the doping process was conducted in air, resulting in lower charge conductivities).[21] Polarized optical microscopy (POM) of the rubbed films shows a colour change upon doping while the films remain birefringent: the pristine orientation of the rubbed layers is not altered in the doping process (Figure 2). Films rubbed at high temperature ($T_R$ > 150°C) are more uniform and birefringent than those oriented at 78°C indicating better alignment. The plot of dichroic ratio and order parameter versus $T_R$ (Figure 2c) further confirms the beneficial effect of using larger rubbing temperatures. No rupture or discontinuity of the films normal to the rubbing are observed as demonstrated in our previous work.[21-23] Rubbing temperatures above $T_R$ > 220°C were not used to avoid plastic deformation of the polymer layer.

As doping introduces charges in the polymer, electron paramagnetic resonance (EPR) spectroscopy can be used to probe the oriented and doped P3HT films (Figure 3).[28,29] This method is sensitive to the local environment of the electron spins associated with both the P3HT polaron and the $F_4TCNQ^-$ radical anion. At X-band frequencies and fields applied here (about 9.8 GHz microwave frequency and 0.35 T magnetic field strength), the contributions of these two species strongly overlap in the doped P3HT films, resulting in a featureless EPR signal whose g value of 2.0023 is close to that of the free electron. This comes to no surprise,

as both, P3HT polaron and $F_4TCNQ^-$ anion, are organic radicals and the overall spectral width of at least one of them seems broader than the difference in g values between the two. Despite the limited resolution of the X-band EPR spectra, evidence for both, orientation and doping is obtained for oriented and doped P3HT films. First, EPR can be used to visualize the doping process as a function of dopant concentration. As seen in Figure 3a, the increase of doping concentration from 0.01 mg/ml to 1 mg/ml results in a clear broadening of the EPR signal. The broadening is attributed to increased dipolar interactions between spins, reflecting a decreased average distance between spins when the doping level augments.[30,31] As an alternative, one could also consider a segregation of dopants in some parts of the films, but this contradicts the UV-vis observations indicating that only P3HT crystals are doped, not the amorphous phase (vide infra). A more direct approach to quantify the doping level would be quantitative EPR.[32] However, in this particular case, determining the amount of rubbed P3HT film on the substrate of each of the consecutively measured samples is far from trivial. However, we are confident that our attribution of the signal broadening to an increased dipolar interaction, hence smaller distance between $F_4$TCNQ and P3HT, hence higher doping level, is accurate. From this, we can infer that the semi-crystalline films allow for more efficient doping as the smectic-like films (Figure 3c), as evident from the broader EPR line of the former. [30, 31] Moreover, the films show a clear anisotropy of the EPR signal in the magnetic field (Figure 3b,d). The shape (intensity and linewidth) of the signal is orientation-dependent, and clearly more for the semi-crystalline than for the smectic-like films. This gives further evidence for the highly oriented and anisotropic character of the films after doping which is further probed by polarized UV-vis-NIR spectroscopy.

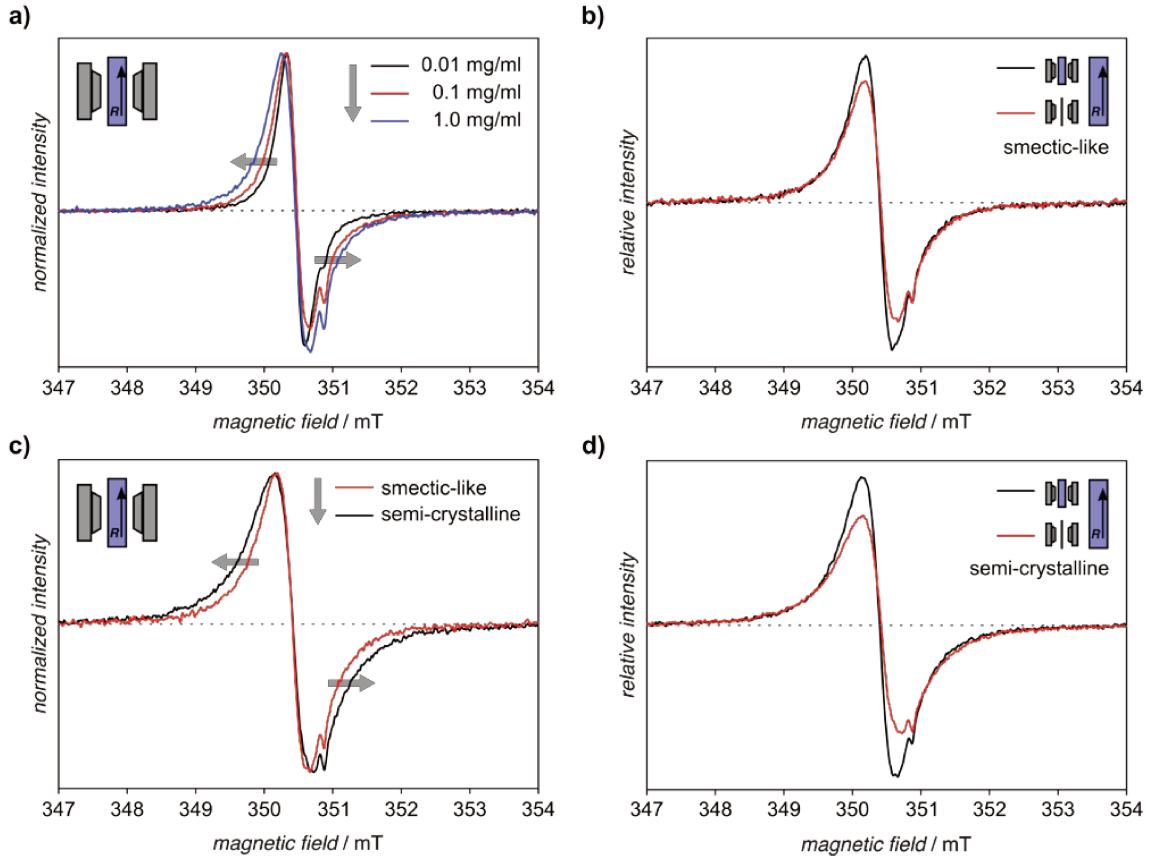


***Figure 3:*** *cw-EPR spectra obtained for P3HT doped with $F_4$TCNQ. (a) Spectral broadening with increasing dopant concentration. (b, d) Orientation-dependence of the signal for smectic-like and semi-crystalline films. (c) Comparison of spectra for smectic-like and semi-crystalline films. The spectral broadening with increasing dopant concentration is attributed to increased dipolar interactions between the spins and can hence be directly related to an increased doping level. Therefore, the broader EPR spectra of the semi-crystalline films compared to the smectic-like films point towards an increased doping efficiency in the former. The orientation dependence of the EPR spectra, while visible for both, smectic-like and semi-crystalline films, is clearly more pronounced for the latter, as expected from their higher degree of order. The insets show the relative orientation of the pole pieces of the EPR spectrometer with respect to the thin film. In a) and c) the magnetic field lies in the film*

*plane and is perpendicular to the rubbing direction. In b) and d) the EPR signal is recorded parallel and perpendicular to the film normal.*

## II.2. Evolution of spectroscopic features with rubbing temperature and doping

As shown previously for P3HT, rubbing temperature impacts the degree of alignment and crystallinity of the films (see Figure 2).[25] It can therefore be used as a handle to probe the impact of structural variation on doping and thermoelectric properties. Polarized UV–Vis–NIR absorption spectroscopy evidences different levels of alignment of the rubbed P3HT films depending on the rubbing temperature $T_R$. The 3-D order parameter (OP) of the non-doped films increases gradually from 0 to 0.8 with increasing $T_R$ up to 171°C and levels off at 0.8 with further increase of $T_R$.[25]

Figure 4 shows the UV–vis–NIR absorption spectra for P3HT films rubbed at different $T_R$ and subsequently doped with a 1 mg $mL^{-1}$ solution of $F_4$TCNQ /AcN. Figure 5a represents the optical spectra of thin P3HT films rubbed at different $T_R$ recorded for light polarisation parallel to the rubbing direction **R** (POL // R) and normalised with respect to the thickness (15-30 nm). Figure 5b represents the optical spectra recorded for the light polarisation perpendicular to the rubbing direction (POL ⊥ R). The alignment is maintained after the sequential doping process (Figure 1).[25] The spectra recorded for light polarization parallel (POL // R) or perpendicular (POL ⊥ R) to the rubbing direction show different and characteristic features dominated by the doped P3HT and the $F_4TCNQ^-$ anions, respectively. For POL // R (Figure 4), the polaronic bands P1 and P2, located at λ > 2500 nm (≈ 0.5 eV) and 795 nm (1.56 eV),

respectively, result from the doped and oriented P3HT backbone. The peak located at ≈ 540 nm corresponds to the neutral form of P3HT (labelled N). The polaronic bands are polarized along the rubbing direction, i.e. the polymer backbone.

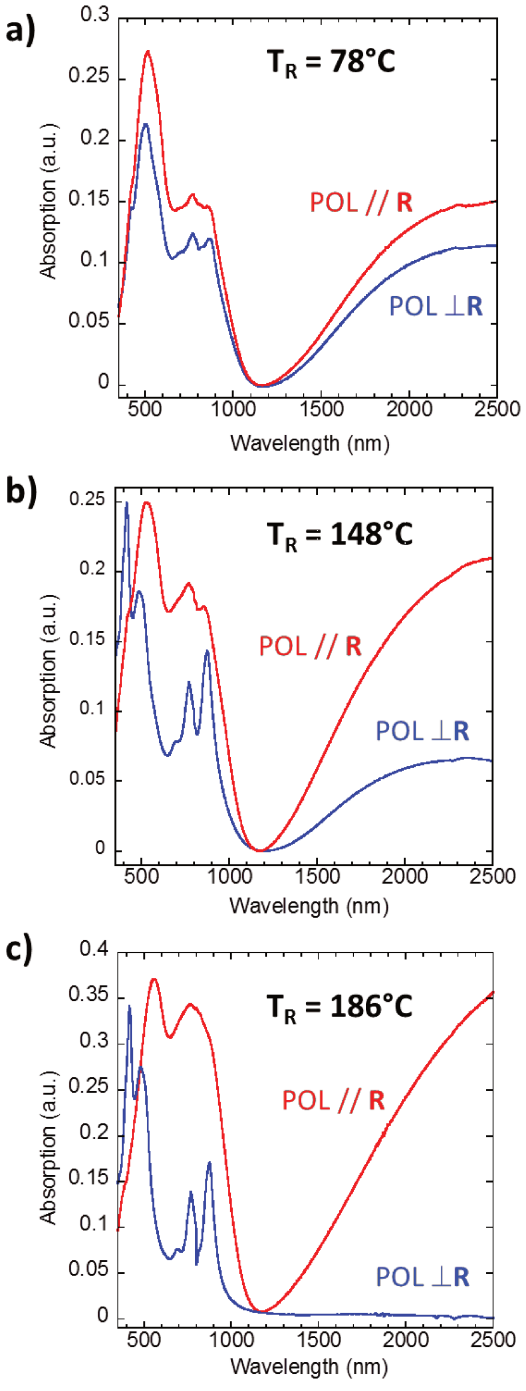


***Figure 4:*** *Polarized UV–Vis–NIR absorption spectra of $F_4$TCNQ-doped oriented P3HT films featuring polarized polaronic bands (P1, P2) and polarized absorption bands of the $F_4TCNQ^-$ anions as a function of the rubbing temperature. The spectra are recorded for the incident light polarized parallel (POL // R, in red) and perpendicular to the rubbing direction (POL ⊥ R in blue): a) $T_R$ = 78°C, b) $T_R$ = 148°C and c) $T_R$ = 186°C.*

We can see that the polaronic bands P1 and P2 are more oriented when $T_R$ increases, resulting in an increase of the dichroic ratio for the P1 band when $T_R$ increases. This is consistent with the change in the OP of the pristine rubbed P3HT films (see Figure 2c). At low $T_R$ (< 150°C), the weak anion features and weak polaronic bands are seen for both light polarization orientations because of the low level of alignment.

On the opposite, for $T_R$ > 150°C, the samples are highly oriented and the different polaronic and $F_4TCNQ^-$ bands are strongly polarized (Figure 4). For POL ⊥ R, the UV-vis spectrum is dominated by three peaks of $F_4TCNQ^-$ centred at 416, 768, and 875 nm. The peak located at 480 nm corresponds to the amorphous fraction of P3HT. Interestingly, no polarons are observed for POL ⊥ R at high $T_R$. This absence suggests that the amorphous interlamellar zones of P3HT are only poorly doped, as stressed in our previous study.[21]

For all samples, the vibronic structure of the neutral form of P3HT (N) disappears upon doping. Both, the position and the shape of the N component change with $T_R$. For POL // **R,** it red-shifts from 517 nm to 561 nm with increasing $T_R$ (Figure 6a, b). This is related to the increasing conjugation length for the P3HT films rubbed at higher $T_R$.[25] For POL ⊥ **R**, the maximum of the absorption of neutral P3HT is slightly blue-shifted with increasing $T_R$ (from 504 nm to 480 nm) (Figure 6a, b). This is due to the fact that for low $T_R$, the films is composed of a fraction of non-oriented crystalline P3HT that absorbs light also for POL ⊥ **R** and shifts the absorption to the red. For high $T_R$, the absorption for POL ⊥ **R** is dominated by the amorphous fraction and the spectrum is thus shifted to the blue.

Further insight into the doping level is obtained by following the spectroscopic variation with increasing $T_R$. The evolution of the absorbance of the neutral and polaronic features is of particular interest (Figure 5.c). As a general trend, the slope of the P1 band at 2500 nm indicates a red-shift of the P1 band with increasing $T_R$. Ghosh et al. demonstrated that the redshift of the polaronic absorption correlates with a larger delocalization of the polarons in the more crystalline films.[33,34] This is consistent with the structural evolution in rubbed P3HT films, i.e. with the increase of the length of the planarized segments in P3HT crystals grown

at increasing $T_R$.[25] Thus the more delocalized polaron for $T_R$ = 186°C reflects the higher crystallinity of the pristine P3HT films.

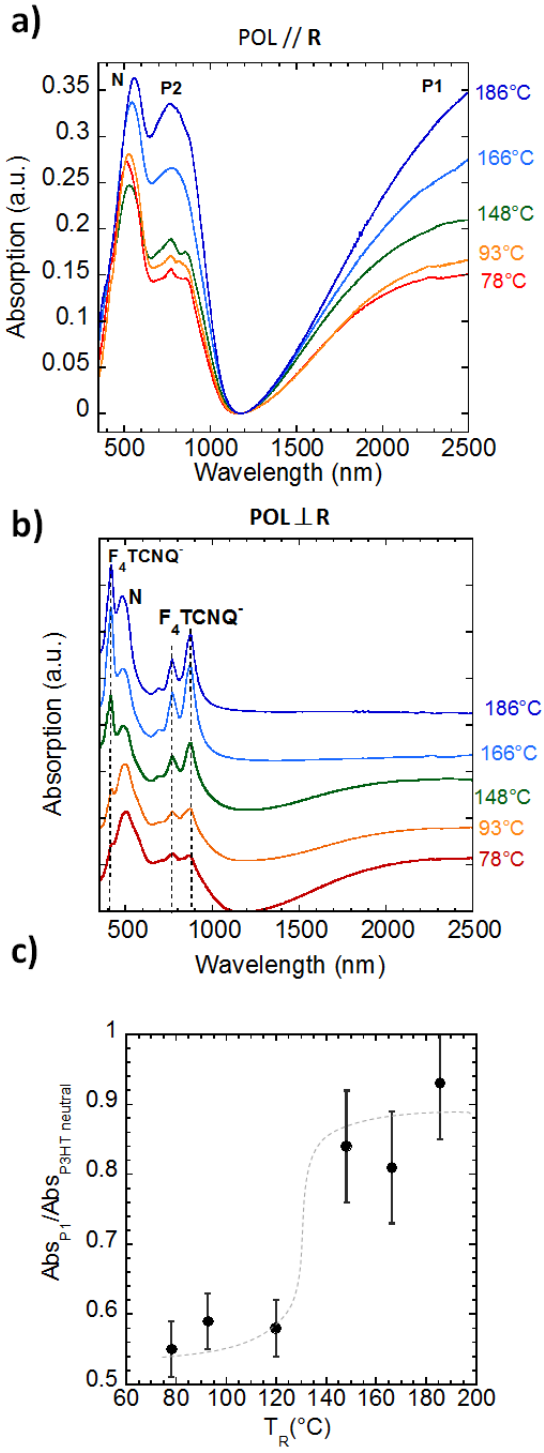


***Figure 5:*** *Evolution of the UV–Vis–NIR spectrum of highly oriented P3HT films doped with $F_4$TCNQ (1 mg/ml) as a function of the rubbing temperature ($T_R$) from 78 to 186°C. The spectra are recorded for different polarizations of the incident light with respect to the rubbing direction (R). a) POL // R spectra showing the polaronic bands P1 and P2 of the doped P3HT and the neutral P3HT (N). b) POL ⊥ R spectra showing the absorption of neutral N P3HT (450 – 530 nm) and the 416, 768 and 875 nm characteristic peaks of the $F_4TCNQ^-$ anions. For clarity, the spectra for different $T_R$, in POL ⊥ R, are shifted along the ordinate axis. c) Evolution of the absorbance ratio Abs(P1) / Abs(N) as a function of $T_R$ for doped P3HT films. The intensity of Abs (N) has been estimated by subtracting the contribution from P2 band after peak deconvolution. The dashed line is a guide*

*for the eye to highlight the transition from the smectic-like to the semi-crystalline form of P3HT.*

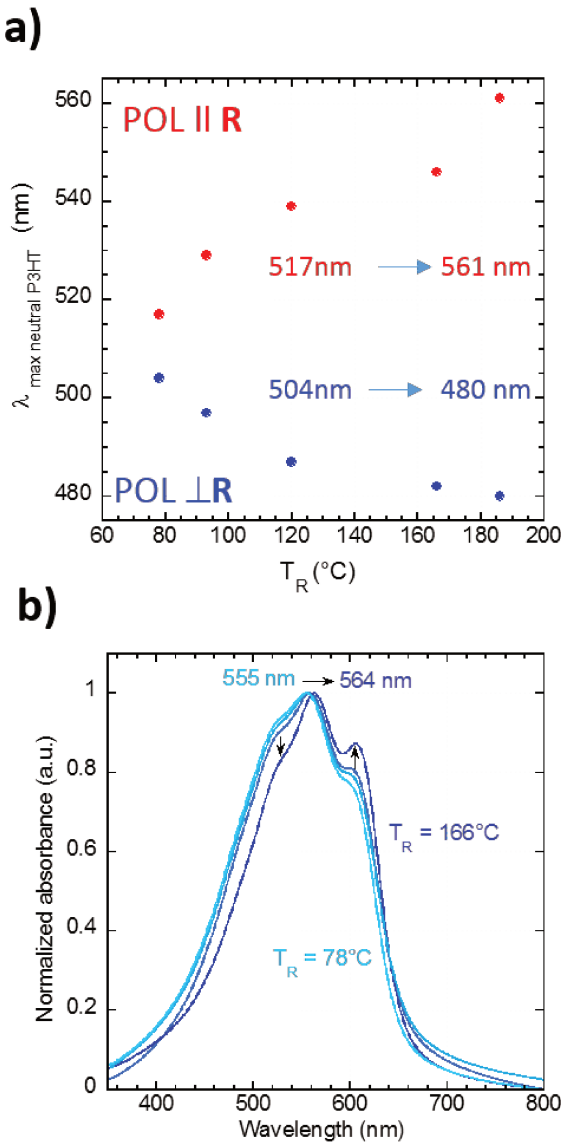


***Figure 6**. a) Maximum peak position of the neutral P3HT fraction in doped films as a function of $T_R$ for both light polarizations. b) Polarized UV–vis absorption spectra of oriented P3HT films prepared by high-T rubbing for $T_R$ range from 78°C to 186°C. The spectra correspond to the incident polarization parallel to the rubbing direction **R** and are normalized with respect to the absorbance of the 0–1 component of the vibronic structure.*

As a rule, the absorbance of P1 and P2 polaronic bands increases at the expense of the neutral form N with increasing $T_R$. This is clearly seen in Figure 5.c showing the ratio r = Abs P1 (at 2500 nm) / Abs N (at 550 nm) as a function of $T_R$. Two temperature ranges can be defined. For $T_R$ < 150°C, r ~ 0.55 whereas for $T_R$ > 150°C, r ~ 0.9. This might indicate a difference in doping level for the two temperature regimes. Interestingly, the discontinuity observed around 150°C coincides with the transition from the smectic-like to the semi-crystalline phase.[25] *Thus the smectic-like phase appears less doped than the semi-crystalline phase.*

Let us now determine how the differences in polymer chain alignment and doping level impact the thermoelectric properties of the doped films rubbed at different temperatures.

### II.3. Dependence of thermoelectric properties on in–plane alignment and crystallinity

In the next step, the impact of thin film structure on thermoelectric properties has been studied as a function of $T_R$. Charge conductivity and Seebeck coefficient were measured on thin P3HT films rubbed at $T_R$ from 78°C to 186°C and subsequently doped by $F_4$TCNQ /AcN (1 mg/mL). Figure 7 a, b demonstrates the evolution of electrical conductivities $\sigma_{//}$ and $\sigma_{\perp}$ and of the Seebeck coefficients $\alpha_{//}$ and $\alpha_{\perp}$, respectively. Both $\sigma$ and $\alpha$ are measured in parallel and in perpendicular to the rubbing direction (typical Seebeck voltage curves are shown in the experimental section). The values of charge conductivity are improved along the polymer chains (delocalisation of the polarons along the polymer chains) over non-oriented films. The conductivity increases drastically above $T_R$=140°C. The highest value obtained for $\sigma_{//}$ is 160 $S{\cdot}cm^{-1}$ which exceeds by one order of magnitude the value obtained for non-oriented vapor phase doped films (12.7 $S{\cdot}cm^{-1}$).[11] As seen in Figure 7a, $\sigma_{\perp}$ is always below 20 $S{\cdot}cm^{-1}$ and changes little with rubbing temperature. The charge conductivity measured perpendicular to the rubbing is close to the one obtained for the non-rubbed reference samples (~ 9 $S{\cdot}cm^{-1}$). It suggests that the conductivity in the non-rubbed films is limited by the contribution of the charge transport perpendicular to the polymer chains. Most interestingly, $\sigma_{//}$ displays a discontinuity at ~150°C that coincides again with the transition from the smectic-like to the semi-crystalline phase.

Similarly to the conductivity, the Seebeck coefficient $\alpha_{//}$ is enhanced along the chain direction and reaches 60 µV $K^{-1}$. This value does not vary much with $T_R$ and no discontinuity is observed around 150°C. In contrast, $\alpha_{\perp}$ shows a much stronger variation and decreases from 35 µV·$K^{-1}$ to 12 µV· $K^{-1}$ when $T_R$ approaches 160°C. In our previous study, the anisotropy of the Seebeck coefficient was explained by a heterogeneous model taking into account the coexistence of crystalline and amorphous phases.[23] In particular, it was shown that $\alpha_{\perp}$ is determined by the Seebeck coefficient of the crystalline domains that channel the majority of charges when the temperature gradient is perpendicular to the rubbing direction. With increasing $T_R$ in the range 150°C - 220°C, the lamellar thickness and the average coherence length of P3HT backbones in the crystalline domains tend to increase.[21] In addition, the proportion of edge-on P3HT crystals increases too. We propose that the observed variation of $\alpha_{\perp}$ with $T_R$ in the semi-crystalline phase reflects these structural changes.[21]

Figure 7.c shows the evolution of the power factor $PF = \sigma \cdot \alpha^2$ as a function of $T_R$. $PF_{//}$ is dominated by the dependence of $\sigma_{//}$ and reaches a maximum value of 56 µW $m^{-1}$ $K^{-2}$ at $T_R$ = 186 °C. This value is higher than the 27 µW $m^{-1}$ $K^{-2}$ value reported recently for P3HT doped by vapour-phase infiltration[19] and clearly reflects the benefits of enhanced alignment and crystallinity on TE properties.

As seen from Figure 7 a, b, explicit anisotropy of both σ and α is observed in the oriented films of P3HT. One can expect the anisotropy in conductivity to be correlated with the degree of in-plane alignment. We therefore plotted the evolution of the charge conductivity anisotropy $a_\sigma = \sigma_{//} / \sigma_{\perp}$ as a function of the order parameter extracted from the dichroic ratio of the polarons ($OP_{P1}$) as shown in Figure 8. As expected, the anisotropy of charge conductivity

scales with the order parameter of the polarons $OP_{P1}$ which emphasizes the importance of in-plane alignment to reach the highest charge conductivities.

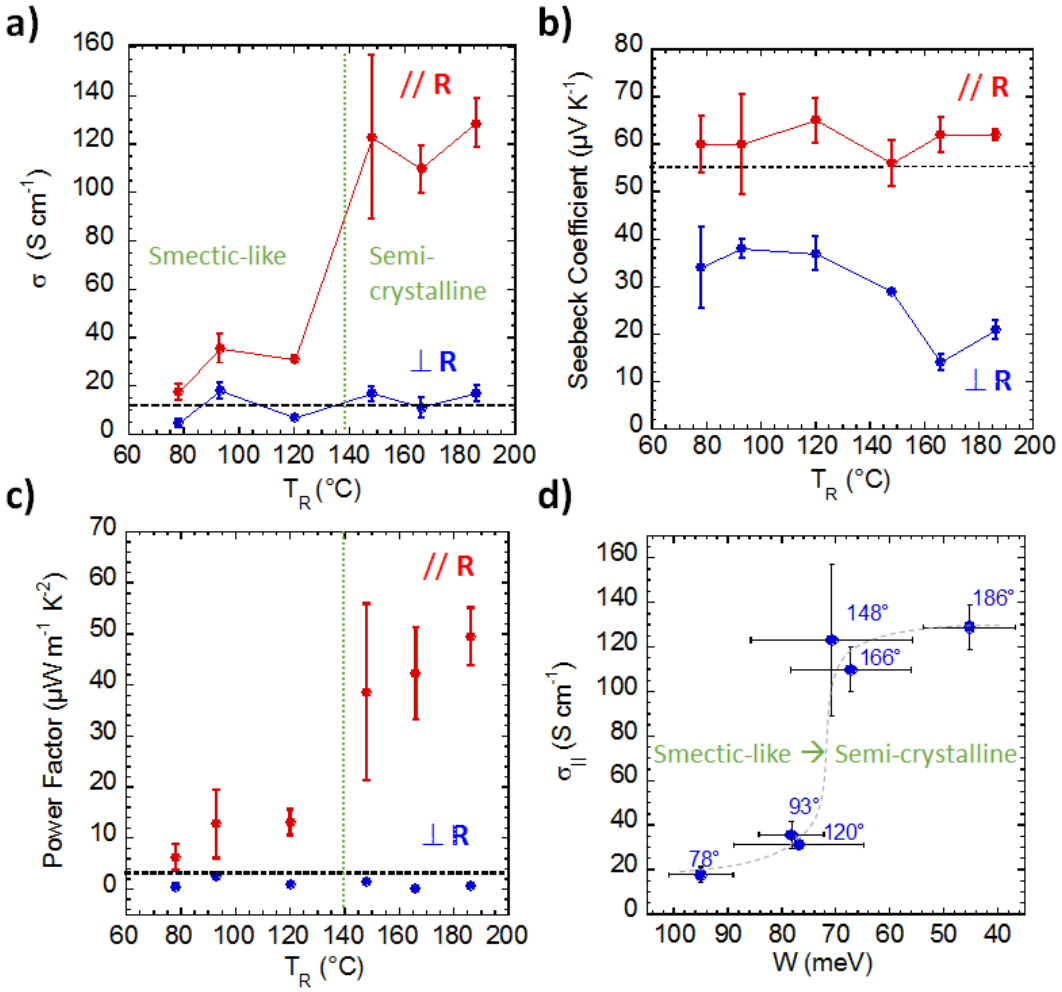


***Figure 7:*** *Evolution of the a) charge conductivity, b) Seebeck Coefficient, and c) power factor measured along (// R) or perpendicular (⊥ R) to the rubbing direction for P3HT films rubbed at different temperatures and doped with $F_4$TCNQ (1 mg/ml). The black dashed lines represent the values for a non-oriented sample. The error bars are mainly related to the statistic dispersion in alignment level of samples. In a and c, the vertical green lines are a guide for the eye to differentiate the ranges of smectic-like and semi-crystalline phases. d)*

*Evolution of the charge conductivity $\sigma_{//}$ measured in the direction of the polymer backbone as a function of the free exciton bandwidth* W (see Experimental section). *The grey dashed line is a guide for the eye to highlight the transition between the smectic-like and the semi-crystalline phases.*

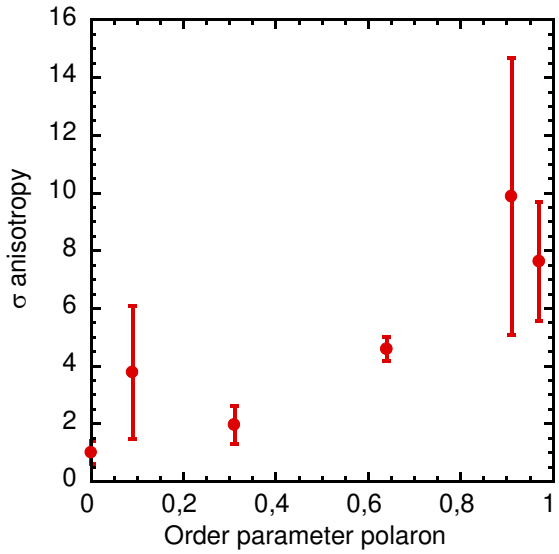


***Figure 8:*** *Anisotropy of electrical conductivity vs order parameter of the polaron.*

Having demonstrated that in-plane alignment plays an important role on charge conductivity and thermoelectric properties, the next section focuses on the impact of crystallinity on TE properties. An elegant mean to do so is to use the excitonic band width, W, as a measure of the film's crystallinity and to correlate it with the charge conductivity $\sigma_{//}$ along the chain direction.[11, 35-37] Referring to work by Hynynen et al. [11] and the weak H-aggregate model of Spano,[36] we have extracted the information on the local intra-chain order from the

UV–vis spectra of P3HT. This intra-chain order can be quantified by the free exciton bandwidth W. As shown by Spano, for weak H-aggregates, W is related to the ratio $\frac{A_{0-0}}{A_{0-1}}$ following the equation:

$$\frac{A_{0-0}}{A_{0-1}} = \left( \frac{1 - 0.24W / E_p}{1 + 0.073W / E_p} \right)^2 \quad (1)$$

where $E_p$ is the intramolecular vibration (0.18 eV) and the $\frac{A_{0-0}}{A_{0-1}}$ is taken from the (POL // R) absorption spectra of oriented P3HT films (Figure 6d). In the present case, we observe that W decreases from 95 meV for $T_R$ = 78 °C to 45 meV for $T_R$ = 186 °C. Such a low value of W for high $T_R$ is the fingerprint of high crystallinity (consistent with the UV-Vis observations).

Figure 7.d depicts the dependence of $\sigma_{//}$ with W. W has been extracted from the absorption spectra (POL // R) of rubbed P3HT for various $T_R$ prior to doping (see Figure 6b). The figure shows a clear discontinuity around 150°C that coincides with the structural transition from the smectic-like to the semi-crystalline phase. The W values of the smectic-like phase are in the 75-95 meV range whereas the semi-crystalline phase reaches W down to 40 meV. This result is in line with the evolution of the apparent doping level extracted from UV-Vis absorption (Figure 5c). Indeed, a similar discontinuity has been observed for the P1/N absorption ratio depending on the rubbing temperature. Both results suggest that two different regimes of conductivities are effective depending on the rubbing temperature, each regime being associated to either the smectic-like or the semi-crystalline phase.

The correlation between W and charge conductivity $\sigma_{//}$ along the chain direction is also possibly related to the change in conjugation length induced by chain alignment upon rubbing.[25] Increasing $T_R$ leads to larger stem length in the P3HT crystals and hence a higher crystallinity. The larger stem length in the crystals is consistent with the larger dichroic ratio in UV-vis absorption. As seen in Figure 9, this interrelation between alignment (dichroic ratio) and crystallinity (excitonic bandwidth W) is clearly reflected in the apparent correlation between W and R. This analysis implies that the benefits of alignment and crystallinity on TE properties are inter-related. In other words, high crystallinity is related to high alignment of P3HT films and it is not possible to disentangle both factors.

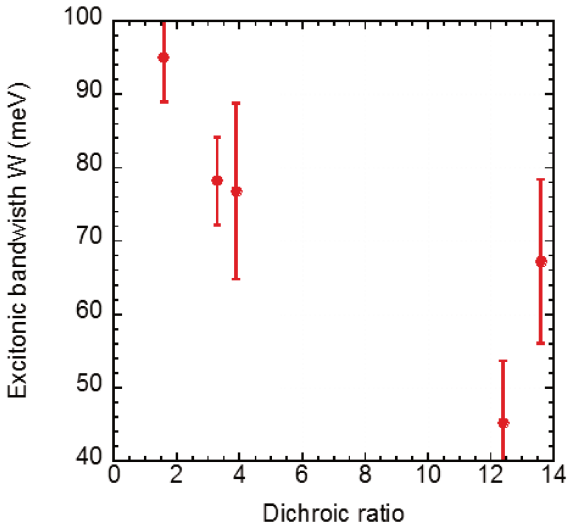


***Figure 9**: Correlation between the excitonic bandwidth W and the dichroic ratio for P3HT films oriented at different rubbing temperatures $T_R$.*

## II.4 Impact of doping on both smectic-like and semi-crystalline structures.

### II.4.1. Structural analysis by Transmission Electron Microscopy.

Let us now identify how the doping impacts the structure of both phases. Low dose electron diffraction was used to explore the impact of $F_4$TCNQ doping on the structure of P3HT thin films rubbed at different $T_R$.

First, we describe the ED patterns of the non-doped films rubbed at different temperatures and identify the characteristic structural features of both smectic-like and semi-crystalline phases. Figure 10 exemplifies the characteristic variation of the $d_{100}$ periodicity with $T_R$ and the diffraction patterns for $T_R$=78°C, 120°C and 186°C. The P3HT films rubbed at $T_R$ = 78°C are composed of a fraction of unoriented edge-on crystal (Scherrer ring *0 2 0*) and a fraction of aligned face-on domains (equatorial *h 0 0*, h= 1-3).(see Figure 10b) These aligned face-on domains correspond to the smectic-like phase of P3HT as they show only equatorial *h 0 0* reflections and no meridional *0 0 2* reflection along the rubbing direction. In other words, there is no well-defined translational order along the chain direction (**c** axis) within π-stacks of polythiophene backbones.[25,26] This is illustrated in Figure 10e: (b,c) stacks show a statistical stacking disorder characterized by $\Delta c_{intra}$ and disordered side chains in the smectic-like phase.

As seen from Figure 10c, for $T_R$ > 120°C (once in the semi-crystalline phase), no other structural variation upon doping takes place in terms of unit cell parameters change as a function of $T_R$ while alignment and/or crystallinity rate still increase. It seems that some kind

of structural saturation has been reached. It could be related to the maximum number of dopant incorporated within the unit cells in the crystalline domains.

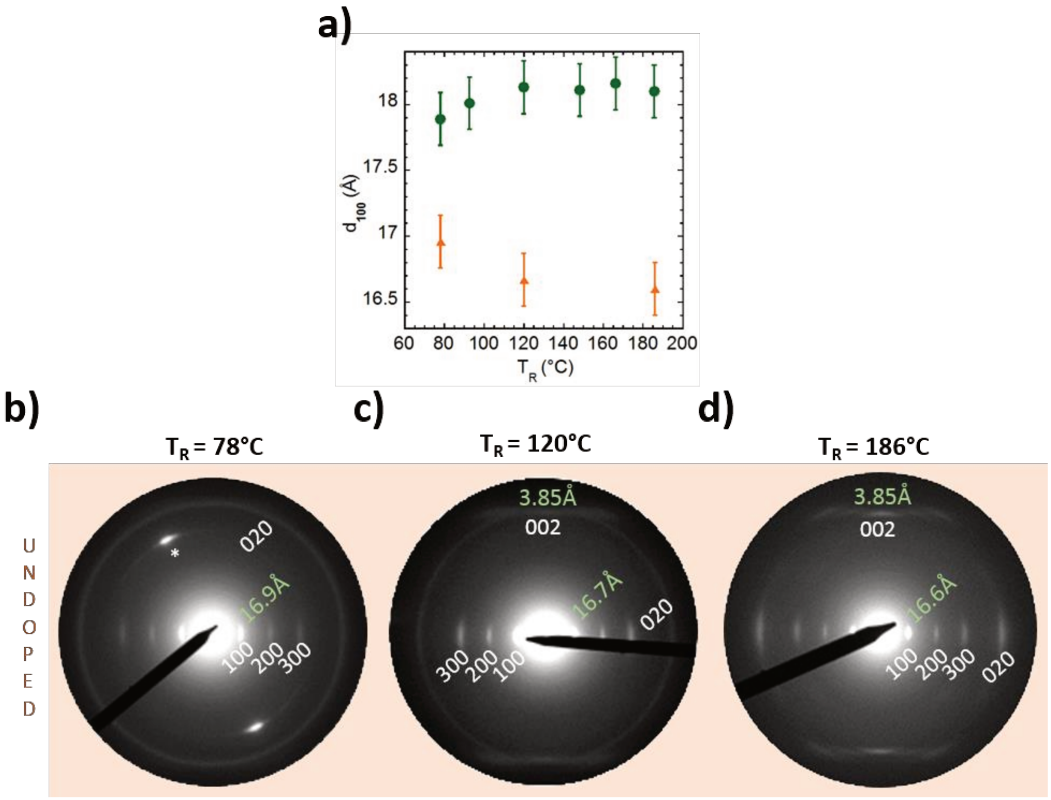


***Figure 10:*** *a) Evolution of the $d_{100}$ reticular distance as a function of $T_R$ for doped (●) and undoped (▲) samples; b), c), d) electron diffraction patterns of undoped films rubbed at 78°C , 120°C and 186°C, respectively. The star in (b) points at an additional PTFE reference reflection used to calculate the reticular distances.*

It is also interesting to point out that the periodicity d100 along the alkyl side chains in the undoped state is slightly smaller for a semi-crystalline phase than for the smectic-like phase. (see Figure 10a) This is mainly related to a better packing of the alkyl side chains in the semi-crystalline phase as validate by the presence of mixed indexes on the ED patterns (i.e. *h*

*0 2* reflections). This leads to a difference in induced structural changes of $\Delta\ d_{100}$ = 0.6 Å between the two doped phases.

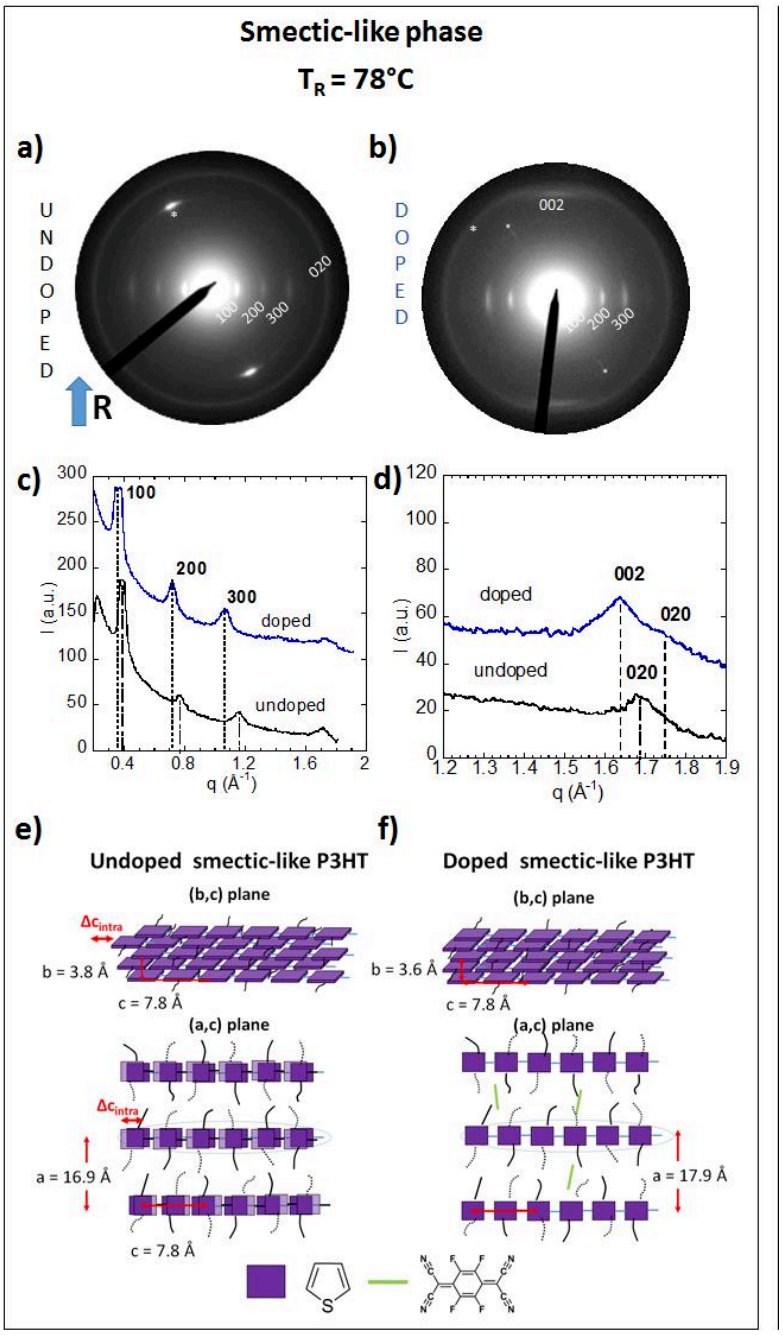


***Figure 11**: Electron diffraction patterns of the smectic-like ($T_R$ = 78°C) films in pristine (a) and doped (b) forms. Equatorial (c) and meridional (d) section profiles of the electron diffraction patterns. The curves in black (blue) correspond to the pristine (doped) films. For*

*clarity, the section profiles are shifted along the ordinate axis. The asterisk seen in a and b indicates reflections from PTFE used for calibration. The rubbing direction R is vertical (blue arrow) for all patterns. (e, f) Schematic illustration of the structural changes in the packing for the smectic-like ($T_R$ = 78°C): undoped pristine structure (e) and after doping with $F_4$TCNQ(f).*

P3HT films oriented at 186°C have the highest degree of alignment (consistent with POM and UV-vis spectroscopy) as seen from Figures 10, 2b and 4c. The films consist of both aligned edge-on and face-on P3HT crystals as indicated by the co-existence of equatorial *0 2 0 and h 0 0 (h= 1-4)*. The *0 0 2* reflection is very sharp and intense, indicating a very high level of translational order along the chain direction **c**. Most characteristic of the semi-crystalline phase is the presence of sharp *h 0 0* reflections (h = 1-4) and well-defined mixed indices *h 0 2* reflections, as a consequence of translational order along both $\mathbf{a_{P3HT}}$ and $\mathbf{c_{P3HT}}$ directions and partially-ordered side chains. The semi-crystalline phase is also visualized by bright field transmission electron microscopy and composed of the typical periodic alternation of crystalline lamellae and amorphous interlamellar zones.[25]

Next, we describe the evolution of the film structure upon doping with $F_4$TCNQ. Figure 11 shows the structural evolution of the P3HT films in the smectic-like phase ($T_R$=78°C) upon doping with $F_4$TCNQ and Figure 12 for the semi-crystalline phase ($T_R$=186°C). Right below the ED patterns, the corresponding section profiles along the equator (c) and along the meridian (d) for doped and undoped states are shown for the films rubbed at 78°C, and 186°C. Plot profiles of the ED patterns along the equator feature the evolution of the structure along the

side chains (*h 0 0*) and the π-stacking (*0 2 0*). Meridional plot profiles help visualize the structural evolution along the polythiophene backbone *(0 0 2)*. Considering the smectic-like phase, doping induces a sizable increase of the layer spacing $d_{100}$ from 16.9 Å to 17.9 Å as well as a slight reduction in π-sacking period $d_{020}$ from 3.8 Å to 3.6 Å. Most interestingly, some order along the monomer direction seems to be induced by doping as indicated by the appearance of the meridional *0 0 2* reflection (Figure 11b,d). In other words, the intercalation of $F_4$TCNQ into the side chain layers induces a reorganisation of the polymer chains within the (b,c) stacks of polythiophene backbones. Intra-stack order has thus been improved and becomes similar to that of the semi-crystalline phase but the side chains remain disordered (See schematic Figure 11f). This result is against the commonly accepted view on doping that would expect dopant intercalation to induce disorder in the pristine polymer structure at low doping concentration.[38]

Herein, dopant intercalation plays a role similar to solvent vapour annealing[39] and allows the chains to reorganize and reach a more ordered state because the smectic-like phase is metastable and is prone to structural reorganization. It is worth noting that Chabinyc and coworkers evidenced ordering of regio-random P3HT upon doping, indicating an effect similar to the presently one for the smectic-like phase of regioregular P3HT.[40]

For the semi-crystalline phase, the variation of unit cell parameters induced by doping is similar to the smectic-like phase one, albeit the variations are slightly larger along the alkyl side chains (from 16.9 Å to 18.1 Å) (see Figure 10a). Doping induces changes in the ED pattern, especially on the second layer line: i) mixed indices *h 0 2* reflections disappear and ii) the *0 0 2* reflection is streaked. Streaking in ED patterns of semi-crystalline polymers is a fingerprint

of disorder.[41] Streaking of the *0 0 2* is observed along the **a** direction (Figure 12b), indicating that the disorder is introduced upon doping along the **c** direction.

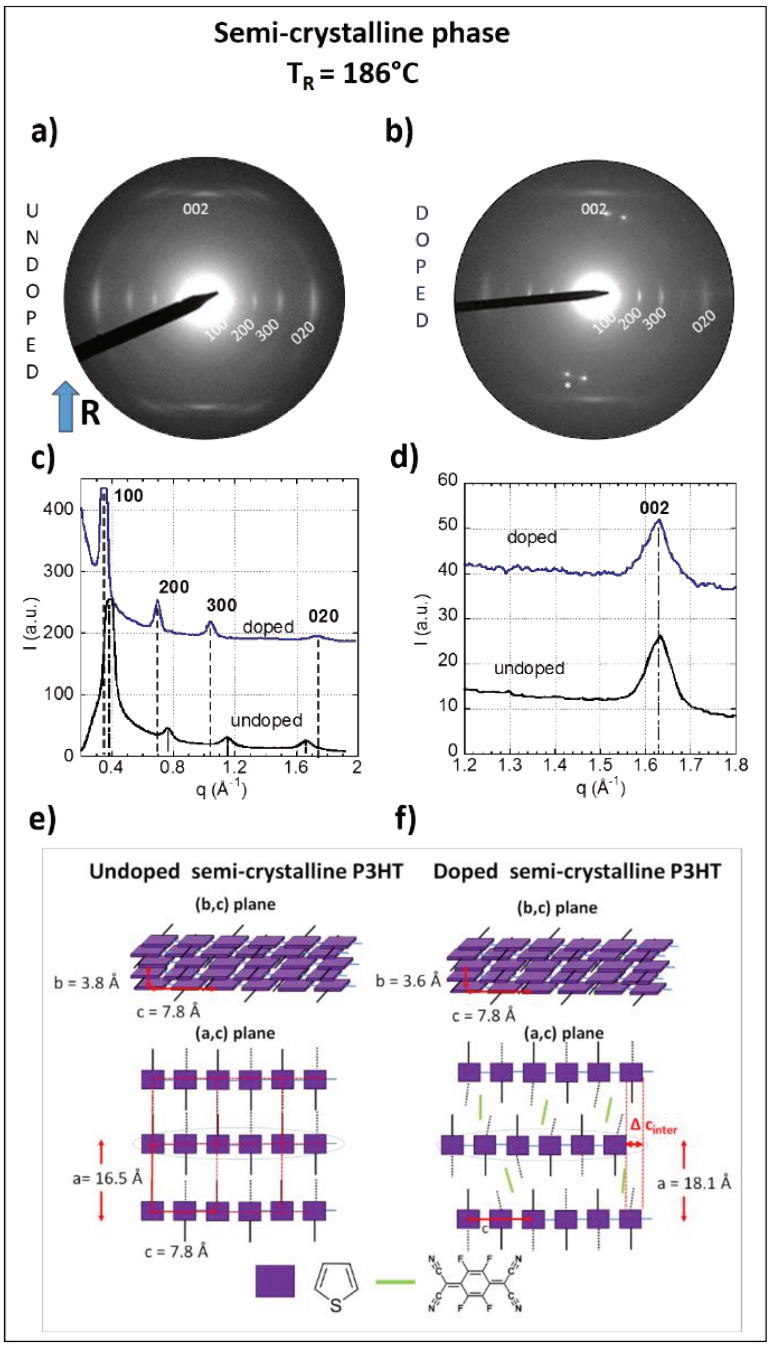


***Figure 12**: Electron diffraction patterns of the semi-crystalline ($T_R$ = 186°C) films in pristine (a) and doped (b) forms. Equatorial (c) and meridional (d) section profiles of the electron diffraction patterns. The curves in black (blue) correspond to the pristine (doped) films. For*

*clarity, the section profiles are shifted along the ordinate axis. The asterisk seen in b indicates reflections from PTFE used for calibration. The rubbing direction R is vertical (blue arrow) for all patterns. (e and f) Schematic illustration of the structural changes in the packing for the semi-crystalline phase ($T_R$ = 186°C): undoped pristine structure (e) and after doping with $F_4$TCNQ (f).*

This disordering is such that successive (b,c) planes are randomly displaced along the **c** direction. In other words, statistical offsets $\Delta c_{inter}$ are introduced between π-stacks of polythiophene backbones (see Figure 12f). Contrary to the smectic-like phase, π-stacking within (b,c) planes is maintained whereas successive stacks experience a statistical shift $\Delta c_{inter}$ upon doping. The intercalation of the $F_4$TCNQ molecules in the side chain layers results in a disordering in the arrangement of the (b,c) stacks along the side chain direction. To conclude, TEM analysis evidences two distinct cases of structural changes upon doping depending on the initial structure of the films. Doping improves stacking order in (b,c) planes in the smectic-like phase whereas it disturbs the side chain packing and thus the relative organization of (b,c) stacks in the semi-crystalline phase.

### II.4.2 Determination of in-plane orientation distribution of polarons and $F_4TCNQ^-$ anions using UV-vis-NIR spectroscopy

In the previous section, doping was shown to affect differently the structures of the smectic-like and the semi-crystalline phases. In particular, ED shows the extension of the unit cell parameters along the side chain direction but fails to determine the proportion and/or the location of the dopant molecules in the polymer matrix. In addition, the spectral features further suggest different doping levels in the two phases. Therefore, we used a detailed study of the angular dependence of the polarized UV-Vis-NIR spectra to quantify both, the angular distribution of the dopant molecules in the polymer matrix and the doping levels of both phases. The angular distribution of the P1 band reflects the in-plane distribution of the P3HT chains after rubbing and doping whereas for the $F_4TCNQ^-$ band, it determines the in-plane angular distribution of the dopant's long axis (the transition dipole of the $F_4TCNQ^-$ absorption bands is oriented along the long axis of the molecule).[42]

Figure 13 a, b shows the evolution of the UV-Vis-NIR spectra *versus* the light polarization angle for smectic-like and semi-crystalline phases, respectively. The angular distribution was extracted for $F_4TCNQ^-$ and P1 polarons at 873 and 2500 nm, respectively.

Since both $F_4TCNQ^-$ and P2 contributions overlap in the 650-1100 nm range, it was necessary to deconvolve the spectra to differentiate the two contributions and obtain meaningful absorbance for the $F_4TCNQ^-$ anion for each angle. Figure 14a shows a representative result of a multi-peak fitting of the sample rubbed at 186°C, for a polarization angle of 70°, whereas Figure 14c depicts the resulting $F_4TCNQ^-$ absorbance as a function of polarization angle for the semi-crystalline films ($T_R$ = 186°C) after subtraction of polymeric P2

features. A multiple peak fitting, shown in grey is applied in the range 0.3-3.5 eV based on four components: P1 band (at 0.44 eV), P2 band (at 1.53 eV), N (neutral P3HT) band (at 2.54 eV) and a high-energy F4TCNQ- band (at 3.00 eV). The sum of these four components is represented in blue, whereas the experimental spectra is shown in red. (see Figure 14a) The sum of the principal components is subtracted from the recorded experimental spectra. Although the peak deconvolution is rough, it allows subtracting most of the P2 band from the F4TCNQ- contribution in the range of 1-2 eV. Similar procedure was reported previously, see the ref [7]. Table 1 compares values of polaronic peak positions in the current work on oriented films and work of Duong et al on non-oriented samples. As seen, the values are pretty close to those reported previously.

In Figure 13c, d, the evolution of P1 at 2500 nm (in purple) and $F_4TCNQ^-$ at 873 nm (in green) bands are depicted as a function of the polarization angle, for the smectic-like and semi-crystalline phases. The curves are fitted according to equation 3:[43,44]

$$A(\lambda,\theta) = A_0 - \log\left[1 - \frac{\beta}{\beta+1}(1 + 3cos2\theta)\right] \quad (3)$$

where,

$$\beta = \frac{1}{3}\tanh(\Delta A \frac{ln10}{2}) \quad (4)$$

with $A_0$, the unpolarised offset absorption contribution related to the non-aligned fraction of P3HT and $\Delta A = A_{max} - A_{min}$, $A_{max}$ (0°, //) and $A_{min}$ (90°, ⊥) for P1 and $A_{max}$ (90°, ⊥) and $A_{min}$ (0°, //) for $F_4TCNQ^-$.[43,44]

As seen in Figure 13 c, d, the angular dependence is well fitted with equation 3 for both anion and polaron contributions. In particular, the maximum of angular distribution of

$F_4TCNQ^-$ band is located at 90° to the P3HT backbone direction (rubbing direction). Thus, the dopant molecules are distributed around ±90° of the P3HT backbone direction.

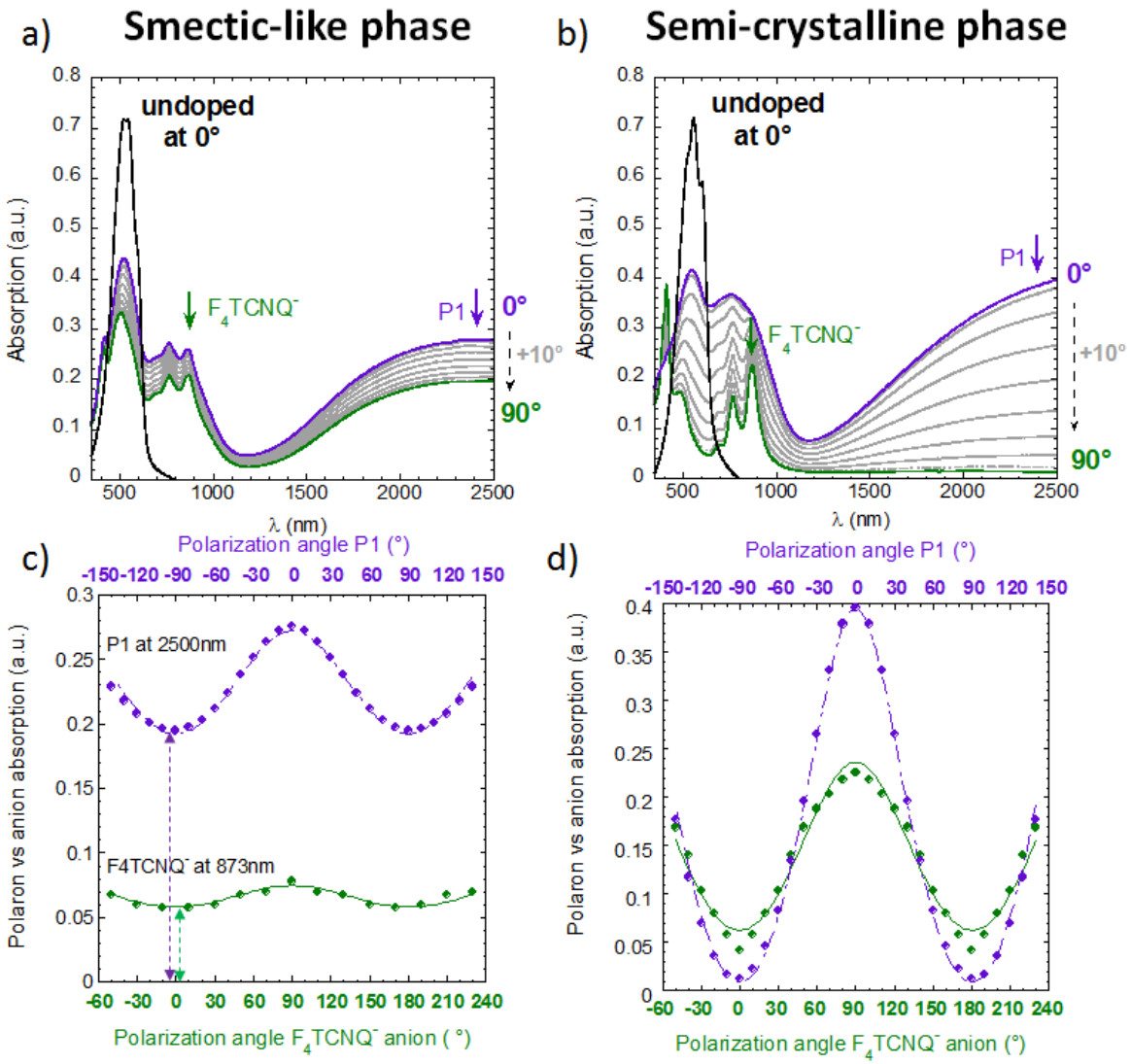


***Figure 13**: a) and b) Polarized UV–Vis–NIR absorption spectra of oriented conducting polymer films for both smectic-like and semi-crystalline phase plotted for different angles (every 10°) between the direction of polarization and the direction of rubbing of the film. 0° corresponds to the incident light polarized parallel to the rubbing direction (POL // R, in violet) whereas 90° corresponds to the incident light polarized perpendicular to the rubbing direction (POL ⊥ R in green). The spectra of the rubbed undoped films at 0° are also shown in*

*black for comparison. c and d) Evolution of the absorbance of the P1 polaron band at 2500 nm (in violet), and of the $F_4TCNQ^-$ band at 873 nm (in green) as a function of the polarization angle for both phases, respectively. The offset in absorption represented by the dashed double arrows observed in particular for the smectic-like phase are due to the poorer alignment.*

For the smectic-like phase, the two curves reflect the poorly aligned structure of the film rubbed at $T_R$= 78°C. Indeed, the absorbance amplitude variations of both P1 and of $F_4TCNQ^-$ are small contrary to the semi-crystalline phase. The absorption offsets $A_0$ observed for both polarons and anions (~0.2 and 0.05, respectively) are related to the residual non-oriented doped P3HT crystals. For the semi-crystalline phase, the curves do not show such an offset in absorption because of the much higher alignment.

*Table 1. Comparison of P1, P2 peak positions with the work reported previously.*

| Band name/position | This work | Duong, Salleo 2013 [7] |
|---|---|---|
| ***P1 polaronic band*** | ~0.44 eV | --- |
| ***P2 polaronic band*** | ~1.53 eV | 1.66 eV |
| ***Neutral band*** | ~2.2 – 2.6 eV | 2.7 eV |

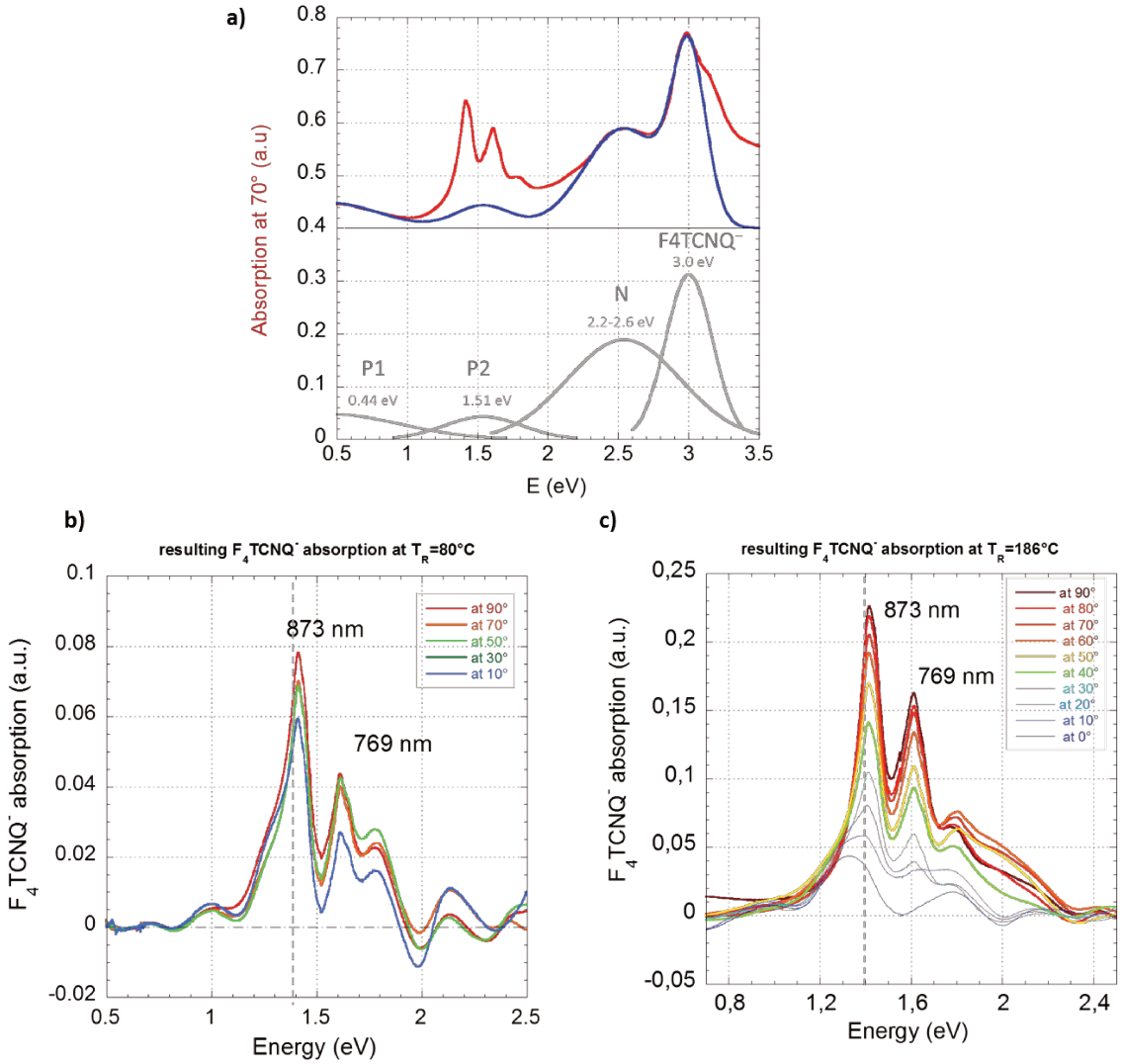


***Figure 14:*** *a) Example of the deconvolution of polarized UV-Vis spectrum of P3HT/F4TCNQ film rubbed at 186°C for a polarization angle of 70° between the rubbing direction and light polarization. The recorded spectrum is shown in red. b) Angular dependence of the $F_4TCNQ^-$ anion absorption in the doped smectic-like phase for every 20° angle between the rubbing and the light polarization directions obtained by subtraction of the four contributions from the recorded spectra. c) Angular dependence of the $F_4TCNQ^-$ anion absorption in the doped semi-crystalline phase for every 10° angle between the rubbing and the light polarization directions obtained by subtraction of four contributions.*

In order to quantify and compare the degree of alignment of the polaron and the anion, the dichroic ratio of both species has been used to calculate the OP, the 3D order parameter according to equation 1 (see Table 2). For the smectic-like phase, both order parameters are similar and very small (OP = 0.12 and 0.09 for P1 and $F_4TCNQ^-$, respectively), as a consequence of the large offsets $A_0$ associated to the fraction of non-aligned P3HT in the films. In contrast, in the semi-crystalline phase, the order parameters reach much higher values (OP= 0.91 and 0.62 for P1 and $F_4TCNQ^-$, respectively). This confirms the higher alignment level of both polymer chains and dopant molecules for the films rubbed at $T_R$ > 150°C.

It is instructive to compare the order parameter of the polaron and the $F_4TCNQ^-$ in the semi-crystalline phase to define to what extent their angular distributions are correlated. A perfect orientation of all dopant molecules perpendicular to the polymer backbone (inside the crystal phase) should translate into identical order parameters for the polarons and the anions. In the present case, the order parameter of the anions (0.62) is smaller than the polaron ones (0.91). The lower order parameter of the anions can have two origins: i) a fraction of $F_4TCNQ^-$ anions is also located in the non-oriented amorphous phase, or ii) the dopants inside the layers of side chains are distributed around an average position orthogonal to the P3HT backbone

The first origin can be ruled out because the absorption spectra recorded for POL 90° (Figure 13b and 4c) do not show any polaronic features, suggesting that the amorphous fraction is little doped. This is also consistent with the fact that the HOMO level of P3HT in the amorphous phase is 0.1-0.2 eV lower than that of crystalline P3HT, making it more difficult to transfer a charge between amorphous P3HT and $F_4TCNQ$. [45,46] Therefore the non-oriented amorphous part is not responsible for the reduced order parameter.

The second origin is supported by TEM observations. The clear streaking of the *0 0 2* reflection along with the disappearance of the *1 0 2* and *2 0 2* reflections indicate a statistical rearrangement of π-stacks ($\Delta c_{inter}$ in Figure 12f) and a disordering of the packing of the side chains upon intercalation of the dopant molecules (Figure 12).

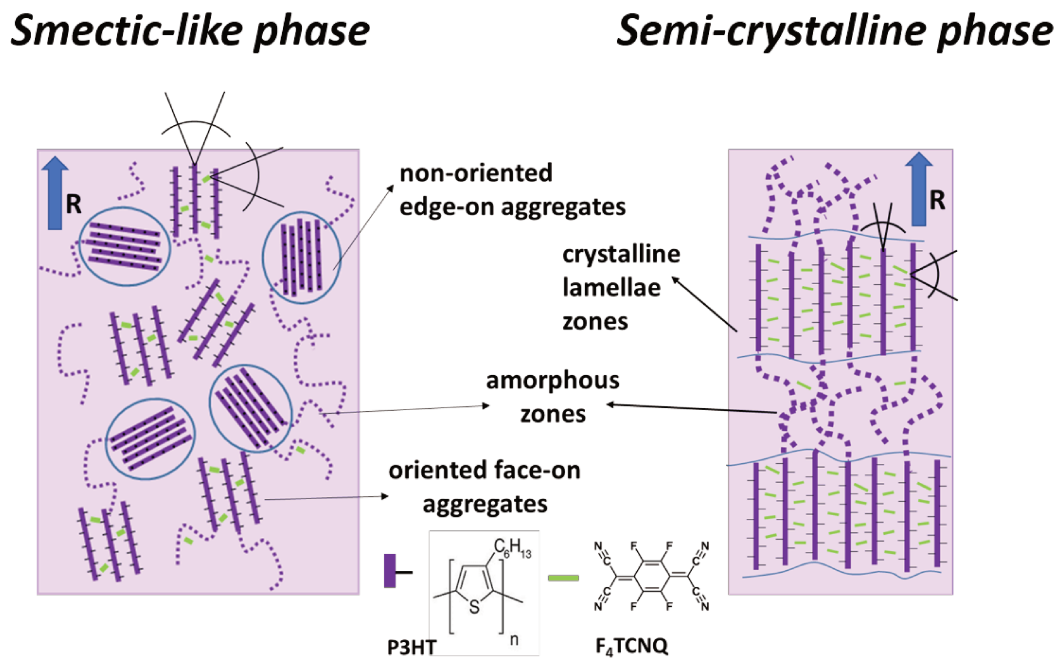


***Figure 15.*** *Schematic representations of the structure of both doped smectic-like and semi-crystalline phases. Average orientation and location of the dopants molecules are shown in green.*

The observation of disordered side chains is consistent with dopant molecules distributed close to a plane perpendicular to the P3HT backbones. The intercalation of dopants in the side chain layers appears therefore as a method to probe the side chain orientation of polymer semiconductors with respect to their backbone. If the side chains of P3HT were

significantly tilted with respect to the backbone in the (a,c) plane, then, the maximum of the absorbance of $F_4TCNQ^-$ anions would also be way off 90°, which is not observed here. Accordingly, this result supports indirectly the model of the structure of form I P3HT proposed by Kayunkid *et al.* stipulating that alkyl side chains are located in a plane perpendicular to the polymer backbone.[27]

Figure 15 depicts schematically structure of both phases in the doped state: lamellar structure in the semi-crystalline phase and partially oriented crystalline domains with non-oriented edge-on fraction for the smectic-like.

### II.4.3 Estimation of doping concentration

As shown previously, the evolution of the ratio r = Abs P1 (at 2500 nm) / Abs N (at 550 nm) as a function of $T_R$ suggests that a higher doping level is obtained in the semi-crystalline phase at high $T_R$. To estimate this doping level in the semi-crystalline phase, differences in the angular distributions of the P3HT and of the $F_4TCNQ^-$ anion absorption bands must be taken into account. Using the extinction coefficient of $F_4TCNQ^-$ at 870 nm (50 000 $M^{-1}$ $cm^{-1}$ )[47] and the angular dependence of the pristine polymer film and the anions, it is possible to estimate a doping level defined as the number of $F_4TCNQ^-$ anions per thiophene cycle for both structures. The obtained values (see Table 2) correspond to 5 ± 2 and 15 ± 2 % for the smectic-like and the semi-crystalline phase, respectively. This result is further in agreement with ESR measurements showing broader signals for the semi-crystalline phase with respect to the smectic-like phase.

*Table 2: Main characteristics of both doped smectic-like and semi-crystalline phases*

| **Main characteristics of both phases** | **Smectic-like phase** | **Semi-crystalline phase** |
|---|---|---|
| Order parameter polaron | 0.12 | 0.91 |
| Order parameter anion | 0.09 | 0.62 |
| $d_{020}$ π-stacking distance (Å) | 3.6 | 3.6 |
| $d_{100}$ alkyl side chains distance (Å) | 17.9 | 18.1 |
| Estimated $F_4$TCNQ molecules per 100 thiophene units | 5 | 15 |
| Charge conductivity $\sigma_{//}$ max (S cm$^{-1}$) | 35 | 160 |
| Power factor $PF_{//}$ max (μW m$^{-1}$ K$^{-2}$) | 18 | 56 |

The upper value of the crystalline phase is consistent with a previous estimate of 17 % for aligned P3HT[21] whereas the smectic-like phase shows a substantially lower doping level. It is also close to the 15% doping level estimated for $F_4TCNQ^-$doped oriented films of $C_{12}$-PBTTT.[22] This result indicates that the initial crystallinity of the P3HT films impact the doping efficiency. This is consistent with the structural study that supports different dopant intercalation mechanisms for the two phases. In the smectic-like phase, doping perturbs the stacking of P3HT backbones whereas in the semi-crystalline phase, intercalation of dopants requires essentially some reorganization of the stacks along the alkyl side chains directions. Moreover, alkyl side chains are more disordered in the smectic-like phase than in the semi-crystalline phase.[26] This result suggests that highly ordered alkyl side chains (non-interdigitated) favor dopant intercalation whereas highly disordered side chain layers in the

smectic-like phase do not. This is consistent with recent results obtained in oriented thin films of a family of PBTTTs with side chain length varying from linear $C_8$ to $C_{18}$. The doping level was found to be lower for $C_8$-PBTTT with disordered $C_8$ side chains than for $C_{12}$-PBTTT showing more ordered side chains.[22] However; the side chains are interdigitated in $C_{12}$-PBTTT which makes the diffusion of dopants more difficult than in the non-interdigitated side chains of P3HT. The ordered side chains of P3HT help orient the dopants in its unit cell and favour fast diffusion and intercalation.

The fact that the structure of the pristine films impacts the doping level in thin films is at variance with recent results by Hynynen *et al.*[11] It was found that the doping level and the charge carrier density remain roughly constant regardless of the crystallinity of P3HT films processed in different solvents. The increase in conductivity with crystallinity was attributed to an increase in carrier mobility. In the present case, the order of the side chains seems to impact the doping level and thus the charge carrier density. A possible reason for this discrepancy could be related to the way the doping level is extracted from the absorbance of the $F_4TCNQ^-$ anions. Indeed, rubbed P3HT films consist of a majority of face-on crystals whereas spin-coated and cast films are essentially composed of edge-on crystals. [11,10] Since the transition dipole of the $F_4TCNQ^-$ is along the molecular long axis, the absorbance of the $F_4TCNQ^-$ molecules probed using polarized UV-vis-NIR spectroscopy depends on the average orientation of the dopant in the film plane. In the work of Hamidi-Sakr et al. on oriented face-on P3HT, the absorption of the $F_4TCNQ^-$ anions was polarized in-plane in a direction orthogonal to the P3HT backbone, supporting the dopant intercalation in the layers of alkyl side chains and parallel to side chains.[21] If the P3HT crystals are essentially edge-on, then, upon intercalation inside the layers of alkyl side chains, the long axis of the $F_4TCNQ^-$ molecules

will be mainly distributed around the normal to the film surface. Such an orientation renders the $F_4TCNQ^-$ invisible using in-plane UV-vis-NIR absorption measurements. Accordingly, UV-vis-NIR spectroscopy on edge-on oriented P3HT can lead to an under-estimation of the proportion of $F_4TCNQ^-$. This simple reasoning uncovers the intrinsic difficulty to evaluate the doping concentration from in-plane spectroscopic measurements based on $F_4TCNQ^-$. A more accurate mean to probe the doping efficiency might be to compare the absorbances of polaronic features. Indeed, contrary to $F_4TCNQ^-$, the polymer chains lie almost exclusively in the film plane, hence, the polaronic bands are polarized in-plane. From that perspective, the comparison of the smectic-like and semi-crystalline phases suggests quite similar levels of doping, which is more in line with the results by Hynynen et al.[11] Accordingly, the difference in charge conductivity between smectic-like and semi-crystalline phases would be more related to the difference in charge mobility due to enhanced aligned in thin films prepared at $T_R$=186°C.

## III. Conclusions

High-temperature rubbing helps to enhance substantially the TE properties in oriented P3HT:$F_4$TCNQ thin films. The rubbing temperature is a precise handle to reach high crystallinity (> 55%) and orientation (order parameter > 0.8) in pristine P3HT films. Sequential doping with $F_4$TCNQ transforms the semi-conducting films into highly conducting polymer films with charge conductivities up to 160 S $cm^{-1}$ and power factor of 56 µW $m^{-1}$ $K^{-2}$ that lie beyond the state of the art for P3HT:$F_4$TCNQ. Furthermore, this particular and efficient tuning method of polymer chain alignment allows the fine structural analyses by TEM (in particular

along the polymer chain) not accessible by conventional GIXD analyses on randomly oriented films. Polarized absorption spectroscopy gives access to the angular distribution of dopants in the polymer matrix. The combination of both techniques provides a clearer view on the doping mechanism which depends on the initial structure of the films, i.e. smectic-like vs semi-crystalline phase. In the semi-crystalline phase, well-ordered side chains help the intercalation of a larger number of dopant molecules that are oriented perpendicular to the polymer backbone. The intercalation of the $F_4$TCNQ molecules in the side chain layers results in a disordering of both, the arrangement of successive (b,c) polymer stacks and the packing of the side chains. In comparison, the less ordered smectic-like phase is less doped and the intercalation of $F_4$TCNQ into the side chain layers seems to induce a reorganisation of the polymer chains within the (b,c) polymer stacks. This counter intuitive phenomenon of doping inducing order is demonstrated for the first time for regioregular P3HT. Although the semi-crystalline phase shows larger thermoelectric power factors than the smectic-like phase, it will be important to further investigate the impact of structural changes on the thermal conductivity to ascertain which of the two phases is most favorable for TE applications.

It is interesting to note that high performances reported in this study have been obtained although an important part of the film is still amorphous. Engineering of polymer crystallinity, prior to doping, could be an efficient strategy to further enhance the thermoelectric properties. Alternatively, one may also try to further preserve the pristine structure of the films, e.g. by vapor phase doping to intercalate the dopants in a less destructive manner. This reinforces the interest for new fabrication methods of highly structure-controlled conducting polymer films for thermoelectric applications.

**References**

1. Poehler, T. O. and Katz, H. E., Prospects for Polymer-based Thermoelectrics: Stat of the Art and Theoretical Analysis. *Energy Environ. Sci.* **2012**, 8, 8110.
2. He, M.; Qiu, F. and Lin, Z., Towards High-Performance Polymer-based Thermoelectric Materials, *Energy Environ. Sci.* **2013**, 6, 1352.
3. Lu, G.; Blakesley, J.; Himmelberger, S.; Pingel, P.; Frisch, J.; Lieberwirth, I.; Salzmann, I.; Oehzelt, M.; Di Pietro, R.; Salleo, A.; Koch, N.; Neher, D., Moderate Doping Leads to High Performance of Semiconductor/Insulator Polymer Blend Transistors. *Nat. Comm.* **2013**, 4, 1588-1596.
4. Panidi, J.; Paterson, A. F.; Khim, D.; Fei, Z.; Han, Y.; Tsetseris, L.; Vourlias, G.; Patsalas, P. A.; Heeney, M.; Anthopoulos, T. D., Remarkable Enhancement of the Hole Mobility in Several Organic Small-Molecules, Polymers, and Small-Molecule:Polymer Blend Transistors by Simple Admixing of the Lewis Acid p-Dopant B(C6F5)3. *Advanced Science* **2017**, 5, 1700290.
5. Fan, Z.; Li, P.; Du, D.; Ouyang, J., Significantly Enhanced Thermoelectric Properties of PEDOT:PSS Films through Sequential Post-Treatments with Common Acids and Bases. *Adv. Energy Mater.* **2017**, 7, 1602116.
6. Duong, D. T.; Wang, C.; Antono, E.; Toney, M. F.; Salleo, A., The Chemical and Structural Origin of Efficient P-type Doping in P3HT. *Org. Elect*. **2013**, 14, 1330-1336.
7. Wang, C.; Duong, D. T.; Vandewal, K.; Rivnay, J.; Salleo, A., Optical measurement of doping efficiency in poly(3-hexylthiophene) solutions and thin films. *Phys. Rev. B* **2015**, *91*, 085205.

8. Jacobs, I. E.; Aasen, E. W.; Oliveira, J. L.; Fonseca, T. N.; Roehling, J. D.; Li, J.; Zhang, G.; Augustine, M. P.; Mascal, M.; Moule, A. J., Comparison of Solution-Mixed and Sequentially Processed P3HT:$F_4$TCNQ Films: Effect of Doping-Induced Aggregation on Film Morphology. *J. Mater. Chem. C* **2016**, 4, 3454–3466.
9. Scholes, D. T.; Hawks, S. A.; Yee, P. Y.; Wu, H.; Lindemuth, J. R.; Tolbert, S. H.; Schwartz, B. J., Overcoming Film Quality Issues for Conjugated Polymers Doped with F4TCNQ by Solution Sequential Processing: Hall Effect, Structural, and Optical Measurements. *J. Phys. Chem. Lett.* **2015**, 6, 4786–4793.
10. Scholes, D. T.; Yee, P. Y.; Lindemuth, J.R.; Kang, H.; Onorato, J.; Ghosh, R.; Luscombe, C. K.; Spano, F. C.; Tolbert, S. H.; Schwartz, B. J., The Effects of Crystallinity on Charge Transport and the Structure of Sequentially Processed F4TCNQ-Doped Conjugated Polymer Films. *Adv. Funct. Mater.***2017**, 27, 1702654.
11. Hynynen, J.; Kiefer, D.; Yu, L.; Kroon, R.; Munir, R.; Amassian, A.; Kemerink, M.; Müller, C., Enhanced Electrical Conductivity of Molecularly P-Doped Poly(3-Hexylthiophene) through Understanding the Correlation with Solid-State Order. *Macromolecules* **2017**, *50*, 8140-8148.
12. Pingel, P.; Neher, D., Comprehensive Picture of p-Type Doping of P3HT with the Molecular Acceptor $F_4$TCNQ. *Phys. Rev. B* **2013**, 87, 115209.
13. Hynynen, J.; Kiefer, D.; Muller, C., Influence of Crystallinity on the Thermoelectric Power Factor of P3HT Vapour-Doped with $F_4$TCNQ. *RSC Adv.* **2018**, 8, 1593–1599.
14. Patel, S. N.; Glaudell, A. M.; Peterson, K. A.; Thomas, E. M.; O'Hara, K. A.; Lim, E.; Chabinyc, M. L., Morphology Controls the Thermoelectric Power Factor of a Doped Semiconducting Polymer. *Science Advances* **2017**, 3, e1700434.

15. Glaudell, A. M.; Cochran, J. E.; Patel, S. N.; Chabinyc, M. L., Impact of the Doping Method on Conductivity and Thermopower in Semiconducting Polythiophenes. *Adv. Energy Mater.* **2015**, 5, 1401072.

16. Kang, K.; Watanabe, S.; Broch, K.; Sepe, A.; Brown, A.;Nasrallah, I.; Nikolka, M.; Fei, Z.; Heeney, M.; Matsumoto, D.;Marumoto, K.; Tanaka, H.; Kuroda, S.; Sirringhaus, H. 2D coherent charge transport in highly ordered conducting polymers doped by solid state diffusion. *Nat. Mater.* **2016**, 15, 896-902.

17. Thomas, E. M.; Davidson, E. C.; Katsumata, R.; Segalman, R. A. and Chabinyc, M. L., Branched Side Chains Govern Counterion Position and Doping Mechanism in Conjugated Polythiophenes. *ACS Macro Lett.* **2018**, 7, 1492.

18. Kroon, R.; Kiefer, D.; Stegerer, D.; Yu, L., Sommer, M.; Müller, C., Polar Side Chains Enhance Processability, Electrical Conductivity, and Thermal Stability of a Molecularly p-Doped Polythiophene. *Adv. Mater.* **2017**, 29, 1700930.

19. Lim, E.; Peterson, K. A; Su, G. M.; Chabinyc, M. L., Thermoelectric Properties of Poly(3-hexylthiophene) (P3HT) Doped with 2,3,5,6-Tetrafluoro-7,7,8,8-tetracyanoquinodimethane (F4TCNQ) by Vapor-Phase Infiltration. *Chem. Mater.* **2018**, 30, 998-1010.

20. Gao, W.; Kahn A., Controlled p-doping of the hole-transport molecular material N,N'-diphenyl-N,N'-bis(1-naphthyl)-1,1'-biphenyl-4,4'-diamine with tetrafluorotetracyanoquinodimethane. *J. Appl. Phys.* **2003**, 94, 359.

21. Hamidi-Sakr, A.; Biniek, L.; Bantignies, J.-L.; Maurin, D.; Herrmann, L.; Leclerc, N.; Lévêque, P.; Vijayakumar, V.; Zimmermann, N.; Brinkmann, M., A Versatile Method to Fabricate Highly In-Plane Aligned Conducting Polymer Films with Anisotropic Charge

Transport and Thermoelectric Properties: The Key Role of Alkyl Side Chain Layers on the Doping Mechanism. *Adv. Funct. Mater.* **2017**, 27, 1700173.

22. Vijayakumar, V.; Zaborova, E.; Biniek, L.; Zeng, H.; Herrmann, L.; Carvalho, A.; Boyron, O.; Leclerc, N. and Brinkmann, M., Effect of alkyl side chain length on doping kinetics, thermopower and charge transport properties in highly oriented $F_4$TCNQ doped PBTTT films, *ACS Appl. Mater. Interfaces* **2019**, 11, 4942.
23. Vijayakumar, V.; Zhong, Y.; Untilova, V.; Bahri, M.; Herrmann, L.; Biniek, L., Leclerc N.; Brinkmann, M., Bringing conducting polymers to high order: towards conductivities beyond 105 S/cm and thermoelectric power factors of 2 $mW{\cdot}m^{-1}{\cdot}K^{-2}$. *Adv. En. Mater.* **2019**, 1900266.
24. Yasuda, T., Anisotropic carrier transport properties of stretch-oriented π- conjugated polymers in organic field-effect transistors. *Phys. Status Solidi C 8*, **2011**, 2, 604–606.
25. Hamidi-Sakr, A.; Biniek, L.; Fall, S.; Brinkmann, M., Precise Control of Lamellar Thickness in Highly Oriented Regioregular Poly(3-Hexylthiophene) Thin Films Prepared by High-Temperature Rubbing: Correlations with Optical Properties and Charge Transport. *Adv. Funct. Mater.* **2016**, 26, 408–420.
26. Hartmann, L.; Tremel, K.; Uttiya, S.; Crossland, E.; Ludwigs, S.; Kayunkid, N.; Vergnat, C. Brinkmann, M., 2D versus 3D Crystalline Order in Thin Films of Regioregular Poly(3-hexylthiophene) Oriented by Mechanical Rubbing and Epitaxy. *Adv. Funct. Mat.* **2011**, 21, 4047.
27. Kayunkid, N.; Uttiya, S. Brinkmann, M., Structural Model of Regioregular Poly(3-hexylthiophene) Obtained by Electron Diffraction Analysis. *Macromolecules* **2010**, 43, 4961.

28. Atherton, N. M. *Electron Spin Resonance: Theory and Applications* (Ellis Horwood Ltd., Chichester, UK, 1973).

29. Weil, J. A. & J. R. Bolton. *Electron Paramagnetic Resonance* 2nd edition (J. Wiley & Sons, Inc., Hoboken, NJ, USA, 2007).

30. Gao, J.; Stein, B. W. ; Thomas, A. K. ; Garcia ; J. A., Yang, J. ; Kirk M. L., Grey J. K., Enhanced Charge Transfer Doping Efficiency in J-Aggregate Poly(3-hexylthiophene) Nanofibers. *J. Phys. Chem. C* **2015,** 119, 16396-16402.

31. Gao, J.; Niles, E.T. ; Grey J.K., Aggregates Promote Efficient Charge Transfer Doping of Poly(3-hexylthiophene). *J. Phys. Chem. Lett.* **2013**, 4, 2953-2957.

32. Eaton, G.R., S. S. Eaton, D. P. Barr & R. T. Weber. *Quantitative EPR* (Springer, Wien, 2010).

33. Ghosh, R.; Pochas, C. M.; Spano, F. C., Polaron Delocalization in Conjugated Polymer Films. *J. Phys. Chem. C* **2016**, 120, 11394-–11406.

34. Ghosh, R.; Chew, A. R.; Onorato, J.; Pakhnyuk, V.; Luscombe, C. K.; Salleo, A.; Spano, F. C., Spectral Signatures and Spatial Coherence of Bound and Unbound Polarons in P3HT Films: Theory Versus Experiment. *J. Phys. Chem. C* **2018**, 122, 18048-–18060.

35. Clark, J.; Chang, J.-F.; Spano, F. C.; Friend, R. H.; Silva, C., Determining exciton bandwidth and film microstructure in polythiophene films using linear absorption spectroscopy. *Appl. Phys. Lett.* **2009**, 94, 163306.

36. Spano, F. C. Modeling disorder in polymer aggregates: The optical spectroscopy of regioregular poly(3-hexylthiophene) thin films. *J. Chem. Phys.* **2005**, 122, 234701.

37. Spano, F. C. Absorption in regio-regular poly(3-hexyl)thiophene thin films: Fermi resonances, interband coupling and disorder. *Chem. Phys.* **2006**, 325, 22−35.

38. Chew, A.R.; Salleo, A., Spectroscopic studies of dopant-induced conformational changes in poly (3-hexylthiophene) thin films. *MRS Communications* **2017**, 7, 728-734.

39. Schulz G. L.; Ludwigs, S., Controlled Crystallization of Conjugated Polymer Films from Solution and Solvent Vapor for Polymer Electronics, *Adv. Funct. Mater.* **2017**, 27, 1603083.

40. Lim, E.; Glaudell, A. M.; Miller, R. and Chabinyc, M. L. The role of Ordering on the Thermoelectric Properties of Blends of Regioregular and Regiorandom Poly(3-hexylthiophene). *Adv. Elect. Materials* **2019**, 1800915.

41. Lovinger, A. J.; Lotz, B.; Davis, D. D.; Padden Jr, F. J., Structure and Defects in Fully Syndiotactic Polypropylene. *Macromolecules* **1993**, 26, 3494-3503.

42. Haller, I.; Kaufman F. B., Spectra of tetracyanoquinodimethane monovalent anion: vibrational structure and polarization of electronic transitions. *J. Am. Chem. Soc.* **1976**, 98, 1464.

43. Sata, R.; Suzuki, H.; Ueno, N.; Morisawa, Y.; Hatanaka, M.; Wakabayashia, T., UV-polarizing linear polyyne molecules aligned in PVA. *J. Chem. Phys.* **2019**, 32, 175.

44. B. Bahadur Ed., Liquid Crystals-Applications and Uses, Vol. 3, World Scientific, 101 (1992)

45. Jiang, X. M.; Österbacka, R.; Korovyanko, O.; An, C. P.; Horovitz, B.; Janssen, R. A. J.; Vardeny, Z. V. Spectroscopic Studies of Photoexcitations in Regioregular and Regiorandom Polythiophene Films. *Advanced Functional M46aterials* **2002**, *12* (9), 587–597

46. Tsoi, W. C.; Spencer, S. J.; Yang, L.; Ballantyne, A. M.; Nicholson, P. G.; Turnbull, A.; Shard, A. G.; Murphy, C. E.; Bradley, D. D. C.; Nelson, J.; et al. Effect of Crystallization on the Electronic Energy Levels and Thin Film Morphology of P3HT:PCBM Blends. *Macromolecules* **2011**, *44* (8), 2944–2952.

47. Dixon, D. A.; Calabrese, J. C.; Miller J. S., Crystal and Molecular Structure of the 2: 1 Charge-Transfer Salt of Decamethylferrocene and Perfluoro-7,7,8,8-tetracyano-p-quinodlmethane: $[[Fe(C5Me5)_2]^+]_2[TCNQF_4]^{2-}$. The Electronic Structure of $[TCNQF_4]_n$ (n = 0, 1-, 2-). *J. Phys. Chem.* **1989** 93, 2284-2291.

# Chapter 3. Intercalation and ordering of $F_6$TCNNQ and $F_4$TCNQ dopants in regioregular poly(3-hexylthiophene) crystals: impact on anisotropic TE properties of oriented thin films

## I. Introduction

In the last decades, polymer semiconductors have gained considerable attention since they combine remarkable optical and electronic properties with mechanical flexibility, light weight and low-temperature processing.[1] Numerous fields of applications exist, to cite but a few: organic photovoltaics, Organic Field Effect Transistors and, more recently, the design of thermoelectric (TE) generators. From a material's perspective, TE properties are observed in polymer semiconductors upon doping and can be adjusted by numerous methods e.g. by tailoring the polymer backbone, tuning the length of side chains, adjusting the energetic offset between the polymer's HOMO and the acceptor's LUMO, tuning the chemical structure of the dopant or choosing the best doping method.[2–5] Much attention is currently focused on doped p-type polymer semiconductors (PSCs) suitable for thermoelectric (TE) applications. Polythiophenes such as regioregular poly(3-hexylthiophene) (P3HT), poly(3,4-ethylenedioxythiophene)-tosylate (PEDOT-Tos) or Poly[2,5-bis(3-alkylthiophen-2-yl)thieno[3,2-b]thiophene] (PBTTTs) doped with acceptor molecules such as $F_4$TCNQ or $FeCl_3$ have been investigated intensively.[6–12] P3HT / $F_4$TCNQ emerged as a model system to better understand the correlations between processing, structure and TE properties.[12–15]

Doping of PSCs is the important step transforming the pristine semiconducting polymer into conducting ones. Doping controls the conductivity of the films and also the resulting TE power factors PF that scales with conductivity following $PF \propto \sqrt{\sigma}$.[16] Redox doping rests on a charge transfer between the polymer and the dopant. It has been shown that integer charge transfer (ICT) occurs from the HOMO ~ −4.8 eV of P3HT to the LUMO ~ −5.2 eV of $F_4$TCNQ.[17] The position of the LUMO of the acceptor is essential and must be well situated with respect to the HOMO of the polymer. Of particular interest are strong dopants such as $F_6$TCNNQ whose LUMO has a lower value around -5.37 eV as compared to $F_4$TCNQ (-5.2 eV).[18,19] (see Figure 1)

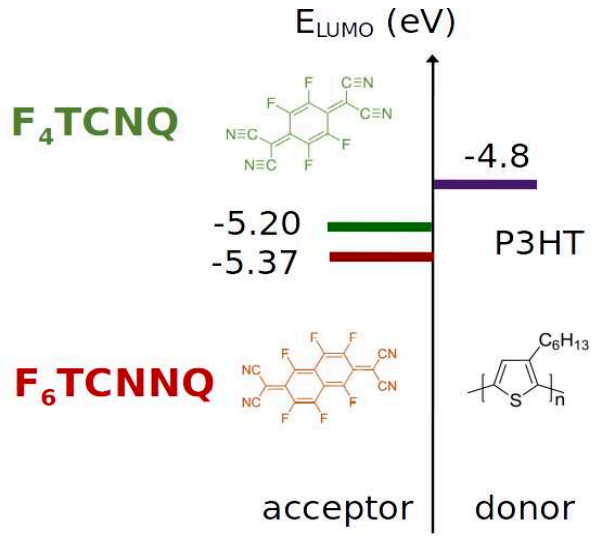


***Figure 1.*** *a) Schematic energy diagram of LUMO levels of $F_4$TCNQ, $F_6$TCNNQ and HOMO of the P3HT.*

Beside the chemical nature of the dopant, the doping method is also key. Various doping methods have been investigated in literature such as mixed solution/ sequential processing,[5,13,16] vapour phase doping[20], and more recently incremental concentration doping (ICD).[21,22] Mixed polymer/dopant solution processing[23,24] has been shown to be quite ineffective due to the poor resulting film quality and low TE performances. In strong

contrast, sequential doping allows to intercalate the dopant molecules into the crystals of PSCs in such a way that the pristine order of the polymer is preserved upon doping.[13,14] Vapour-phase doping is also very effective as it allows to intercalate dopant molecules progressively into the pristine polymer structure without the need for an organic solvent that can interact with the polymer during doping.[14] Similar to vapor phase doping, a variant of sequential doping, namely Incremental Concentration Doping (ICD), can lead to improved TE properties in $F_6$TCNNQ-doped PBTTT[22]. ICD consists in introducing increasing amounts of dopants into the PSC films. The progressive doping with solutions of increasing concentration allows to reach higher conductivities in comparison to direct doping due to the gradual dopant intercalation e.g. for PBTTT films doped by $F_6$TCNNQ. (see Figure 2)

The improved conductivity is related to the fact that ICD preserves best the pristine structure of the films and hence helps reach larger charge conductivities (see Figure 3). ICD of oriented $C_{12}$-PBTTT films doped with $F_4$TCNQ and $F_6$TCNNQ leads to a substantial increase of charge conductivities.[22]

The dopant location also impacts the final TE properties of semi-crystalline PSCs whether it enters only the crystalline part or both the crystalline and the amorphous parts. It is still under discussion whether $F_4$TCNQ dopes the amorphous, the crystalline or both phases in P3HT. There is a general consensus that the observed result depends on the dopant, the doping method and in particular, on the solvent used for doping.[5,14,17–20] Limited doping of amorphous P3HT is possibly due to the different energetic offsets between the dopant's LUMO and the different HOMO levels in the crystalline and amorphous zones. Several tenth of eV difference between both crystalline and amorphous zones can already complicate a charge transfer between polymer and dopant.[25] It has been recently demonstrated that

bulkier dopant molecules such as Molybdenum complex (e.g. Mo(tfd-$COCF_3$)$_3$) are able to dope both amorphous and crystalline regions of P3HT.[26,27] Several recent studies on P3HT and PBTTT have demonstrated that the dopant molecules are located in the layers of alkyl side chains and that the amorphous part remains little-doped with $F_4$TCNQ.[3,28,29]

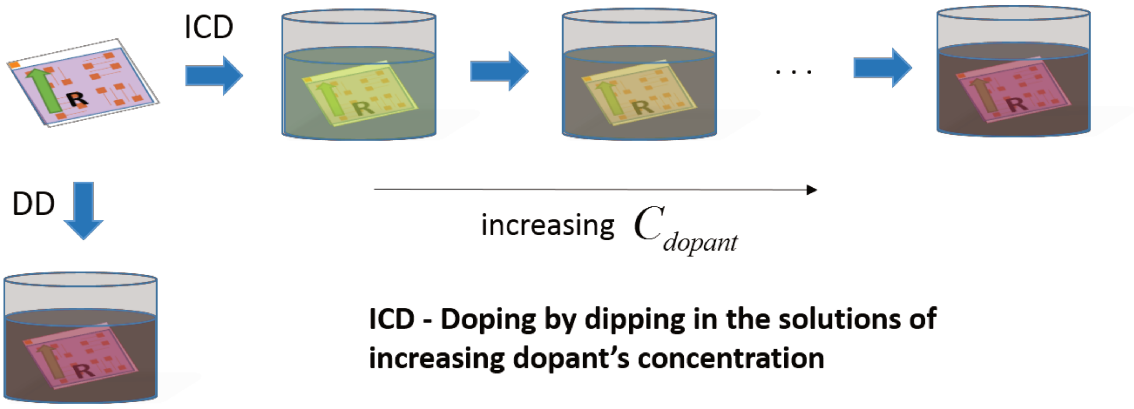


***Figure 2.*** *Schematic illustration of incremental concentration doping (ICD) and direct doping (DD).*

Equally important for TE properties is the polymer's crystallinity in the pristine state prior to doping. Hynynen et al. demonstrated the correlation between the initial crystallinity of P3HT and the final conductivity after doping with $F_4$TCNQ.[30] Scholes et al. showed that a higher degrees of film crystallinity leads to higher mobility and greater polaron delocalization.[14] A similar result was also evidenced in oriented films of P3HT where improved alignment and crystallinity result in improved TE properties.[27] Exploiting the anisotropic transport of PSCs is a further means to improve TE properties of doped PSCs because charge conductivity is usually maximal along the chain and π-stacking directions.[27–29,31] In this regard, high-temperature rubbing proved highly effective because both alignment

and film crystallinity can be readily controlled by adjusting the temperature of rubbing $T_R$.[31] In average, a ten-fold increase in conductivity is observed parallel to the chain direction in doped and oriented P3HT and PBTTT films as compared to isotropic thin films.[17,26,27] Most interestingly, polymer alignment also enhances the Seebeck coefficient and is therefore a simple method to reach larger power factors in thin films.

In this chapter we investigate the effect of the dopant on optical, structural and thermoelectric properties in aligned P3HT films doped sequentially with $F_4$TCNQ and $F_6$TCNNQ. We evaluate how the dopant size and electron affinity affect the final film structure as a function of dopant concentration. We used a combination of polarized UV-Vis-NIR spectroscopy and low dose electron diffraction to provide an insight into how the doping by different molecules affects the final polymer structure and how the dopant molecules are distributed in the P3HT crystals. Measurements of DC conductivity and Seebeck coefficients in anisotropic films help to draw correlations between doped polymer structure and TE properties. Differences in doping mechanism and film structure *versus* dopant concentration are evidenced. Both absorption spectroscopy and electron diffraction provide compelling evidence for the intercalation of $F_6$TCNNQ dopants inside the crystal lattice of P3HT. A tentative model for the structure of $F_6$TCNNQ-doped P3HT is obtained from ED analysis.

## II. Results

### II.1 Incremental Concentration Doping *versus* Direct Doping

Similarly to $C_{12}$PBTTT, we have first verified if the ICD protocol leads to higher charge conductivities as compared to the direct doping method used for sequential doping. We have therefore compared the charge conductivities in thin films doped by ICD and DD with $F_4$TCNQ in acetonitrile. In ICD, for a given doping concentration C, the sample has been doped at all lower doping concentrations (see Figure 2).

As seen in Figure 3, ICD allows to reach larger charge conductivities for all doping concentrations. The conductivity at 1g/l is improved by a factor 1.6 using ICD instead of DD, reaching a conductivity of 205 S/cm for $F_4$TCNQ *versus* 122 S/cm for DD. Therefore, we show that this new doping method is general and applicable to other polymer semiconductors. In the case of $C_{12}$PBTTT, we have shown that the ICD protocol does not lead to larger charge carrier concentrations since the polaronic band absorbance for DD and ICD are almost identical. Therefore, it was concluded that the benefits in ICD lies in the fact that the structure is better preserved upon doping in solutions of increasing concentration since the dopants are introduced in a more progressive manner. Likewise, we used ED to verify if ICD and DD correspond to different structural characteristics of the doped films. Figure 3 depicts diffraction patterns of $F_6$TCNNQ-doped P3HT at 2g/l by both ICD and DD. No significant structural changes can be evidenced by electron diffraction between the two doping methods beside a marginal change in the $d_{100}$. Differences in microstructure between the two type of doped films using the two methods are accordingly quite subtle and not visible in ED.

Therefore, we stress that ICD leads to better performances due to a more regular intercalation of the dopants in the pristine crystal lattice of P3HT.

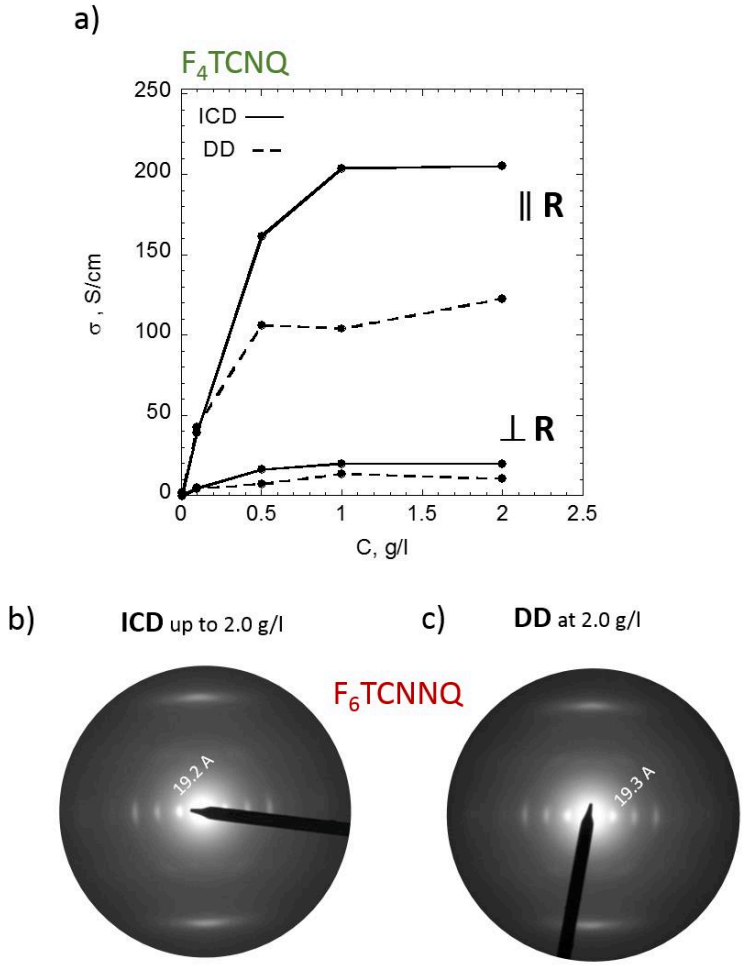


***Figure 3.*** *a) Electrical conductivity of oriented P3HT films doped by $F_4$TCNQ by both ICD and DD for comparison; b, c) Electron diffraction patterns of $F_6$TCNNQ-doped samples at 2 g/l using ICD and DD doping methods.*

### II.2 Spectroscopic evidence of doping

The difference in the doping mechanism of oriented P3HT with $F_4$TCNQ and $F_6$TCNNQ was first probed using polarized UV-vis-NIR absorption spectroscopy. Figure 4 and 5 depict the polarized UV-vis-NIR spectra of doped P3HT films at different doping concentrations of $F_4$TCNQ and $F_6$TCNNQ both in parallel and in perpendicular direction to the rubbing.

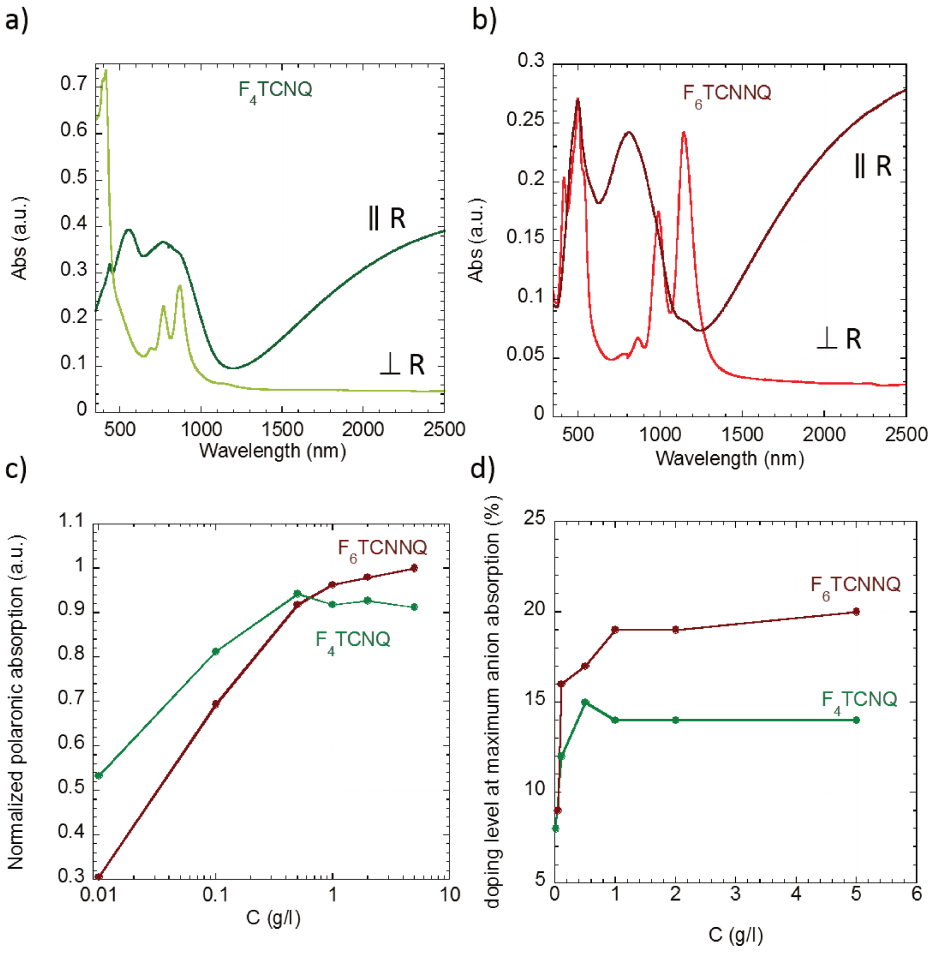


***Figure 4***. *Polarized UV–vis–NIR spectra of oriented P3HT films featuring highly polarized polaronic absorption bands (P1, P2) for incident light polarized parallel to the rubbing direction (∥) and the polarized absorption bands of the anion for incident light polarized perpendicular to the rubbing direction (⊥). P3HT films are sequentially doped using a 5 g/l*

*solution in acetonitrile of a) $F_4$TCNQ and b) $F_6$TCNNQ. c) Normalized polaronic absorption as a function of the dopant concentration, d) doping level at maximum anionic absorption. Green and dark red curves correspond to $F_4$TCNQ and $F_6$TCNNQ, respectively.*

Both polaronic and anionic signals are strongly polarized with respect to the rubbing direction. As seen in Figure 4.a and 5.c, the $F_4$TCNQ anion has characteristic absorption peaks at 413, 690,770 and 873 nm polarized in the direction perpendicular to the rubbing.[22] In the direction of rubbing, the spectrum is dominated by the neutral polymer fraction at 525 nm and the two polaronic P1 and P2 bands located respectively at 2500 nm and 795 nm (Figure 4 and 5). In the case of $F_6$TCNNQ (Figure 4.b and 5.d) the main $F_6$TCNNQ anionic absorption are centered at 864, 988 and 1143 nm and polarized perpendicular to the rubbing. The positions of the $F_6TCNNQ^-$ bands are consistent with those of the anion found in solution.[22]

A few additional $F_6TCNNQ^-$ absorption peaks are centered at 414, 474 and 502 nm. The polaronic absorption peaks P1 and P2 are located at the same position as in case of $F_4$TCNQ and are polarized along the rubbing direction. The relative polarizations of the dopant anions and the polaron indicates that both $F_4$TCNQ and $F_6$TCNNQ are oriented with their long axis in a plane perpendicular to the P3HT chain direction. For POL//R, the comparison of the absorption of doped films indicates a higher oxidation level for $F_6$TCNNQ as indicated by a higher ratio between P1 and neutral polymer absorbances. This is consistent with the lower LUMO level of $F_6$TCNNQ versus $F_4$TCNQ.

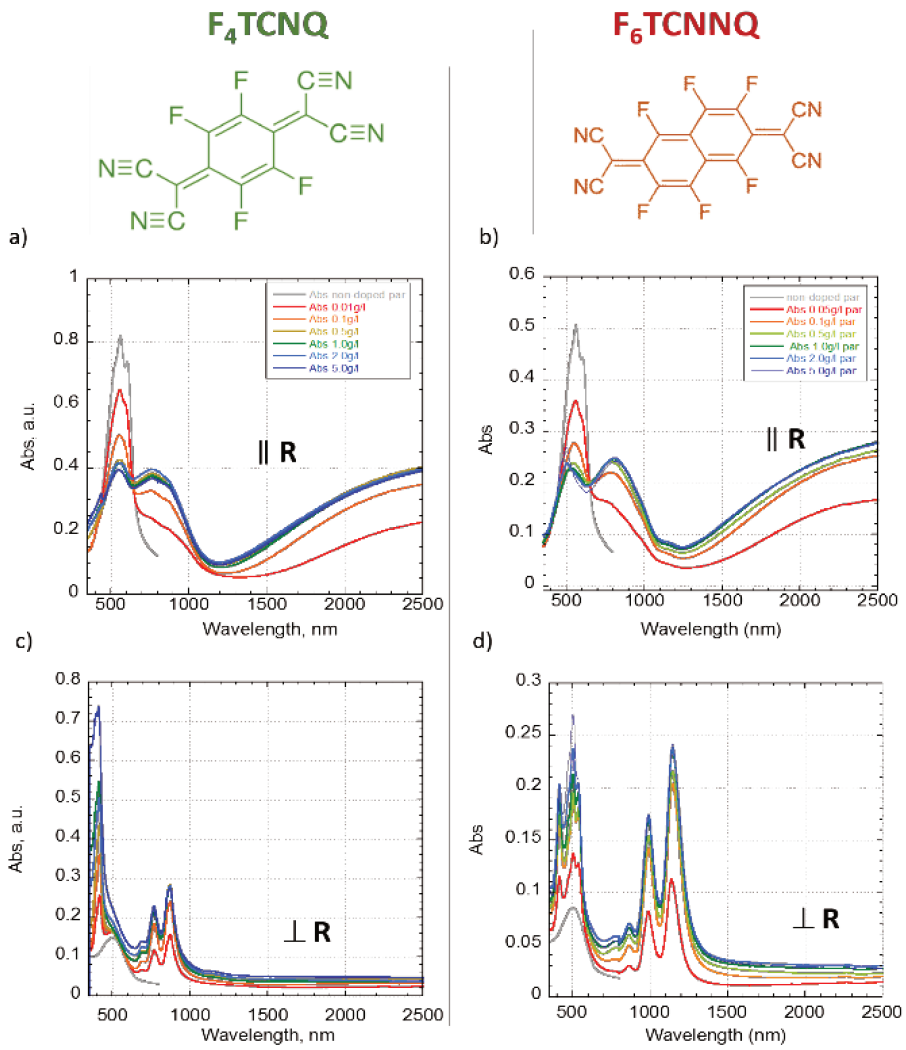


***Figure 5.*** *a) - d) Polarized UV–Vis–NIR absorption spectra of oriented conducting polymer films for both $F_4$TCNQ- (a,c) and $F_6$TCNNQ-doped (b,d) films plotted for different dopant concentrations. The spectra are recorded for different polarizations of the incident light with respect to the rubbing direction (**R**). a), b) - POL **∥ R** spectra showing the polaronic bands P1 and P2 of the doped P3HT and the neutral P3HT. c), d) - POL **⊥ R** spectra showing the absorption of neutral P3HT (450 – 530 nm) as well as the 416, 768, and 875 nm characteristic peaks of the $F_4TCNQ^-$ anions (c) and 857, 989 and 1138 nm characteristic peaks of the $F_6TCNNQ^-$ anions (d). The absorption spectra of undoped P3HT films are shown in light grey.*

Following the absorbance of the polaronic P1 band *versus* doping concentration helps evidence further differences in the doping process. At very low concentration (0.01 mg/ml), there is already a strong P1 band for $F_4$TCNQ whereas for $F_6$TCNNQ the absorbance is substantially lower (see Figure 5). Only for C≥0.5 mg/ml are similar P1 absorbances observed for both dopants. In other words, equivalent doping with $F_6$TCNNQ occurs for higher concentrations as compared to $F_4$TCNQ and there might be a threshold concentration to be able to dope P3HT with $F_6$TCNNQ. The doping level (dopant per thiophene) can be estimated from the absorbance of the anions, knowing the extinction coefficients ε for both dopants and the film thickness (see experimental section). As seen in Figure 4.d, the final doping levels is larger for $F_6$TCNNQ (20 dopants/100 thiophene) as compared to $F_4$TCNQ (14 dopants per 100 thiophenes). The larger doping with $F_6$TCNNQ is consistent with the lower LUMO level of $F_6$TCNNQ as compared to $F_4$TCNQ.

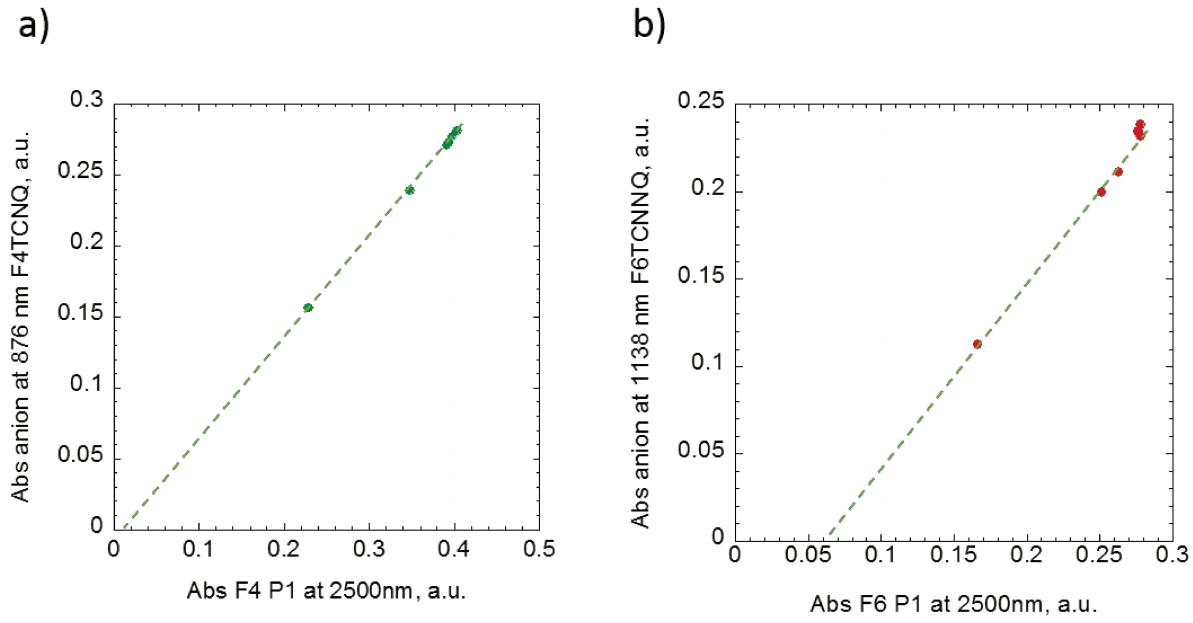


***Figure 6.*** *a), b) Linear correlation between the absorbance of the main dopant anion band (875 nm for $F_4$TCNQ and 1138 nm for $F_6$TCNNQ) and the absorbance of the polaronic P1*

*band to highlight integer charge transfer between P3HT and the dopants $F_4$TCNQ (a) and $F_6$TCNNQ (b).*

Interestingly, the linear correlation between the absorbance of the anion and the polaron was found for both dopants, supporting Integer Charge Transfer for both dopants. (see Figure 6)

## II.3 Structural difference between $F_4$TCNQ- and $F_6$TCNQ-doped P3HT films

### II.3.1 Evolution of the structure with doping concentration.

Figure 7 compares the structural modifications followed by electron diffraction (ED) in aligned P3HT films. Figure 7 shows the ED patterns of oriented P3HT doped sequentially with 0.01 g/l and 2.0 g/l solutions of $F_4$TCNQ and $F_6$TCNNQ in acetonitrile. Figure 7c represents the section profiles along the equatorial reflections from the complete set of experiments at different doping concentrations using incremental concentration doping (the same sample is doped in solutions of increasing concentration).

For $F_4$TCNQ, the structure of oriented P3HT films shows an expansion of the unit cell along the alkyl side chain direction up to 18.1 Å and reduced $\pi$-stacking to 3.6Å already for a doping concentration as low as 0.01 g/l. As seen from Figure 8, once the doped phase is formed at 0.01g/l, the structure changes slightly upon doping at higher concentrations. This is consistent with the absorption data showing that the polaron intensity changes also little above 0.1 g/l. As observed in our previous study, the h 0 2 reflections present in the pristine

oriented P3HT films[28,29] are replaced by an intense and streaked 0 0 2 reflection. This is a clear indication for the intercalation of $F_4$TCNQ in the P3HT crystals that leads to the shifts between planes of π-stacked P3HT chains to accommodate the dopants in the lattice.[29]

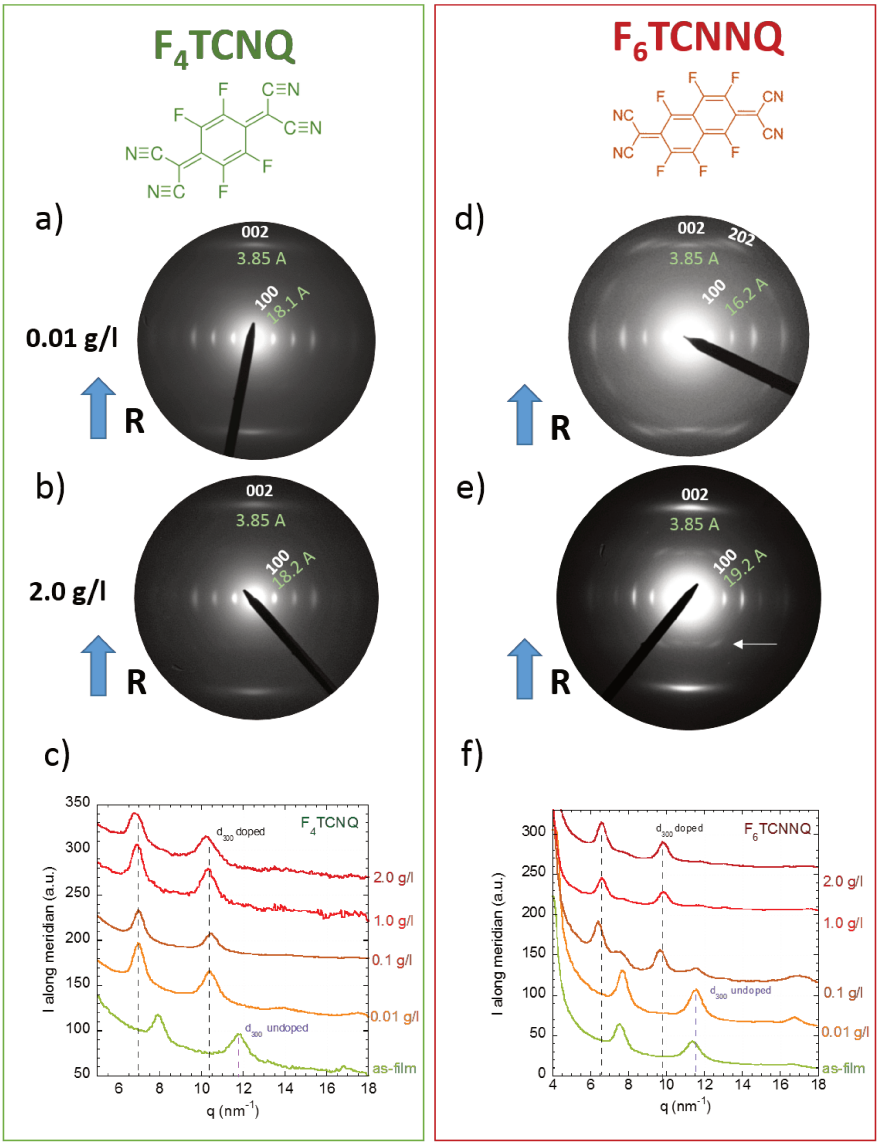


***Figure 7.*** *Electron diffraction patterns of oriented P3HT films doped with $F_4$TCNQ (a, c) and with $F_6$TCNNQ (b, d) for low and high doping concentrations of 0.01 g/l (a, b) and 2.0 g/l (c, d), respectively. Equatorial (e, f) section profiles of the electron diffraction patterns at different doping concentrations. For clarity, the section profiles are shifted along the ordinate axis and the intensity of the patterns are normalized to the intensity of the 2 0 0*

*peak. The rubbing direction* **R** *is indicated by the blue arrow for all patterns. The 0 0 2 reflection was used to calibrate the ED patterns. In the diffraction pattern (e), additional new reflections related to the $F_6$TCNNQ-doped P3HT phase are highlighted by a white arrow.*

The situation in the case of $F_6$TCNNQ doping is different as indicated by ED in Figure 7d, e, f that shows the diffractions patterns at 0.01 g/l and 2.0 g/l and a section profile along the equator, respectively. The diffraction pattern for 0.01 g/l is identical to the undoped phase, indicating no intercalation of $F_6$TCNNQ at this concentration whereas some polaronic and anion bands are already visible for this concentration.

For 0.1 g/l the doped and undoped phases coexist as indicated by the presence of two $d_{100}$ peaks with different periodicities. The $d_{100}$ of the $F_6$TCNNQ-doped P3HT phase is 19.2 Å *versus* 16.4Å for the undoped P3HT phase (see Figure 8). As for $F_4$TCNQ, the intercalation of dopants results in changes of the ED patterns in terms of reflection intensity. The h 0 2 (h=1,2) reflections disappear and are replaced by a streaked and very intense 0 0 2. Interestingly, for 2.0 g/l, the ED pattern is typical of the pure doped phase without traces of undoped P3HT. Accordingly, doping is more progressive in the case of $F_6$TCNNQ. The coexistence of doped and undoped phases with $F_6$TCNNQ may indicate that the diffusion of the dopant molecules inside the alkyl side chain layers is more difficult for the larger $F_6$TCNNQ molecules. Coexistence of doped and undoped phases may point at a spatially inhomogeneous distribution of dopants in the films for the concentrations below 0.1 g/l. ED analysis shows that the $F_6$TCNNQ-doped phase has additional reflections in the l=1 layer line. It must be

stressed that these new reflections are absent in the pristine P3HT films, demonstrating that doping has substantially modified the original structure of P3HT in the case of $F_6$TCNNQ.

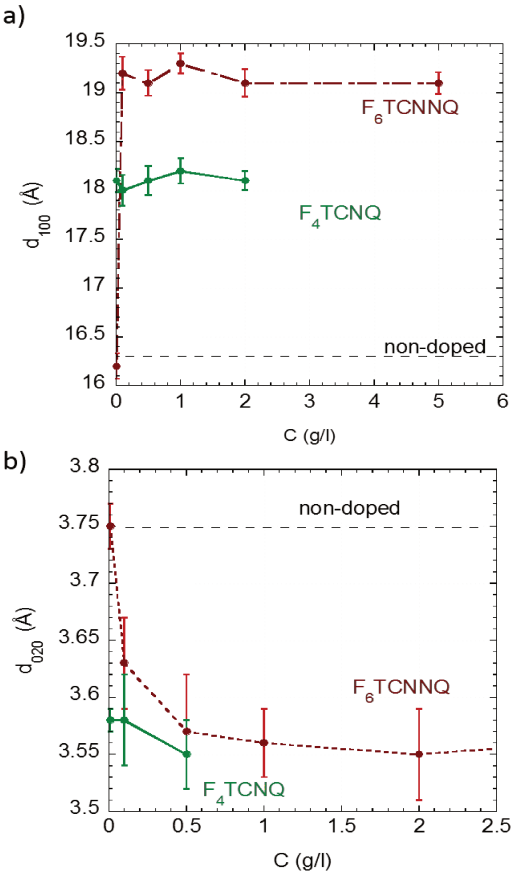


***Figure 8.*** *Evolution of the layer spacing along the alkyl side chain direction $d_{100}$ (a) and the $\pi$-stacking periodicity (b) as a function of doping concentration. The curves in green (dark red) correspond to the $F_4$TCNQ ($F_6$TCNNQ) doped films.*

The enhanced intensity of the 0 0 2 is synonymous of shifted/translated PT backbones within $\pi$-stacks.[29]

Overall, the final $d_{100}$ periodicity is larger for $F_6$TCNNQ (19.1 Å) than for $F_4$TCNQ (18.2 Å), which is consistent with the larger long axis dimension for $F_6$TCNNQ whereas the $\pi$-stacking periods are quite similar in both doped phases. A detailed structural analysis is presented in the following for $F_6$TCNNQ-P3HT.

### II.3.2 Structural model for P3HT:$F_6$TCNNQ.

For a $F_6$TCNNQ concentration of 5 g/l, ED indicates that the film has undergone a substantial structural re-organization as depicted in Figure 9 that compares the ED patterns of pristine (form I) and $F_6$TCNNQ-doped phases of P3HT.

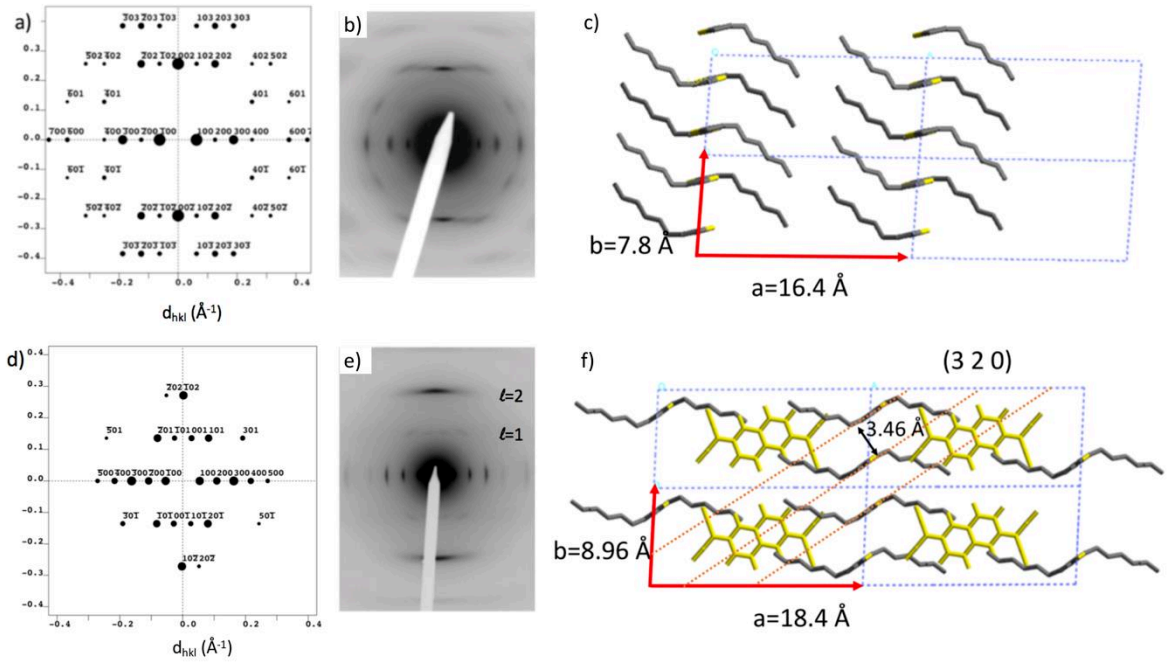


***Figure 9**. Experimental (a and d) and calculated (b and e) electron diffraction patterns for the [0 1 0] zone for P3HT (form I) (a and b) and P3HT-$F_6$TCNNQ (d and e). The form I structure is taken from reference*[32] *whereas the doped P3HT structure is refined and corresponds to the model illustrated in Figure 11. In c) and f), the* **c***-axis projection of the pristine and doped structures are shown, respectively.*

Beside the changes in the lattice periodicity along the alkyl side chains (**a** axis) and the π-stacking direction (**b** axis), the ED pattern of the doped phase shows additional reflections in the l=1 layer line. In the pristine form I of P3HT, all *h k 1* reflections are forbidden for symmetry reasons ($2_1$ axis along **c**). The additional reflections of the doped P3HT phase cannot be indexed as *h 0 1* since they are not located on the h=1 and h=2 layer lines (see Figure 10) but they are situated on intermediate layer lines. The new reflections can be indexed assuming that the unit cell of the doped phase is doubled along the **a** axis (side chain direction).

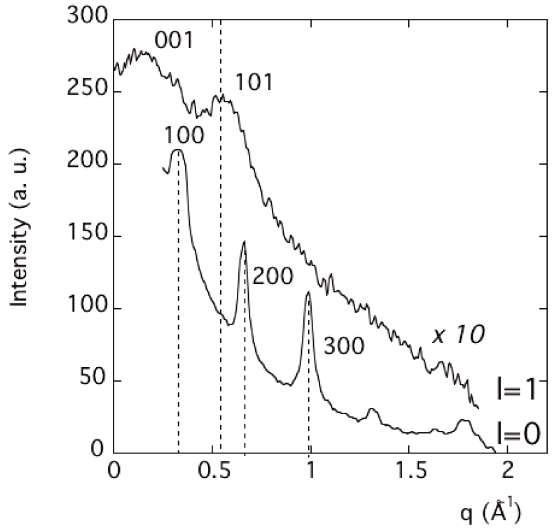


***Figure 10**. Section profile of the ED pattern of $F_6$TCNNQ-doped P3HT for the equatorial (l=0) and first layer line (l=1) of the pattern. Indexation is according to the model shown in Figure 11.*

Both, polarized UV-vis-NIR and electron diffraction provide evidence for the inclusion of dopant molecules in the crystal lattice of P3HT. This intercalation provides an ordered arrangement of dopants in the P3HT lattice, albeit with some statistical disorder. Therefore, to establish a structural model of P3HT/$F_6$TCNNQ, it is essential to understand the intercalation mechanism of the dopant molecules in the P3HT crystals.

Let us start with the structure of undoped P3HT (form I) as depicted in Figure 11. In the following, we use the structural model by Kayunkid et al. that was established by electron diffraction analysis.[32] In form I, the alkyl side chains of P3HT are not interdigitated. To ensure

a dense packing of side chains, it is necessary to have a shift Δc in the direction of the **c** axis between the PT backbones of two successive π-stacked P3HT chains. Therefore, there are no "cavities" to host dopant molecules in pristine P3HT. Accordingly, to intercalate $F_4$TCNQ or $F_6$TCNNQ in the P3HT unit cell, it is necessary to modify the π-stacking of P3HT chains within individual (b,c) planes. As noted in our previous study for P3HT/$F_4$TCNQ, ED indicates that the doping mechanism induces a structural reorganization of polymer chains within (b,c) planes in the P3HT crystal.[29]

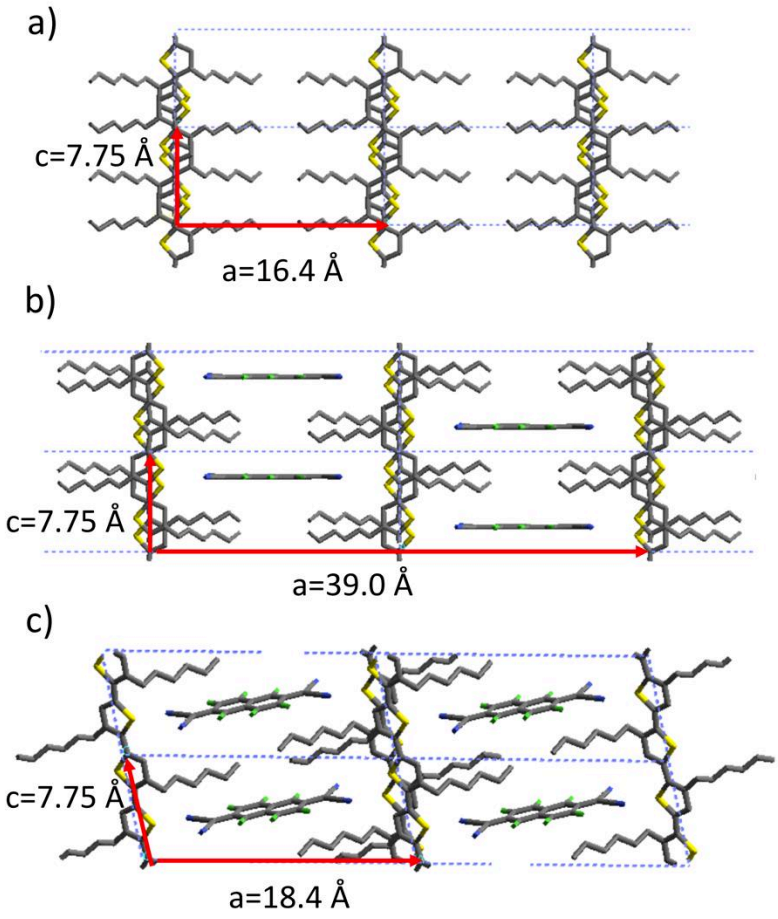


***Figure 11**. **b**-axis projections of the structural models of a) P3HT (form I), ii) the trial structure of P3HT-$F_6$TCNNQ and c) the final refined structure after energy minimization. Hydrogen atoms are omitted for clarity.*

As seen in Figure 11, it is possible to create cavities to host the dopant molecules by translating every second PT backbone along the **c** axis direction to group the side chains in planes that are roughly perpendicular to the polythiophene backbone. The size of the cavities depends on the dopant's dimensions and in particular the long axis of the dopant molecule. A larger dopant should in principle induce a larger lattice expansion along the side chain direction. This is verified in the present case for $F_4$TCNQ and $F_6$TCNNQ that show expanded $d_{100}$ of 18.0 Å and 19.2 Å, respectively. This is consistent with most experimental observations showing that doping induces an extension of the lattice along the **a** axis (alkyl side chain direction). [28]

The trial structure (Figure 11b) is an orthorhombic unit cell that is doubled along the **a** axis direction (side chains) with parameters a=39.0 Å, b=7.8 Å, c=7.75 Å. It contains two dopants at positions (0.25, 0.5, 0.25) and (0.75, 0.5, 0.75). The C2/c space group is suggested from the extinction rules:

$h0l$ with $h+l=2n$

$h00$ with $h=2n$

and $0k0$ with $k=2n$

The calculated ED pattern for this trial structure reproduces very nicely the additional observed reflections indexed as 1 0 1 and 1 0 3 and the intense 0 0 2 reflection.

In a second step, we subjected this trial structure to energy minimization using only van der Waals interactions. The obtained unit cell is triclinic with P1 space group. It is defined by a=38.44 Å, b=8.96 Å, c=7.75 Å, $\alpha$=107.96°, $\beta$=85.5° and $\gamma$=106.25°. This "double" cell is further reduced into a simpler unit cell with P-1 symmetry with |**a**|=18.8 Å, |**b**|=8.95 Å, |**c**|=7.75 Å,

$\alpha$=107.6°, $\beta$=101.5° and $\gamma$=89.3° (see Figure 11.c). The corresponding calculated ED pattern in Figure 9a accounts quite well for the presence of the additional reflections and for the enhanced intensity of the 0 0 2 reflection. The additional reflections in the l=1 layer line are indexed as h 0 1 with h=-2, -1, 0 and 1. This model yields an interlayer spacing $d_{100}$=18.4 Å and a $\pi$-stacking periodicity $d_{020}$=3.45Å in close concordance with the experimental values (see Table 1). The asymmetry in the intensity of the h 0 1 reflections is related to the triclinic character of the unit cell.

Let us describe more precisely the refined structural model. Within $\pi$-stacks, the intercalation of dopants results in i) the increase of the distance between PT backbones along the **b** axis and ii) an increase of the backbone tilt with respect to the **b** axis. Due to this tilt, short intermolecular contacts between PT backbones are possible. PT backbones are contained in 3 2 0 planes with a short 3.46 Å reticular distance corresponding to the apparent $\pi$-stacking distance $d_{020}$. The 2 -2 0 planes containing side chains should also result in a strong reflection. However, this reflection is not observed experimentally because in the real doped structure, 3-hexyl side chains are quite disordered contrary to the ideal calculated model. This disorder possibly accounts also for the larger expansion of the lattice along the side chains with a larger $d_{100}$ due to the non-optimal packing of alkyl side chains.

It is highly instructive to compare the refined structure of $F_6$TCNNQ-doped P3HT with the structure of other doped polythiophenes. Tashiro et al. investigated the structure of P3HT upon doping with iodine.[33] They found that iodine doped P3HT possess a “tunnel” structure due to the incorporation of polyiodide ions such as $I_3^-$ and $I_5^-$ into the layers of the alkyl side chains. Structural modeling indicated that the polyiodide chains are oriented along the **b** axis of P3HT contrary to the present case where the long axis of $F_6$TCNNQ is oriented along the **a**

axis (side chain direction). Most interestingly, as in our case, the introduction of dopants in the unit cell causes a shift of PT chains along the **c**-axis to generate the "cavities" along the **b**-axis wherein dopant anions can be hosted.

Let us also compare the present structure with PEDOT doped with Tos identified by Aasmunsveit et al. and further modeled by Kim and Brédas.[34,35] PEDOT-Tos adopts a lamellar structure with layers of highly π-stacked poly(thiophene) backbones separated by layers of dopants. Interestingly, the stoichiometry of the doped phases of P3HT:$F_6$TCNNQ and of PEDOT:Tos are identical and corresponds to one dopant per four thiophene monomers i.e. a maximum doping concentration of approximately 25%. This stoechiometry is larger than the apparent doping level extracted by UV-vis-NIR absorption spectroscopy (see table 1). This is not surprising since the P3HT films oriented by high-T rubbing at 186°C show a crystallinity of 50-60% and the amorphous phase is poorly doped (no polaron seen for light polarization perpendicular to the chain direction).

***Table 1**. Main structural characteristics of the doped P3HT crystal structures refined from electron diffraction and following energy minimization.*

| Dopant | $F_6$TCNNQ | $F_4$TCNQ |
|---|---|---|
| $d_{020}$ (Å) experimental | 3.55±0.05 | 3.55±0.05 |
| $d_{020}$ (Å) calculated | 3.42 | 3.46 |
| $d_{100}$ (Å) experimental | 19.2 | 18.0 |
| $d_{100}$ (Å) calculated | 18.4 | 17.5 |
| Density (g/cm$^3$) | 1.40 | 1.36 |

| | | |
|---|---|---|
| E (kCal/mol) | -106.9 | -96.6 |

To consolidate this result, we followed the same approach to determine the structure of P3HT/$F_4$TCNQ phase. For $F_4$TCNQ we are equally able to find a stable intercalated structure (see Table 1). The $d_{020}$ and $d_{100}$ periodicities show the same evolution upon doping with $F_4$TCNQ as for $F_6$TCNNQ: reduction of $\pi$-stacking distance and expansion along the alkyl side chain direction. However, there is one major difference between $F_4$TCNQ and $F_6$TCNNQ-doped structures, namely the h 0 1 reflections seen for $F_6$TCNNQ are absent in the case of $F_4$TCNQ. For $F_4$TCNQ-doped P3HT, one can only evidence the enhanced intensity of the 0 0 2 and the changes in lattice dimensions. The difference in the ordering of $F_4$TCNQ and $F_6$TCNNQ in the P3HT crystal is possibly a reason for this. Indeed, polarized UV-vis-NIR spectroscopy evidences a better ordering of $F_6$TCNNQ as compared to $F_4$TCNQ. Following the recent work by Vijayakumar et al., it has been shown that $F_4$TCNQ diffuses more readily into the $C_{12}$-PBTTT film than $F_6$TCNNQ.[22] As a consequence, $F_6$TCNNQ was also better ordered in the $C_{12}$-PBTTT lattice than $F_4$TCNQ due to a slower diffusion constant. Moreover, the diffusion of $F_4$TCNQ is substantially faster in P3HT than $C_{12}$-PBTTT (diffusion times are of the order of a few seconds for P3HT and 40-50s for $C_{12}$-PBTTT). Accordingly, both ED and spectroscopy results clearly suggest larger disorder in the intercalated $F_4$TCNQ than $F_6$TCNNQ.

More generally, for both dopants, the structure found in the films is much more disordered than the ideal model retrieved from ED analysis. In particular, streaking in the ED pattern along the **a** axis is clear evidence for disorder in the arrangement of successive (b,c) planes of stacked PTs.

To conclude, electron diffraction provides compelling evidence for the presence of dopant molecules inside the unit cell of P3HT. Dopants are intercalated in the layers of alkyl side chains in a plane perpendicular to the polythiophene chains. Rearrangement of P3HT chains generates two cavities within a doubled unit cell that can host two dopant molecules. The question is why the same structural features i.e. the presence of additional reflections in the l=1 layer are not observed in the case of $F_4$TCNQ? To answer this question, we used polarized UV-vis-NIR spectroscopy and more precisely angular dependent spectroscopy to try to quantify the ordering of dopants inside the P3HT host matrix.

## II.4 Probing the ordering of $F_4$TCNQ and $F_6$TCNNQ dopants in the polymer matrix of P3HT using polarized UV-vis-NIR spectroscopy.

We wanted to investigate how both dopant molecules are oriented with respect to the polymer backbone in case of $F_4$TCNQ and $F_6$TCNNQ. Therefore, polarized UV-vis-NIR spectra of aligned P3HT films were recorded as a function of the angle between the P3HT chain direction (rubbing direction) and the direction of the light polarization. Figure 12a,b show the two sets of polarized UV-vis recorded every 10° between the polarizer and the rubbing direction within the range between 0° - 90°. To extract the angular dependence of the dopant's absorption, we used a multipeak analysis to remove the underlying polaronic contributions (see experimental section).

Figure 13a and 13b show the absorption of the $F_4$TCNQ and $F_6$TCNQ anions, respectively, versus orientation of the sample to the light polarization after subtraction of the underlying polaronic baseline.

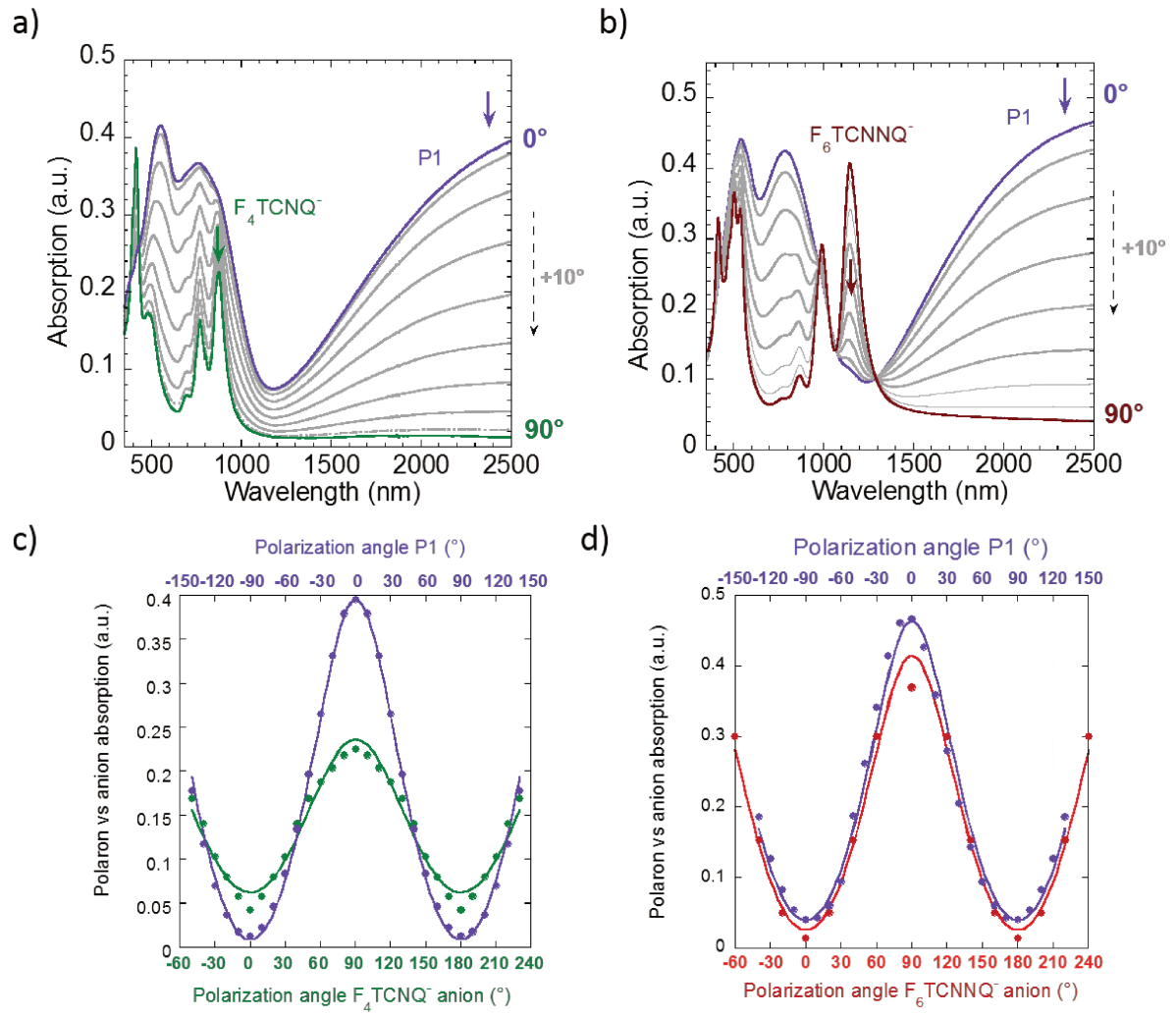


***Figure 12**: a) and b) Polarized UV–Vis–NIR absorption spectra of oriented conducting P3HT films doped with $F_4$TCNQ and $F_6$TCNNQ as a function of the polarization angle measured with respect to the rubbing direction* **R**. *0° corresponds to the incident light polarized parallel to the rubbing direction (POL* ∥ **R**, *in red) whereas 90° corresponds to the incident light polarized perpendicular to the rubbing direction (POL* ⊥ **R** *in blue). c), d) - Angular dependence of the absorbance of the P1 polaron band at 2500 nm (in purple), and of the dopant anion band at 873 nm (in green) for $F_4TCNQ^-$ (c)and 1138 nm (in red) for the*

*$F_6TCNNQ^-$ (d). The continuous lines correspond to the fit following the equation given in the previous chapter.*

Figure 13.c exemplifies the result of a multipeak fitting to extract the $F_4TCNQ^-$ absorbance at a given angle. A similar procedure of peak deconvolution was reported earlier by Wang et al.[24] Comparing the values of polaronic peak positions in the current work on oriented films and work of Wang et al. on non-oriented samples - the values are consistent with ref[24]. It is based on four components: P1 at 0.44 eV, P2 at 1.53 eV, N (neutral P3HT) at 2.54 eV and a $F4TCNQ^-$ band (D) at 3.00 eV. The sum of these four bands is represented in blue (see Figure 13c). It is the baseline that is subsequently subtracted from the experimental spectra. Although the peak deconvolution is not perfect, it allows to remove most of the P2 absorption band from the $F_4TCNQ^-$ contribution in the range of 1-2 eV.

The two graphs in Figure 12c and d depict the angular dependence of the polaron (P1 peak at 2500 nm) and the anion absorption for $F_4$TCNQ and $F_6$TCNNQ-doped films, respectively. The anion absorptions at 873 nm ($F_4TCNQ^-$) and 1138 nm ($F_6TCNNQ^-$) for each angular position are obtained by subtracting the polaronic contribution of P3HT (see Figure 13.c).

Most telling is the comparison of the order parameter extracted for the polaron and for the anions of $F_4$TCNQ and $F_6$TCNNQ (see Table 2). The OP of the polaron is a measure of the *in-plane* orientation of polymer chains in the rubbed and doped films whereas the OP of the dopants gives an idea of the way the dopants are oriented with respect to the polymer crystals when intercalated in the layers of alkyl side chains.

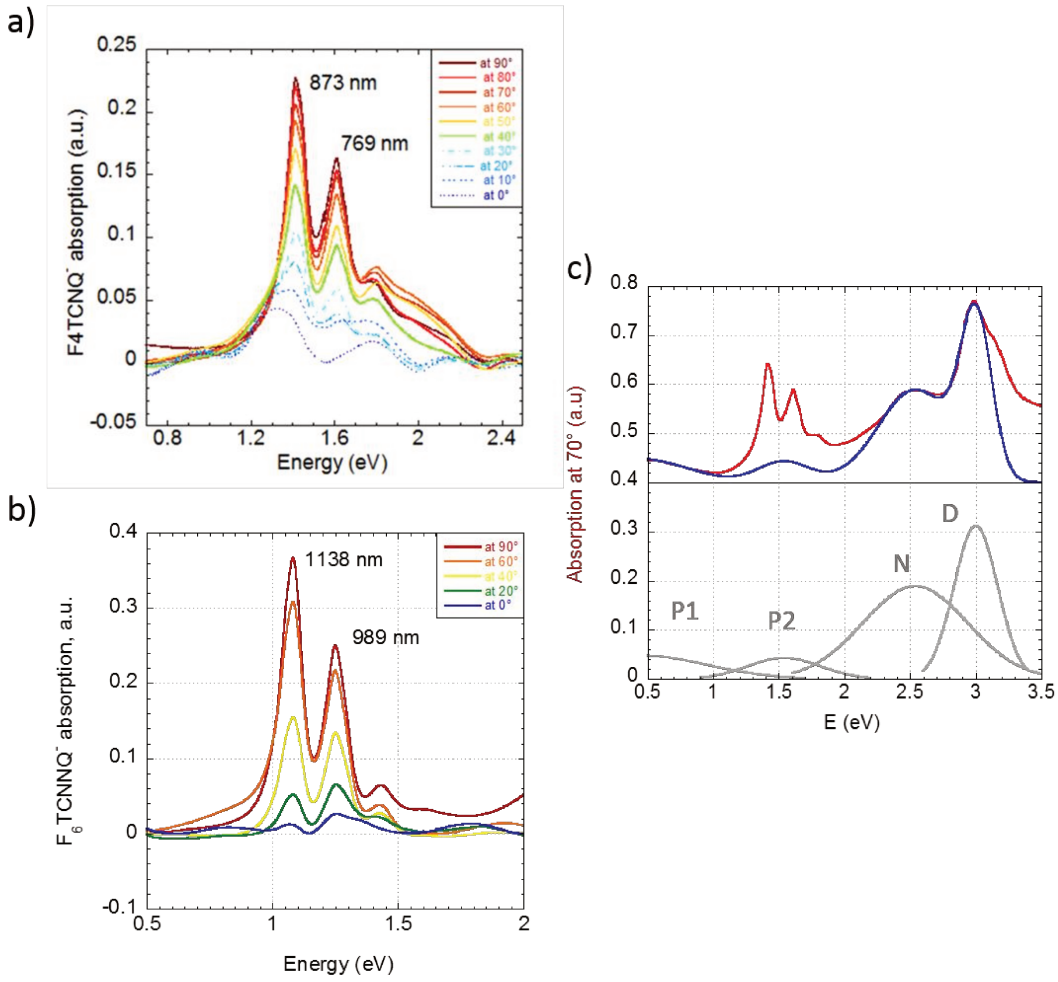


***Figure 13**: a) Angular dependence of the anion absorption band (873 nm) in the $F_4$TCNQ-doped P3HT films ($T_R$=186°C) after deconvolution and subtraction of underlying P1, P2, N and D components. The spectra are recorded every 10°. The angle of light polarization is measured with respect to the rubbing direction. b) Angular dependence of the anion absorption band (1138 nm) in the $F_6$TCNNQ-doped P3HT films after deconvolution and subtraction of underlying P1, P2, N and D components. The spectra are recorded every 20°. The angle of light polarization is measured with respect to the rubbing direction. c) Example of the deconvolution of a polarized UV-Vis spectrum of P3HT/$F_4$TCNQ for a polarization angle of 70° between the rubbing direction and the light polarization. The recorded spectrum is shown in red. A multiple peak fitting, shown in grey is used (0.3-3.5 eV).*

Similar OPs for anion and polaron bands suggest that the orientation of the dopant follows quite strictly the orientation of the side chains perpendicular to the PT backbones. The values of the OP in Table 2 show a simple trend: for $F_6$TCNNQ, the OPs of polaron and anion are almost identical whereas they are substantially different for the $F_4TCNQ^-$ anions. This suggests that $F_4$TCNQ anions are oriented in a more random manner in the P3HT lattice (see schematic illustration of the $F_4$TCNQ and $F_6$TCNNQ molecules orientation with respect to the polymer backbone in Figure 14). Accordingly, the intercalation of $F_6$TCNNQ seems to lead to a more ordered structure of the doped phase of P3HT than for $F_4$TCNQ (see Figure 14).

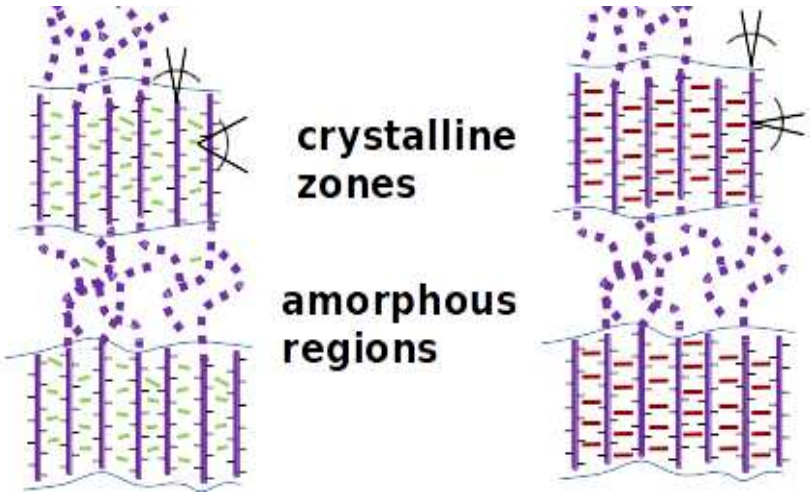


***Figure 14**. Schematic illustrations of the difference in mutual arrangement between the polymer and both $F_4$TCNQ (left) and $F_6$TCNNQ(right) dopant molecules hosted in the P3HT side chain layers of the semi-crystalline structure.*

This is consistent with the results of TEM showing well-defined additional reflections, accounting for a regular lattice of P3HT/$F_6$TCNNQ. The absence of *h 0 1* reflections for $F_4$TCNQ

is therefore a fingerprint for a more disordered intercalation of the dopants in the unit cell of P3HT, consistent with the results obtained from polarized UV-vis-NIR spectroscopy. In the case of $F_4$TCNQ, the angular distribution is larger, whereas in case of $F_6$TCNNQ the degree of orientation is high as evidenced by similar OP of polymer and the dopant (see Table 2).

It is worth to note that a similar effect has been observed for doped $C_{12}$-PBTTT films.[22] The lower ordering of $F_4$TCNQ was explained by the fact that the diffusion coefficient of this dopant in the polymer film is almost one order of magnitude larger as compared to $F_6$TCNNQ. A faster diffusion of $F_4$TCNQ could accordingly explain the more disordered distribution of the dopant orientation in the side chain layers of P3HT.

***Table 2**: Main characteristics of oriented P3HT films doped with $F_4TCNQ^-$ and $F_6TCNNQ^-$.*

| Main characteristics of both phases | P3HT:$F_4$TCNQ | P3HT:$F_6$TCNNQ |
|---|---|---|
| Order parameter polaron | 0.91 | 0.78 |
| Order parameter anion | 0.62 | 0.82 |
| $d_{020}$ π-stacking distance (Å) | 3.6 | 3.6 |
| $d_{100}$ alkyl side chains separation (Å) | 18.1 | 19.2 |
| Estimated $F_4$TCNQ molecules per 100 thiophene units | 14 | 20 |
| Charge conductivity $\sigma_{//}$ max (S cm$^{-1}$) | 205 | 343 |
| Power factor $PF_{//}$ max (μW m$^{-1}$ K$^{-2}$) | 73 | 79 |

**II.5 Resulting thermoelectrical properties of doped films.**

Finally, we evaluated the impact of the structural evolution with doping concentration on the charge conductivity and thermopower. Figure 15 features the evolution of the charge conductivity, Seebeck coefficient and power factor as a function of dopant concentration for aligned P3HT films doped with $F_4$TCNQ and $F_6$TCNNQ. In the case of $F_4$TCNQ, the conductivity saturates already for 1 g/l reaching 205 S/cm, whereas for $F_6$TCNNQ the conductivity is almost saturated at 10 g/l at 343 S/cm. The larger conductivity for $F_6$TCNNQ is consistent with the slightly larger oxidation level evidenced by UV-vis-NIR spectroscopy (see Figure 5d) and the larger dopant concentration extracted from UV-vis-NIR absorption spectroscopy. The same trend is observed in the perpendicular direction, the charge conductivity $\sigma_{\perp}$ reaches its maximum at 20 S/cm and 70 S/cm for $F_4$TCNQ and $F_6$TCNNQ, respectively. It is worth to note that the conductivity reached here for $F_4$TCNQ is larger than the previous one reported in reference 28 (150 S/cm) due to the use of the ICD doping method.

Regarding the Seebeck coefficient, it tends to decrease with increasing dopant concentration. This dependence looks pretty similar for both dopant molecules reaching the values of 50 μV/K and 12 μV/K parallel and perpendicular to the rubbing direction, respectively. The anisotropy of conductivity is always larger than that of the Seebeck coefficient which is quite consistent with previous studies.[28,29,36] Figure 16a shows the evolution of the anisotropy in charge conductivity for both systems versus dopant concentration. In general, the anisotropy in conductivity is larger for $F_4$TCNQ than for $F_6$TCNNQ. Conversely, Figure 16b demonstrates that the anisotropy of the Seebeck coefficient depends little on the doping level and is quite constant around 4 for both systems.

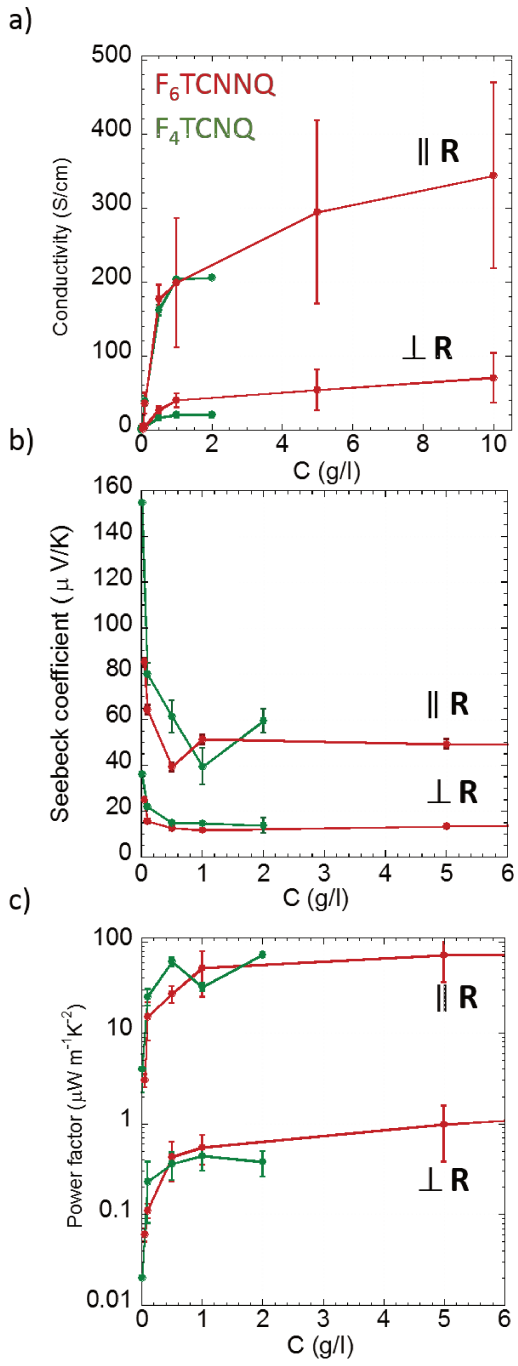


***Figure 15:*** *Evolution of the a) charge conductivity, b) Seebeck coefficient, and c) power factor in oriented semi-crystalline P3HT films ($T_R$=186°C) doped with $F_4$TCNQ (green)/ $F_6$TCNNQ (dark red). The measurements are performed in the direction parallel (∥) and perpendicular (⊥) to the rubbing **R**. The error bars are essentially related to a sample dispersion in alignment degree.*

A lower anisotropy of charge transport in $F_6$TCNNQ-doped films may indicate that charges can hop more readily between successive layers of π-stacked PT backbones. This seems first in contradiction with the fact that the lattice expansion along the alkyl side chains is stronger upon intercalation of $F_6$TCNNQ than $F_4$TCNQ. The observed trend in charge transport anisotropy may indicate a stronger coupling between successive PT layers through the intercalated $F_6$TCNNQ dopants as compared to $F_4$TCNQ. It is still unclear to what extent interchain transport can be mediated via the π-electron system of the intercalated dopants. Inter-chain coupling between polarons has been proposed in the analysis of polaronic charge transport in conducting polymers by Zuppiroli et al. [37]

Regarding the power factor PF for both systems, similar trends are observed for both dopants. The larger conductivity for P3HT films doped with $F_6$TCNNQ is not sufficient to counter-balance the reduction of the Seebeck factor. The PF values of $F_6$TCNNQ-doped samples saturate at 5g/l reaching the values of around 72 μW $m^{-1}$ $K^{-2}$ and 1 μW $m^{-1}$ $K^{-2}$ in parallel and perpendicular directions to the rubbing, respectively.

Accordingly, while improved dopant ordering is likely the reason for the improved charge conductivity for $F_6$TCNNQ, it is not sufficient to improve TE properties in thin films.

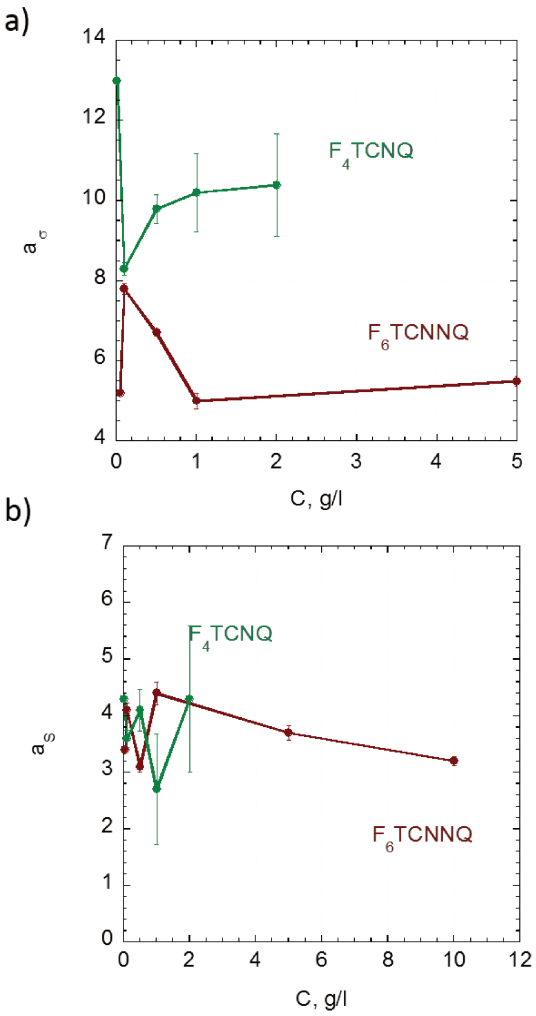


***Figure 16.*** *Anisotropy of the charge conductivity $\sigma_{//}/\sigma_{\perp}$ (a) and of the Seebeck coefficient $S_{//}/S_{\perp}$ (b) as a function of the dopant concentration for oriented P3HT films doped with $F_4$TCNQ and $F_6$TCNNQ.*

## III. Conclusions

Combining polarized UV-vis-NIR spectroscopy and electron diffraction analysis helps give clear-cut evidence for the intercalation of $F_4$TCNQ and $F_6$TCNNQ dopants in the crystal lattice of P3HT. Differences in doping mechanism have been highlighted. $F_6$TCNNQ is intercalated in a more ordered manner as compared to $F_4$TCNQ. A tentative structural model based on ED analysis is proposed for P3HT:$F_6$TCNNQ leading to a triclinic structure with $P_{-1}$ symmetry (a = 18.8 Å, b = 8.95 Å, c = 7.75 Å, $\alpha$=107.6°, $\beta$ = 101.5° and $\gamma$ = 89.3°). The structure of doped P3HT bears similarity with the structure of PEDOT-Tos in terms of P3HT/dopant stoichiometry which is consistent with the doping level extracted from absorbance measurements. Despite larger charge conductivities for $F_6$TCNNQ, the power factors remain similar for both dopants and close to 79 $\mu W\ m^{-1}\ K^{-2}$ at the maximum. This study demonstrates that highly ordered P3HT/dopant intercalates can be prepared by sequential doping. The level of ordering of dopants in the polymer crystals might be further improved by playing on the kinetics of dopant diffusion or the geometry of the dopants. Adapting the dopant dimensions to the possible cavities in the layers of side-chains in the P3HT lattice might be an interesting strategy for highly ordered P3HT/dopant intercalates. In this respect, the choice of rod-like dopants such as $F_6$TCNNQ might be more adapted to fabricate ordered intercalates with respect bulky “spherical” dopants such as Mo(tfd-$COCF_3$)$_3$.

Beyond the importance of dopant intercalation in the possibility to reach large charge conductivities, this study opens the question relative to the change of the thermal conductivity of the lattice. Possibly, the intercalation of long and rigid dopants could rigidify the polymer lattice through enhanced Coulombic interactions between successive layers of

π-stacked PTs, hence, it could increase the corresponding thermal conductivity of the doped polymers. It will be of high importance to evaluate the changes in thermal conductivity associated with dopant intercalation in general.

**References:**

[1] Ogawa S., *Organic Electronics* **2015**, *Springer Japan*, 1.

[2] M. Goel, M. Thelakkat, *Polymer Thermoelectrics: Opportunities and Challenges*, Vol. 53, AMER CHEMICAL SOC, 1155 16TH ST, NW, WASHINGTON, DC 20036 USA, **2020**, pp. 3632–3642.

[3] V. Vijayakumar, E. Zaborova, L. Biniek, H. Zeng, L. Herrmann, A. Carvalho, O. Boyron, N. Leclerc, M. Brinkmann, *ACS Appl. Mater. Interfaces* **2019**, *11*, 4942.

[4] R. Kroon, D. Kiefer, D. Stegerer, L. Yu, M. Sommer, C. Müller, *Adv Mater* **2017**, *29*, 1700930.

[5] I. E. Jacobs, A. J. Moulé, *Adv. Mater.* **2017**, *29*, 1703063.

[6] O. Bubnova, X. Crispin, *Energy Environ. Sci.* **2012**, *5*, 9345.

[7] J. E. Cochran, M. J. N. Junk, A. M. Glaudell, P. L. Miller, J. S. Cowart, M. F. Toney, C. J. Hawker, B. F. Chmelka, M. L. Chabinyc, *Macromolecules* **2014**, *47*, 6836.

[8] S. N. Patel, M. L. Chabinyc, *J Appl Polym Sci* **2017**, *134*, 44403.

[9] S. N. Patel, A. M. Glaudell, K. A. Peterson, E. M. Thomas, K. A. O'Hara, E. Lim, M. L. Chabinyc, *Sci. Adv.* **2017**, *3*, e1700434.

[10] I. E. Jacobs, E. W. Aasen, J. L. Oliveira, T. N. Fonseca, J. D. Roehling, J. Li, G. Zhang, M. P. Augustine, M. Mascal, A. J. Moulé, *J Mater Chem C* **2016**, *4*, 3454.

[11] J. Hynynen, D. Kiefer, C. Müller, *RSC Adv* **2018**, *8*, 1593.

[12] D. T. Scholes, P. Y. Yee, J. R. Lindemuth, H. Kang, J. Onorato, R. Ghosh, C. K. Luscombe, F. C. Spano, S. H. Tolbert, B. J. Schwartz, *Adv Funct Mater* **2017**, *27*, 1702654.

[13] D. T. Scholes, S. A. Hawks, P. Y. Yee, H. Wu, J. R. Lindemuth, S. H. Tolbert, B. J. Schwartz, *J. Phys. Chem. Lett.* **2015**, *6*, 4786.

[14] D. T. Scholes, P. Y. Yee, J. R. Lindemuth, H. Kang, J. Onorato, R. Ghosh, C. K. Luscombe, F. C. Spano, S. H. Tolbert, B. J. Schwartz, *Adv. Funct. Mater. 27*, 1702654.

[15] R. Kroon, D. A. Mengistie, D. Kiefer, J. Hynynen, J. D. Ryan, L. Yu, C. Müller, *Chem. Soc. Rev.* **2016**, *45*, 6147.

[16] A. M. Glaudell, J. E. Cochran, S. N. Patel, M. L. Chabinyc, *Adv Energy Mater* **2015**, *5*, 1401072.

[17] P. Pingel, D. Neher, *Phys. Rev. B* **2013**, *87*, 115209.

[18] Y. Karpov, T. Erdmann, M. Stamm, U. Lappan, O. Guskova, M. Malanin, I. Raguzin, T. Beryozkina, V. Bakulev, F. Günther, S. Gemming, G. Seifert, M. Hambsch, S. Mannsfeld, B. Voit, A. Kiriy, *Macromolecules* **2017**, *50*, 914.

[19] M. Tietze, L. Burtone, M. Riede, B. Lüssem, K. Leo, *Phys. Rev. B* **2012**, *86*, 035320.

[20] E. Lim, K. A. Peterson, G. M. Su, M. L. Chabinyc, *Chem. Mater.* **2018**, *30*, 998.

[21] V. Vijayakumar, Y. Zhong, V. Untilova, M. Bahri, L. Herrmann, L. Biniek, N. Leclerc, M. Brinkmann, *Adv. Energy Mater. 0*, 1900266.

[22] Vijayakumar V., Durand P., Zeng H., Untilova V., Herrmann L., Algayer P., Leclerc N., Brinkmann M., *Journal of Materials Chemistry C* **2020**, *under review*.

[23] D. T. Duong, C. Wang, E. Antono, M. F. Toney, A. Salleo, *Org. Electron.* **2013**, *14*, 1330.

[24] C. Wang, D. T. Duong, K. Vandewal, J. Rivnay, A. Salleo, *Phys. Rev. B* **2015**, *91*, 085205.

[25] M. Mladenović, N. Vukmirović, *J. Phys. Chem. C* **2015**, *119*, 23329.

[26] J. Hynynen, E. Järsvall, R. Kroon, Y. Zhang, S. Barlow, S. R. Marder, M. Kemerink, A. Lund, C. Müller, *ACS Macro Lett.* **2019**, *8*, 70.

[27] V. Untilova, J. Hynynen, A. I. Hofmann, D. Scheunemann, Y. Zhang, S. Barlow, M. Kemerink, S. R. Marder, L. Biniek, C. Müller, M. Brinkmann, *Macromolecules* **2020**.

[28] A. Hamidi-Sakr, L. Biniek, J.-L. Bantignies, D. Maurin, L. Herrmann, N. Leclerc, P. Lévêque, V. Vijayakumar, N. Zimmermann, M. Brinkmann, *Adv. Funct. Mater.* **2017**, *27*, 1700173.

[29] V. Untilova, T. Biskup, L. Biniek, V. Vijayakumar, M. Brinkmann, *Macromolecules* **2020**.

[30] J. Hynynen, D. Kiefer, L. Yu, R. Kroon, R. Munir, A. Amassian, M. Kemerink, C. Müller, *Macromolecules* **2017**, *50*, 8140.

[31] A. Hamidi-Sakr, L. Biniek, S. Fall, M. Brinkmann, *Adv. Funct. Mater.* **2015**, *26*, 408.

[32] N. Kayunkid, S. Uttiya, M. Brinkmann, *Macromolecules* **2010**, *43*, 4961.

[33] K. Tashiro, M. Kobayashi, T. Kawai, K. Yoshino, *Polymer* **1997**, *38*, 2867.

[34] K. E. Aasmundtveit, E. J. Samuelsen, O. Inganäs, L. A. A. Pettersson, T. Johansson, S. Ferrer, *Synth. Met.* **2000**, *113*, 93.

[35] E.-G. Kim, J.-L. Brédas, *J. Am. Chem. Soc.* **2008**, *130*, 16880.

[36] D. Scheunemann, V. Vijayakumar, H. Zeng, P. Durand, N. Leclerc, M. Brinkmann, M. Kemerink, *Adv. Electron. Mater.* **2020**, *6*, 2000218.

[37] L. Zuppiroli, S. Paschen, M. N. Bussac, *Proc. Int. Conf. Sci. Technol. Synth. Met.* **1995**, *69*, 621.

# Chapter 4. High thermoelectric power factor of poly(3-hexylthiophene) through in-plane alignment and doping with a molybdenum dithiolene complex

## I. Introduction

Conjugated polymers currently receive considerable attention as thermoelectric materials because they are composed of abundant elements and offer ease of processing, low weight and mechanical robustness.[1–3] The thermoelectric efficacy of a material can be described by either the dimensionless figure of merit $ZT = \alpha^2\sigma T/\kappa$ or the power factor $\alpha^2\sigma$, where $\alpha$ is the Seebeck coefficient, $\sigma$ and $\kappa$ the electrical and thermal conductivites and $T$ the absolute temperature. Power factors reported for unoriented conjugated polymers now reach values of $10^2$ μW m$^{-1}$ K$^{-2}$,[4–8] and in case of aligned materials more than $10^3$ μW m$^{-1}$ K$^{-2}$.[9,10] The majority of studies focuses on polythiophenes because they are widely available and can be synthesized with a wide range of molecular weights, side-chain lengths and regioregularities. As a result, polythiophenes are ideal for elucidating fundamental structure-property relationships that underpin the thermoelectric performance of conjugated polymers. The archetypal semi-crystalline conjugated polymer is poly(3-hexylthiophene) (P3HT), which has been employed as a model system in a considerable number of studies related to organic thermoelectrics. However, so far, the highest thermoelectric power factor reported for P3HT has remained well below $10^2$ μW m$^{-1}$ K$^{-2}$ (see Table 1), as a result of which many researchers question the relevance of structure-property relationships established with this material.

The power factor of a wide range of organic materials approximately scales according to the empirical power law PF= $\alpha^2\sigma \propto \sqrt{\sigma}$.[11–13] Hence, the majority of strategies for increasing the power factor focus on improving the electrical conductivity, which is given by:

$$\sigma = N_v \cdot \mu \cdot e \quad (1)$$

where $N_v$ and $\mu$ are the density and mobility of charge carriers, and $e$ is the elementary charge.

Charges are created through molecular doping, i.e. dopant molecules are added to the semiconductor, which in case of p-doping take up an electron, leaving a hole behind. To reach a high conductivity it is paramount that the fraction of mobile charges created per dopant molecule is as high as possible. However, hole-anion pairs generated upon doping remain Coulombically bound to each other meaning that most charges are unable to contribute to transport.[14,15] For instance, Pingel and Neher concluded that only 5% of charges contribute to transport in P3HT doped with the small-molecular dopant 2,3,5,6-tetrafluoro-7,7,8,8-tetracyanoquinodimethane ($F_4$TCNQ).[14] Several studies have recently shown that the size of the dopant molecule has a pronounced impact on the electrical conductivity of p-doped P3HT.[16,17] Liang et al. found that the use of large molybdenum dithiolene complexes, which have a diameter of 11-14 Å, promotes delocalization of the polaron.[17] Further, Aubry et al. were able to effectively shield the hole polaron from its anion through the use of a large dodecaborane-based dopant with a diameter of 20 Å, which boosts the fraction of mobile charge carriers. [16]

In addition to ensuring a high number of mobile charges, it is important that the nanostructure of the polymer enables a high charge-carrier mobility. For molecularly doped P3HT the electrical conductivity strongly depends on the crystallinity of the polymer.[12,18] Furthermore, uniaxial alignment has been widely explored as a tool to enhance the electrical

conductivity and power factor in one direction. Qu et al. used directional epitaxial crystallization of P3HT with help of 1,3,5-trichlorobenzene, followed by doping with $Fe(TFSI)_3$ to reach a power factor of 38 μW $m^{-1}$ $K^{-2}$.[19] Further, some of us have used tensile drawing of bulk samples[20] or high-temperature rubbing of thin films[9,21] to orient P3HT, achieving a power factor of 16, 21 and 56 μW $m^{-1}$ $K^{-2}$ upon subsequent doping with $Mo(tfd\text{-}COCF_3)_3$, $FeCl_3$, and $F_4TCNQ$, respectively (see Table 1).

**Table 1.** Selected literature values for the thermoelectric properties of P3HT at room temperature; [a]for oriented samples highest reported values measured along the direction of alignment are given.

| **dopant** | **alignment**[a] | $\sigma$ (S $cm^{-1}$) | $\alpha$ (μV $K^{-1}$) | $\alpha^2\sigma$ (μW $m^{-1}$ $K^{-2}$) | **ref.** |
|---|---|---|---|---|---|
| $Fe(TFSI)_3$ | no | 87 | 48 | 20 | Zhang et al.[22] |
| $Fe(TFSI)_3$ | yes | 251 | 39 | 38 | Qu et al.[19] |
| $F_4TCNQ$ | no | 12.7 | 46 | 2.7 | Hynynen et al.[12] |
| $F_4TCNQ$ | no | 48 | 85 | 27 | Lim et al.[23] |
| $F_4TCNQ$ | yes | 22 | 60 | 8.5 | Hamidi-Sakr et al.[21] |
| $F_4TCNQ$ | yes | 160 | 59 | 56 | Untilova et al.[24] |
| $Mo(tfd\text{-}COCF_3)_3$ | yes | 12.7 | 112 | 16 | Hynynen et al. [20] |
| $Mo(tfd)_3$ + $FeCl_3$ | no | 68.5 | 8.1 | 4.7 | Liang et al.[17] |

| | | | | | |
|---|---|---|---|---|---|
| $FeCl_3$ | no | 42 | 105 | 46 | Jung et al.[6] |
| $FeCl_3$ | yes | 570 | 5.4 | 21 | Vijayakumar et al.[9] |
| FTS | no | 27.7 | 60 | 10 | Glaudell et al.[11] |

Here, we combine the aforementioned strategies with the aim of increasing the thermoelectric power factor that can be achieved with P3HT. To increase the order of the polymer, we chose to employ high-temperature rubbing, a technique that allows the preparation of highly aligned polymer films with an effective thickness of a few tens of nanometers. As the dopant we selected the molybdenum dithiolene complex Mo(tfd-$COCF_3$)$_3$ (see Figure 1 for chemical structure), which due to a high electron affinity EA ~ 5.6 eV[25,26] offers a large driving force for oxidation of P3HT.

## II. Results and Discussion

### II.1 Low electron affinity molybdenum-based dopant

The organic p-dopant, $Mo(tfd\text{-}COCF_3)_3$ used in this study is a soluble version of the dopant $Mo(tfd)_3$.[26,27] Both of them exhibiting a low electron affinity ~5.6 eV were shown to be effective and stable p-doping agents.[20,27]

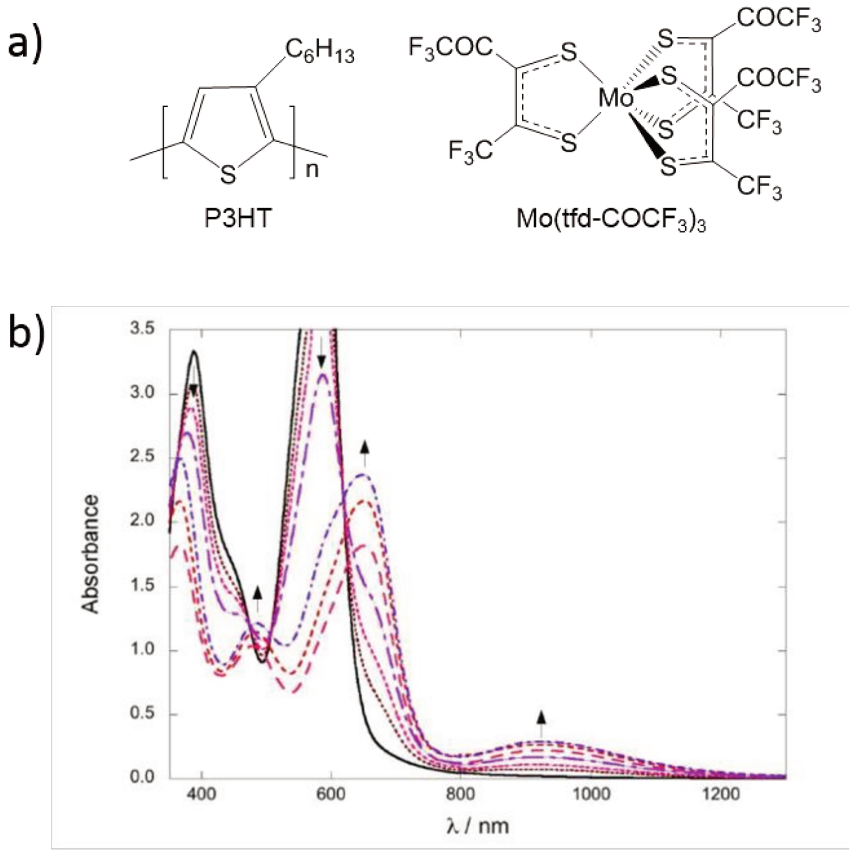


***Figure 1.*** *a) Chemical formulae of P3HT $Mo(tfd\text{-}COCF_3)_3$ on top, b) the spectra showing the neutral (black curve) and reduced by ferrocene forms of $Mo(tfd)_3$. Reproduced from ref.*[28]

Figure 1 illustrates the chemical structure of Mo(tfd-$COCF_3$)$_3$. Figure 1b depicts the spectra of the neutral and reduced forms (ferrocene fis used in the solution of $CH_2Cl_2$ as reported by Qi et al.). Reduction of the complex with ferrocene leads to the disappearance of the absorption peaks at 584 nm and 390 nm of the neutral form and their replacement by a few relatively weak peaks around 484, 650, and 920 nm. The maximum of absorbance of $Mo(tfd)_3^-$ is located at 650 nm and is superposed with ferrocenium ion absorption at 629 nm.[28]

### II.2 Film fabrication and doping procedure

Both oriented and isotropic films were prepared by sequential doping. Isotropic films were prepared by doctor-blading a hot polymer solution. Oriented samples were prepared by high-temperature rubbing at 186 °C (see Experimental section and refs for details[21,29,30]). Doping was carried out by drop-casting solutions of Mo(tfd-$COCF_3$)$_3$ in 1:1 acetonitrile:chloroform (AcN:$CHCl_3$) onto rubbed and/or doctor-bladed P3HT films. We used an AcN:$CHCl_3$ solvent mixture because it resulted in a higher degree of doping than AcN solutions ($CHCl_3$ would dissolve P3HT). The use of such a mixture allows to better dope the amorphous part of the film. The dopant solution was allowed to remain on top of the film for 3 min, followed by spinning off the excess solution (see experimental section for details).

### II.3 Effect of rinsing

First of all, we verified whether the excess dopant on top of the film upon doping should be rinsed or not. We performed UV-Vis-NIR measurements as well as electron diffraction and conductivity measurements on oriented P3HT films doped by Mo(tfd-$COCF_3$)$_3$ before and after rinsing the excess dopant by simply dipping the doped films into acetonitrile (AcN).

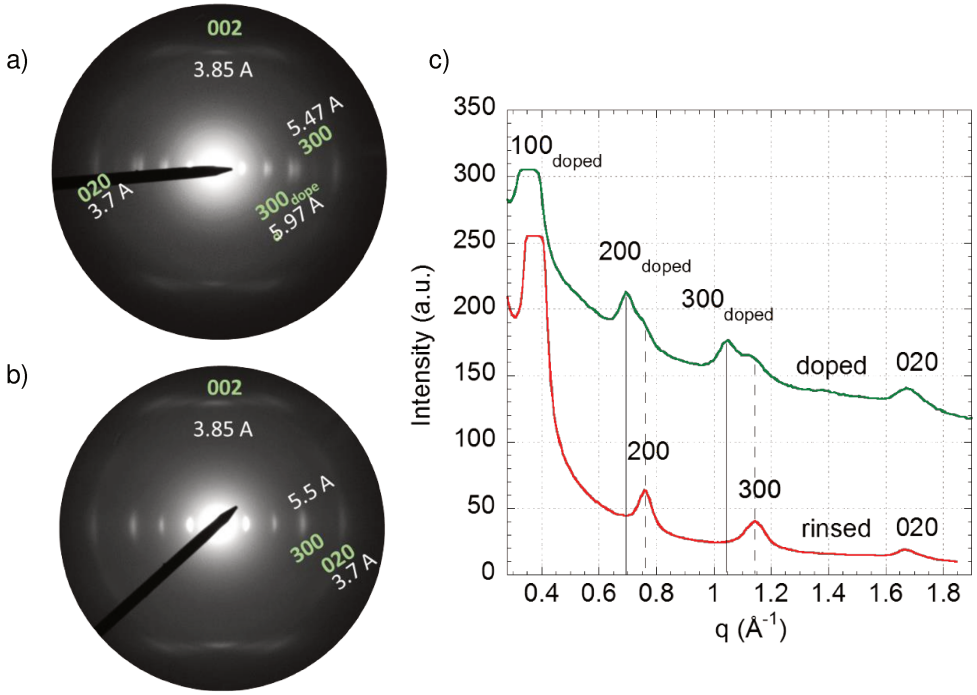


***Figure 2**. Electron diffraction (ED) patterns of rubbed and Mo(tfdCOCF$_3$)$_3$-doped P3HT film (a) before and (b) after rinsing the doped film with AcN. (c) Section profiles of ED patterns along the equator indicating doubling of the h 0 0 reflections due to the presence of two populations of crystallites (green curve); upon rinsing the ED pattern returns to the neat P3HT form (red curve).*

Figure 2 depicts electron diffraction patterns of doped and rinsed films (Figure 2 a, b) as well as the section profiles along the equator (Figure 2c). Interestingly, rinsing of as-doped samples with AcN reverts the diffraction pattern to that of neat undpoed P3HT (Figure 2c). Figure 3 depicts the spectra of doped (violet solid line) and rinsed (dashed line) films: the polaron intensity is significantly reduced upon rinsing. Rinsing removes the neutral excess dopant on top of the film and reduces the oxidation level as indicated by an increase in the neutral polymer absorbance (Figure 3). Regarding the electrical conductivity, films doped by 2.5 g/l solution exhibited conductivites in the direction parallel to rubbing of ~598 S/cm which was immediately reduced to ~205 S/cm upon rinsing with AcN leading to a threefold reduction in electrical conductivity. Analysis of the P2 absorbance band indicates a slight reduction in charge-carrier density to $N_v \sim (3.3 \pm 0.4) \cdot 10^{26}$ m$^{-3}$ (see the subsection II.6 for details). We argue that the dopant that remains after rinsing is only located in amorphous regions. Therefore, in further experiments films were doped without rinsing due to the apparent detrimental effect of the rinsing procedure that obviously dedopes the crystalline domains of P3HT.

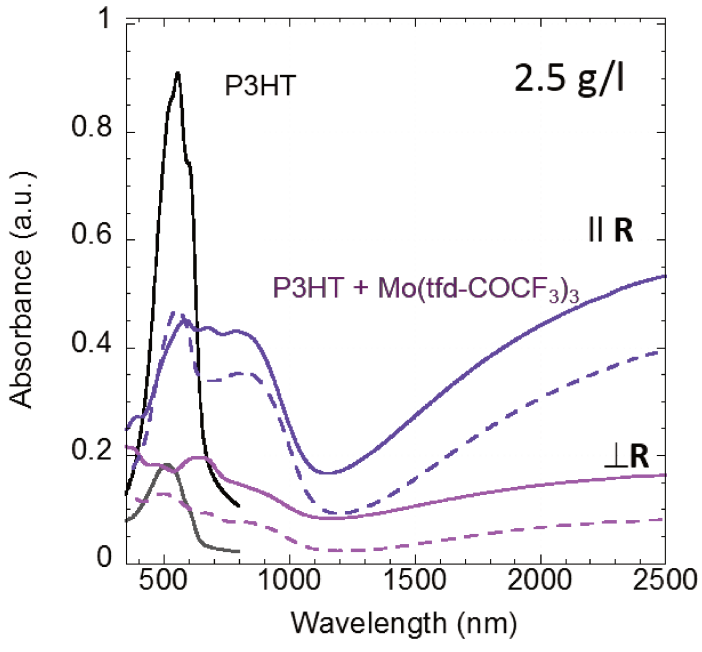


***Figure 3.*** *Polarized UV-vis-NIR absorbance spectra of rubbed P3HT (black), rubbed P3HT doped with $c_{Mo}$ ~2.5 g L$^{-1}$ Mo(tfd-COCF$_3$)$_3$ (violet solid line) and the same doped film after rinsing with AcN (violet dashed line) measured parallel (||) (violet) and perpendicular (⊥) (purple) to the rubbing direction; rinsing with AcN*

*reduces the charge-carrier concentration from $N_v$ ~(3.6 ±0.4)·10$^{26}$ m$^{-3}$ to (3.3 ±0.4)·10$^{26}$ m$^{-3}$ and leads to an increase in the neutral polymer absorbance at 550 nm. Note the decrease in the vertical offset of the UV-vis-NIR spectra upon rinsing with AcN, which we explain with removal of excess dopant from the top of the film.*

### II.4 Structural changes upon doping

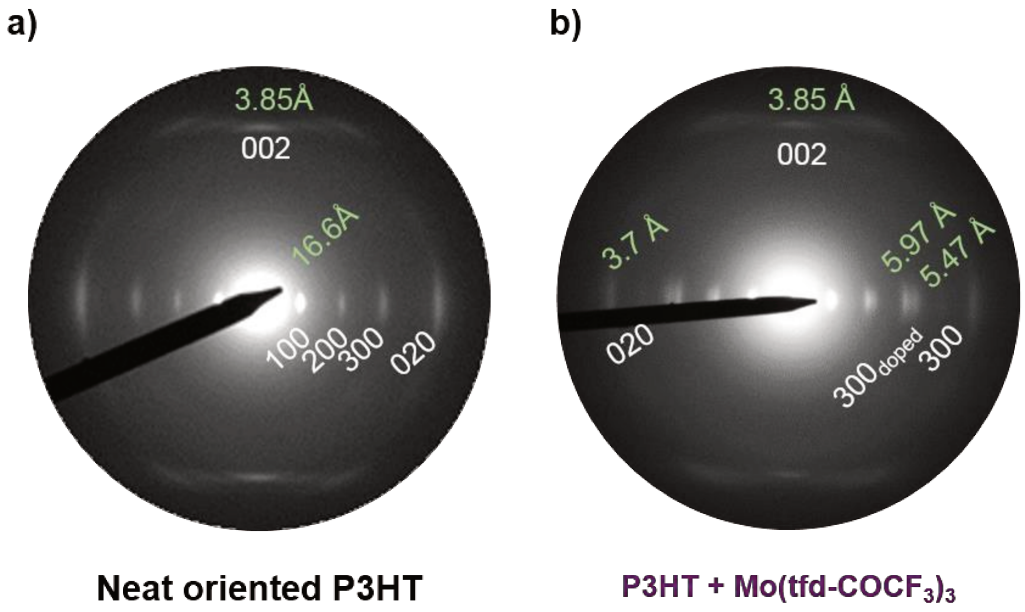


***Figure 4.*** *Electron diffraction patterns of neat (a) rubbed P3HT and rubbed P3HT doped (b) with Mo(tfd-COCF$_3$)$_3$.*

Electron diffraction shows, that the 0 0 2 reflection related to the monomer repeat periodicity ($d_{002}$ ~ 3.85 Å) is located along the meridian, i.e. along the rubbing direction R (Figure 4a). Instead, both the *h* 0 0 reflections (*h* = 1-3; $d_{100}$ ~ 16.6 Å) associated with lamellar

stacking of P3HT and the 0 2 0 reflection ($d_{020}$ ~ 3.8 Å$^{-1}$) from π-stacking are oriented along the equator (Figure 4a). The simultaneous presence of both *h* 0 0 and 0 2 0 reflections is characteristic for a mixture of face-on and edge-on crystalline domains within the polymer films.

We note that the positions of the *h* 0 0 reflections (*h* = 1-3) split upon doping with Mo(tfd-$COCF_3$)$_3$ (Figure 4b). For instance, we observe two 3 0 0 reflections, one close to the original position at $q_{300}$ ~ 5.47 Å and one at $q_{300}$ ~ 5.97 Å. The 0 2 0 peak related to π-stacking does not split but slightly shifts to $d_{020}$ ~ 3.7 Å whereas the 0 0 2 reflection is unchanged. These observations indicate that the films contain both non-doped and doped P3HT crystallites al low doping concentrations, with the dopant intercalated in the side chain layers as suggested by the expansion of the lattice along the side chain direction.

### II.5 Spectroscopic evidence of doping of both oriented and isotropic films

We recorded UV-vis-NIR spectra of isotropic films doped with solutions containing 0.1, 2.5 and 7.5 g $L^{-1}$ of the dopant. Doping gives rise to two pronounced absorption bands, P1 located in the infrared part of the spectrum and P2 centered at $\lambda_{P2}$ ~ 850 nm, while the absorption of the neat polymer is diminished in the doped samples (Figure 5).

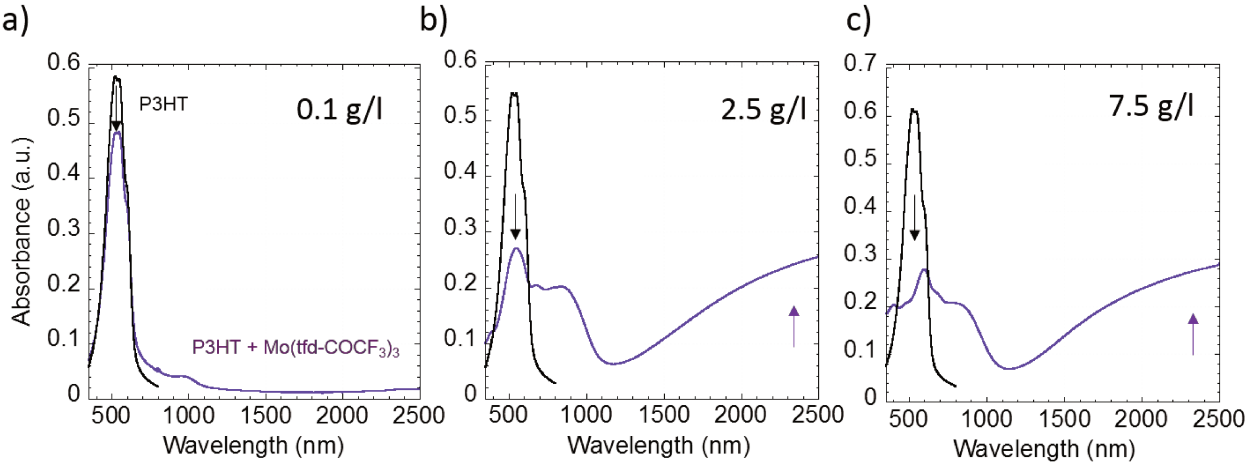


***Figure 5.*** *UV-vis-NIR absorbance spectra of a P3HT film before (back) and after (violet) doping with Mo(tfd-COCF₃)₃: $c_{Mo}$ ~0.1 g $L^{-1}$ (a), $c_{Mo}$ ~2.5 g $L^{-1}$ (b) and $c_{Mo}$ ~7.5 g $L^{-1}$ (c).*

Several anionic features arise upon doping. Figure 6 compares the positions of the neutral form and anionic forms of Mo(tfd-$COCF_3$)$_3$ at 399 nm and 596 nm, and 374 nm, 491 nm, 669 nm and 957 nm, respectively. Therefore, a broad absorption around 450-1100 nm in the doped P3HT spectra (Figure 6 – violet line) is an overlap of neutral P3HT both crystalline and amorphous, polaronic band P2 and the above stated anionic features. Contrary to $F_4TCNQ^-$, the

anionic bands of the dopant are not polarized which makes their identification particularly tedious.

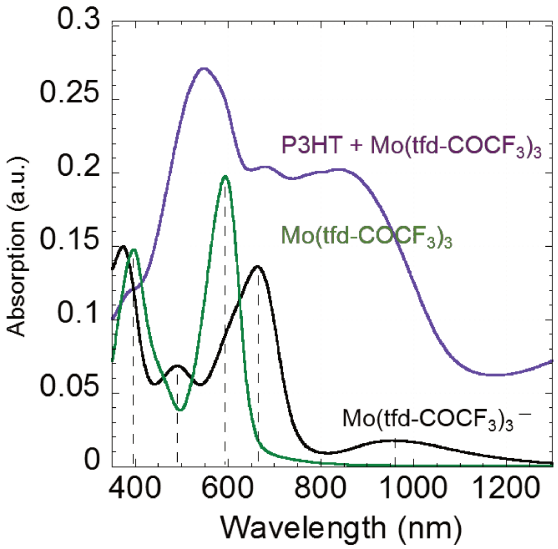


***Figure 6.*** *UV-vis-NIR absorbance spectra of doped P3HT film (violet line) overlapped with the neutral dopant signal (green line) and anionic dopant oxidation states (black curve). Anionic signals are taken from reference.*[31]

The degree of alignment of highly oriented and doped P3HT films were characterized with polarized optical microscopy (Figure 8 c, d) and polarized UV-vis-NIR spectroscopy (Figure 8 a, b). The absorption of P3HT is considerably stronger when measured parallel to the rubbing direction, with a maximum dichroic ratio of $A_{\parallel}/A_{\perp} \sim 11.5$ at 633 nm, measured for rubbed P3HT (Figure 7), which confirms uniaxial alignment of the conjugated backbone.

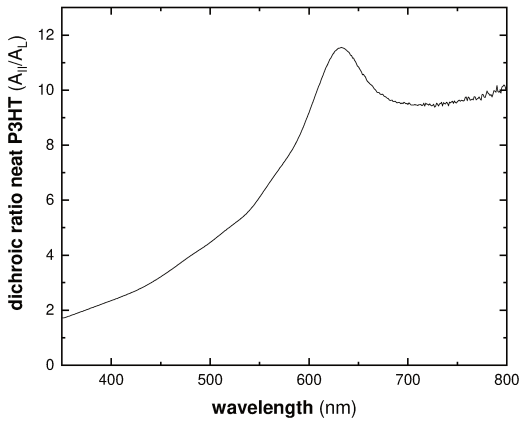


***Figure 7****. Dichroic ratio of neat rubbed P3HT versus wavelength; at 633 nm a maximum dichroic ratio of* $A_{\parallel}/A_{\perp} \sim 11.5$ *is obtained.*

The polarized UV-vis-NIR spectra reveal a significant reduction of the neutral polymer absorption independent of the dopant concentration ($c_{Mo} \sim 1$, 2.5 and 7.5 g $L^{-1}$), indicating that

all samples were strongly doped. The two polaronic absorption peaks in the near and far-IR display considerable anisotropy with the stronger absorbance when measured parallel to the rubbing direction (cf. Figure 8 a, b). Consistently with previous results reported in this thesis, this implies that the polarons delocalize along the oriented polymer backbone.[32]

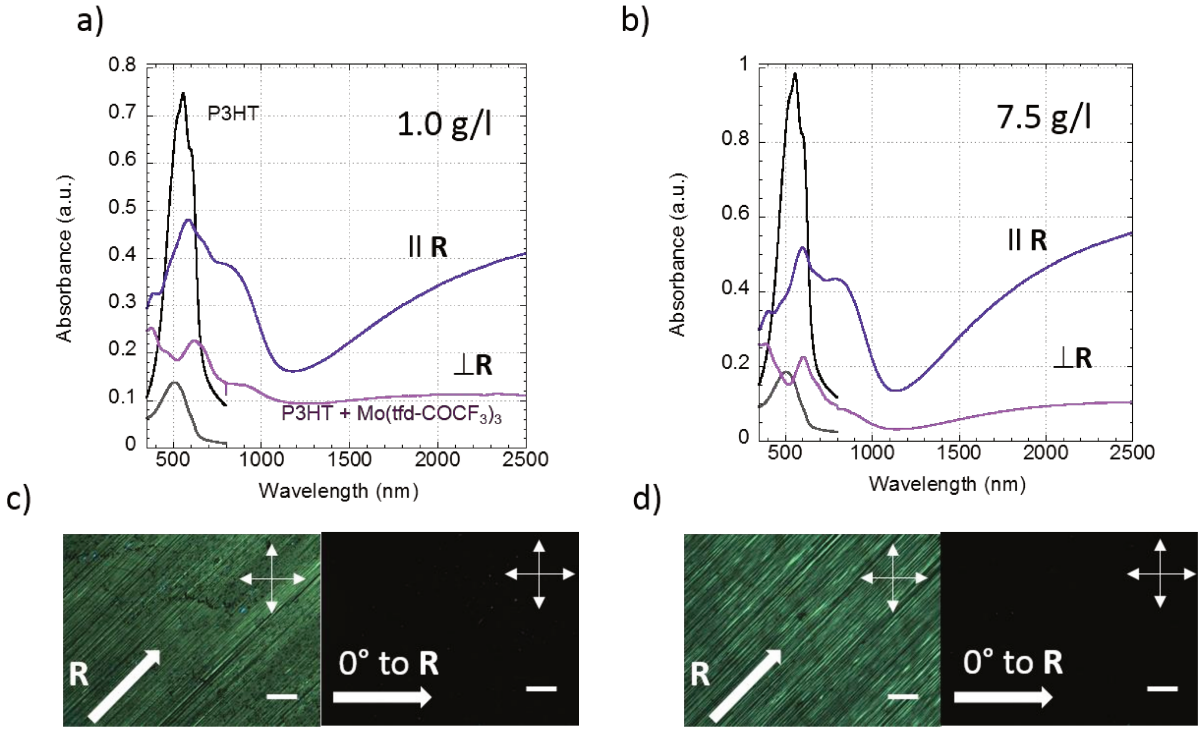


***Figure 8.*** *Polarized UV-vis-NIR absorbance spectra of rubbed P3HT and the same P3HT film sequentially doped with Mo(tfd-COCF₃)₃, $c_{Mo}$ ~1.0 g L$^{-1}$ (a) and $c_{Mo}$ ~7.5 g L$^{-1}$ (b), measured parallel (∥) and perpendicular (⊥) to the rubbing direction R. Corresponding polarised optical microscopy images (c, d) under crossed polariser and analyser 0° and 45° to the rubbing direction. White bold arrows indicate the rubbing direction R.*

We again used the molar attenuation coefficient $\varepsilon_{P2}$ to estimate the number of charge carriers. To be able to compare the polarized absorbance of the rubbed samples with the

isotropic absorbance of electrochemically oxidized P3HT, we used the average absorbance $\Delta A_{P2} = (\Delta A_{\parallel} + \Delta A_{\perp})/2$ at 800 nm (cf. Fig. 3b). From this value we subtracted $A_{\perp}$ of rubbed and doped films at 1200 nm to account for the apparent vertical offset of the UV-vis-NIR spectra, which we tentatively assign to light scattering by excess dopant on top of the film (cf. Figure 8 a, b). The deduced charge-carrier density of the rubbed films is comparable to values extracted for isotropic samples (Table 3). For rubbed P3HT films doped with $c_{Mo} \sim$ 1 g $L^{-1}$ Mo(tfd-$COCF_3$)$_3$ we obtain $N_v \sim (4.0 \pm 0.4) \cdot 10^{26}$ $m^{-3}$ (see the subsection II.6 for details). This corresponds to an oxidation level of 10 %. It must be stressed that the determined value is strongly dependent on the accurate film thickness determination.

### II.6 Estimation of the number of charge carriers

We were interested in estimating the number of generated charges, which (assuming that only polarons and no bipolarons are present) can be probed by examining the *absolute absorbance of the polaronic peaks*. Furthermore, neither neutral Mo(tfd-$COCF_3$)$_3$ nor its anion absorb at 800 nm.[31] A combination of spectroelectrochemistry and chronoamperometry was performed in the group of Prof. Sabine Ludwigs and helped determine the molar attenuation coefficient $\varepsilon_{P2}$ of the first sub-bandgap polaron peak P2. The used electrochemical setup consisted of a spin-coated P3HT film on the indium tin oxide (ITO) working electrode, a platinum wire counter electrode and a silver wire as pseudo reference electrode, immersed in an electrolyte solution of 0.1M tetrabutylammonium hexafluorophosphate ($TBAPF_6$) in AcN (see Experimental for details). A cyclic voltammogram of P3HT indicates an oxidation onset of $E_{ox} \sim$ 0.55 V in the electrochemical setup (Figure 9a; note that the onset of P3HT vs

ferrocene/ferrocenium is located at 0 V).[33] A series of oxidation reactions were realized at constant potentials between 0.55 and 0.75 V and the transient current $I(t)$ were recorded (Figure 9b). Integration of the transients over time $t$ yielded the total number of charges $Q$:

$$Q = \int_{t=0}^{\infty} I(t)dt \qquad (2)$$

Normalization by the sample volume in contact with the electrolyte yielded the charge density $Q_v$. At the end of each oxidation step a UV-vis-NIR spectrum was recorded and the difference in absorbance $\Delta A$ between doped and undoped P3HT at 800 nm was plotted (normalized by the film thickness $d$ = 48 nm) (Figure 9c). A plot of $\Delta A/d$ vs. $Q_v$ shows a linear trend (Figure 9d), which indicates that only one absorbing species, i.e. polarons, is present up to a charge density of at least $Q_v$ = $3 \cdot 10^{26}$ $m^{-3}$.

In agreement, Enengl et al. have shown that a significant amount of bipolarons only starts to form in P3HT at potentials larger than 0.5 V above the oxidation onset.[34] The slope of $\Delta A/d$ vs. $Q_v$ yields $\varepsilon_{P2} \sim (4.1 \pm 0.2) \cdot 10^3$ $m^2$ $mol^{-1}$ at 800 nm ($\varepsilon_{P2} \sim 41000$ $M^{-1}$ $cm^{-1}$). We would like to point out that cyclic voltammograms of P3HT can display several anodic waves that correspond to oxidation of ordered and disordered material.[33] Our analysis is limited to the first anodic wave where ordered P3HT is oxidized and hence the here reported value for $\varepsilon_{P2}$ corresponds to polarons in crystalline domains.

The P2 polaron peak of electrochemically oxidized P3HT is centered at $\lambda_{P2} \sim 800$ nm, i.e. at a lower wavelength than chemically doped P3HT (cf. Figure 5). We explain this shift in $\lambda_{P2}$ with the difference in anion size. During electrochemical oxidation, $PF_6^-$ counterions, which have a thermochemical radius of $r$ = 2.4 Å,[35] enter the polymer from the electrolyte.

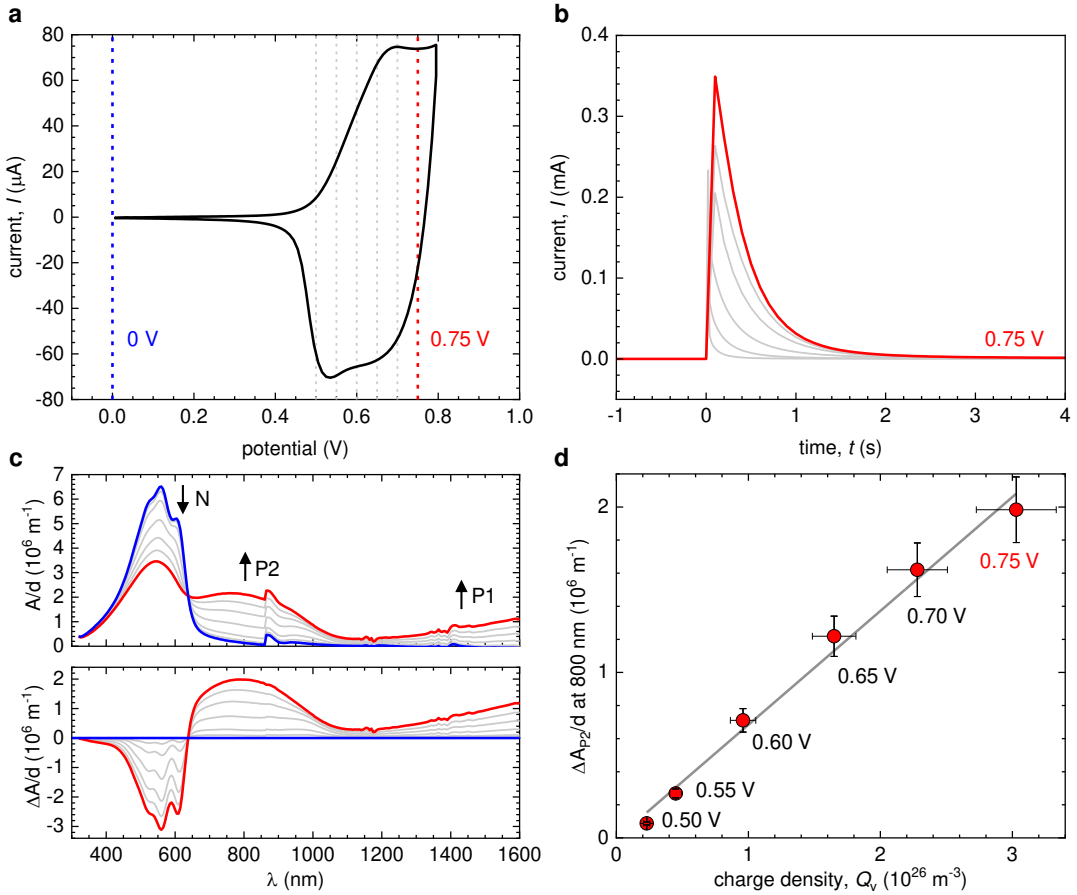


***Figure 9.*** *(a) Cyclic voltammogram of P3HT (P3HT has an oxidation onset around 0 V vs. ferrocene/ferrocenium according to ref[33]); (b) charging current from chronoamperometry, (c) UV-vis-NIR absorbance spectra from spectroelectrochemistry measurements recorded at different electrochemical potentials between 0 V (blue) and 0.75 V (red); thickness normalized absorbance $A/d$ (top) and difference in normalized absorbance $\Delta A/d$ between spectra of P3HT oxidized at different potentials and undoped P3HT at 0 V; (d) the differential absorbance $\Delta A_{P2}/d$ at 800 nm vs. charge density $Q_v$ from integration of the charging currents; the slope of the linear fit (gray) is the molar attenuation coefficient $\varepsilon_{P2}$.*

Chemical doping instead produces $Mo(tfd\text{-}COCF_3)_3^-$ counterions, which have a much larger radius of $r$ ~7.5 Å (based on an estimate of the smallest sphere that could encompass the molecule/ion),[31] and hence results in a larger average polaron-anion distance.[36] Since the P2 polaron absorbance is broad we deem the difference in peak position to be minor. Hence, we used $\varepsilon_{P2}$ obtained from our electrochemistry experiments to estimate the charge-carrier density $N_v$ of chemically doped P3HT according to the Beer-Lambert law:

$$\Delta A_{P2} = \varepsilon_{P2} \cdot d \cdot N_v \quad (3)$$

where $\Delta A_{P2}$ is the difference in absorbance at 800 nm between doped and undoped P3HT (Table 2). $Mo(tfd\text{-}COCF_3)_3$ can dope both ordered and disordered P3HT because of its high electron affinity of 5.6 eV. The here reported value for $\varepsilon_{P2}$ was measured by oxidizing ordered P3HT, and may differ in case of disordered material, which would introduce an error in the here presented analysis of the charge-carrier density. Recent study reports the same approach to estimate the charge-carrier density of chemically doped diketopyrrolopyrrole (DPP) which could confirm the value obtained for $N_v$ with electron paramagnetic resonance (EPR).[37] For samples sequentially doped with $c_{Mo}$ ~ 1 g $L^{-1}$ $Mo(tfd\text{-}COCF_3)_3$ in $AcN:CHCl_3$ we extract a value of $N_v \sim (4.4 \pm 0.5) \cdot 10^{26}$ $m^{-3}$. P3HT has a density of about 1.1 g $cm^{-3}$,[38] and hence contains $4 \cdot 10^{27}$ thiophene rings per $m^3$, which implies an oxidation level of 11 %, i.e. one polaron for every ten thiophene repeat units. The same samples display an electrical conductivity of $\sigma \sim (260 \pm 26)$ S $cm^{-1}$, which according to equation 1 translates to a charge-carrier mobility of $\mu \sim (3.3 \pm 0.5)$ $cm^2$ $V^{-1}$ $s^{-1}$ (Table 2). Note that this value is only slightly higher than the 1 $cm^2$ $V^{-1}$ $s^{-1}$ reported for P3HT doped with F4TCNQ.[39] Furthermore, we measured a high Seebeck coefficient of $\alpha \sim 44$

μV $K^{-1}$, yielding a thermoelectric power factor of $\alpha^2\sigma \sim (50 \pm 10)$ μW $m^{-1}$ $K^{-2}$, which is comparable to the highest values reported for isotropic P3HT (cf. Table 1).

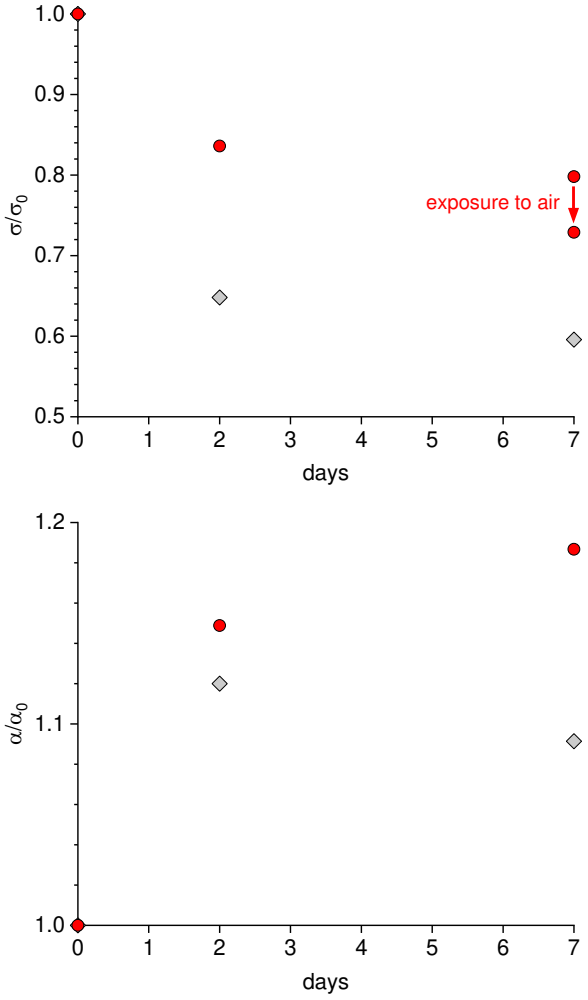


***Figure 10.*** *Change in conductivity $\sigma/\sigma_0$ (top) and Seebeck coefficient $\alpha/\alpha_0$ (bottom) of P3HT doped with $c_{Mo}$ ~ 7.5 g $L^{-1}$ during storage in a glove box; gray diamonds: neat P3HT ($\sigma_0$ ~ 285 S $cm^{-1}$; $\alpha_0$ ~ 35 μV $K^{-1}$); red circles: rubbed P3HT parallel to rubbing direction ($\sigma_0$ ~ 681 S $cm^{-1}$; $\alpha_0$ ~ 43 μV $K^{-1}$); after 7 days storage in a glove box the rubbed samples was exposed to air.*

***Table 2.*** *Electrical conductivity $\sigma$, Seebeck coefficient $\alpha$ (error $\pm$ 2 µV K$^{-1}$), power factor $\alpha^2\sigma$, density and mobility of charges, $N_v$ and $\mu$, and oxidation level for doctor-bladed films with a thickness $d$ sequentially doped with an AcN:CHCl$_3$ solution containing a concentration of $c_{Mo}$ of Mo(tfd-COCF$_3$)$_3$; $\sigma$ and $\alpha$ were measured immediately after doping but remained relatively stable during storage in a glove box for one week (Figure 10).*

| $c_{Mo}$ (g L$^{-1}$) | $d$ (nm) | $N_v$ ($10^{26}$ m$^{-3}$) | ox. level (wt %) | $\sigma$ (S cm$^{-1}$) | $\alpha$ (µV K$^{-1}$) | $\alpha^2\sigma$ (µW m$^{-1}$ K$^{-2}$) | $\mu$ (cm$^2$ V$^{-1}$ s$^{-1}$) |
|---|---|---|---|---|---|---|---|
| 0.1 | 55 ± 6 | 0.9 ± 0.1 | 2 | 1.1 ± 0.1 | 139 | 2.0 ± 0.3 | 0.07 ± 0.01 |
| 1 | 57 ± 6 | 4.4 ± 0.5 | 11 | 260 ± 26 | 44 | 50 ± 10 | 3.3 ± 0.5 |
| 7.5 | 51 ± 5 | 5.0 ± 0.6 | 13 | 285 ± 29 | 35 | 35 ± 8 | 3.2 ± 0.5 |

### II.7 Thermoelectric characterization of doped films

The electrical conductivity is considerably higher along the rubbing direction, e.g. $\sigma_\parallel$ ~ (509 $\pm$ 51) S cm$^{-1}$ versus $\sigma_\perp$ ~ (84 $\pm$ 8) S cm$^{-1}$ for P3HT doped with $c_{Mo}$ ~ 1 g L$^{-1}$ Mo(tfd-COCF$_3$)$_3$ (Table 3), which gives rise to an anisotropy of $\sigma_\parallel/\sigma_\perp$ ~ 6 (see Figure 10 for stability of conductivity over time). Together with our estimate for $N_v$ we calculate a charge-carrier mobility of $\mu_\parallel$ ~ (7.1 $\pm$ 0.1) cm$^2$ V$^{-1}$ s$^{-1}$ and $\mu_\perp$ ~ (1.2 $\pm$ 0.2) cm$^2$ V$^{-1}$ s$^{-1}$, which represent average values for all mobile plus bound charges. We note that $\mu_\parallel$ is significantly higher than values measured for isotropic samples (cf. Table 2), while $\mu_\perp$ is lower.

In agreement with previous studies,[9,21,24] the Seebeck coefficient also displays a high degree of in-plane anisotropy, e.g. $\alpha_\parallel/\alpha_\perp$ ~ 4 in case of P3HT doped with $c_{Mo}$ ~ 1 g L$^{-1}$ Mo(tfd-COCF$_3$)$_3$. An absolute Seebeck coefficient of $\alpha_\parallel$ ~ (56 $\pm$ 2) µV K$^{-1}$ gives rise to a maximum power factor of $\alpha_\parallel^2\sigma_\parallel$ ~ (160 $\pm$ 27) µW m$^{-1}$ K$^{-2}$ (Table 3), which is the highest value so far reported for P3HT (cf. Table 1). We note that $\alpha_\parallel^2\sigma_\parallel$ slightly exceeds the empirical trend $\alpha^2\sigma \propto \sqrt{\sigma}$ that is

often observed for isotropic samples,[11–13] while $\alpha_{\perp}^{2}\sigma_{\perp}$ falls short of the predicted value (Figure 11). The anisotropy of the Seebeck coefficient and conductivity was recently studied using kinetic Monte Carlo (kMC) simulations to describe thermoelectric measurements on doped poly(2,5-bis(3-dodecyl-2-thienyl)thieno[3,2-*b*]thiophene) (PBTTT).[40] In brief, these kMC simulations account for variable-range hopping on a regular lattice. Structural anisotropy is reflected in the model by an increased delocalization in the parallel direction compared to the perpendicular direction, i.e. $\xi_{\parallel} > \xi_{\perp}$ where $\xi$ is the localization length (cf. ref for details[40]). This model can reproduce the trend of the experimental data in the parallel and perpendicular direction measured for rubbed P3HT doped with Mo(tfd-$COCF_3$)$_3$, when assuming an anisotropy ratio of $\xi_{\parallel}/\xi_{\perp} = 4$ and an attempt-to-hop frequency of $\nu_0 = 2 \cdot 10^{13}$ $s^{-1}$ (cf. Figure 12).

***Table 3.*** *Electrical conductivity σ, Seebeck coefficient α (error ± 2 μV K$^{-1}$), power factor $\alpha^2\sigma$, density and mobility of charges, $N_v$ and μ, and oxidation level for rubbed films with a thickness d sequentially doped with an AcN:$CHCl_3$ solution containing a concentration of $c_{Mo}$ of Mo(tfd-$COCF_3$)$_3$; subscripts ∥ and ⊥ refer to in-plane values measured parallel and perpendicular to the rubbing direction; σ and α were measured immediately after doping but remained relatively stable during storage in a glove box for one week, and even after subsequent exposure to air (Figure 10).*

| $c_{Mo}$ (g L$^{-1}$) | $d$ (nm) | $N_v$ ($10^{26}$ m$^{-3}$) | ox. level (%) | $\sigma_{\parallel}$ (S cm$^{-1}$) | $\sigma_{\perp}$ (S cm$^{-1}$) | $\alpha_{\parallel}$ (μV K$^{-1}$) | $\alpha_{\perp}$ (μV K$^{-1}$) | $\alpha_{\parallel}^2\sigma_{\parallel}$ (μW m$^{-1}$ K$^{-2}$) | $\alpha_{\perp}^2\sigma_{\perp}$ (μW m$^{-1}$ K$^{-2}$) | $\mu_{\parallel}$ (cm$^2$ V$^{-1}$ s$^{-1}$) | $\mu_{\perp}$ (cm$^2$ V$^{-1}$ s$^{-1}$) |
|---|---|---|---|---|---|---|---|---|---|---|---|
| 1 | 44 | 4.0 ± 0.4 | 10 | 509 ± 51 | 84 ± 8 | 56 | 13 | 160 ± 27 | 1.0 ± 0.5 | 7.1 ± 1.1 | 1.2 ± 0.2 |
| 2.5 | 58 | 3.6 ± 0.4 | 9 | 593 ± 59 | 116 ± 12 | 47 | 17 | 131 ± 12 | 3.0 ± 0.8 | 9.3 ± 1.4 | 1.8 ± 0.3 |
| 7.5 | 53 | 4.4 ± 0.5 | 11 | 681 ± 68 | 50 ± 5 | 43 | 6 | 126 ± 12 | 0.2 ± 0.1 | 8.7 ± 1.3 | 0.6 ± 0.1 |

We argue that transport in the highly doped samples studied here is dominated by hopping between discrete sites along the direction of orientation, while inter-chain transport only plays a minor role.[18,40] In a system with such a distinct orientation, carriers are forced to hop along the parallel direction and therefore have a limited ability to optimize their path with respect to energy. This results in an upward shift of the transport energy $E_{tr}$ in the parallel direction and as $\alpha \propto (E_F - E_{tr})/T$ with $E_F$ the Fermi energy also in an increase of $\alpha_{\parallel}$ compared to $\alpha_{\perp}$.[40]

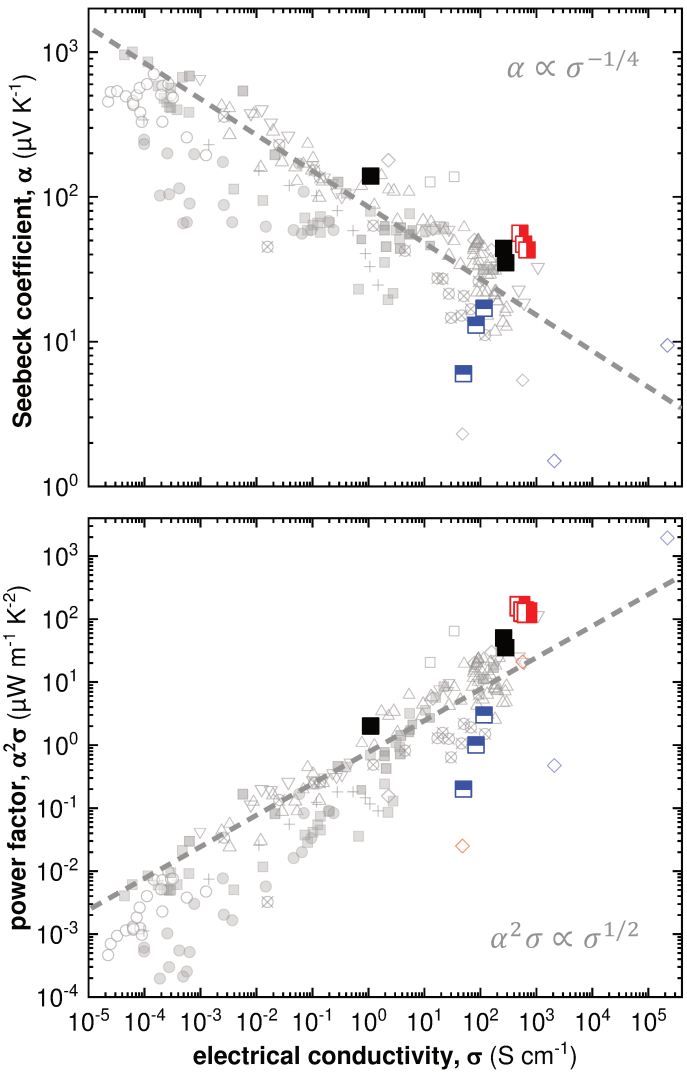


***Figure 11.*** *(a) Seebeck coefficient $\alpha$ and (b) power factor $\alpha^2\sigma$ versus electrical conductivity $\sigma$ of isotropic P3HT (black square), and rubbed P3HT measured parallel (red square) and perpendicular to the rubbing direction (blue square); grey data points are literature values extracted from ref[12]. as well as references therein; literature values are from ref[9] (red and blue diamonds); dashed lines represent the empirical trends $\alpha \propto \sigma^{-0.25}$ and $\alpha^2\sigma \propto \sqrt{\sigma}$.*

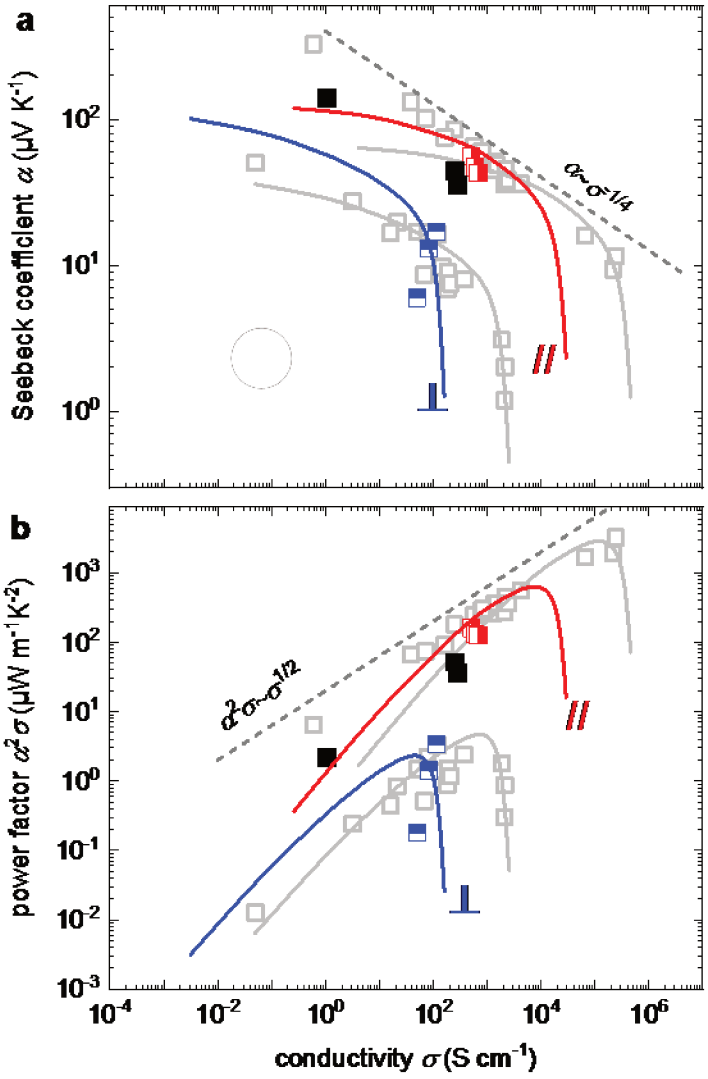


***Figure 12.*** *(a) Seebeck coefficient $\alpha$ and (b) power factor $\alpha^2\sigma$ versus electrical conductivity $\sigma$ of isotropic P3HT (black squares), and rubbed P3HT measured parallel (red squares and line) and perpendicular to the rubbing direction (blue squares and line); grey data points are literature values extracted from refs for PBTTT[9,40]. Full lines correspond to simulations calculated from the kMC model, with an anisotropy ratio of $\xi_{\parallel}/\xi_{\perp} = 4$, where $\xi$ is the localization length in the parallel and perpendicular direction, respectively. The attempt to hop frequency was set to $v_0 = 2 \cdot 10^{13}$ $s^{-1}$ and the thermopower was rescaled by a factor of 0.1 in both directions. $\parallel$ and $\perp$ refer to the parallel and perpendicular direction, respectively. The dashed gray line shows the empirical trends $\alpha \propto \sigma^{-0.25}$ and $\alpha^2\sigma \propto \sqrt{\sigma}$.*

## III. Conclusions

We conclude that the combination of a large dopant such as $Mo(tfd\text{-}COCF_3)_3$ in combination with structural anisotropy, here achieved by high-temperature rubbing, is a powerful means to improve the thermoelectric properties of conjugated polymers. From the point of view of sample preparation, we investigated the effect of rinsing the doped films with the pure solvent (ACN). The detrimental impact of rinsing is evidenced. Rinsing de-dopes the films and results a threefold reduction of conductivity and a loss of the polaronic absorption. TEM shows that de-doping results in a structural change from a doped to undoped crystalline phase while the amorphous phase should remain somehow doped. Both charge conductivity $\sigma$ and thermopower $\alpha$ show a strong anisotropy in doped films with $a_\sigma \approx 8$, $a_\alpha \approx 5$. Upon optimization of the doping of aligned P3HT, a high conductivity of $\sigma_{\parallel} \sim (509 \pm 51)$ S cm$^{-1}$ is obtained thanks to a high charge-carrier mobility along the rubbing direction. Importantly, the Seebeck coefficient remains also high with $\alpha_{\parallel} \sim (56 \pm 2)$ μV K$^{-1}$, and as a result we achieve a record thermoelectric power factor of $\alpha_{\parallel}^2 \sigma_{\parallel} \sim (160 \pm 27)$ μW m$^{-1}$ K$^{-2}$ for P3HT. Most importantly, spectro-electrochemistry helps determine the density of charge carriers in the oriented films by determination of the polaron extinction coefficient. The average charge carrier density in the aligned samples reaches $4 \cdot 10^{20}$ cm$^{-3}$ i.e. one polaron for approximately ten monomers. Overall, these results highlight the importance to select the right dopant to achieve effective oxidation of the polymer i.e. obtain a high charge carrier density while keeping the Seebeck coefficient to a high level. A more systematic investigation of doping with a library of dopants might help identify further the relevant parameters e.g. electron affinity, dopant dimension

and diffusion coefficient that could maximize the thermopower and charge conductivity of aligned thin films of P3HT.

**References**

1. Bubnova, O. & Crispin, X. Towards polymer-based organic thermoelectric generators. *Energy Environ. Sci.* **5**, 9345–9362 (2012).
2. Russ, B., Glaudell, A., Urban, J. J., Chabinyc, M. L. & Segalman, R. A. Organic thermoelectric materials for energy harvesting and temperature control. *Nature Reviews Materials* **1**, 16050 (2016).
3. Kroon, R. *et al.* Thermoelectric plastics: from design to synthesis, processing and structure–property relationships. *Chem. Soc. Rev.* **45**, 6147–6164 (2016).
4. Bubnova, O. *et al.* Optimization of the thermoelectric figure of merit in the conducting polymer poly(3,4-ethylenedioxythiophene). *Nature Materials* **10**, 429–433 (2011).
5. Kim, G.-H., Shao, L., Zhang, K. & Pipe, K. P. Engineered doping of organic semiconductors for enhanced thermoelectric efficiency. *Nature Materials* **12**, 719–723 (2013).
6. Jung, I. H. *et al.* High Thermoelectric Power Factor of a Diketopyrrolopyrrole-Based Low Bandgap Polymer via Finely Tuned Doping Engineering. *Scientific Reports* **7**, 44704 (2017).
7. Patel, S. N. *et al.* Morphology Controls the Thermoelectric Power Factor of a Doped Semiconducting Polymer. *Science Advances* **3**, e1700434 (2017).
8. Vijayakumar, V. *et al.* Effect of alkyl side chain length on doping kinetics, thermopower and charge transport properties in highly oriented F4TCNQ doped PBTTT films. *ACS Appl. Mater. Interfaces* **11**, 4942 (2019).
9. Vijayakumar, V. *et al.* Bringing conducting polymers to high order: towards conductivities beyond 105 S/cm and thermoelectric power factors of 2 mW·m–1.K–2. *Adv. Energy Mater.* **9**, 1900266 (2019).

10. Nogami, Y. *et al.* On the metallic states in highly conducting iodine-doped polyacetylene. *Solid State Communications* **76**, 583–586 (1990).
11. Glaudell, A. M., Cochran, J. E., Patel, S. N. & Chabinyc, M. L. Impact of the Doping Method on Conductivity and Thermopower in Semiconducting Polythiophenes. *Adv. Energy Mater.* **5**, 1401072 (2015).
12. Hynynen, J., Kiefer, D. & Müller, C. Influence of crystallinity on the thermoelectric power factor of P3HT vapour-doped with F4TCNQ. *RSC Adv.* **8**, 1593–1599 (2018).
13. Beretta, D. *et al.* Thermoelectrics: From history, a window to the future. *Materials Science and Engineering: R: Reports* **138**, 100501 (2019).
14. Pingel, P. & Neher, D. Comprehensive picture of $p$-type doping of P3HT with the molecular acceptor $F_4$TCNQ. *Phys. Rev. B* **87**, 115209 (2013).
15. Zuo G., Abdalla H. & Kemerink M. Impact of doping on the density of states and the mobility in organic semiconductors. *Phys. Rev. B* **93**, 235203 (2016).
16. Aubry, T. J. *et al.* Dodecaborane-Based Dopants Designed to Shield Anion Electrostatics Lead to Increased Carrier Mobility in a Doped Conjugated Polymer. *Advanced Materials* **31**, 1805647 (2019).
17. Liang, Z. *et al.* Influence of dopant size and electron affinity on the electrical conductivity and thermoelectric properties of a series of conjugated polymers. *J. Mater. Chem. A* **6**, 16495–16505 (2018).
18. Hynynen, J. *et al.* Enhanced Electrical Conductivity of Molecularly p-Doped Poly(3-hexylthiophene) through Understanding the Correlation with Solid-State Order. *Macromolecules* **50**, 8140–8148 (2017).

19. Qu, S. *et al.* Highly anisotropic P3HT films with enhanced thermoelectric performance via organic small molecule epitaxy. *NPG Asia Materials* **8**, e292–e292 (2016).
20. Hynynen, J. *et al.* Enhanced Thermoelectric Power Factor of Tensile Drawn Poly(3-hexylthiophene). *ACS Macro Lett* **8**, 70–76 (2019).
21. Hamidi-Sakr, A. *et al.* A Versatile Method to Fabricate Highly In-Plane Aligned Conducting Polymer Films with Anisotropic Charge Transport and Thermoelectric Properties: The Key Role of Alkyl Side Chain Layers on the Doping Mechanism. *Advanced Functional Materials* **27**, 1700173 (2017).
22. Zhang, Q., Sun, Y., Xu, W. & Zhu, D. Thermoelectric energy from flexible P3HT films doped with a ferric salt of triflimide anions. *Energy Environ. Sci.* **5**, 9639–9644 (2012).
23. Lim, E., Peterson, K. A., Su, G. M. & Chabinyc, M. L. Thermoelectric Properties of Poly(3-hexylthiophene) (P3HT) Doped with 2,3,5,6-Tetrafluoro-7,7,8,8-tetracyanoquinodimethane (F4TCNQ) by Vapor-Phase Infiltration. *Chem. Mater.* **30**, 998–1010 (2018).
24. Untilova, V., Biskup, T., Biniek, L., Vijayakumar, V. & Brinkmann, M. Control of Chain Alignment and Crystallization Helps Enhance Charge Conductivities and Thermoelectric Power Factors in Sequentially Doped P3HT:F4TCNQ Films. *Macromolecules* **53**, 2441–2453 (2020).
25. Belasco, J. *et al.* Molecular doping and tuning threshold voltage in 6,13-bis(triisopropylsilylethynyl)pentacene/polymer blend transistors. *Appl. Phys. Lett.* **105**, 063301 (2014).
26. Paniagua, S. A. *et al.* Production of heavily n- and p-doped CVD graphene with solution-processed redox-active metal–organic species. *Mater. Horiz.* **1**, 111–115 (2014).

27. Qi, Y. *et al.* A Molybdenum Dithiolene Complex as p-Dopant for Hole-Transport Materials: A Multitechnique Experimental and Theoretical Investigation. *Chem. Mater.* **22**, 524–531 (2010).
28. Qi, Y. *et al.* Use of a High Electron-Affinity Molybdenum Dithiolene Complex to p-Dope Hole-Transport Layers. *J. Am. Chem. Soc.* **131**, 12530–12531 (2009).
29. Biniek, L., Leclerc, N., Heiser, T., Bechara, R. & Brinkmann, M. Large Scale Alignment and Charge Transport Anisotropy of pBTTT Films Oriented by High Temperature Rubbing. *Macromolecules* **46**, 4014–4023 (2013).
30. Biniek, L. *et al.* High-Temperature Rubbing: A Versatile Method to Align π-Conjugated Polymers without Alignment Substrate. *Macromolecules* **47**, 3871 (2014).
31. Mohapatra, S. K. *et al.* Synthesis, characterization, and crystal structures of molybdenum complexes of unsymmetrical electron-poor dithiolene ligands. *Polyhedron* **116**, 88–95 (2016).
32. Ghosh, R. *et al.* Anisotropic Polaron Delocalization in Conjugated Homopolymers and Donor–Acceptor Copolymers. *Chem. Mater.* **31**, 7033–7045 (2019).
33. Bruchlos K. *et al.* Poly(3-hexylthiophene) revisited - Influence of film deposition on the electrochemical behaviour and energy levels. *Electrochim. Acta* 299 (2018).
34. Enengl, C. *et al.* Doping-Induced Absorption Bands in P3HT: Polarons and Bipolarons. *ChemPhysChem* **17**, 3836–3844 (2016).
35. Simoes, M. C., Hughes, K. J., Ingham, D. B., Ma, L. & Pourkashanian, M. Estimation of the Thermochemical Radii and Ionic Volumes of Complex Ions. *Inorg. Chem.* **56**, 7566–7573 (2017).

36. Ghosh, R. *et al.* Spectral Signatures and Spatial Coherence of Bound and Unbound Polarons in P3HT Films: Theory Versus Experiment. *J. Phys. Chem. C* **122**, 18048–18060 (2018).
37. Hofmann, A. I. *et al.* Chemical Doping of Conjugated Polymers with the Strong Oxidant Magic Blue. *Advanced Electronic Materials* **6**, 2000249 (2020).
38. Bounioux, C. *et al.* Thermoelectric composites of poly(3-hexylthiophene) and carbon nanotubes with a large power factor. *Energy Environ. Sci.* **6**, 918–925 (2013).
39. Lim, E., Glaudell, A. M., Miller, R. & Chabinyc, M. L. The role of Ordering on the Thermoelectric Properties of Blends of Regioregular and Regiorandom Poly(3-hexylthiophene). *Adv. Elect. Materials* **5**, 1800915 (2019).
40. Scheunemann, D. *et al.* Rubbing and Drawing: Generic Ways to Improve the Thermoelectric Power Factor of Organic Semiconductors? *Advanced Electronic Materials* **6**, 2000218 (2020).

# Conclusions and perspectives

The aim of my thesis was to compare the effect of doping of P3HT – a working horse among the polymer semiconductors by different dopants. The doping mechanism of highly oriented and crystalline P3HT films was carefully investigated using polarized UV-vis spectroscopy, TEM and thermoelectrical measurements. High-T rubbing is a unique alignment method to render thin polymer films highly anisotropic and to control their semi-crystalline structure, leading to a high degree of anisotropy of their TE properties. Most importantly, we demonstrate that alignment is a general means to improve TE performances in doped polymer thin films. This thesis has focused on the model system RR-P3HT doped with various dopants ($F_4TCNQ$, $F_6TCNNQ$, $FeCl_3$, $Mo(tfd\text{-}COCF_3)_3$) in order to identify the impact of the pristine polymer film structure and of the dopant (molecular structure, dimensions and electron affinity) on the resulting structure and TE performances of doped aligned thin films. We also investigated the impact of the doping method (direct doping versus incremental doping) on the structure-property correlations of doped and aligned P3HT films.

Sequential doping with $F_4TCNQ$ was found to transform the semi-conducting films into highly conducting ones with charge conductivities up to 160 S $cm^{-1}$ and power factor of 56 µW $m^{-1}$ $K^{-2}$ which outperforms the TE properties observed for non-oriented P3HT:$F_4TCNQ$ .[1] The 2nd Chapter explored in details the effect of the temperature of rubbing on optical, structural and TE properties of doped P3HT films. The combination of all techniques provided a clear view on the doping mechanism that depends substantially on the initial structure of the films, i.e. smectic-like vs semi-crystalline phase. The smectic-like phase was found to be less ordered and less doped than the semi-crystalline phase. The later phase shows well-

ordered and crystallized side chains as well as a high degree of orientation that both help to intercalate more dopant molecules within the layer of the alkyl side-chains. Moreover, a clear correlation is observed between the unidirectional alignment of the P3HT backbones and of the $F_4$TCNQ dopants that are oriented in a plane roughly perpendicular to the polymer chains. Electron diffraction gave clearcut evidence for the structural modification of the P3HT crystalline domains depending on the structure of pristine P3HT films (smectic-like or semi-crystalline).

In the third chapter, we have studied the impact of doping P3HT with a similar conjugated and flat molecule - $F_6$TCNNQ, possessing lower electron affinity than $F_4$TCNQ. The 3$^{rd}$ chapter is dedicated to a detailed comparison of both dopants on the TE performances and structure of aligned P3HT films. Higher ordering of dopants in the polymer matrix and higher oxidation level of P3HT resulted in a higher electrical conductivity up to 343 S/cm *versus* $F_4$TCNQ-doped films whereas similar PF values are obtained for both dopants. Polarized UV-Vis spectroscopy evidenced a better ordering of $F_6$TCNNQ dopant molecules as compared to $F_4$TCNQ. A tentative structural model of P3HT:$F_6$TCNNQ was proposed using the new electron diffraction data on oriented and doped P3HT films. Structural modeling helped identify a triclinic structure with $P_{-1}$ symmetry with the following parameters: a = 18.8 Å, b = 8.95 Å, c = 7.75 Å, $\alpha$=107.6°, $\beta$=101.5° and $\gamma$=89.3° and a stoichiometry of one dopant per four thiophene cycles.

In the fourth chapter, we have investigated the structure and TE properties in aligned P3HT films doped with the bulkier low-electron affinity molybdenum-based dopant, namely Mo(tfd-$COCF_3$)$_3$.[2] A remarkable conductivity of $\sigma_{\parallel} \sim 509$ S cm$^{-1}$ was obtained for this system thanks to the enhancement of the charge-carrier mobility along the rubbing direction.

Although very high conductivities were obtained for this dopant, relatively high Seebeck coefficients were retained, resulting in record power factor close to 160 μW $m^{-1}$ $K^{-2}$. Polarized UV-vis-NIR spectroscopy indicates that both crystalline and amorphous interlamellar zones of P3HT are doped with Mo(tfd-$COCF_3$)$_3$ explaining in part the high charge conductivities obtained for this dopant.

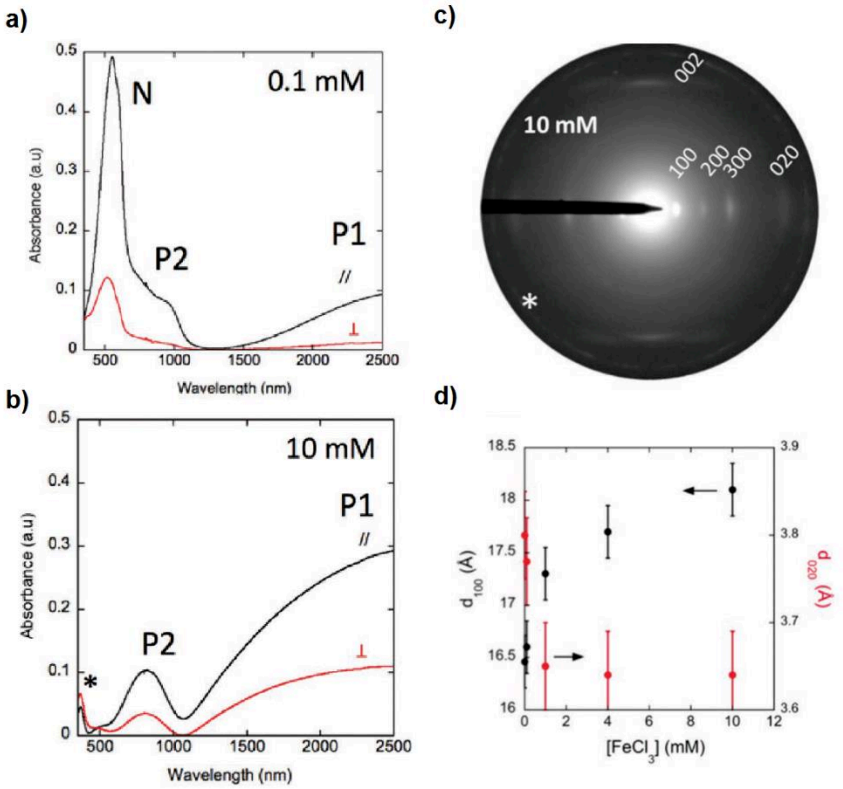


***Figure C1**. a, b) Polarized UV–vis–NIR spectrum in oriented P3HT thin films ICD doped in solution of FeCl3/nitromethane up to 0.1 mM and 10mM. The light polarization is parallel (//) to the rubbing direction or perpendicular to it (⊥). The asterisk highlights the absorption peak of the excess $FeCl_3$ present on the film surface. c) Electron diffraction patterns of $FeCl_3$-doped P3HT film at 10mM concentration. The asterisk marks a Scherrer ring from excess FeCl3 on the surface of the doped P3HT film. d) Interlayer spacing $d_{100}$ and π-stacking distance versus $FeCl_3$ doping concentration.*

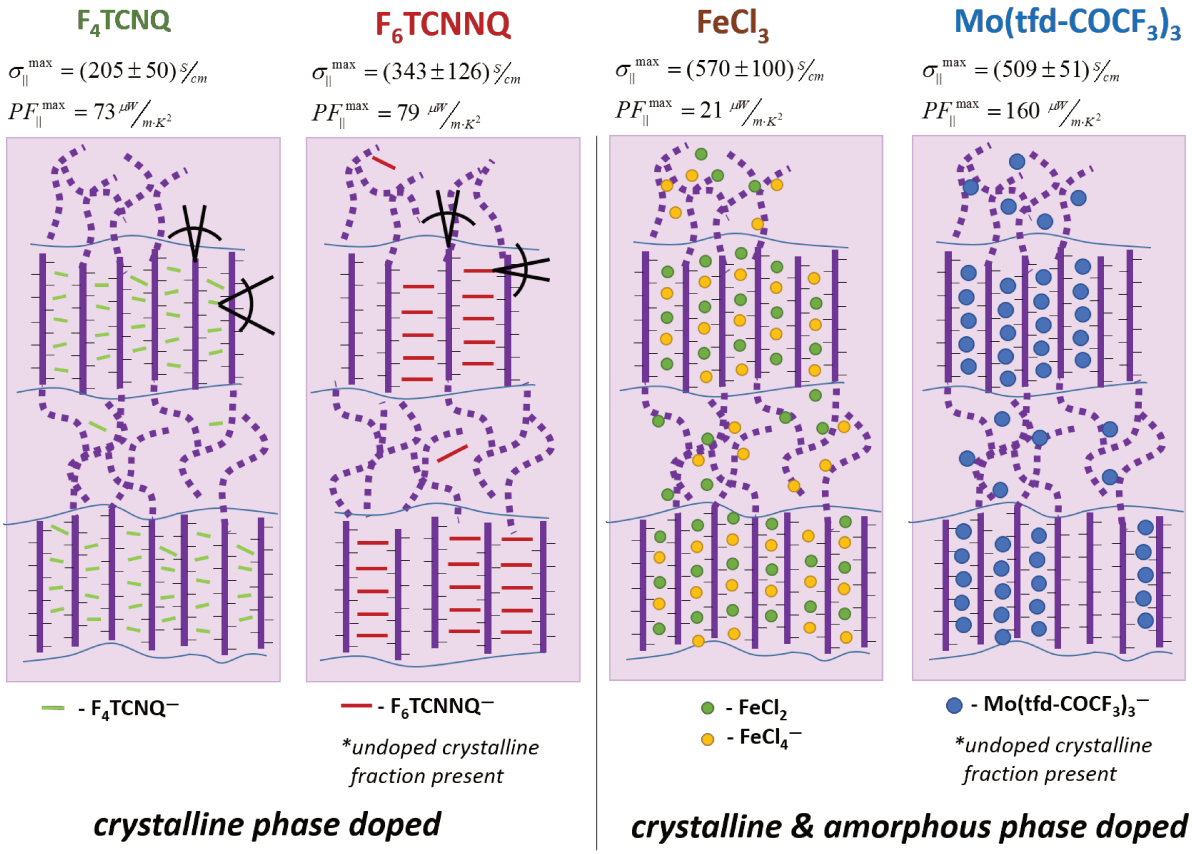


***Scheme C1.*** *Representation of the doped structures of semi-crystalline P3HT. Average orientation and location of the dopant molecules are shown in corresponding color.*

In a different study, not included in the scope of this thesis, we also investigated the doping of P3HT by $FeCl_3$, a so-called strong Lewis acid.[3] Similarly to Mo(tfd-$COCF_3$)$_3$, UV–vis-NIR spectroscopy indicates that both amorphous and crystalline domains of P3HT are doped by $FeCl_3$ (see Figure C1). However, doping P3HT with $FeCl_3$ is a more complex process that leads to the coexistence of two dopant species upon oxidation of the polymer: $FeCl_4^-$ and $FeCl_2$. Remarkably and contrary to the other studied polymer:dopant systems, $FeCl_3$ leads to a full oxidation of P3HT chains at 10 mM, as evidenced by UV-vis-NIR measurements: the UV-vis-NIR signal of the neutral polymer was totally removed for [$FeCl_3$]=10mM (see Figure

C1).The unit cell expansion upon doping is moderate around $\Delta d_{100}$~1.5 Å. A conductivity along the rubbing direction was around 570 S/cm similar to those obtained for Mo(tfd-$COCF_3$)$_3$. However, the resulting PF values remain modest around 21 $\mu W\ m^{-1}\ K^{-2}$ due to a very low Seebeck coefficient (19 $\mu V\ K^{-1}$).

As a general conclusion, we have represented the important structural and TE properties for all aligned semi-crystalline P3HT films investigated in this thesis in a general illustration (scheme C1) and collect the important data relative to these systems in Table C1. Regarding the principal structural changes upon doping, Scheme C1 represents the doped structure on the scale of the crystalline lamellae. In case of flat dopant molecules, the doping occurs only in the crystalline zones, no doping of the amorphous regions occurs due to the fact that charge transfer is almost impossible between the HOMO of amorphous P3HT and the LUMO of both dopants. The poor doping of the amorphous zones limits the ultimate conductivity values reached in these systems. On the contrary, doping by $FeCl_3$ and Mo(tfd-$COCF_3$)$_3$ occurs in both crystalline and amorphous regions and this results in much larger charge conductivities.

From a structural point of view, we demonstrate that doping with $F_6$TCNNQ and Mo(tfd-$COCF_3$)$_3$ results in a progressive doping of the crystalline domains with a co-existence of doped and undoped crystalline phases of P3HT. The crystalline phase is observed to be easily doped by the smaller dopants $FeCl_3$ and $F_4$TCNQ without coexistence of doped and undoped P3HT crystals. Differences in diffusions coefficients of the dopants might be one of the reasons for explaining this difference between the two classes of dopants.

***Table C1:*** *Thermoelectric, optical and structural characteristics for doped oriented P3HT films*

| **Rubbed SC phase P3HT film's properties** | **$F_4TCNQ$** | **$F_6TCNNQ$** | **$FeCl_3$** | **$Mo(tfd\text{-}COCF_3)_3$** |
|---|---|---|---|---|
| Electron Affinity (eV) | ~5.2 | ~5.4 | --- | ~5.6 |
| $d_{100}$ doped (Å) | 18.1 | 19.4 | 18.1 | 17.9 |
| $\Delta d_{100}$ (Å) | 1.5 | 2.8 | 1.5 | 1.3 |
| Doping efficiency | 14%(from $\varepsilon_{anion}$) | 20% (from $\varepsilon_{anion}$) | 20%( $_{S/Fe = 2.5}$ stoichiometry) | 11%(from $\varepsilon_{polaron}$) |
| | **Incremental Concentration Doping** | | | **Direct doping** |
| $\sigma_{\parallel}$ max ($S{\cdot}cm^{-1}$) | $205 \pm 50$ | $343 \pm 126$ | $570 \pm 100$ | $509 \pm 51$ |
| $\sigma_{\perp}$ max ($S{\cdot}cm^{-1}$) | $20 \pm 7$ | $70 \pm 34$ | $48 \pm 20$ | $84 \pm 8$ |
| $S_{\parallel}$ ($\mu V{\cdot}K^{-1}$) | 60 | 48 | 19 | 56 |
| $S_{\perp}$ ($\mu V{\cdot}K^{-1}$) | 14 | 15 | 8 | 13 |
| $PF_{\parallel}$ max ($\mu W{\cdot}m^{-1}{\cdot}K^{-2}$) | 73 | 79 | 21 | 160 |
| $PF_{\perp}$ max ($\mu W{\cdot}m^{-1}{\cdot}K^{-2}$) | 0.4 | 1.6 | 0.3 | 1 |
| | | | | |
| Dopes: | ***Crystalline*** | | ***Crystalline and Amorphous*** | |
| | | *Coexistence of both doped and undoped phases* | | *Coexistence of both doped and undoped phases* |

Overall these results underline the complexity of the doping mechanism for semi-crystalline polymers as there is a general competition between the doping of crystalline and amorphous phases that depends closely on i) the position of the dopant's LUMO with respect to the HOMO of the amorphous phase and ii) the dimensions of the dopants that determine their diffusion coefficients in the polymer matrix.

This conclusion was further an incentive to probe the S-σ correlation in aligned and semi-crystalline P3HT films. Interestingly, collecting the conductivities and Seebeck coefficients of the aforementioned doped systems, two clear-cut correlations between electrical conductivity and Seebeck coefficient were evidenced regardless of the dopant for the directions parallel and perpendicular to the P3HT chain direction. Figure C2a collects all average values of the Seebeck coefficients as a function of electrical conductivity collected parallel to the chain direction.

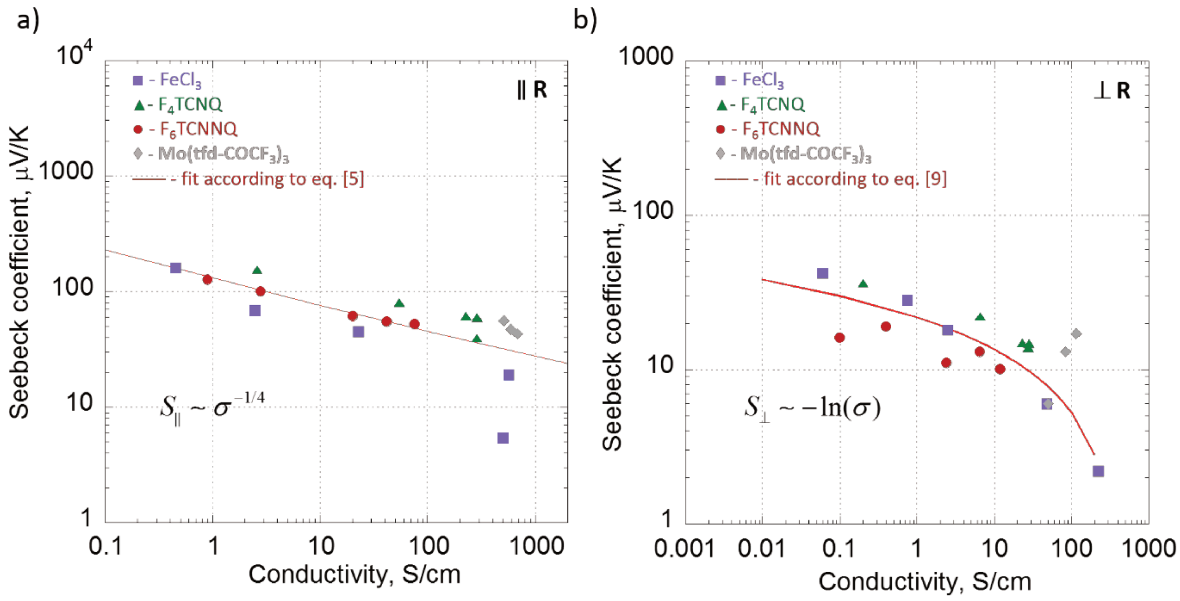


***Figure C2.*** *Seebeck coefficients as a function of electrical conductivity for three dopants measured parallel (a) and perpendicular (b) to the rubbing direction.*

The overall trend is following over the four orders of magnitude the well-known law identified by Chabinyc and coworkers as well as others[4–8]: $S \sim \sigma^{-1/4}$. Lepinoy et al. managed to explain this scaling behaviour using the concept of Dirac fermions, namely massless pseudo-relativistic quasiparticles that are scattered by unscreened ionized impurities.[8] Noteworthy, the data points for the Mo(tfd-$COCF_3$)$_3$ dopant tend to lie outside the master curve. This might indicate that structural aspects related e.g. to the doping of the amorphous phase could come into play. Indeed, the scaling law is essentially observed for doped systems sharing the same structure independently of the oxidation level[3]. This is why the ICD doping protocol developed within the frame of this thesis is particularly appealing as it helps investigate a large range of doping levels while preserving the pristine polymer structure to

the extent possible. More generally, the structural variability in the pristine polymer films prior to doping is certainly one of the reasons explaining the large data dispersion around the average scaling law. In the frame of this study, we also show that a different trend is observed in the direction perpendicular to the chain direction: $S \sim -\ln\sigma$ Such a trend was previously reported for polyaniline and polypyrrole by Mateeva et al.[9] These results clearly indicate different intrinsic limitations in charge transport in the directions parallel and perpendicular to the polymer backbone. [3] Recently, Scheunemann et al. have studied the impact of structural anisotropy on the TE properties in disordered organic semiconductors namely PBTTT using kinetic Monte Carlo simulations.[10] The departure from the common law in the direction perpendicular to the rubbing/stretching can be explained due to an introduced anisotropy of the localization length of the charge carriers. The simulations showed that variable-range hopping (VRH) can efficiently describe charge transport in both directions provided different localization lengths are used in the directions parallel and perpendicular to the chains.

Table C1 summarizes the main TE results obtained for four different P3HT:dopant systems. It highlights the efficiency of metal-organic based compounds reaching a record conductivity value of 570 S/cm in the direction parallel to rubbing for $FeCl_3$-doped films. The fact that the record PF value of 160 $\mu W \cdot m^{-1} \cdot K^{-2}$ is obtained for Mo(tfd-$COCF_3$)$_3$ highlights the importance of both having high conductivity while preserving high enough Seebeck coefficient. The reason why high Seebeck coefficients are obtained for Mo(tfd-$COCF_3$)$_3$ remains unclear. One potential reason could be that the presence of fluorine atoms helps reduce the Coulombic interactions between the polaron and the anion and thus ensure large charge mobilities despite lower oxidation level as compared to $FeCl_3$. A very recent paper by

Hofmann et al. demonstrates the use of a strong oxidant – tris(4-bromophenyl)ammoniumyl hexachloroantimonate (Magic Blue) (EA ~ 5.8 eV) to dope efficiently a large palette of conjugated polymers.[11] Upon doping with Magic Blue most polymers displayed intense polaronic absorption features, while the electrical conductivity ranged from $10^{-2}$ to $10^{2}$ S cm$^{-1}$ (when doped in air) and the PF were in the range $10^{-1}$ - 10 µW m$^{-1}$ K$^{-2}$ for non-oriented thin films. Preliminary results recently obtained in our group for P3HT:Magic Blue managed to reach conductivities of ~2000-3000 S cm$^{-1}$ leaving a promising perspective for another highly efficient organic TE system.

This thesis was an important opportunity to investigate the correlations between structure and charge transport in doped aligned P3HT films. However, to fully validate our approach on alignment of polymers for TE applications, it remains essential to retain low thermal conductivities, especially along the chain direction. The TE efficiency of the aligned devices is related to the resulting anisotropy of the thermal conductivity which enters the eq. (2) of the figure of merit ZT. To have high thermoelectric device efficiency it is important to have both high electrical conductivity and thermopower and low thermal conductivity in the same direction.

Preliminary experiments were conducted in the frame of a collaboration with the group of prof. Oliver Fenwick from the Queen Mary University of London initiated by L. Biniek. The anisotropic thermal conductivity of oriented $F_4$TCNQ-doped P3HT films was measured and the resulting figures of merit ZT were determined for both isotropic and aligned P3HT films.[12]

***Table C2.*** *Thermoelectric properties of $F_4TCNQ$-doped P3HT films for both isotropic and oriented samples. The directions are in regard of the rubbing direction.*

| Average values | Non-rubbed | ∥ | ⊥ |
|---|---|---|---|
| $\sigma$, S.cm$^{-1}$ | 8.9 ± 1.8 | 110 ± 10 | 11 ± 4 |
| $\alpha$, µV.K$^{-1}$ | 55 ± 2 | 62 ± 3.8 | 14 ± 1.7 |
| $\kappa$, Wm$^{-1}$K$^{-1}$ | 1.08 ± 0.01 | 0.69 ± 0.04 | 0.14 ± 0.05 |
| PF, µW.m$^{-1}$K$^{-2}$ | 2.7 ± 0.8 | 42 ± 9 | 0.2 ± 0.12 |
| ZT x 10$^{-4}$ | 7.30 ± 2 | 180 ± 28 | 4.5 ± 1.1 |

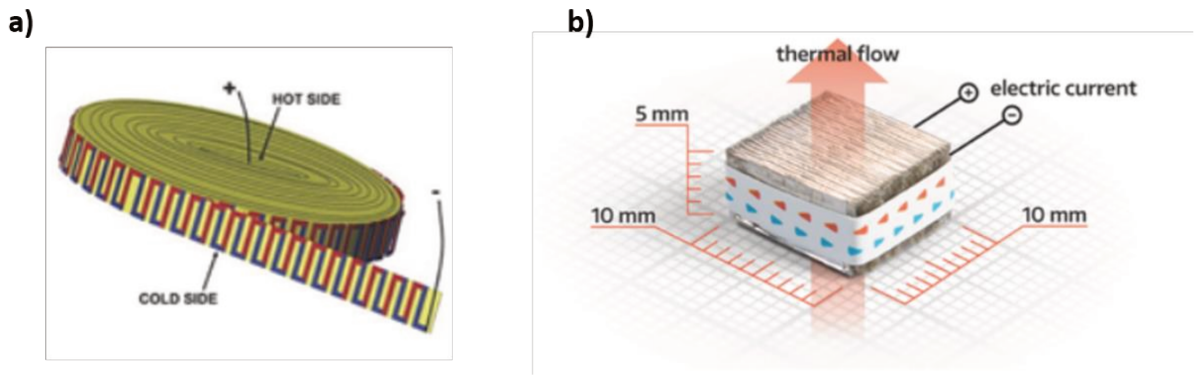


***Figure C3.*** *A schematic representation of possible TEG geometries. a) coin-shape coiled-up geometry and b) "accordion-like shape" printed on a foil and then folded to a 3D shape. Reproduced from ref.*[13,14]

Table C2 shows room temperature thermoelectric properties, power factor and figure of merit of non-rubbed doped P3HT and rubbed doped P3HT. As it can be seen from Table C2,

the effect of the in-plane thermal conductivity on resulting figure of merit is an important factor which is very sensitive to the film morphology and furthermore to the nature of the dopant. Most importantly, despite increased thermal conductivity along the chain direction, the PF of the oriented films is indeed improved by a factor 20-25 with respect to non-oriented P3HT.

The previous results evidence the benefits of using oriented and doped systems to boost TE properties in comparison to isotropic polymer films. Therefore, the alignment method used in this study, i.e. high-T rubbing, can be a very promising tool for preparing high-ZT flexible thermoelectric generators (TEGs). To this aim, different complex large-scale device geometries could be implemented such as e.g. coin-shape coiled-up[13] or printed on a foil and then folded to a 3D shape.[14] The later geometry has been successfully used by the start-up company Otego GmbH (Germany) (see Figure C3b). It would be perfectly adapted to the high-T rubbing method. Indeed, rubbing could be applied to large printed sheats of p and/or n-type polymer semiconductors that could further be doped once aligned. Folding would then be used in the final step to realize the TEG shown in Figure C3b with the rubbing direction parallel to the temperature gradient.

We believe that some of the results presented in this thesis might be of high interest for the experimental and theoretical physicist for further investigations of physical processes associated with thermoelectricity. However further investigations accounting for the role of the thermal conductivity in anisotropic systems as well as stability experiments are needed to further advance in the field of organic thermoelectrics.

The complexity of such organic-based systems challenges the development and accuracy of predicted theoretical models e.g. for charge transport in doped polymer

semiconductors. Going one step ahead, we believe that a high amount of empirically studied polymer:dopant systems reported in the literature could serve as a data collection for further development of organic thermoelectrics by means of data science methodologies such as machine learning algorithms and combinatorial screening. Both are already successfully applied in the neighboring field of organic photovoltaics. [15–19] One of the key feature of machine-learning based methods is the ability to forecast material properties, even when fundamental understanding of the chemistry/physics behind the property is lacking.[18] Recently, Sahu and coworkers have shown that by using artificial intelligence machine-learning methods one is able to capture the complexity of a device and build a model that can efficiently foresee the efficiency (not just simple properties such as a bandgap) of photovoltaic device from its constituents with an outstanding correlation of r = 0.79.[19] Another inspiring work of Cao et al. applies a so-called Design of Experiments approach toward the optimization of a bulk heterojunction (the core element of an organic photovoltaics device) from a low band gap polymer, poly[N-9′ - heptadecanyl-2,7-carbazole-alt-5,5-(4′ ,7′ -di-2-thienyl-2′ ,1′ ,3′ - benzothiadiazole)] (PCDTBT). The authors demonstrate how the experimentalist can save time by using such an approach that *"enables one to 'see the big picture' before walking through a narrow valley of one-dimensional data".* This allows to avoid enormous amount of time needed for the conventional "one factor/one variable" approach at a time - a standard scientific approach. The most efficient combination of parameters found by machine-learning algorithms can lead the scientist towards the most productive experiments to be performed in the laboratory.[18]

**References:**


1. Untilova, V., Biskup, T., Biniek, L., Vijayakumar, V. & Brinkmann, M. Control of Chain Alignment and Crystallization Helps Enhance Charge Conductivities and Thermoelectric Power Factors in Sequentially Doped P3HT:F4TCNQ Films. *Macromolecules* (2020) doi:10.1021/acs.macromol.9b02389.
2. Untilova, V. *et al.* High Thermoelectric Power Factor of Poly(3-hexylthiophene) through In-Plane Alignment and Doping with a Molybdenum Dithiolene Complex. *Macromolecules* (2020) doi:10.1021/acs.macromol.0c01223.
3. Vijayakumar, V. *et al.* Bringing conducting polymers to high order: towards conductivities beyond 105 S/cm and thermoelectric power factors of 2 mW·m–1.K–2. *Adv. Energy Mater.* **9**, 1900266 (2019).
4. Glaudell, A. M., Cochran, J. E., Patel, S. N. & Chabinyc, M. L. Impact of the Doping Method on Conductivity and Thermopower in Semiconducting Polythiophenes. *Adv. Energy Mater.* **5**, 1401072 (2015).
5. Patel, S. N. *et al.* Morphology controls the thermoelectric power factor of a doped semiconducting polymer. *Science Advances* **3**, (2017).
6. Hynynen, J., Kiefer, D. & Muller, C. Influence of Crystallinity on the Thermoelectric Power Factor of P3HT Vapour-Doped with F4TCNQ. *RSC Adv.* **8**, 1593 (2018).
7. Kang, S. D. & Snyder, G. J. Charge-transport model for conducting polymers. *Nature Materials* **16**, 252 (2016).
8. Lepinoy, M., Limelette, P., Schmaltz, B. & Van, F. T. Thermopower scaling in conducting polymers. *Scientific Reports* **10**, 8086 (2020).

9. Mateeva, N., Niculescu, H., Schlenoff, J. & Testardi, L. Correlation of Seebeck coefficient and electric conductivity in polyaniline and polypyrrole. *JOURNAL OF APPLIED PHYSICS* vol. 83 3111–3117 (1998).

10. Scheunemann, D. *et al.* Rubbing and Drawing: Generic Ways to Improve the Thermoelectric Power Factor of Organic Semiconductors? *Advanced Electronic Materials* **6**, 2000218 (2020).

11. Hofmann, A. I. *et al.* Chemical Doping of Conjugated Polymers with the Strong Oxidant Magic Blue. *Advanced Electronic Materials* **6**, 2000249 (2020).

12. Degousée T. *et al.* In-plane thermal conductivity of aligned P3HT for thermoelectric application. to be submitted.

13. Weber, J. *et al.* Coin-size coiled-up polymer foil thermoelectric power generator for wearable electronics. *Sensors and Actuators A: Physical* **132**, 325–330 (2006).

14. Russ, B., Glaudell, A., Urban, J. J., Chabinyc, M. L. & Segalman, R. A. Organic thermoelectric materials for energy harvesting and temperature control. *Nature Reviews Materials* **1**, 16050 (2016).

15. Teichler, A. *et al.* Combinatorial Screening of Polymer:Fullerene Blends for Organic Solar Cells by Inkjet Printing. *Advanced Energy Materials* **1**, 105–114 (2011).

16. Lopez, S. A., Sanchez-Lengeling, B., de Goes Soares, J. & Aspuru-Guzik, A. Design Principles and Top Non-Fullerene Acceptor Candidates for Organic Photovoltaics. *Joule* **1**, 857–870 (2017).

17. Sánchez-Díaz, A., Rodríguez-Martínez, X., Córcoles-Guija, L., Mora-Martín, G. & Campoy-Quiles, M. High-Throughput Multiparametric Screening of Solution Processed Bulk Heterojunction Solar Cells. *Advanced Electronic Materials* **4**, 1700477 (2018).

18. Cao, B. *et al.* How To Optimize Materials and Devices via Design of Experiments and Machine Learning: Demonstration Using Organic Photovoltaics. *ACS Nano* **12**, 7434–7444 (2018).

19. Sahu, H., Rao, W., Troisi, A. & Ma, H. Toward Predicting Efficiency of Organic Solar Cells via Machine Learning and Improved Descriptors. *Advanced Energy Materials* **8**, 1801032 (2018).

# Experimental details

## 1. Materials used in this study

Regioregular P3HT was purchased from Merck ($M_W$ = 43.6 kDa, PDI = 1.8, RR~95.9%). $F_4$TCNQ was purchased from TCI. Anhydrous solvents such as acetonitrile and orthodichlorobenzene were obtained from Sigma-Aldrich and used without purification.

F6TCNNQ was synthesized in the group of Nicolas Leclerc (ICPEES) following the general method given by Vijayakumar and coworkers in the ref.[1]

Sodium polystyrenesulfonate (NaPSS) was purchased from Sigma-Aldrich.

Mo(tfd-$COCF_3$)$_3$ was synthesized as previously described.[2] Anhydrous acetonitrile (AcN; purity >99.9%), chloroform ($CHCl_3$; purity >99.5%), o-dichlorobenzene (oDCB; purity >99%), $FeCl_3$ and $TBAPF_6$ were purchased from Sigma-Aldrich and used as received.

## 2.1 Preparation of glass slides

Prior its use, the glass slides for thin film deposition were cleaned in a sonication bath in different solvents. Glass slides were sonicated successively in acetone, isopropanol and an aqueous solution of Hellmanex (diluted to 1:50 in distilled water) for about 10 minutes each time. Afterwards, these glass slides were sonicated three times for 10 minutes each in pure distilled water to remove the excess Hellmanex traces. The films were dried under a nitrogen flow prior to thin film deposition.

## 2.2 Film deposition

Films were deposited using a home-made so-called doctor-blading machine. (see Figure E1). The machine consists of a PTFE flat blade that spreads a given amount of polymer solution (30 μl) across a hot substrate (160°C) at a constant speed (1 mm/s). Prior to deposition, the P3HT solution in oDCB (10 mg/ml) was stirred at 100°C for around 3 h.

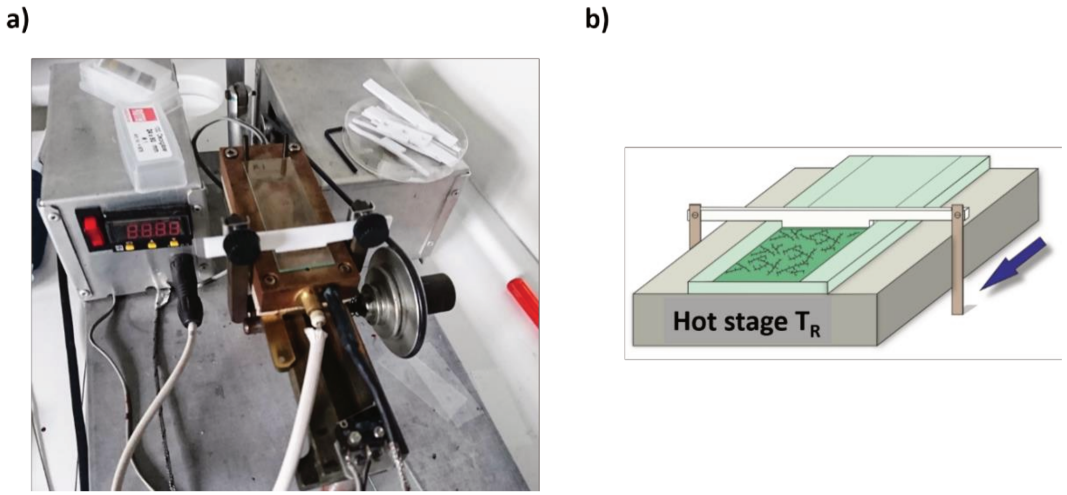


***Figure E1.*** *a) Image of the home-made doctor-blading machine for thin film deposition and its schematic illustration (b).*

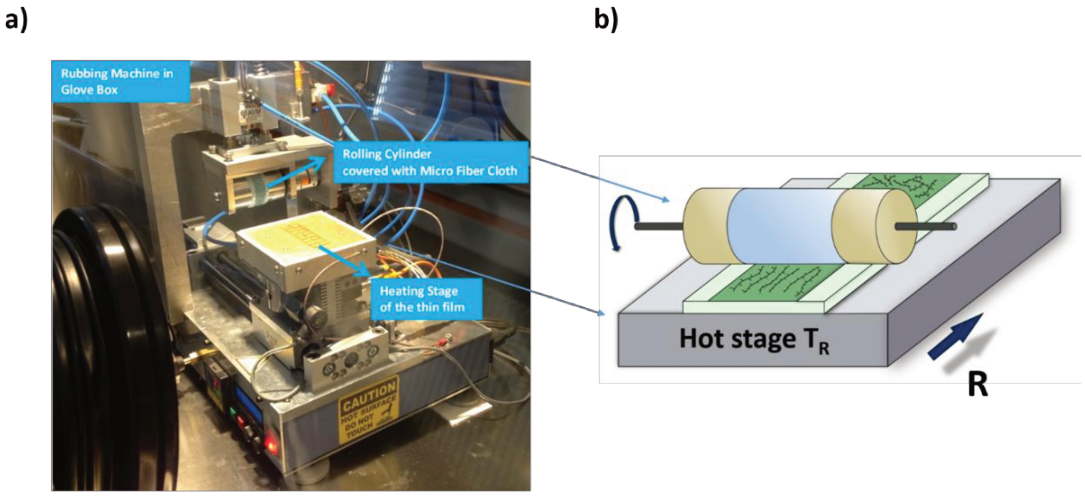


***Figure E2.*** *a) A picture of the rubbing machine, b) a schematic illustration of the rubbing method.*

## 2.3 Thin film orientation by high-temperature rubbing

High-T rubbing method was developed in the SYCOMMOR group in the early 2012.[3,4] The rubbing machine consists of a metallic cylinder (~4 cm in diameter) covered with a microfiber cloth (see Figure E2). The cylinder is rotated at a constant rate of ~300 RPM during the rubbing process and can be adjusted if needed. The cylinder is applied with a 2-3 bar pressure on top of the thin film placed on the hot stage with controlled temperature $T_R$. The hot stage is translated at a speed of 5 mm/s. A calibration using the IR thermometer was performed in order to account for the temperature difference between the glass slide and the temperature of the hot stage.

In the 2nd Chapter the P3HT-films were rubbed at different rubbing temperatures ($T_R$) in order to explore its effect on film morphology and thermoelectric properties. The rubbing was performed inside a Plaslabs glove box under nitrogen atmosphere ($P_{O2}$<0.1 %) in order to avoid oxidation of the polymer.

## 2.4 Doping methods

All doping experiments were performed under an inert atmosphere in a glovebox from Jacomex with $P_{O_2} < 3$ ppm and $P_{H_2O} < 1$ ppm. All dopant solutions were prepares right before doping of the films to avoid aging of solutions. Unless specified, we did not rinse the films after solution doping.

### A) Doping by $F_4TCNQ/F_6TCNNQ$

In the 1st Chapter, the doping was performed following the sequential doping method[5] with full sample immersion for 10 s in the dopant solution. The $F_4TCNQ$ solution for doping was prepared with acetonitrile (AcN) at a concentration of 1 g/l. Such short doping times are sufficient to reach saturation of the film doping level as shown earlier by Jacobs et al.[6] No rinsing step was conducted as it may lead to dedoping of the films. Both doping and rubbing were performed under nitrogen atmosphere.

In the Chapter 3, the doping by both $F_4TCNQ$ and $F_6TCNNQ$ was performed following the incremental concentration doping (ICD) procedure[7] with full sample immersion for 10 s in the dopant solution of increasing concentration. The following concentrations were used:

| | Concentration, g/l | | | | | |
|---|---|---|---|---|---|---|
| $F_4TCNQ$ | 0.01 | 0.1 | 0.5 | 1 | 2 | -- |
| $F_6TCNNQ$ | 0.05 | 0.1 | 0.5 | 1 | 5 | 10 |

### B) Doping by $Mo(tfd\text{-}COCF_3)_3$

Dopant solutions were prepared by mixing equal amounts of AcN and $CHCl_3$, followed by addition of $Mo(tfd\text{-}COCF_3)_3$ powder yielding a concentration of 7.5 g/l. Lower concentrations (0.1, 1, and 2.5 g/l) were obtained by dilution of the 7.5 g/l stock solution with 1:1 AcN:$CHCl_3$. Doping was performed by drop-casting the dopant solution on top of P3HT films, which was left in contact for 3 min before spinning off the solution. Sequential doping did not alter the film thickness as indicated by atomic force microscopy (AFM) of a spin-coated P3HT film before and after doping (30 vs 31 nm) using a Digital Instruments Nanoscope IIIA.

### C) Doping by $FeCl_3$

10 mM $FeCl_3$ solutions were prepared by dissolving 8 mg of $FeCl_3$ in 5 mL anhydrous nitromethane in a glass vial and subsequent dilution yielded the solutions with concentration in the range (0.1–5) mM. Doping was done by dipping the oriented polymer film in the dopant solution for 30 s to 1 min until no color change was any more visible. The clear decrease in polaronic absorption correlated with the increase of sample resistance. Typically, the sample's resistance increased by a factor 5 after 1 h in ambient. Therefore, all electrical characterizations were performed in a glovebox, whereas UV–vis–NIR measurements were performed within 1–2 min after transfer of the sample to the spectrometer in ambient to avoid substantial dedoping.

## 3. Polarized UV-Vis-NIR spectroscopy

The orientation of the polymer films was probed by UV−vis−NIR absorption (350−2500 nm) using a Varian Cary5000 spectrometer with polarized incident light (spectral resolution of 1 nm). The UV-Vis-NIR spectra of the doped polymer film were measured using the light polarization in parallel and in perpendicular to the direction of rubbing. The parallel/perpendicular configurations are the positions where the polymer backbone axis was parallel/perpendicular to the light polarization. Angle-dependent polarized UV-Vis-NIR spectroscopic measurements were performed by rotating the polarizer with respect to the rubbing direction from 0° to 90° recording the spectra each 10°.

**4. Doping level estimation for $F_4TCNQ$/$F_6TCNNQ$-doped P3HT films**

The apparent doping level n was calculated as the ratio between the molar concentration of the dopant anion concentration $C_{molar}^{F_4TCNQ^-}$ and the molar concentration of thiophenes $C_{molar}^{thiophene}$ namely

$$n = \frac{C_{molar}^{F_4TCNQ^-}}{C_{molar}^{thiophene}} \quad [1]$$

The thiophene molar concentration $C_{molar}^{thiophene}$ was calculated from the volume of the unit cell of P3HT and the fact that it contains four thiophene monomers: $C_{molar}^{thiophene} = \frac{4}{V}$, where $V$ - is the unit cell volume (of the doped phase). The Beer-Lambert-Bouger law served to evaluate $C_{molar}^{F_4TCNQ^-}$ using the absorbance of the characteristic anion bands and the corresponding extinction coefficient:

$$A = \varepsilon LC \quad [2]$$

where A – absorbance, ε - extinction coefficient of the dopant, L – optical path length (film thickness) and $C$ - concentration of the attenuating species (dopant concentration).

For oriented films, the dopant absorbance was determined as the average value extracted from the angular dependent polarized UV-Vis measuments for both dopants (curves are presented in the Chapter 2). The extinction coefficient for $F_4TCNQ^-$ and $F_6TCNQ^-$ anions are $\varepsilon^{F_4TCNQ} = 50000\frac{l}{mol \cdot cm}$ and $\varepsilon^{F_6TCNNQ} = 53667\frac{l}{mol \cdot cm}$, respectively. The latter

was found from the slope of the absorbance curve as a function of the dopant concentration. (see Figure E3)

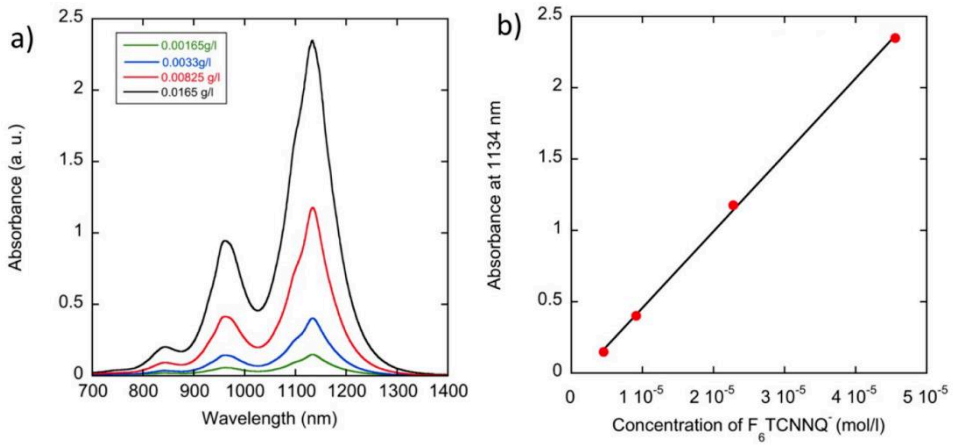


*Figure E3. a) UV-Vis spectra of $F_6TCNNQ^-$ anion absorption spectrum in AcN in the presence of ferrocene. b) absorbance versus $F_6TCNNQ^-$ anion concentration yielding an extinction coefficient* $\varepsilon^{F_6TCNNQ} = (53667 \pm 1000)\frac{l}{mol \cdot cm}$ .

**5. Transmission Electron Microscopy**

Oriented areas were identified for TEM analysis by optical microscopy (Leica DMR-X Microscope). The polymer films were coated with a thin amorphous carbon layer using an Auto 306 evaporator (Edwards). P3HT films were removed from the glass substrate by floating on water and subsequent recovery on TEM copper grids. TEM was performed in bright field and diffraction modes using a CM12 Philips microscope equipped with a MVIII (Soft Imaging System) charge coupled device camera.

Calibration of the reticular distances in the ED patterns was made with an oriented polytetrafluoroethylene (PTFE) film on the patterns where the monomer periodicity

reflection was not present, otherwise $\mathbf{c}_{monomer}$ was used for the calibration. Beam exposure was set to a minimum using the low dose system to avoid dedoping under the electron beam that is observed when the same zone is exposed for a prolonged period of time. Dedoping is clearly manifested in the ED pattern by a change in reticular distances to those of the pristine undoped P3HT films.

### 6. Electron Paramagnetic Resonance measurements

The films for EPR measurements were prepared by floating doctor-bladed and rubbed films on quartz substrates (Ilmasil PS, QSIL GmbH) with dimensions of 3 × 25 mm and a thickness of 0.2 mm. Inside the glovebox, each sample was carefully sealed in a synthetic quartz glass tube (Ilmasil PS, QSIL GmbH) with dimensions of 3.8 × 3.0 × 240 $mm^3$ using Critoseal vinyl plastic. X-Band EPR spectroscopy was performed at room temperature on an Elexsys 580 (Bruker Biospin GmbH) spectrometer equipped with a 4119HS-W1 (Bruker) cavity. Typical acquisition parameters are as follows: microwave frequency, 9.830 GHz; microwave power, 150 mW (30 dB attenuation, 150 mW source power); modulation frequency, 100 kHz; modulation amplitude, 0.1 mT.

### 7. Electrical conductivity and thermopower measurements

All devices were fabricated on glass substrates cleaned by ultrasonication in acetone, ethanol, Hellmanex, and deionized water (×3 times). The cleaned substrates were dried under nitrogen and exposed to plasma prior to film deposition. Gold electrical contacts (40 nm thick) in a four-point probe geometry (1 mm spacing between electrodes, 5 mm length) were

deposited via controlled thermal evaporation through a shadow mask, at an average rate of 4−6 Å/s by Nicolas Zimmermann from ICUBE. A first layer of chromium (2.5 nm thick) was deposited prior the gold to promote good adhesion on the glass substrates (evaporation rate 0.5−1 Å/s). The geometry of deposited gold electrodes allows determining the charge transport and thermopower on a same substrate in both parallel and perpendicular direction to rubbing. Oriented films of P3HT were floated on water and carefully recovered on the device with predeposited gold electrodes following the doping procedure described above. (see Figure E4).

Four-point probe measurements of electrical conductivity were performed using a Keithley 4200-SCS instrument and a Lab Assistant Semiprobe station in a Jacomex glovebox under $N_2$ atmosphere. The resistivity ρ was derived from the sheet resistance R such that $\rho = R \cdot C \cdot t$, where t is the film thickness and C is a geometrical correction factor. The latter was determined using a classical four-point probe apparatus, yielding $\rho = 1.81Rt$. The average conductivity value for a given rubbing temperature was taken as the average of two to four devices.

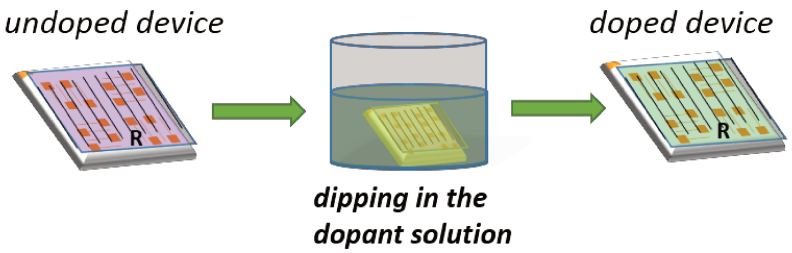


***Figure E4****. The schematic of the doping of devices for conductivity measurements for most of the samples in current study.*

Thermopower measurements were conducted in nitrogen atmosphere on the same devices. (see Figure E5) The thermopower was measured using a differential temperature method whereby a temperature gradient was established across the sample along or perpendicular to the rubbing direction.

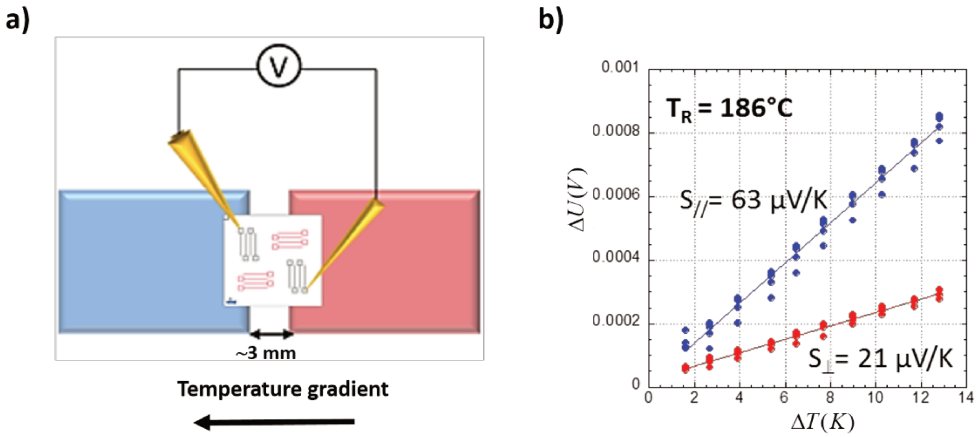


*Figure E5. a) Schematic of the Seebeck coefficient measurements, b) a typical example of the curve of Seebeck voltage versus applied temperature difference measured both in parallel (blue) and in perpendicular (red).*

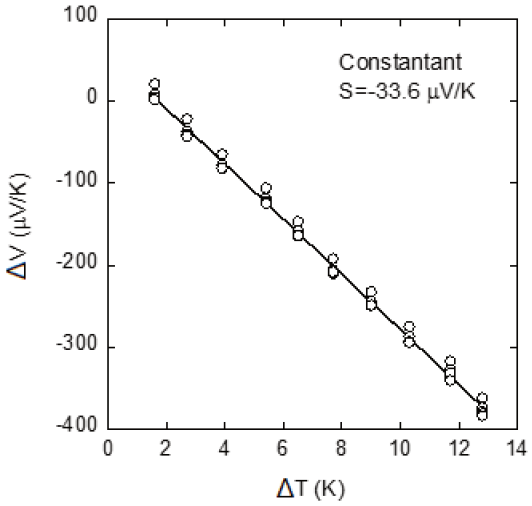


***Figure E6:*** *Calibration curve for the Seebeck coefficient measurement setup using constantan as as a reference.*

The measurements were performed by using a homemade setup made of one heating and one cooling Peltier cells (3 mm gap) (see Figure E5a) providing a controllable temperature difference ΔT. Temperatures of the cold and warm sides were measured in a non-contact mode using two IR sensors avoiding thus thermal contact issues. The Seebeck tension was measured using a Keithley 2634B source meter and a semiprobe lab assistant probe station in ambient conditions. The Seebeck coefficient is calculated from the slope of Seebeck voltage versus temperature difference for ΔT varying in a range ±10K around T=23±2°C.

Calibration of the Seebeck coefficient measurement was performed using a constantan wire (see Figure E6). Most importantly, the temperatures of the hot and cold gold/doped-polymer junctions are precisely defined as they lie atop the underlying Peltier elements whose temperatures are well-defined and determined by an IR sensor.[8] As a consequence, we do not observe a dependence of the Seebeck coefficient with the contact geometry.

**8. Thin film thickness determination**

In order to determine film thickness or oriented samples we melt-annealed thin films at ~300°C in order to randomize the in-plane chain orientation as well as de-dope the films. This was done under nitrogen atomosphere using a Linkam hot stage (HS-95 controller and LTS420 stage). The UV-Vis absorption spectra of melted films were recorded. In the 2nd Chapter, the film thickness was determined using a reference determined by Podzorov et al.[9] for the absorption spectra of a thin films of known thickness. In the Chapter 3 and 4, we used the same melting procedure to randomize the chain orientation and further extracted the thickness form the absorbance of melted samples. The thickness calibration was done using

AFM measurements on multiple polymer films of increasing nominal thickness (see Figure E7 red points).

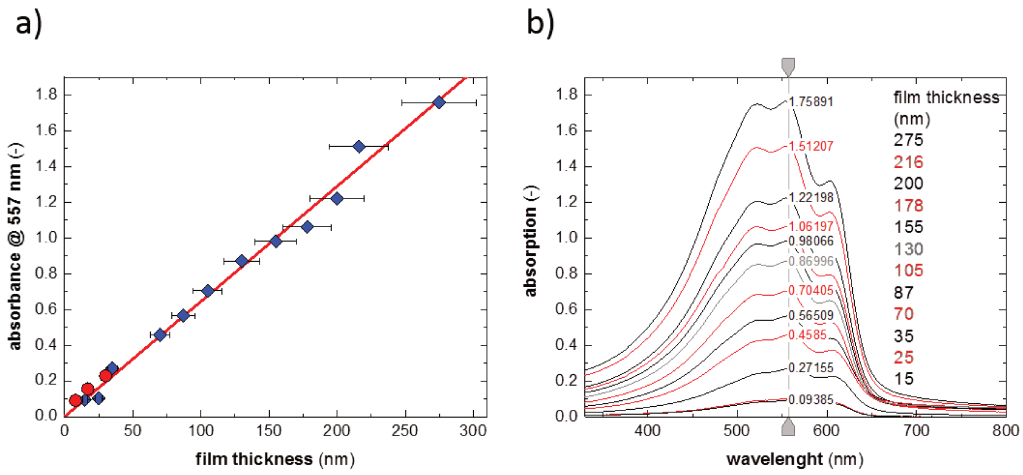


***Figure E7.*** *(a) Calibration curve for P3HT film thickness obtained by plotting the absorption at 557 nm versus film thickness. Average measurement deviation was ~ 5%, error bars in the graph represent an error of 10%. Red circles: absorbance vs. thickness measured for films prepared with the P3HT batch used in this study ($M_W$ ~ 43.6 kg mol$^{-1}$, RR ~ 95.9 %, PDI ~ 1.8) obtained from AFM measurements; Blue diamonds: absorbance vs. thickness measured for films prepared with other P3HT batch ($M_W$ ~ 63.8 kg mol$^{-1}$, RR ~ 96 %, PDI ~ 2.2) of spectra shown in b); (b) Representative absorption spectra of spin-coated P3HT ($M_W$ ~ 63.8 kg mol$^{-1}$, RR ~ 96 %, PDI ~ 2.2) from a 1:1 mixture of chlorobenzene:oDCB, the concentration of P3HT was varied from 2 to 30 g L$^{-1}$ to obtain films with different thicknesses. The UV-vis absorption spectra were measured with a Pekin Elmer Lambda 950 spectrophotometer and the thickness was measured with a KLA Tencor AlphaStep D-100 profilometer. Both methods show a good agreement for both batches.*

**9. Spectroelectrochemistry**

For the spectroelectrochemical measurements, thin P3HT films were cast onto ITO-coated glass (width 6 mm) via spin-coating from a solution of 10 g/l P3HT in oDCB. The spectroelectrochemical setup consisted of a 1 cm × 1 cm UV−Vis quartz cuvette with a custom-made Teflon lid, which holds a three electrode setup comprising the ITO/polymer sample as a working electrode, a platinum wire counter electrode, and a silver wire as pseudo-reference electrode. All electrochemical measurements were performed in a solution of 0.1 M $TBAPF_6$ in dry and degassed acetonitrile; the potential scale of our setup lies at 0.4−0.5 V relative to ferrocene/ferrocenium. Cyclic voltammetry was performed at 100 mV/s. For chronoamperometry measurements the film was first dedoped upon application of a potential of 0 V for 60 s, before the respective positive oxidation potential between 0.55 and 0.75 V was applied for 300 s. UV−vis−NIR absorption spectra were recorded by using a PerkinElmer Lambda 1050 spectrophotometer after 120 s once the electrochemical current had stabilized. The amount of injected charges was calculated by integrating the electrochemical current over time by using the background current as the baseline.

The charge-carrier density was calculated by diving the amount of the injected charge carriers by the film volume in contact with the electrolyte. The film thickness was estimated by comparing the peak absorbance of undoped P3HT at 557 nm with the calibration curve provided in Figure E6.

**References**

1. Vijayakumar, V. *et al.* Influence of dopant size and doping method on the structure and thermoelectric properties of PBTTT films doped with F6TCNNQ and F4TCNQ. *J. Mater. Chem. C* (2020) doi:10.1039/D0TC02828B.

2. Paniagua, S. A. *et al.* Production of heavily n- and p-doped CVD graphene with solution-processed redox-active metal–organic species. *Mater. Horiz.* **1**, 111–115 (2014).

3. Brinkmann, M. *et al.* Segregated versus Mixed Interchain Stacking in Highly Oriented Films of Naphthalene Diimide Bithiophene Copolymers. *ACS Nano* **6**, 10319–10326 (2012).

4. Biniek, L., Leclerc, N., Heiser, T., Bechara, R. & Brinkmann, M. Large Scale Alignment and Charge Transport Anisotropy of pBTTT Films Oriented by High Temperature Rubbing. *Macromolecules* **46**, 4014–4023 (2013).

5. Scholes, D. T. *et al.* Overcoming Film Quality Issues for Conjugated Polymers Doped with F4TCNQ by Solution Sequential Processing: Hall Effect, Structural, and Optical Measurements. *J. Phys. Chem. Lett.* **6**, 4786–4793 (2015).

6. Jacobs, I. E. *et al.* Comparison of solution-mixed and sequentially processed P3HT:F4TCNQ films: effect of doping-induced aggregation on film morphology. *J. Mater. Chem. C* **4**, 3454–3466 (2016).

7. Vijayakumar, V. *et al.* Bringing Conducting Polymers to High Order: Toward Conductivities beyond 105 S cm−1 and Thermoelectric Power Factors of 2 mW m−1 K−2. *Advanced Energy Materials* **0**, 1900266.

8. Hamidi-Sakr, A. *et al.* A Versatile Method to Fabricate Highly In-Plane Aligned Conducting Polymer Films with Anisotropic Charge Transport and Thermoelectric Properties:

The Key Role of Alkyl Side Chain Layers on the Doping Mechanism. *Advanced Functional Materials* **27**, 1700173 (2017).

9. Kao, C. Y. *et al.* Doping of Conjugated Polythiophenes with Alkyl Silanes. *Advanced Functional Materials* **19**, 1906–1911 (2009).

# *Résumé de la thèse*

**Viktoriia Untilova**

Titre : Elaboration, structure et propriétés thermoélectriques de films minces orientés et dopés séquentiellement de poly(3-hexylthiophène) régiorégulier

**Directeur de thèse :** Martin Brinkmann

## *Résumé de la thèse*

La consommation nette d'électricité dans le monde a considérablement augmenté de 1980 à 2017, en passant respectivement de 7,3 à 22,3 TWh. La consommation de l'énergie produite s'accompagne du dégagement de la chaleur résiduelle qui est généralement perdue dans l'environnement. La conversion de la chaleur perdue en électricité peut être réalisée à l'aide de la thermoélectricité (TE). Les technologies inorganiques TE ont été bien développées au cours des dernières décennies pour atteindre une efficacité TE élevée. [1] Cependant, les matériaux TE inorganiques sont coûteux à micro-fabriquer et contiennent des éléments toxiques tels que le tellure, l'antimoine et le plomb.[2] Contrairement aux matériaux TE inorganiques, les matériaux organiques sont faciles à fabriquer. Une simple modification de leur structure moléculaire permet d'ajuster les propriétés physico-chimiques dans une gamme assez vaste. La recherche et le développement de matériaux TE organiques permettront de construire des modules TE portables capables de transformer la chaleur résiduelle à basse température (par exemple la chaleur du corps, de l'électronique portable, etc.) en électricité. [2,3]

Dans le cadre du projet, nous avons étudié les propriétés TE, optiques et structurales de films minces orientés de P3HT (poly(3-hexylthiophène)) dopés. La technique de brossage à haute température permet d'aligner les chaînes polymères de P3HT dans les films minces.[4] Il s'agit de comprendre comment contrôler et améliorer les propriétés TE du P3HT dopé en tirant parti de l'alignement par brossage mécanique à haute température et d'une intercalation optimale des molécules de dopant dans la matrice de P3HT.

Le premier chapitre de thèse présente les éléments de compréhension et l'état de l'art dans le domaine des polymères conjugués pour la thermoélectricité.

Dans le 2ème chapitre, nous avons étudié l'effet de la température du brossage sur les propriétés structurales et TE du polymère dans les films minces de P3HT dopé par $F_4TCNQ$.

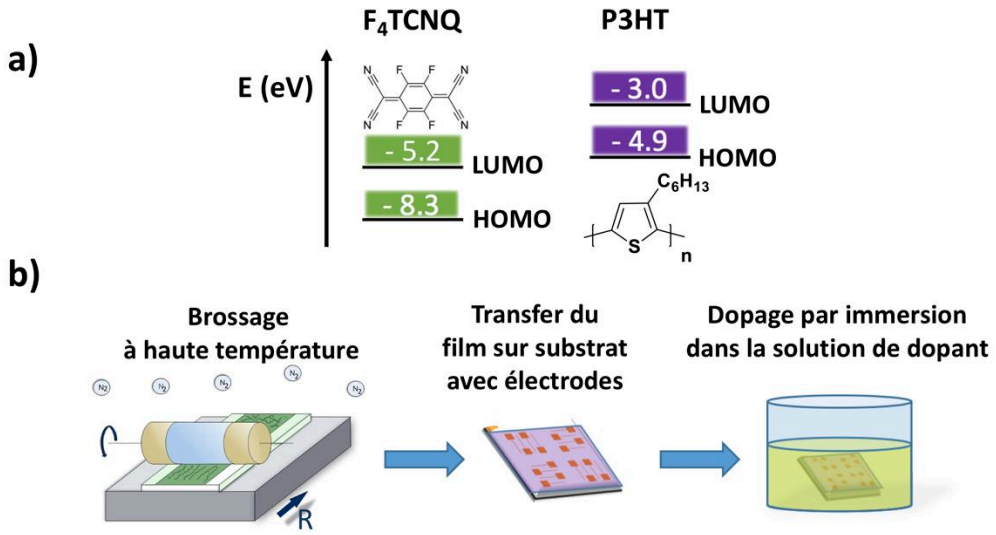


**Figure 1.** a) Structures moléculaires et niveaux HOMO/LUMO du P3HT et du F4TCNQ. b) méthode d'élaboration des films orientés et dopés de P3HT.

Plus, précisément, nous avons comparé les propriétés TE dans les deux phases qui se forment en brossant les films à différentes températures, c'est-à-dire la phase smectique et la phase semi-cristalline de P3HT (cf Figure 2). Les questions principales traitées sont : Comment la structure originale des films de P3HT (smectique versus semi-cristalline) affecte-t-elle le niveau de dopage final ? Comment les molécules de dopantes sont-elles réparties dans la structure de P3HT et dans quelle mesure les propriétés TE sont-elles affectées ? Pour répondre à ces questions, nous utilisons une combinaison de spectroscopies d'absorption UV-vis-NIR, de résonance paramagnétique électronique (EPR), microscopie électronique en transmission et diffraction électronique, mesures de conductivité et de coefficient Seebeck.

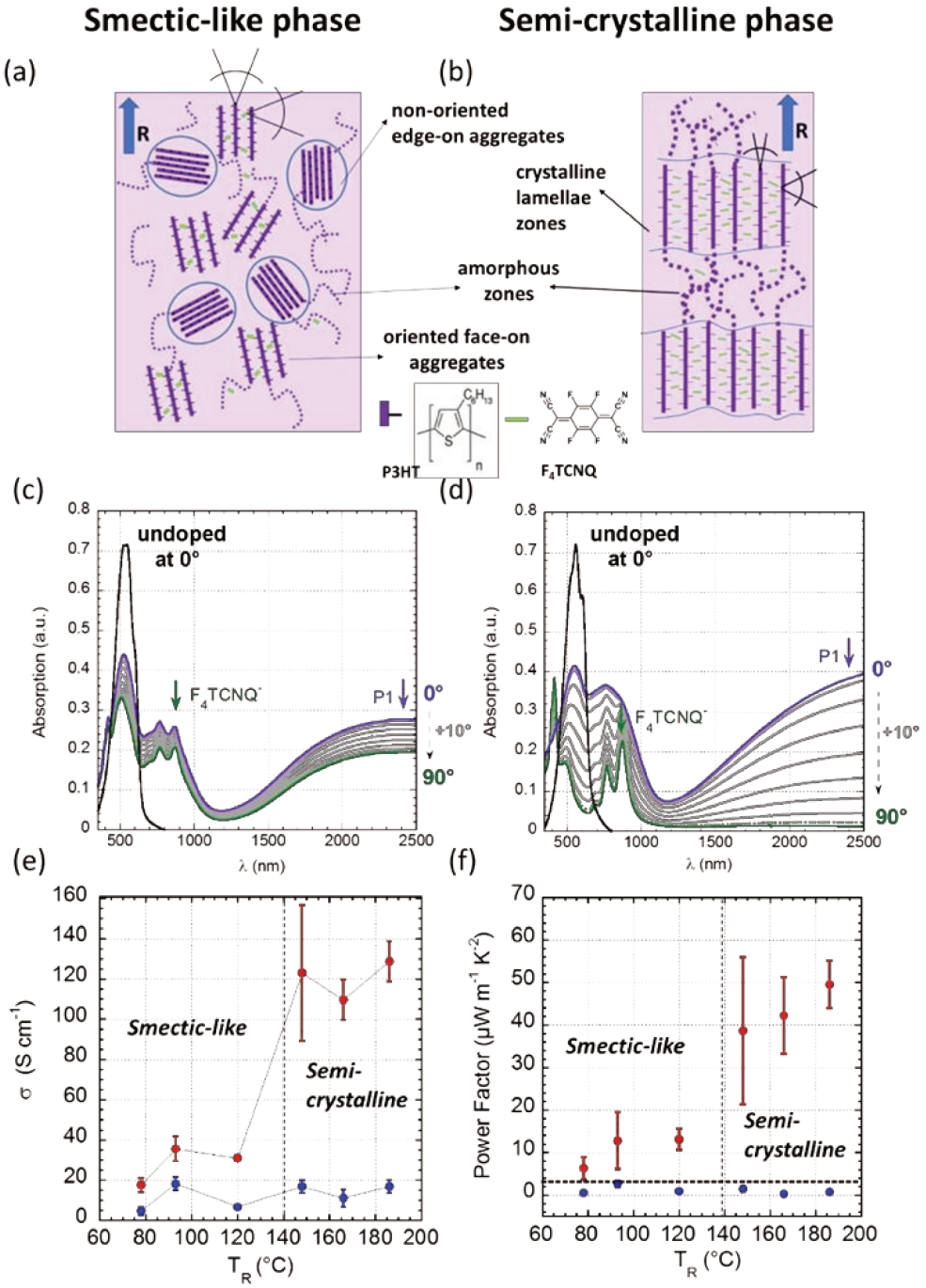


***Figure 2.*** *(a), (b) Représentations schématiques de la structure des phases smectiques et semi-cristallines du P3HT dopé avec $F_4TCNQ$. Les molécules de dopant intercalées dans les domaines de P3HT sont illustrées en vert. (c), (d) - Spectres d'absorption UV-vis-NIR polarisés de films polymères conducteurs orientés pour les phases smectiques et semi-cristallines, tracés pour différents angles (tous les 10°) entre la direction de polarisation et la direction du*

*brossage. 0° correspond à la lumière incidente polarisée parallèlement à la direction du brossage (POL//R, en violet), alors que 90 ° correspond à la lumière incidente polarisée perpendiculairement à la direction du brossage (POL⊥R en vert). Les spectres des films non dopés brossés à 0° sont représentés en noir.*[5]

La figure2 illustre les résultats obtenus dans ce 2ème chapitre.[5] En particulier, nous avons démontré que dans la phase semi-cristalline, des chaînes alkyls sont mieux ordonnées et cela permet l'intercalation d'un plus grand nombre de molécules dopantes qui sont orientées perpendiculairement à la chaîne principale du polymère. L'intercalation des molécules de $F_4TCNQ$ dans les couches de chaîne latérale résulte dans un dérèglement dans l'arrangement des piles polymère successives dans les plans (b, c) et dans l'arrangement des chaînes alkyls. En comparaison, la phase smectique est moins ordonnée est moins dopée et l'intercalation du $F_4TCNQ$ dans les couches de chaînes alkyls semble induire une réorganisation des chaînes de polymères au sein des empilements de polymères dans le plan (b, c).

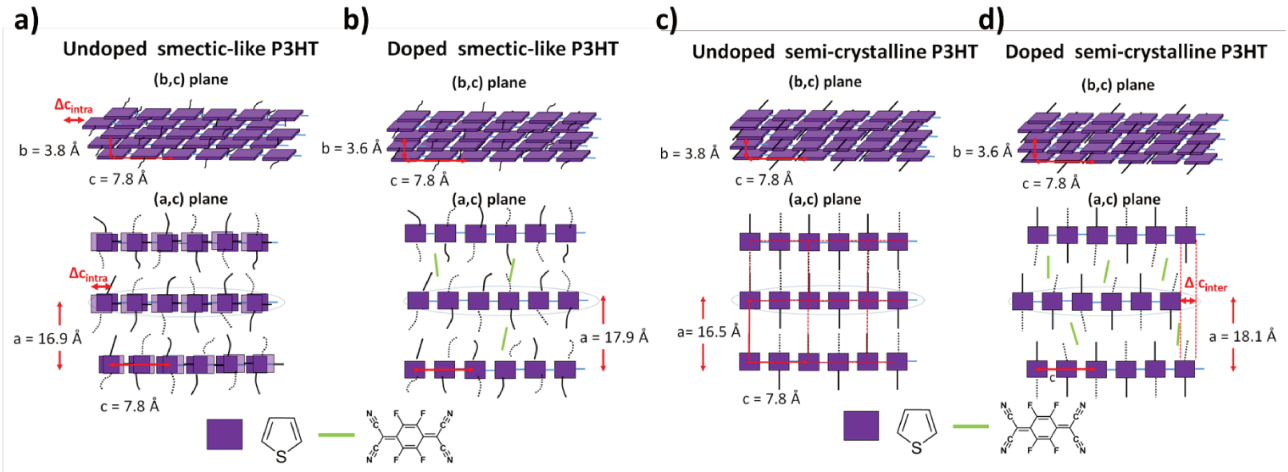


***Figure 3**. (e,f,k,l) Illustration schématique des changements structurels dans l'empilement du P3HT dopé avec $F_4TCNQ$ pour la phase smectique ($T_R$ = 78 ° C) et la phase semi-cristalline ($T_R$ =*

*186 ° C): structure non dopée (e, k) et dopée (f, l). Le dopage de la phase smectique favorise l'ordre des chaînes polymères de P3HT le long direction de la chaîne polymère dans les empilements $\pi$ individuels, tandis que pour la phase semi-cristalline, l'intercalation des dopants réorganise l'empilements $\pi$ successifs et perturbe l'organisation des chaînes latérales alkyle.*[5]

La phase semi-cristalline montre des plus grands facteurs de puissance thermoélectriques que la phase smectique (56 et 18 $\mu W \cdot m^{-1} \cdot K^{-2}$ respectivement). La figure 3 résume les transformations structurales induites lors du dopage des phases smectique et semi-cristalline du P3HT par $F_4TCNQ$.

L'étude en diffraction électronique des films dopés de P3HT permet de mieux comprendre le mécanisme d'intercalation des dopants dans la maille du P3HT de la phase semi-cristalline. Ainsi la disparition des raies *h 0 2* (h=1,2) du cliché lors du dopage et l'apparition d'une raie 0 2 0 intense et élargie montre que l'intercalation du dopant modifie la manière dont les plans adjacents de chaînes $\pi$-stackées sont déplacées selon l'axe c pour permettre l'intercalation des dopants dans la maille. De manière remarquable, l'intercalation des dopant dans la phase smectique, moins organisée, induit un degré d'ordre supérieur de cette phase après dopage. Ainsi la raie 0 2 0 initialement absente pour la phase smectique apparaît après dopage. Ceci indique que les chaînes de P3HT ont été déplacées au sein des empilements de chaînes $\pi$-stackées de P3HT.

Dans le 3ème chapitre de la thèse, nous comparons deux systèmes similaires de P3HT semi-cristallin dopés par $F_4TCNQ$ et $F_6TCNNQ$. Dans cette contribution, nous étudions l'effet du dopant sur les propriétés optiques, structurales et thermoélectriques dans des films P3HT alignés dopés séquentiellement avec $F_4TCNQ$ et $F_6TCNNQ$. Nous évaluons comment la taille du dopant et l'affinité électronique affectent la structure finale du film en fonction de la concentration de

dopant. Les principales questions abordées dans cette étude sont les suivantes : Quelles sont les différences entre $F_4TCNQ$ et $F_6TCNNQ$ en termes de structure, de propriétés optiques et TE ? Comment les molécules dopantes et leur volume moléculaire modifient la structure résultante du film dopé ? Quel est le niveau de dopage dans un tel système ? Une attention particulière est accordée aux modifications structurales qui se produisent lors du dopage de P3HT avec $F_6TCNNQ$.

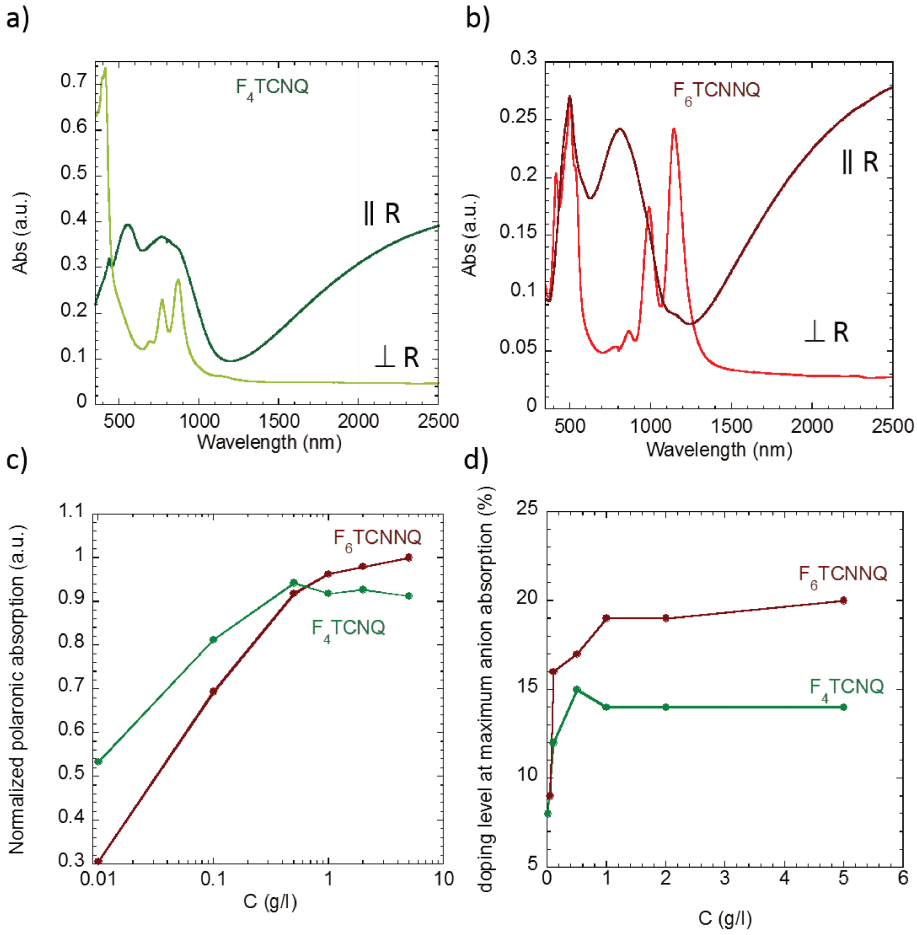


***Figure 4***. *Spectres UV–vis–NIR polarisées de films orientés de P3HT films dopés avec $F_4TCNQ$ (a) et $_{F6TCNNQ}$ (b) montrant des bandes d'absorption polaroniques très polarisées (P1, P2) lorsque la polarisation de la lumière est parallèle au sens du brossage (∥) and les bandes d'absorption caractéristiques du dopant lorsque la polarisation est perpendiculaire au brossage (⊥). Les films de p3HT sont dopés séquentiellement avec une solution à 5 g/l solution dans l'acetonitrile. c) Evolution de l'absorbance normalisée de la bande polaronique P1 à 2500 nm en fonction de la concentration en*

*dopant. d) évolution du taux de dopage (pourcentage de dopant par cycle thiophène) en fonction de la concentration de la solution de dopant.*

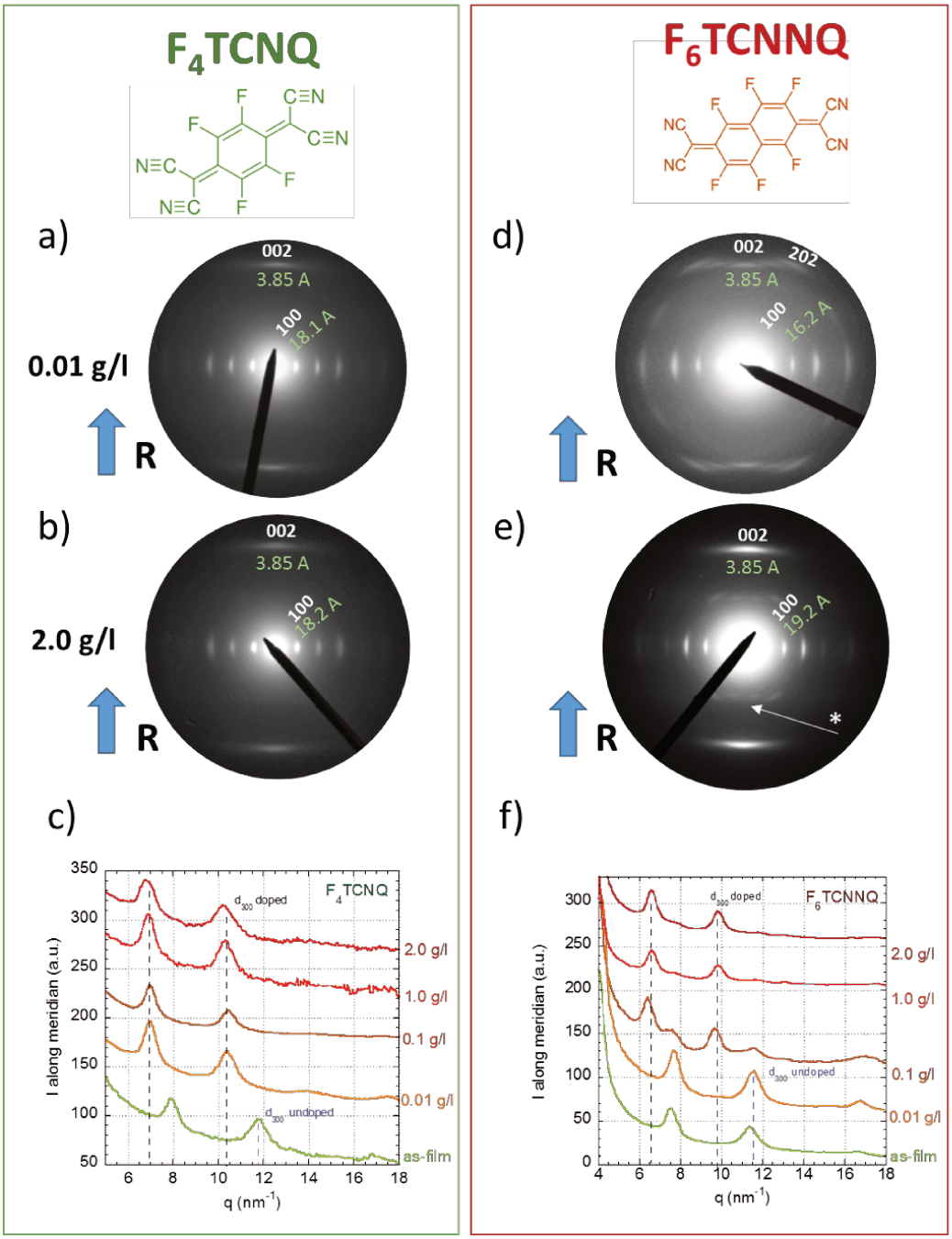


***Figure 5**: Evolution du cliché de diffraction électronique de films orientés de P3HT ($T_R$=180°C) en fonction de la concentration de dopant en solution dans l'acétonitrile. (a-c) $F_4$TCNQ et (d-f) $F_6$TCNNQ (formule chimique des dopant illustrées sur le haut de la figure). En c et f on montre les profils de section des clichés de diffraction selon l'équateur en fonction*

*de la concentration de la solution de dopant. Les traces obtenues ont été décalées arbitrairement selon l'axe des ordonnées pour clarifier la figure. Noter la présence de réflexions additionnelles (astérisque) pour les films dopés avec $F_6$TCNNQ. Pour tous les clichés, la direction de brossage est indiquée par une flèche bleue.*

Pour le $F_6$TCNNQ la situation est différente. Jusqu'à 0.01 mg/ml, on ne voit que la structure non dopée du P3HT malgré la présence de polarons en spectroscopie UV-vis-NIR. En revanche à partir de 0.1 mg/ml, les structures dopée et non-dopée coexistent. A partir de 1.0 mg/ml, l'échantillon est constitué presque exclusivement de la phase dopée.

La diffraction électronique (DE) fournit des preuves convaincantes de l'intercalation des dopants $F_6$TCNNQ dans le réseau cristallin de P3HT. Un modèle minimisé en énergie a été obtenu pour la structure de P3HT dopé avec $F_6$TCNNQ. On obtient une maille triclinique de symétrie P-1 avec a=18.8 Å, b=8.95 Å, c=7.75Å, $\alpha$=107.6°, $\beta$=101.5° and $\gamma$=89.3°. Cette structure obtenue à partir d'une analyse de la diffraction électronique montre que la stoechiométrie maximale de la phase dopée est d'un dopant pour quatre monomères thiophène, soit une concentration de dopage maximale d'environ 25%. Ceci est cohérent avec les valeurs obtenues par la méthode spectroscopique en tenant compte du fait que la phase amorphe du P3HT n'est pas ou très peu dopée. La structure obtenue rend compte des modifications de la maille du P3HT (expansion selon l'axe **a** et réduction de la distance entre plans thiophènes $\pi$-stackés).

La spectroscopie UV-vis-NIR polarisée a été utilisée pour suivre le mécanisme de dopage des couches orientées et semi-cristallines de P3HT en fonction de la concentration de dopant $F_4$TCNQ et $F_6$TCNNQ (cf Figure 4). Nous avons pu mesurer des taux de dopage maximum de l'ordre de 14% et 20% pour les dopants $F_4$TCNQ et $F_6$TCNNQ. Cette différence est cohérente avec la position de la

LUMO du $F_6$TCNNQ plus faible que pour le F4TCNQ, donnant lieu à un taux d'oxydation des chaînes de P3HT plus élevé.

En ce qui concerne la structure, le $F_4$TCNQ et le $F_6$TCNNQ dopent essentiellement la partie cristalline du P3HT, mais les mécanismes de dopage sont différents. Dans le cas du $F_4$TCNQ, le dopage modifie la structure dès les très faibles taux de dopage (0.01 mg/ml) et la diffraction électronique ne montre qu'une seule structure dopée présente. Les paramètres de la maille de cette structure dopée évoluent avec le taux de dopage.

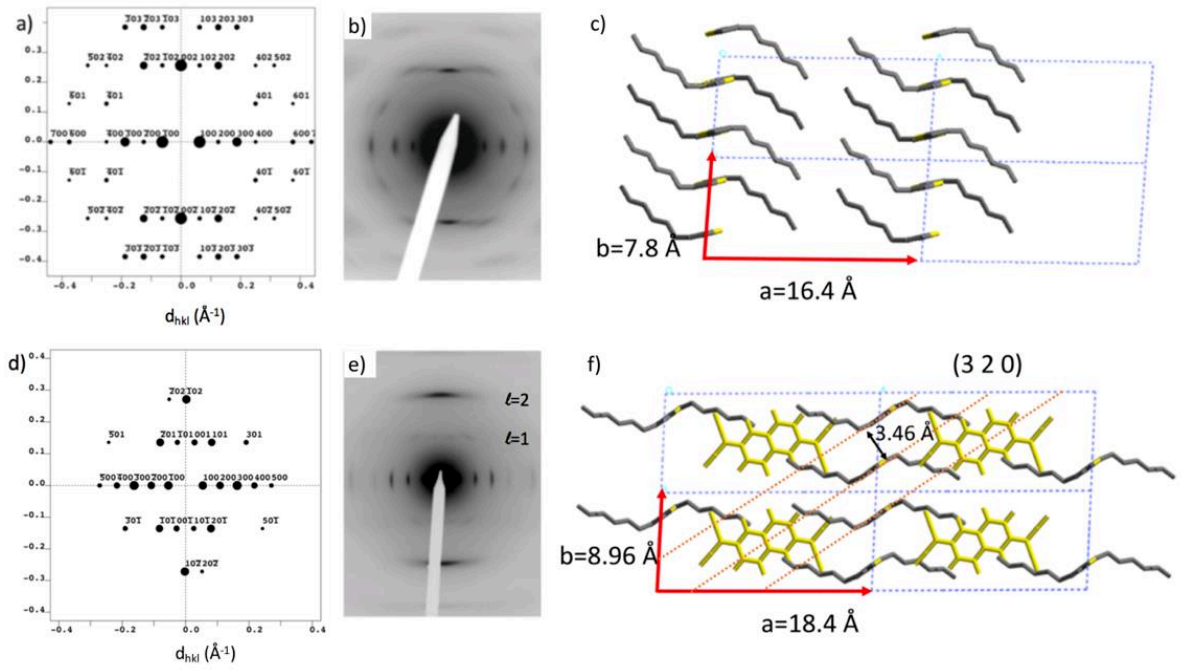


***Figure 6.*** *Comparaison des clichés de diffraction expérimentaux et calculés pour les films orientés de P3HT en forme non dopée (a,b) et dopés avec $F_6$TCNNQ (d,e) en utilisant la structure de la forme I de Kayunkid et al. (ref) et un modèle déterminé dans le cadre de cette thèse (f) respectivement. (c,f) projection selon l'axe c de la maille du P3HT et de la maille du P3HT :$F_6$TCNNQ modélisé dans le cadre de cette étude. Les dopants $F_6$TCNNQ sont illustrés en jaune.*

***Tableau 1**. Principales caractéristiques, structurales, spectroscopiques et thermoélectriques des films dopés de P3HT orientés et semi-cristallins.*

| Main characteristics of both phases | P3HT:$F_4$TCNQ | P3HT:$F_6$TCNNQ |
|---|---|---|
| Order parameter polaron | 0.91 | 0.78 |
| Order parameter anion | 0.62 | 0.82 |
| $d_{020}$ π-stacking distance (Å) | 3.6 | 3.6 |
| $d_{100}$ alkyl side chains separation (Å) | 18.1 | 19.2 |
| Estimated $F_4$TCNQ molecules per 100 thiophene units | 14 | 20 |
| Charge conductivity $\sigma_{//}$ max (S $cm^{-1}$) | 205 | 343 |
| Power factor $PF_{//}$ max (µW $m^{-1}$ $K^{-2}$) | 73 | 79 |

Afin de mieux rendre compte de la différence des mécanismes de dopages des couches avec $F_4$TCNQ et $F_6$TCNNQ, nous avons utilisé la spectroscopie polarisée UV-vis-NIR. Nous avons déterminé quelle est la distribution angulaire des bandes d'absorption caractéristiques des dopants et des polarons. La comparaison de ces deux distributions nous a permis de comprendre quel est le degré d'orientation des dopants par rapport aux chaînes polymères. Pour ce faire, nous avons calculé les paramètres d'ordre pour les dopants et les chaînes polymères. Nous montrons que les paramètres d'ordre sont quasi identiques pour les polarons et les dopants $F_6$TCNNQ alors qu'une différence importante est notée pour le $F_4$TCNQ. Nous attribuons ces différences à l'organisation des dopants aux sein des cristaux de P3HT. La diffusion rapide du $F_4$TCNQ empêche aux dopants d'atteindre un degré d'ordre élevé lors de leur intercalation contrairement au $F_6$TCNNQ.

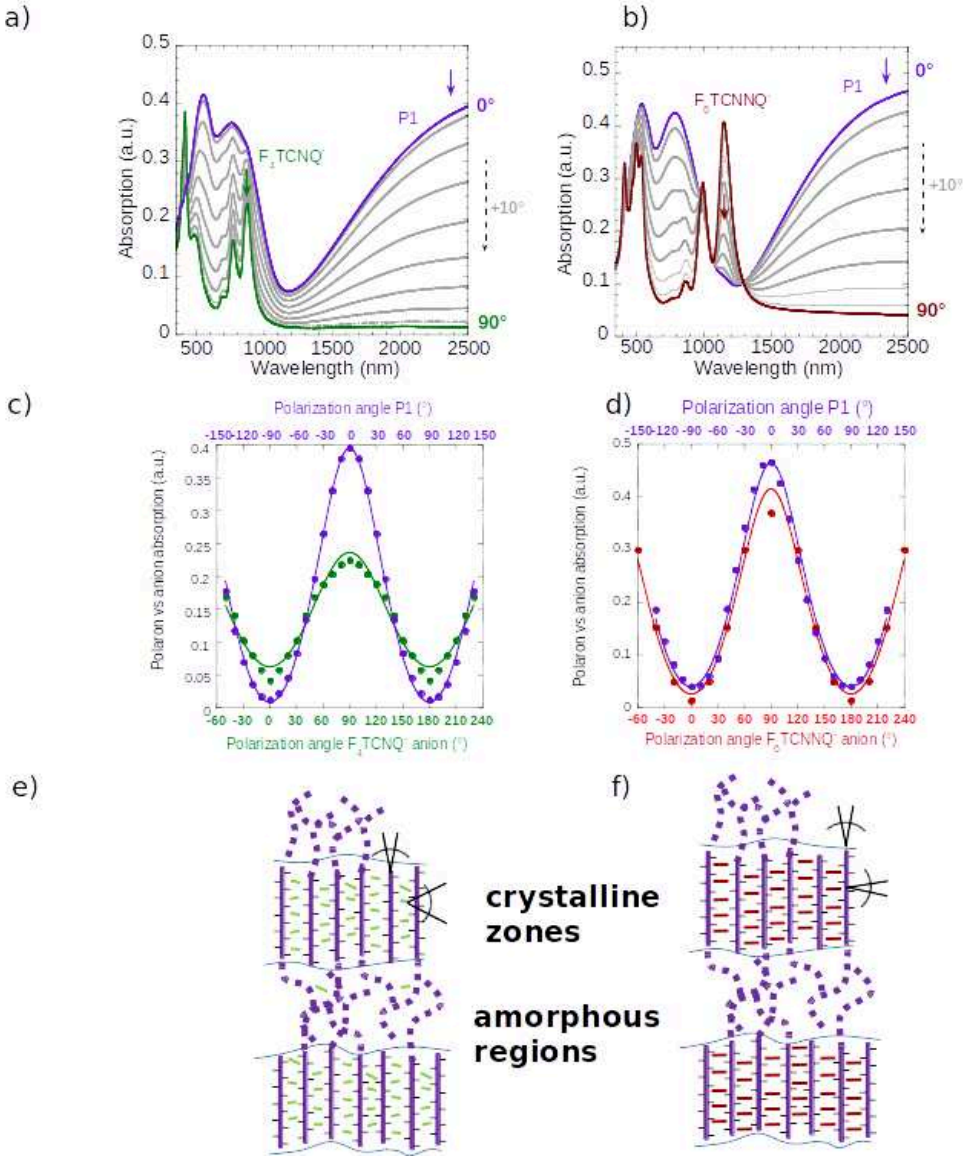


***Figure 6**: a) et b) Spectres d'absorption UV – Vis – NIR polarisés de films polymères conducteurs orientés pour les films dopés avec F4TCNQ et F6TCNNQ tracés pour différents angles (tous les 10°) entre la direction de polarisation et la direction du brossage du film. (0 ° correspond à la lumière incidente polarisée // R (en rouge) alors que 90 ° correspond à la lumière incidente polarisée ⊥ R (en bleu)). c), d) – Dépendance angulaire de l'absorbance de la bande polaronique P1 à 2500 nm (en rouge) , et du dopant à 873 nm (en vert) pour $F_4TCNQ^-$ (c) et à 1138 nm (en rouge) pour $F_6TCNNQ^-$ (d). e), f) illustration de la différence de l'organisation des dopants dans la structure cristalline du P3HT.*

a)

b)

c)

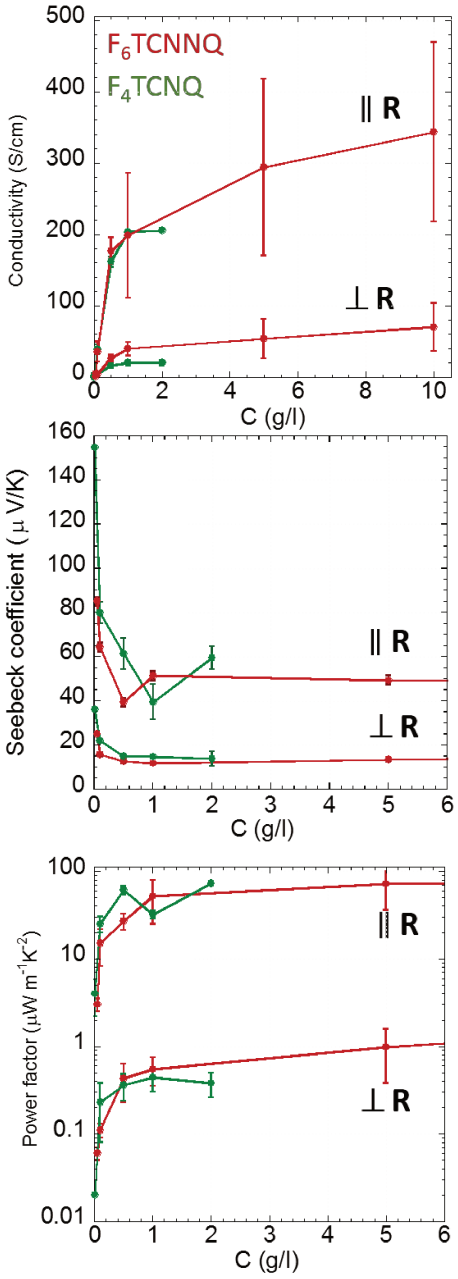


**Figure 7.** *Evolution de la conductivité électrique (a), du coefficient Seebeck(b) et du facteur de puissance (c) mesurés le long de la direction parallèle (// R) et perpendiculaire (⊥ R) à la direction du brossage pour les films orientés de P3HT dopés avec $F_4$TCNQ (vert) et $F_6$TCNNQ (rouge foncé). Les barres d'erreur sont principalement liées à une dispersion des points de mesure due à la variation du degré d'alignement obtenu par brossage.*

Les performances TE obtenues pour les films dopés avec $F_4$TCNQ et $F_6$TCNNQ sont assez semblables (voir Figure 7). Les films présentent une anisotropie forte de la conductivité et aussi du coefficient Seebeck. Dans le cas de $F_6$TCNNQ, on peut atteindre une conductivité plus élevée de l'ordre de 343 S/cm contre 205 S/cm pour $F_4$TCNQ. Toutefois, les facteurs de puissance obtenus restent très semblables pour les deux systèmes lorsqu'on est proche de la saturation, proche de 75 $\mu W.m^{-1}.K^{-2}$. Il est toutefois intéressant de voir que la conductivité continue à augmenter pour $F_6$TCNNQ même lorsqu'on passe à des concentrations de 10g/l alors que pour $F_4$TCNQ on a clairement une saturation de conductivité électrique dès 2 g/l.

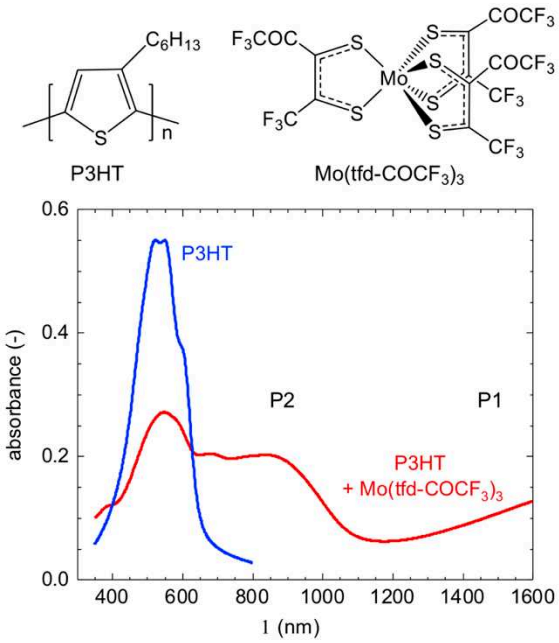


***Figure 8**. Illustration des structures moléculaires du P3HT et du dopant Mo(tdf-COCF₃)₃ et comparaison des spectres UV-vis-NIR de films de P3HT non-orientés avant et après dopage en solution de Mo(tdf-COCF₃)₃ en solution dans un mélange chloroforme/acétonitrile.*

Dans le 4ème chapitre, nous étudions le dopage de films P3HT semi-cristallins orientés avec le dopant composé métal-organique - Mo (tfd-$COCF_3$)$_3$ ((Molybdenum tris (1- (trifluoroacetyl) -2 - (trifluorométhyl) éthane-1,2-dithiolène))).[6] Nous rapportons un facteur de puissance thermoélectrique record allant jusqu'à 160 $\mu W \cdot m^{-1} \cdot K^{-2}$ pour le P3HT. Ce résultat est obtenu grâce à la combinaison du brossage à haute température de films minces avec l'utilisation d'un nouveau dopant, un complexe de molybdène dithiolène ayant une affinité électronique élevée (Mo(tfd-$COCF_3$)$_3$). La comparaison des spectres UV-vis des échantillons chimiquement dopés avec un matériau électro-chimiquement oxydé révèle un taux d'oxydation de 10%, soit un polaron pour 10 unités répétitives de 3-hexylthiophène. Le facteur de puissance élevé est dû à une augmentation de la mobilité des porteurs de charge et donc de la conductivité électrique dans la direction du

brossage. De plus, les propriétés TE de ces films dopés sont comparées à celles du P3HT dopé au $FeCl_3$. Les différences de structure et de propriétés TE sont mises en évidence.

La combinaison d'un dopant volumineux tel que Mo $(tfd\text{-}COCF_3)_3$ en combinaison avec une anisotropie structurale, ici réalisée par le brossage à haute température, est un moyen efficace pour améliorer les propriétés TE des polymères conjugués. Une conductivité élevée de $\sigma_{\parallel} \simeq (509 \pm 51)\ \mathrm{S/cm}$ est obtenue grâce à une forte mobilité des porteurs de charge le long de la direction de brossage. Dans le même temps, le coefficient Seebeck reste élevé $\alpha_{\parallel} \simeq (56 \pm 2)\ \mu\mathrm{V/K}$ , et par conséquent nous obtenons un facteur de puissance thermoélectrique record de $\alpha_{\parallel}^2 \cdot \sigma_{\parallel} \simeq (160 \pm 27)\ \mu\mathrm{W \cdot m^{-1} \cdot K^{-2}}$ pour P3HT. Ces résultats remarquables pour P3HT sont en partie aussi expliqués par le fait que le dopant peut doper à la fois les zones cristallines et amorphes du P3HT en raison de sa LUMO plus faible que pour $F_4TCNQ$ et $F_6TCNNQ$. L'autre raison expliquant l'efficacité de ce dopant est lié au fait que la cage organique du complexe de molybdène permet sans doute d'écranter les interactions Coulombiennes et donc de réduite le piégeage possible des porteurs de charge sur le squelette conjugué du P3HT.

L'anisotropie du coefficient Seebeck a été analysée dans le cadre de simulations du transport de charge utilisant la cinétique de Monte Carlo par scheunemann et al. (ref) On tient compte d'un modèle de transport dit à saut à portée variable (variable range hopping). L'anisotropie des films induite par le brossage est prise en compte dans le modèle en utilisant une longueur de délocalisation des porteurs plus grande dans la direction des chaînes (. $\xi_{\parallel} > \xi_{\perp}$). En supposant une anisotropie $\xi_{\parallel}/\xi_{\perp} = 4$ et une fréquence de sauts $\nu_0 = 2 \cdot 10^{13}\ s^{-1}$ on peut reproduire les tendances observes expérimentalement. Le transport est dominé par le « hopping » entre sites discrets dans la direction d'alignement. Les porteurs ne peuvent pas optimiser leur parcours par rapport à leur énergie, ce qui conduit à une augmentation de l'énergie de transport des porteurs $E_{tr}$ dans la

direction de l'alignement. Ainsi comme le coefficient Seebeck varie selon la formule $\alpha \propto (E_F - E_{tr})/T$ ($E_F$ est le niveau de Fermi), on a une augmentation de $\alpha_{\parallel}$ par rapport à $\alpha_{\perp}$.

La thèse se conclue par une mise en parallèle des différents systèmes étudiés en terme de dopants. Des perspectives générales ont été données quant à l'amélioration des propriétés thermoélectriques des films orientés de P3HT.

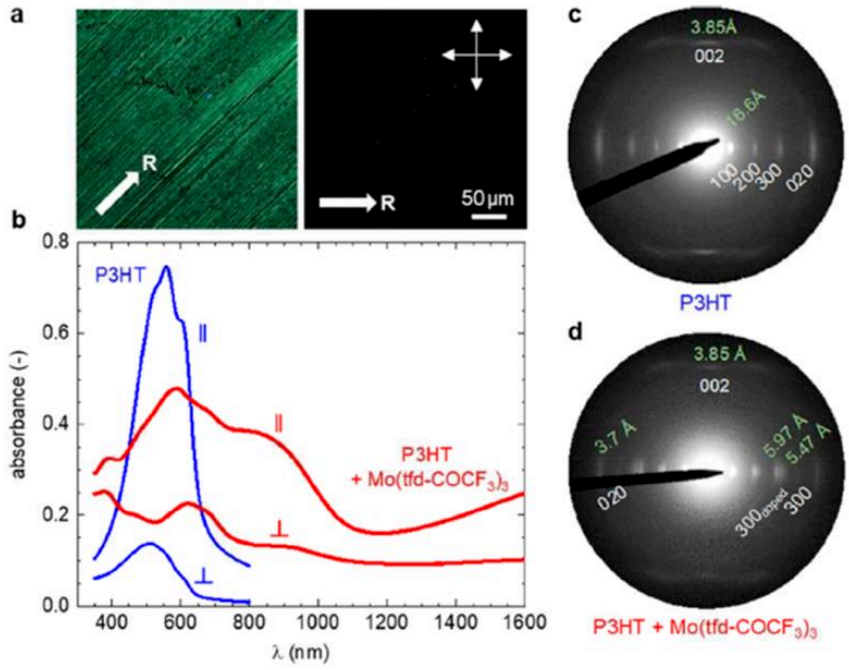


***Figure 3. (a)*** *Images sous microscope optique polarisé des films de P3HT après brossage et dopage séquentiel avec une solution de Mo(tfd-COCF₃)₃ (ACN/CHCl₃) avec $C_{Mo} \sim 1$ g L$^{-1}$; les doubles flèches croisées indiquent les orientations du polariseur et de l'analyseur; la flèche blanche indique la direction du brossage (R). (b) Spectre d'absorption UV - vis - NIR polarisé pour des films orientés de P3HT avant et après dopage avec $C_{Mo} \sim 1$ g L$^{-1}$ mesuré // R et perpendiculaire ⊥ R. (c, d) Clichés de diffraction électronique des films orientés de P3HT avant (bleu) et après (rouge) dopage avec une solution de Mo(tfd-COCF₃)₃.* [6]

***Tableau 1.*** *Conductivité électrique σ, coefficient Seebeck α (erreur ± 2 μV $K^{-1}$), facteur de puissance $\alpha^2\sigma$, densité ($N_v$) et mobilité des charges (μ), et niveau d'oxydation pour les films brossés d'épaisseur d dopés séquentiellement avec une mélange des solvant AcN:$CHCl_3$ ayant la concentration du dopant $c_{Mo}$; σ et α ont été mesurés immédiatement après le dopage mais sont restés relativement stables pendant le stockage dans une boîte à gants pendant une semaine, et même après une exposition ultérieure à l'air.*[6]

| $c_{Mo}$ (g $L^{-1}$) | $d$ (nm) | $N_v$ ($10^{26}$ $m^{-3}$) | ox. level (%) | $\sigma_{\parallel}$ (S $cm^{-1}$) | $\sigma_{\perp}$ (S $cm^{-1}$) | $\alpha_{\parallel}$ (μV $K^{-1}$) | $\alpha_{\perp}$ (μV $K^{-1}$) | $\alpha_{\parallel}^2\sigma_{\parallel}$ (μW $m^{-1}$ $K^{-2}$) | $\alpha_{\perp}^2\sigma_{\perp}$ (μW $m^{-1}$ $K^{-2}$) | $\mu_{\parallel}$ ($cm^2$ $V^{-1}$ $s^{-1}$) | $\mu_{\perp}$ ($cm^2$ $V^{-1}$ $s^{-1}$) |
|---|---|---|---|---|---|---|---|---|---|---|---|
| 1 | 44 | 4.0 ± 0.4 | 10 | 509 ± 51 | 84 ± 8 | 56 | 13 | 160 ± 27 | 1.0 ± 0.5 | 7.1 ± 1.1 | 1.2 ± 0.2 |
| 2.5 | 58 | 3.6 ± 0.4 | 9 | 593 ± 59 | 116 ± 12 | 47 | 17 | 131 ± 12 | 3.0 ± 0.8 | 9.3 ± 1.4 | 1.8 ± 0.3 |
| 7.5 | 53 | 4.4 ± 0.5 | 11 | 681 ± 68 | 50 ± 5 | 43 | 6 | 126 ± 12 | 0.2 ± 0.1 | 8.7 ± 1.3 | 0.6 ± 0.1 |

**References**

1. Jaziri, N. *et al.* A comprehensive review of Thermoelectric Generators: Technologies and common applications. *Energy Reports* (2019) doi:10.1016/j.egyr.2019.12.011.

2. Kroon, R. *et al.* Thermoelectric plastics: from design to synthesis, processing and structure–property relationships. *Chem. Soc. Rev.* **45**, 6147–6164 (2016).

3. Bubnova, O. *et al.* Optimization of the thermoelectric figure of merit in the conducting polymer poly(3,4-ethylenedioxythiophene). *Nature Materials* **10**, 429–433 (2011).

4. Hamidi-Sakr, A. *et al.* Highly Oriented and Crystalline Films of a Phenyl-Substituted Polythiophene Prepared by Epitaxy: Structural Model and Influence of Molecular Weight. *Macromolecules* **49**, 3452–3462 (2016).

5. Untilova, V., Biskup, T., Biniek, L., Vijayakumar, V. & Brinkmann, M. Control of Chain Alignment and Crystallization Helps Enhance Charge Conductivities and Thermoelectric Power Factors in Sequentially Doped P3HT:F4TCNQ Films. *Macromolecules* **53**, 2441–2453 (2020).

6. Untilova, V. *et al.* High Thermoelectric Power Factor of Poly(3-hexylthiophene) through In-Plane Alignment and Doping with a Molybdenum Dithiolene Complex. *Macromolecules* (2020) doi:10.1021/acs.macromol.0c01223.